Investigation of magnetic microstructures using novel transmission electron microscopy techniques.

by Alan Biggar Johnston.

submitted for the degree of Doctor of Philosophy at the Department of Physics and Astronomy, University of Glasgow.

October 1995

ProQuest LLC.
789 East Eisenhower Parkway
P.O. Box 1346
Ann Arbor, MI 48106 – 1346

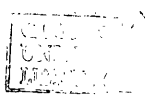

"The force is strong in you young Skywalker…but you're not a Jedi yet"

Darth Vader, The Empire Strikes Back, © George Lucus (1983).

Contents

Chapter 3. An analytical approach to coherent Foucault imaging.

Chapter 4. Computer simulation of coherent Foucault imaging.

Chapter 5. Experimental CF imaging.

Chapter 6. Transmission electron microscope investigations of ferrite (Fe_3O_4) thin films.

Chapter 7. Investigation of NiFe-Ag granular thin films.

Chapter 8. Conclusions and future work.

Acknowledgements

This thesis would not have been possible without the help of many others throughout the course of this work. Foremost I would like to thank Professor J.N. Chapman for his help and invaluable discussions and Professor R.P. Ferrier for his encouragement and provision of the electron microscope facilities in the Solid State Group at the University of Glasgow. Also I am grateful to Dr. L.J. Heyderman, Dr. S. McVitie and Dr. W.A.P. Nicholson for assistance in operating the CM20 (S)TEM and the HB5 STEM at Glasgow. I am greatly indebted to all those who have prepared the samples used in these studies; Dr. L. Zhou, Dr. B. Khamsehpour, Dr. D. Margulies and Dr. M.L. Watson. A special mention should also be given to (the soon to be) Dr M.F. Gillies and Dr R.J. Neville.

For maintenance of the electron microscope facilities at Glasgow I would like to thank the late Mr. J. Simms, the late Miss M. Low and Mr S. Conner for maintaining the CTEM machines, and Mr A. Howie for maintaining the CM20, the HB5 and the computer facilities.

I would like to thank SERC (ESPRC) and Philips Electron Optics for the provision of funding and equipment.

It only remains for me to thank Mary, Sandie and my family who have put up with me for the last few years.

Declaration

This thesis is a record of my work carried out in the Department of Physics and Astronomy at the University of Glasgow. The work described herein is my own, apart from the preparation of the electron microscope samples; the small permalloy elements (Chapter 5) were fabricated by L. Zhou and B. Khansehpour of the University of Glasgow, the Fe_3O_4 ferrite thin films (Chapter 6) were prepared by D. Margulies of the University of California, the NiFe-Ag granular thin films (Chapter 7) where prepared by M.L. Watson of the University of Coventry. Some of the work contained in this thesis has been published in the following papers:

"Lorentz Microscopy with Application of Large Magnetic Field."
L J Heyderman, S Young, A B Johnston and J N Chapman.
ICEM 13-Paris 17-22 July 1994 (1195-1196).

"Coherent Foucault imaging - A New Method of Imaging Magnetic Microstructures."
A B Johnston, J N Chapman and L J Heyderman.
ICEM 13-Paris 17-22 July 1994 (1197-1198).

"Coherent Foucault Imaging: A method for imaging magnetic domain structures in thin films."
J N Chapman, A B Johnston and L J Heyderman.
J. Appl. Phys. **76** (9), 1 November 1994.

"Coherent Magnetic Imaging by TEM."
J N Chapman, A B Johnston, L J Heyderman, S McVitie and W A P Nicholson.
IEEE transactions on Magnetics, **Vol. 30**,No 6, November 1994.

"The development of coherent Foucault imaging magnetic domain structures in thin films"
A B Johnston and J N Chapman.
J. Microscopy, **Vol. 179**, Pt2, 119 (1995).

Summary

The work described in this thesis is concerned with the high spatial resolution magnetic imaging which can be realised on the Philips CM20 transmission electron microscope (TEM). Central to the thesis is the novel TEM technique of coherent Foucault (CF) imaging which is used here to investigate small regularly shaped magnetic elements. In particular details are given relating to studies of the image formation process analytically, by computer simulations and, finally, by implementing CF imaging experimentally on the CM20. In the final chapters we look at Fe_3O_4 thin films which show a very complex, small scale magnetic microstructure, and we describe a TEM and compositional study of NiFe-Ag thin films.

The first chapter begins with an outline of basic ferromagnetism and the energy considerations governing domain configurations in ferromagnetic thin films. There is a brief discussion about the magnetic microstructure found in small elements and the different types of domain walls commonly found in thin films.

The second chapter considers the instrumental requirements of a TEM for imaging magnetic microstructure and formally introduces the Philips CM20 TEM at the University of Glasgow. Here we discuss the flexibility of the imaging column, along with the range of modifications which provide a 'micromagnetic laboratory' around the specimen region. We then consider the interaction between the incident electron beam and a ferromagnetic or electrostatic specimen. Finally, we discuss image formation in the TEM and the Lorentz imaging modes which are used to reveal magnetic microstructure.

An analytical description of coherent Foucault imaging provides insight into how a fringe pattern relating to the induction distribution within a magnetic specimen is produced. The interferogram can be thought of as an 'in-line hologram' which is capable of providing a quantitative description of the induction distribution across the specimen. In chapter 3 a basic theory shows how a suitable model is created and how the corresponding diffraction pattern and image are calculated. These ideas are expanded by analysing two systems, a semi-infinite uniformly magnetised thin film and a two domain element. Here, we discuss

the CF images which are obtained when an opaque aperture is positioned carefully in the back focal plane (BFP). Finally, the advantages of using a phase-shifting aperture, rather than the opaque aperture, are discussed.

The one-dimensional computer simulation of CF imaging, presented in chapter 4, goes beyond the simple analytical study and allows us to investigate how fringe visibility and spacing vary with precise positioning of the aperture in the diffraction plane. CF imaging with a small-hole phase-shifting aperture is also studied, with specific attention being paid to how the imaging conditions vary with the size of the small-hole. The magnitude of phase-shift introduced by the phase-shifting apertures is then discussed, to find how important its precise value is for experimental use. Thereafter, calculations are performed in which the angle subtended by the source is extended to show why a FEG source is favoured for CF imaging. These considerations are further discussed in the context of two-dimensional simulations which facilitate direct comparison with experimental images. A simple two domain element and a small element containing four domains in a closure structure are investigated.

In chapter 5 we discuss the implementation of CF imaging on the modified Philips CM20 TEM to obtain magnetic interferograms of small permalloy elements. These have been fabricated by electron beam-lithographic and evaporation techniques to create individual elements of thicknesses of 50nm and 30nm with in-plane dimensions between 0.2μm and 4.0μm. Elements studied were rectangular, triangular or rhomboidal in shape, forming a near-ideal model micromagnetic system. Their dimensions are comparable with what might be expected for the next generation magnetoresistive sensors in ultra-high density recording systems. Initially, the different aperture types are discussed to confirm the CF imaging theory discussed in chapters 3 and 4. High visibility fringes with the predicted periodicity are apparent across the magnetic element as a whole and give a direct and immediate picture of the spatial variation of induction. This study also provides insight into the effect of size and shape on the magnetic properties of the elements. Thereafter, the elements are investigated while being magnetised along their easy and hard axes. The effect of increasing the temperature in-situ is considered, the domain structures and the changes in the magnetisation of the elements being analysed as they approach the Curie temperature. Finally, two different samples prepared using different etching techniques

are compared, for the purpose of determining how the magnetic properties of material change during the fabrication process.

In chapter 6 we investigate Fe_3O_4 thin films. Previous studies have revealed that the epitaxial growth of Fe_3O_4 on single crystal MgO leads to the presence of a large anisotropy component randomising the moments; the origin of this is still unknown. These moments do not all lie in the plane of the film which shows that the local anisotropy component in these films is larger than the shape anisotropy. Here we would like to see if high resolution domain studies can provide any information on the spatial distribution of the random anisotropy. However, Fe_3O_4 specimens grown on MgO substrates have proved difficult to remove, so instead, polycrystalline films have been prepared on silicon nitride (Si_3N_4) window substrates. Initial measurements show these films to have good magnetic properties and to contain a random anisotropy component as in the epitaxially grown specimens. These specimens provide a challenge to the microscopist in that they are rather weakly magnetic (low M_s) whilst crystal contrast is high. Furthermore it transpires that both are on a comparable length scale. The TEM study undertaken here investigates the crystallite structure and magnetisation distribution in four Fe_3O_4 thin films of different thicknesses. The samples are initially imaged in the as-grown state and are subsequently magnetised in-situ to gain insight into the magnetisation process at a microscopic level.

In chapter 7 two sets of NiFe-Ag granular thin films which show the GMR effect are studied. This chapter exemplifies how a range of TEM techniques can be usefully deployed for characterising inhomogeneous nano-systems. Initially we discuss the bright field and diffraction imaging conditions, implemented on the Philips CM20 TEM. In the sections following, an extended VG HB5 scanning transmission electron microscope (STEM) is introduced. Included are a discussion of the microscope column, the detector systems and the equipment required to carry out energy dispersive x-ray (EDX) compositional analysis. When acquiring EDX spectral data the high-angle annular dark field (HADF) imaging mode is implemented which reveals contrast dependent on the atomic number ('Z contrast') of the investigated elements. The first specimens investigated are of similar composition and have been post-annealed at different temperatures. The TEM study reveals the size, texturing and phase boundary abruptness of the individual crystallites. EDX spectral analysis is also utilised to investigate small areas

showing different Z contrast in the HADF images to reveal the local compositions of Ni, Fe and Ag. The second set of specimens are of identical composition and have also been post-annealed at different temperatures. However, only the TEM study is achieved due to these samples being prepared on Ni grids rendering an accurate compositional study impossible.

In the final chapter we conclude this thesis and discuss possible future experiments following on from this work. We discuss the application of the CF imaging technique to samples in which the electrostatic contribution to the phase function is dominant. We then combine the electrostatic and magnetic terms into the phase function for a study of special magnetic force microscopy (MFM) tips. Finally, future experiments which could be carried out on the Fe_3O_4 and NiFe-Ag thin films are discussed.

Chapter 1

Magnetic properties of thin ferromagnetic films.

1.0 Introduction.

This chapter describes the origin of ferromagnetism (section 1.1) and how the total energy of the magnetic system is made up from various contributing energies (section 1.2). There is then a brief discussion about the magnetic microstructure found in small elements (section 1.3) and the different types of domain walls commonly found in thin films (section 1.4).

1.1 Ferromagnetic Materials.

A ferromagnetic material is one which possesses a spontaneous magnetic dipole moment, below a certain temperature called the 'Curie temperature (T_c)'. When the atoms are above the Curie temperature they act as paramagnets, showing a random orientation due to thermal agitation.

Ferromagnetism originates primarily from the orbital motion and spin of the electrons within an atom giving rise to a magnetic moment. The alignment of the atomic magnetic moments in ferromagnetic materials was proposed by Weiss[1]. Here, a molecular field ($\underline{H}_m$) within the material, proportional to the magnetisation $\underline{M}$, describes the interaction between neighbouring magnetic moments. The spin alignment can be explained by quantum

mechanical theory. The Pauli exclusion principal shows that the electron wavefunction has to be anti-symmetrical. Heisenburg[2] modelled this phenomenon defining the exchange energy which is responsible for ferromagnetism. The exchange energy is related to the relative orientation of two spins $\underline{s_i}$ and $\underline{s_j}$ of the atomic moments and is given by,

$$E_a = -J(r_{ij})\underline{s}_i \cdot \underline{s}_j \qquad [1.1]$$

where r_{ij} is the moment separation and $J(r)$ is the exchange integral, found to be positive in ferromagnetic materials. This implies that the minimum energy state is when the moments lie parallel to each other. In a larger magnetic system this gives rise to regions where all the moments lie in the same direction known as 'domains'.

1.2 Magnetic systems.

A micromagnetic theory[3] must be employed to examine systems on a larger than atomic scale. The magnetisation of a solid is described by a vector field,

$$\underline{M} = M_s \sum_i \underline{m}_i \qquad [1.2]$$

where m_i is the unit vector defining the orientation of each dipole moment and M_s is the saturation magnetisation. The total potential energy of a magnetic system is made up from many contributing energies,

$$E_{tot} = E_A + E_k + E_m + E_H \qquad [1.3]$$

Here the exchange energy (E_A), anisotropy energy (E_k), magnetostatic energy (E_m) and Zeeman energy (E_H) are considered. The resultant magnetic distribution within the sample is given by the minimum of the total potential energy. How the individual energies effect the magnetisation will be discussed in the following sections.

1.2.1 Exchange energy.

The exchange energy of a magnetic specimen is due to the relative orientation of the dipole moment spins (Section 1.1). On a larger scale the exchange integral involves only the nearest neighbours. With α,β and γ representing the direction cosines of the magnetisation vector, $\underline{M_i}=M_S\underline{m_i}(\alpha(\underline{r}), \beta(\underline{r}), \gamma(\underline{r}))$.

$$E_A = A\int_V \left[(\nabla\alpha)^2 + (\nabla\beta)^2 + (\nabla\gamma)^2\right]dV \qquad [1.4]$$

where A is the exchange constant of the material given by,

$$A = \frac{nJs^2}{a} \qquad [1.5]$$

a is the lattice constant of the material, n is a constant depending on the crystalline structure (1 simple cubic, 2 body centred cubic (BCC) and 4 face centred cubic (FCC)) and s^2 is dimensionless square of the spin of the magnetic moment. The exchange constant J is positive for ferromagnetic materials which gives the lowest energy for parallel spins. This leads to the magnetic moments of the sample aligning to give a non-zero magnetisation.

1.2.2 Anisotropy energy.

The ferromagnetic anisotropy energy[4] allows for a preferred direction of magnetisation dependent on crystallographic orientation. The anisotropy energy can be given as a series expansion of the directional cosines. For a cubic crystal, taking the first two terms gives,

$$E_k = \int_V \left[K_1\left(\alpha^2\beta^2 + \alpha^2\gamma^2 + \beta^2\gamma^2\right) + K_2\alpha^2\beta^2\gamma^2\right]dV \qquad [1.6]$$

where the crystal and co-ordinate axes are co-incident. For hexagonal or uniaxial crystals,

$$E_k = \int_V \left[K_1\left(1-\gamma^2\right) + K_2\left(1-\gamma^2\right)^2 \right] dV \qquad [1.7]$$

where the *c*-axis coincides with the symmetry axis. K_1 and K_2 are the anisotropy constants of the material. The minimum potential energy occurs when the magnetisation is lying along the preferred 'easy axis'. Perpendicular to the easy axis lies the 'hard axis' which is an energy maximum.

Another crystallographic phenomenon is represented by the magnetostriction energy[4]. This is related to the stress within the system and its effect on the magnetisation. It will not be considered fully here.

1.2.3 Magnetostatic energy.

Magnetostatic interaction of the dipoles within the material lead to magnetic fields. The demagnetising field energy expression is,

$$E_m = -\frac{1}{2}\mu_0 \int_V \underline{M}.\underline{H}_d dV \qquad [1.8]$$

where H_d is the demagnetising field calculated from,

$$\underline{H}_d(\underline{R}) = \frac{1}{4\pi}\int_V \frac{-\nabla.\underline{M}}{R^2} dV + \frac{1}{4\pi}\int_S \frac{\underline{M}.\underline{n}}{R^2} dS \qquad [1.9]$$

$\underline{n}$ is the unit vector normal to the surface and $\underline{R}$ is the directed between the source and the field points. The term $\nabla.\underline{M}$ is equivalent to the magnetic volume charge and $\underline{M}.\underline{n}$ is the magnetic surface charge. The magnetostatic energy is highly dependant on the sample geometry. It is at a minimum when the magnetisation forms a closed structure with no free poles (Section 1.3). This is in direct opposition with the exchange energy.

1.2.4 Zeeman energy.

The Zeeman energy from an external field on the sample is given by,

$$E_m = -\mu_0 \int \underline{M}.\underline{H} dV \qquad [1.10]$$

where μ_0 is the magnetic permittivity of free space and $\underline{H}$ is the applied field. The magnetic moments align along the direction of the applied field in the minimum energy state.

1.3 Micromagnetics of soft magnetic materials.

The form of the micromagnetic structure[5] of the system is determined by the minima of the total potential energy. This leads to areas of near uniform magnetisation known as 'domains', separated by 'domain walls' where the magnetisation rotates to the direction of the neighbouring domain magnetisation.

Here consider the potential energy of a small element fabricated from a 'soft' magnetic material, one which has a negligible anisotropy energy. Figure 1.1 shows three possible domain structures.

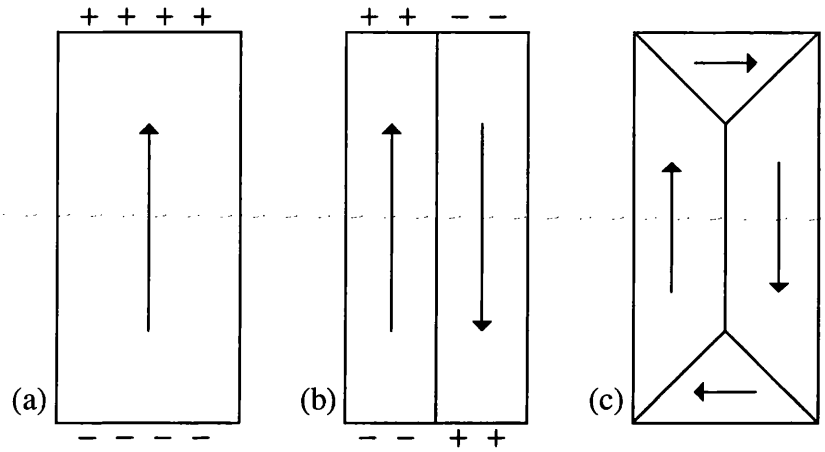

Figure 1.1 *Small element showing different micromagnetic structure.*

Initially the element is uniformly magnetised (figure 1.1a). The exchange energy is at a minimum because all of the magnetic moments are lying parallel. However, the free poles at either end of the element give rise to a large magnetostatic energy. Figure 1.1b shows an element containing two uniformly magnetised domains pointing in opposite directions, separated by a domain wall. Here a domain wall energy must be considered due to the slight increase in the exchange energy. This structure has the advantage of reducing the magnetostatic energy. A further development is for the magnetisation to form closure domains at either end (figure 1.1c). There are no longer any surface poles giving a minimum magnetostatic energy. The actual structure that would be present in the material is given by the minimum of the total energy. The equilibrium structure that would form is highly dependant on the strength of the exchange coupling and the saturation magnetisation of the material. In the case of a 'hard' magnetic material the anisotropy would also contribute to the micromagnetic structure.

1.4 Domain walls.

Domain walls form to reduce the magnetostatic energy of the magnetic system. In turn there is an increase in the exchange energy and anisotropy energy which is described by a domain wall energy. Three types of domain wall are discussed; the Bloch wall[6] , the Néel wall[7] and the cross-tie wall.

The type of wall which occurs is dependant on the sample thickness. In one-dimension, the Bloch wall (figure 1.2a) occurs in bulk ferromagnetic material and is only present in thicker thin films. The magnetisation vector rotates out of the plane of the thin film. As the sample thickness is reduced a Néel wall (figure 1.2b) can form. Here the magnetisation rotates in the plane of the film. This wall structure occurs when the magnetostatic energy of the film becomes significant and this type of wall becomes energetically favourable.

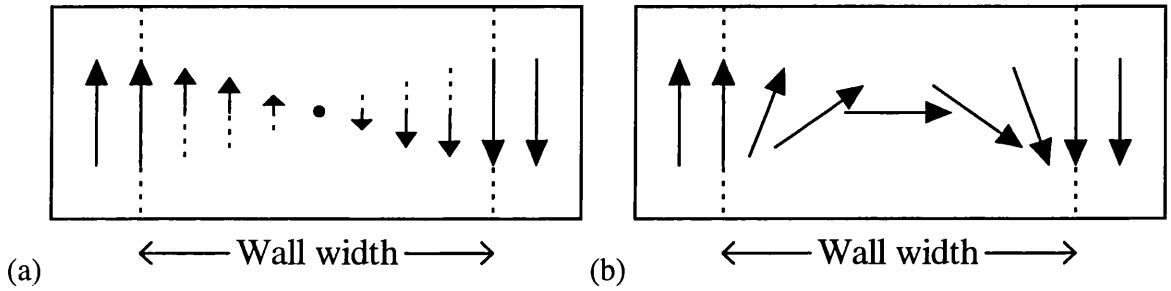

Figure 1.2 *A schematic representation of the (a) Bloch wall and the (b) Néel wall.*

A more complex wall structure is the two dimensional cross-tie wall (figure 1.3). This can occur when the sample thickness is in the transition region between the Bloch and Néel wall. The cross-tie wall is a combination of these wall types, such that the magnetisation vector rotates both in and out of the plane of the film.

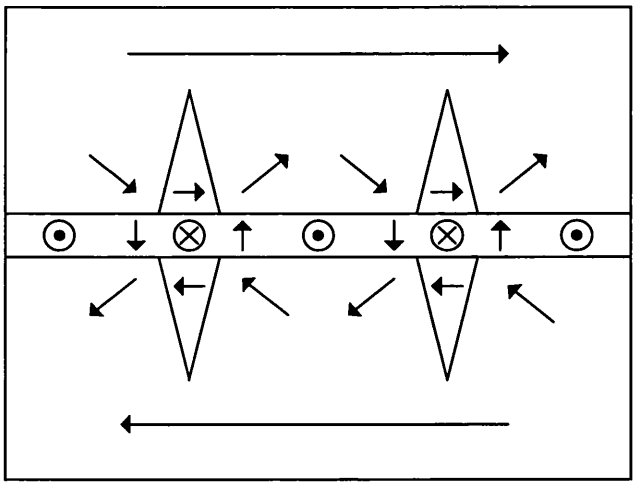

Figure 1.3 *Schematic diagram of a cross-tie wall.*

1.5 Conclusion

In this chapter we have discussed the magnetic properties of thin ferromagnetic films. Ferromagnetism originates primarily from the orbital motion and spin of the electrons within an atom giving rise to a magnetic moment. We have discussed the total energy of the magnetic system which is made up from contributions from the exchange, anisotropy, magnetostatic and Zeeman energies. The minimum of the total energy gives rise to regions where the magnetisation lies in the same orientation as its neighbours, known as domains, which are separated by regions where the magnetisation vectors rotate, within the domain walls. We have also investigated some of the basic domain structures to be found in small rectangular elements. Here, we discussed the individual terms that contribute to the total energy of the system and how they lead to different micromagnetic structures forming within the elements.

In chapter 2 we discuss the Lorentz imaging modes of the transmission electron microscope (TEM). These techniques can be utilised to reveal information on the magnetic microstructure. Different imaging modes are discussed which can reveal the orientation of the magnetisation within domains and the positions of domain walls.

In chapters 3 and 4 the novel transmission electron microscopy technique of CF imaging is discussed analytically and by computer simulations respectively. The samples that we simulate are small elements of soft magnetic material which show domain and domain wall configurations which are readily explained in terms of the total magnetic energy of the system. This approach is also successfully applied in chapter 5, when the CF imaging technique is applied experimentally to image complex domain structures. Here, elements are imaged when applying an in-situ external field which leads to the inclusion of the Zeeman energy term in the total energy equation. We also heat the elements which leads to changes in the micromagnetic structure because the contributing energies are all highly dependent on temperature.

The investigation of Fe_3O_4 crystalline thin films (chapter 6) reveals a complex domain structure on a very small scale. These films show a large anisotropy component which leads to the formation of small domains in which the magnetisation is randomly orientated.

In chapter 7 we look at NiFe-Ag granular thin films with show the giant magnetoresistance (GMR) effect. The magnetisation within these types of thin film forms a super-paramagnetic matrix which is discussed further in section 7.0. It should be noted, that in this study we do not reveal the magnetic microstructure but are concerned with the changes in the crystallographic structure when the samples are subjected to different annealing conditions.

References

[1] P. Weiss, J. Phys., **6**, 661, (1907).

[2] W. Heisenberg, Z. Physik, **49**, 619, ,(1928).

[3] W.F. Brown, 'Micromagnetics', pubs. Interscience (1963).

[4] S. Chikazumi, 'Physics of Magnetism', John Wiley and Sons, (1964).

[5] L. Landau and E. Lifshitz, Phys. Z. Sowjetunion, **8**, 153 (1935).

[6] F. Bloch, Z. Physik, **74**, 295 (1932).

[7] A. Hubert, Phys. Solidi, **38**, 699 (1970).

Chapter 2

Transmission electron microscopy to investigate magnetic microstructure.

2.0 Introduction

This chapter considers the instrumental requirements of a transmission electron microscope (TEM) for imaging magnetic microstructure. The Philips CM20 TEM at the University of Glasgow is introduced in section 2.1. Here we discuss the flexibility of the imaging column, along with the range of modifications which provide a 'micromagnetic laboratory' around the specimen region.

In sections 2.2 and 2.3 we consider the interaction between the incident electron beam and a ferromagnetic or electrostatic specimen. Finally, we discuss image formation in the TEM (section 2.4) and the 'Lorentz imaging' modes which are used to reveal magnetic microstructure.

2.1 TEM instrumental requirements and the modified CM20.

Novel thin film technology demands an ever increasing need for a higher spatial resolution in magnetic images. Many of the materials of interest are markedly inhomogeneous, containing feature sizes on a nanometer scale. Traditional TEM imaging of magnetic microstructure has shown a typical resolution of 40-80nm with a maximum magnification

of ≤5000 times[1]. Here, imaging is carried out with the objective lens switched off because the fields present would drastically alter the magnetic microstructure. The modified CM20 provides a ten fold improvement for magnetic imaging with a spatial resolution of <2nm and a maximum magnification of 60000 times[2].

To fully understand this increase in resolution and maximum magnification we must consider the components of the TEM.

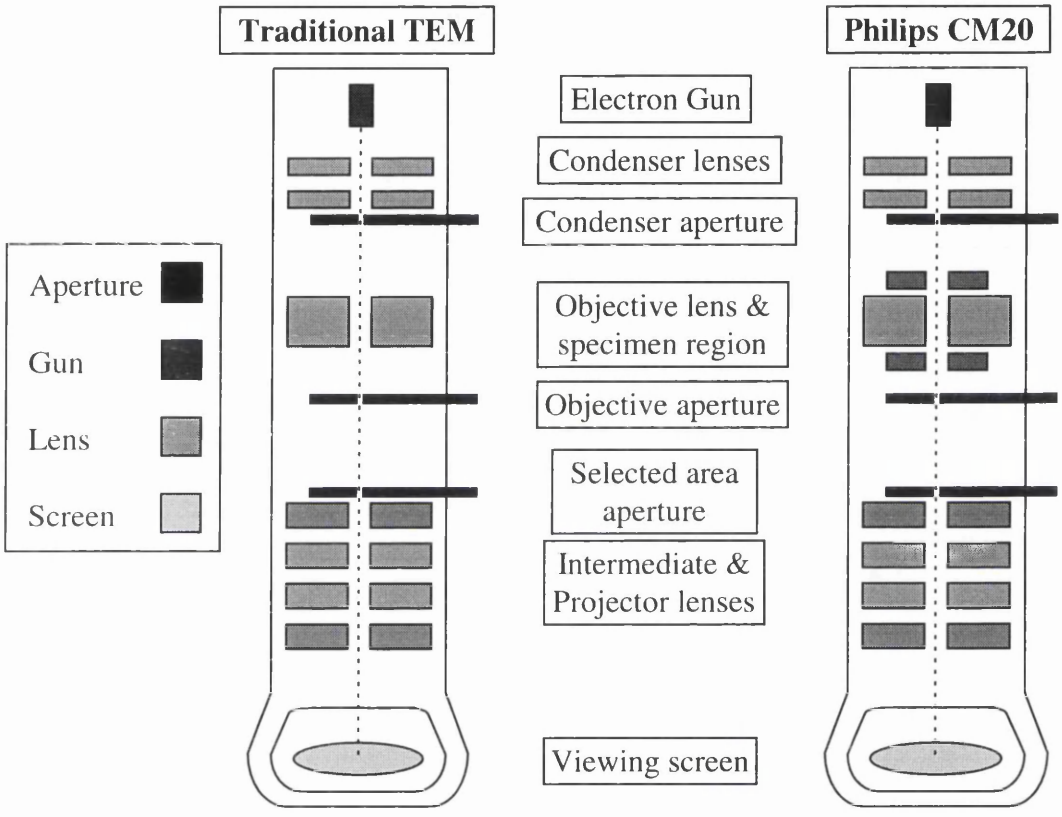

Figure 2.1 *Lens diagram of the traditional TEM and the modified Philips CM20*

An electron microscope consists of an electron gun and an assembly of electron lenses. A schematic diagram of the column region of a traditional TEM and the modified CM20 are shown in figure 2.1. Instantly apparent modifications to the CM20 are the extended lens setup, with the inclusion of two mini-lenses above and below the objective lens. The individual regions of the TEM column will be discussed in the following sections.

2.1.1 Electron gun system.

The electrons in the TEM are produced in the gun region[3]. Here there is a small source from which the electrons are emitted. There is an electrostatic lens to provide a limited focusing effect and initially accelerate the emerging electrons to typically 40keV. Further acceleration comes from a series of accelerating anodes to give electron energies of up to 400keV. In the case of the CM20 (figure 2.2) the electrons can have energies from 40-200keV. For 200keV the corresponding electron wavelength is 0.0251Å.

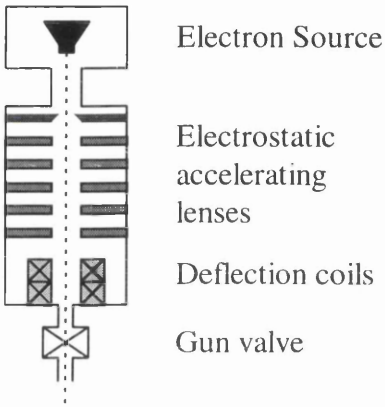

Figure 2.2 *A schematic diagram of the gun section of the CM20.*

There are three main types of electron source used in TEMs; the tungsten filament, LaB_6 and field emission gun (FEG)[4]. The main criterion to be considered in a TEM electron source is the brightness, a measure of the current density per steradian. The tungsten filament provides an inexpensive but rather limited thermionic electron source. The LaB_6 filament comprises a small LaB_6 crystal mounted upon a tungsten filament. This provides an increase in brightness, 10 times higher than that of tungsten, by reducing the electron work function on the surface of the source. The field emission gun provides an almost point source with a very high brightness, 1000 times higher than that of a tungsten filament. Field emission takes place when a material with a suitable work function is placed in a strong extraction electric field. A cold FEG uses a pointed tungsten cathode. This gun is prone to short term instability and drift, and also requires flashing on a regular basis. An improvement on this is the thermal field emitter or Schottky emitter which uses a tungsten tip which is zirconiated to reduce the work function. This gun provides greater

stability than the cold FEG at the expense of a slight reduction in the brightness. The CM20 is fitted with a Schottky FEG for these reasons.

2.1.2 Magnetic lenses and their aberrations.

The TEM lenses may be electrostatic or magnetic in type. Magnetic lenses are preferred to electrostatic lenses because of their small optical aberrations and their freedom from troubles associated with high voltages. The most critical component of a magnetic lens (figure 2.3) is the soft-iron pole-piece, which produces an axially symmetric field for focusing the electrons. The rest of the lens is a magnetic yoke containing the windings for energising the lens with d.c. current; such current variations lead to changes in the focal length.

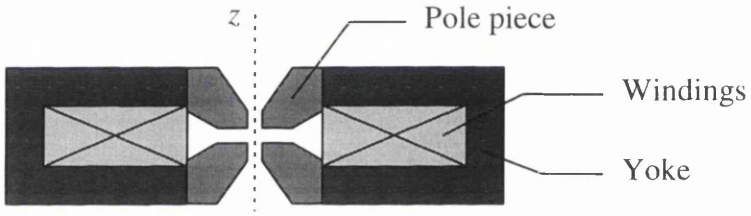

Figure 2.3 *Cross section of an electron lens.*

It can be shown[5] that electrons travelling at small angles to the axis are focused by the magnetic field H of the pole piece. The equations of motion of the electron in the axially symmetric magnetic field lead to the paraxial ray equation, which predicts quite generally the image forming properties of the field. When the axial extent of the magnetic field is small compared with the focal length f,

$$\frac{1}{f} \propto \frac{1}{E} \int_{gap} H_z^{\,2} dz \qquad [2.1]$$

where E is the electron energy and H_z is the z-component of the field. Owing to the radial velocity component of the electron and axial field H_z, the plane of motion of the electron also rotates. The rotation in a thin lens is given by,

$$\theta = \left(\frac{1}{E}\right)^{\frac{1}{2}} \int_{gap} H_z dz \qquad [2.2]$$

where θ is in radians. Related formulae, complicated by geometric factors, also hold for thick lenses.

Electron lenses have aberrations which limit the resolution attainable in various ways. The aberrations in the objective lens[6] are by far the most important. We shall be concerned with the spherical aberration, astigmatism and chromatic astigmatism.

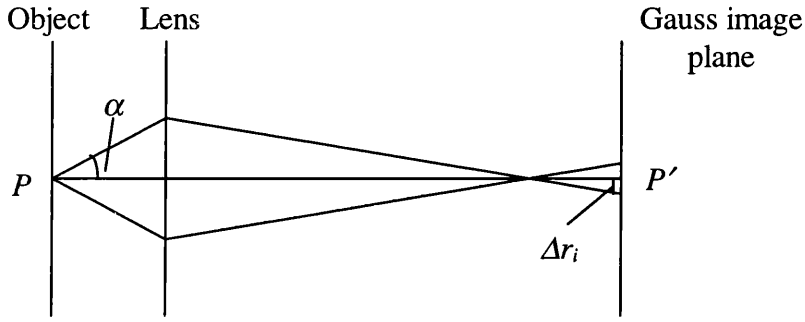

Figure 2.4 *Illustrating the phenomenon of spherical aberration*

Spherical aberration is the chief defect in the objective lens since at present there is no convenient way of correcting it. Figure 2.4 shows how electrons leaving a point P on the object at an angle α to the axis arrive at the Gaussian image plane at a distance $\Delta r_i = MC_s\alpha^3$ away from the Gauss image point P'. A pencil of semi-angle α thus gives rise to a disk of confusion of radius Δr_i in the image plane. Referred back to the object, the corresponding disc of confusion is of radius,

$$\Delta r_s = C_s\alpha^3 \qquad [2.3]$$

where C_s is the spherical aberration coefficient of the lens and is usually of the order of two or three millimetres in high resolution objective lenses. It should be noted that the spherical aberration of a magnetic lens is always positive. The off axis ray is always bent

more than it should be and marginal rays are always brought to a focus closer to the lens than axial rays.

Astigmatism results from asymmetry in the objective lens field produced by inaccuracies in manufacture or by inhomogeneities in the soft-iron pole-piece. The lens effectively has different focal lengths for paraxial rays in the two principal planes of asymmetry. Figure 2.5 shows a conical pencil of rays which form two different line foci P_h' and P_v' at right angles.

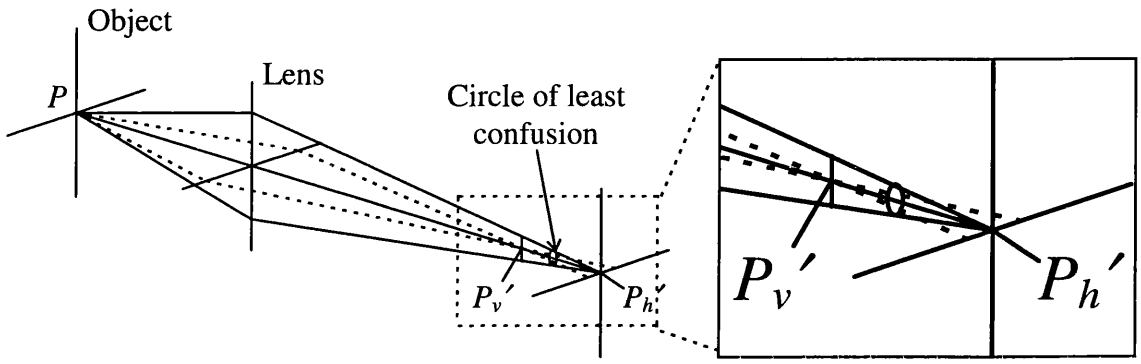

Figure 2.5 *Illustrating the phenomenon of astigmatism.*

To compensate the astigmatism an adjustable correcting device known as a stigmator is usually built into the lens for producing equal and opposite astigmatism to the residual astigmatism of the pole-piece. The CM20 has stigmators in the second condenser lens for correcting astigmatism in the illumination, the objective as discussed above and the diffraction lens to correct asigmatism in the diffraction pattern.

Chromatic aberration arises if there is an energy spread of the imaging electrons, introduced by the specimen or by instability in the beam voltage supply. In terms of equation 2.1 the focal length of the objective varies if E varies. Electrons which have lost energy are bent more by the objective field and therefore again a disc of confusion forms in the image plane. From equation 2.1 and the thin lens formula, the radius of the disc in object space is,

$$\Delta r_c = f\alpha\frac{\Delta E}{E} \qquad [2.4]$$

where ΔE is the energy spread. For a thick lens,

$$\Delta r_c = C_c\alpha\frac{\Delta E}{E} \qquad [2.5]$$

where C_c is the chromatic aberration coefficient, usually of the same order but slightly less than f.

2.1.3 Condenser lenses and aperture.

There are generally two condenser lenses that are used to illuminate the specimen with electrons[6]. The function of the first condenser, which is usually a strong lens, is to demagnify the beam source. The second condenser projects this demagnified image onto the specimen and allows for user control of the illuminated area. The condenser aperture is required to define the angle subtended by the source and can increase the coherence of the system as its size is reduced. The CM20 is fitted with the standard two condenser lenses setup.

2.1.4 Objective lens and aperture.

The specimen to be examined is placed in the centre of the objective lens pole-piece gap. The objective lens provides a limited magnification (≈50x) in the TEM for normal imaging modes. Figure 2.6 shows a cross-section of the cylindrically symmetrical objective 'twin lens' present in the CM20. In the Glasgow University instrument the bore is extended to 20mm. The objective lens is the most influential in determining the electron optical performance (Section 2.1.2). In fixed beam mode[2] the 0.14nm gold lattice fringes have been resolved although the point resolution has dropped to 0.36nm on account of the expanded gap.

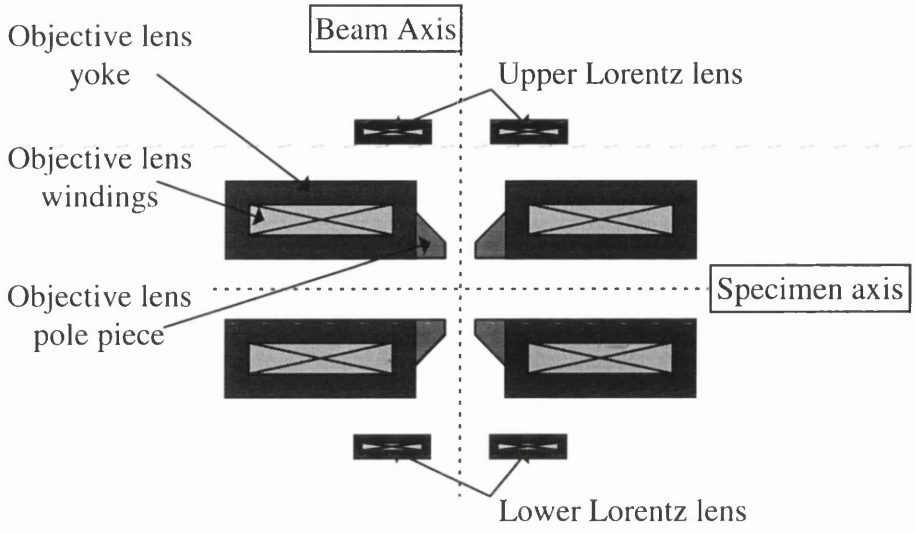

Figure 2.6 *The CM20 objective twin lens and the Lorentz lenses.*

The objective lens is not used in magnetic imaging modes because it drastically alters the magnetic fields around and within the specimen. Compensation for the loss of the objective lens when imaging magnetic structures is by the addition of two super mini-lenses situated above and below the objective, all fitting into the standard CM20 column. Use of these non-immersion 'Lorentz lenses' mean the specimen in its normal location is in a field free space, enabling the magnetic microstructure to be observed. In fixed beam mode[2], where the lower Lorentz lens becomes the principal imaging lens, 1.3nm lattice fringes have been resolved and the point resolution is calculated to be 2.1nm. It should be noted that whilst the standard objective lens plays no imaging role during the observation of the magnetic microstructure, it can be used to change the magnetic state of the specimen. Imaging has been carried out successfully over an extensive field range 0 to 0.65T.

The objective aperture is positioned at the bottom of the pole-piece gap. This is used to produce diffraction contrast images (Section 2.4.1).

2.1.5 Diffraction, intermediate and projector lenses.

The first intermediate lens determines whether an image or a diffraction pattern is seen on the viewing screen. It is often referred to as the 'diffraction lens'. The other intermediate lenses provide additional magnification (up to 100x) and are used to compensate any rotation in the image. The projector lens provides the majority of the magnification, typically 200x. The objective and projector lenses are usually at a fixed excitation (focal length) and the intermediate lenses allow for different magnifications by changing their excitation. In the CM20 these lenses act in the same manner in normal imaging, where the objective lens is the principal imaging lens, and in magnetic imaging modes, where the Lorentz lenses are the principal imaging lenses.

2.1.6 Specimen region

The typical space around the specimen region is very limited. The CM20 has a larger region available, due to a larger gap between the pole pieces. This extended gap allows for what can be thought of as a 'micromagnetic laboratory'. Figure 2.7 shows a schematic cross section normal to the z-axis.

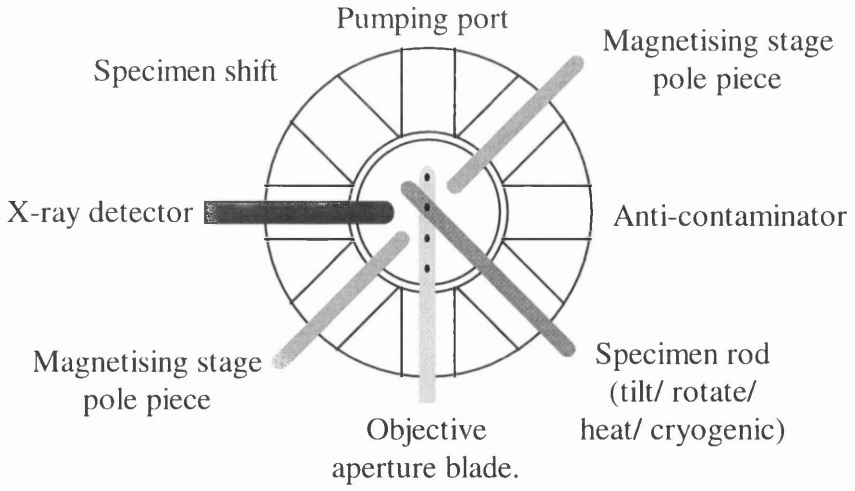

Figure 2.7 *Cross-section of the CM20 specimen region.*

Principally, there is room for a magnetising stage and an x-ray detector to be accommodated close to the specimen. Other features have been incorporated in the specimen rod. There is a heating stage which covers a temperature range of 30-1000°C which is sufficient for heating the majority of ferromagnetic materials to above the Curie temperature (Section 1.1). There is also a specimen stage with cryogenic capabilities to reduce the temperature from 30 to -160°C. This has uses in superconducting[7] and giant magnetoresistant materials[8] which show interesting properties at a reduced temperature.

2.1.7 Methods of recording/acquiring the image

The type of film used in my project was CEA Reflex-15 which typically required a 5 second exposure time for images at a magnification of 20kx and 0.1s for diffraction patterns using a camera length of 60cm. In preliminary experiments, on a JEOL 2000 fitted with a tungsten hairpin filament, Kodak 4489 has been used to record some diffraction patterns; exposure times were about 10 times longer than with the Reflex film.

A TV pick-up with video system is also incorporated on the CM20, underneath the camera chamber. This comprises a camera with a RCA silicon intensifier target tube (SIT) viewing a single crystal YAG screen. Images are acquired using an Agar camera control unit T1570 followed by an Arlunya image processor TF 6000. This allows the image to be enhanced by integrating the signal over several frames, either statically or dynamically. The images can readily be stored directly onto video tape or a PC with frame grabbing capabilities.

2.1.8 Vacuum system

A typical TEM has operates in a vacuum of $\approx 10^{-5}$Pa. The CM20 has three separate vacuum regions which are connected by differential pumping apertures. There are two ion-getter pumps around the gun region to maintain a vacuum of 5×10^{-7}Pa, which ensures that the gun does not flashover. The specimen region has a vacuum of 2.7×10^{-5}Pa using another ion-

getter pump and an anti-contamination large surface, gold-plated finger. The viewing chamber has an average vacuum of 10^{-6}Pa using an oil diffusion pump with buffer tank and intermittently pumping rotary pump. Additionally, for clean specimen changes the specimen rod is pumped by a turbo pump and back filled with dry N_2 in an automatic cycle sequence.

2.2 Electron-Ferromagnetic Specimen Interaction

The electron beam interaction with a ferromagnetic specimen[9] can be explained classically in terms of the Lorentz force. Figure 2.8 shows a ferromagnetic sample containing two domains where the magnetisation is orientated in opposite directions, separated by a domain wall.

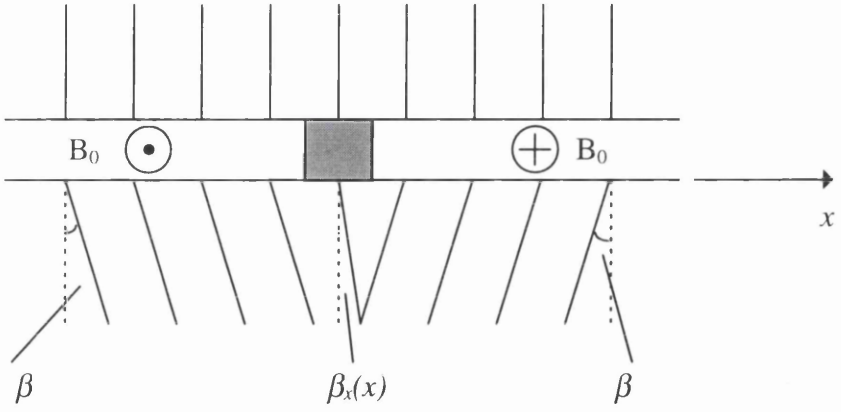

Figure 2.8 *Interaction between the incident electron beam and a uniform ferromagnetic thin film specimen.*

Electrons passing through the specimen are deflected towards the x-direction through an angle,

$$\beta_x(x) = \frac{e\lambda}{h}\int_{-\infty}^{\infty} B_y(x,y)dz \qquad [2.6]$$

where $B_y(x,y)$ is the component of magnetic induction in the y-direction at the point (x,y), e is the electronic charge, λ is the electron wavelength and h is Plank's constant. For a

region of uniform magnetisation (M_s) and a constant thickness (t) the deflection angle is given by,

$$\beta = \frac{eB_0 \lambda t}{h} \qquad [2.7]$$

where the magnetic induction is given by $B_0=\mu_0 M_s$. The Lorentz deflection for 200keV electrons passing through a 50nm thick film with a saturation induction of 1T gives $\beta \approx 3\text{x}10^{-5}$rad. This angle is much smaller than a typical Bragg deflection of $\approx 10^{-2}$rad.

The interaction between the beam and the specimen must also be explained from a quantum mechanical viewpoint in order to understand the interference effects present in imaging modes such as electron holography (Section 2.4.4). Aharonov and Bohm[11] (1959) showed that the magnetic induction introduces a phase shift between two electron rays originating from the same initial point which rejoin after travelling along different equidistant paths. If the electrons enclose a magnetic flux N the phase-shift can be written as,

$$\phi = \frac{e}{\hbar} N \qquad [2.8]$$

In the case of an electron plane wave incident on the magnetic specimen the phase shift between any two points along the x-axis is given by,

$$\phi(x_2 - x_1) = \frac{2\pi et}{h} \int_{x1}^{x2} B_y(x) dx \qquad [2.9]$$

A ferromagnetic specimen can be considered as a pure phase object to the electron beam. Lorentz microscopy is therefore a branch of phase contrast microscopy.

2.3 Electron-Electrostatic Specimen Interaction

This section covers the electron beam interaction with an electrostatic component of a specimens phase function. The energy expression of an electron in free space is given by,

$$E = \frac{\hbar^2 k^2}{2m} \qquad [2.10]$$

where $\hbar$ is $h/2\pi$, k is the wave number and m the electron mass. When the electron passes through an electrostatic field, equation 2.10 is modified to,

$$E = \frac{\hbar^2 k'^2}{2m} - V_0 \qquad [2.11]$$

where V_0, is the inner potential of the material, typically 7-17V. The ratio of the wavenumbers, considering the first term of a binomial expansion gives,

$$\frac{k'}{k} = \left(1 + \frac{V_0}{E}\right)^{\frac{1}{2}} \approx 1 + \frac{V_0}{2E} \qquad [2.12]$$

This gives the ratio of the wavelengths to be,

$$\frac{\lambda}{\lambda'} = 1 + \frac{V_0}{2E} \qquad [2.13]$$

where λ is the wavelength of the electron in free space and λ' is the wavelength in the electrostatic media. Using equation 2.13, the difference in phase α introduced by an electron passing through a specimen of thickness t is given by,

$$\alpha = \frac{2\pi t}{\lambda'} - \frac{2\pi t}{\lambda} = \frac{\pi V_0 t}{\lambda E} \qquad [2.14]$$

Consider an electrostatic sample of varying thickness (figure 2.9).

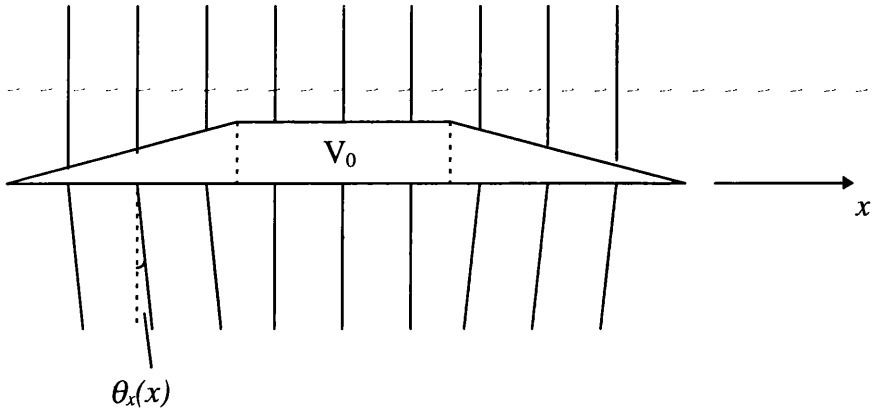

Figure 2.9 *Interaction between the incident electron beam and an electrostatic thin film specimen.*

For a region of uniform electrostatic inner potential and a constant thickness the phase introduced is constant given by equation 2.14. For regions of varying thickness the electrons are deflected by an angle,

$$\theta_x(x) = \frac{\lambda}{2\pi}\frac{d(\alpha_x(x))}{dx} = \frac{V_0}{2E}\frac{dt(x)}{dx} \qquad [2.15]$$

Consider 200keV electrons passing through film with a mean inner potential of 10V. If the film thickness changes from 50nm to 0nm over a distance of 50nm, the deflection angle is θ=2.5x10^{-5}rad. This angle is much smaller than a typical Bragg deflection of 10^{-2}rad, but is comparable with the typical Lorentz deflection of 3x10^{-5}rad.

2.4 Image formation and contrast in conventional transmission electron microscopy.

This section discusses how the image is formed in a conventional transmission electron microscope[9]. This is achieved by following the propagation of the wavefunction through the electron-optical system.

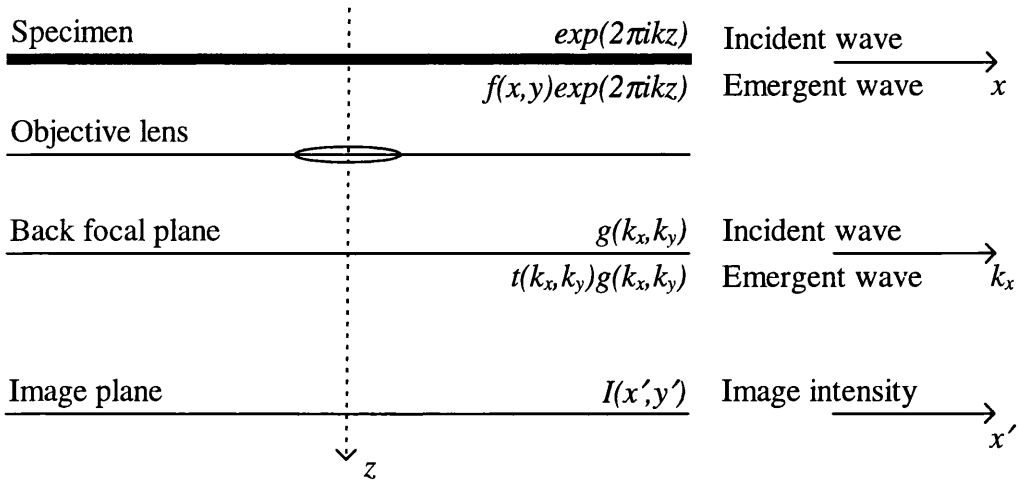

Figure 2.10 *Image formation in the CTEM*

The assumption is made that a plane-wave *exp(2πikz)* is incident on the specimen. As the beam passes through the specimen the electron disturbance can be given by *f(x,y)exp(2πikz),* where *f(x,y)* is the specimen transmission function.

The complex disturbance in the back focal plane is obtained upon taking the Fourier transform of the specimen transmittance,

$$g(k_x,k_y)=\int\int f(x,y)\exp\left[-2\pi i\left(k_x x+k_y y\right)\right]dxdy \qquad [2.16]$$

The wave is then modified by the transfer function of the imaging system,

$$t(k_x,k_y)=A(k_x,k_y)\exp\left\{-2\pi i\left[C_s\lambda^3\left(k_x^2+k_y^2\right)^2/4\right]-\left[\Delta z\lambda\left(k_x^2+k_y^2\right)/2\right]\right\} \qquad [2.17]$$

where $A(k_x,k_y)$ is the pupil function representing the objective aperture, C_s is the spherical aberration coefficient of the objective lens and Δz is the defocus. A second Fourier transform gives the complex disturbance in the image plane. Intensities can be obtained by taking the square modulus of the complex disturbance.

$$I(x',y') = \left| \iint g(k_x,k_y) t(k_x,k_y) \exp\left[-2\pi i\left(k_x x' + k_y y'\right)\right] dk_x dk_y \right|^2 \qquad [2.18]$$

The following sections will deal with standard imaging and various magnetic imaging modes which are relevant to this thesis. The branch of electron microscopy which deals with observing magnetic microstructure is known as 'Lorentz microscopy'. It should be noted that for a magnetic specimen with no amplitude modulation the specimen transmission function is,

$$f(x,y) = \exp\left[i\phi(x,y)\right] \qquad [2.19]$$

where $\phi(x,y)$ is the phase function.

2.4.1 Bright and dark field imaging.

To reveal specimen features there must be contrast in the image. If the transfer function $t(k_x,k_y)$ was everywhere unity $I(x',y')$ would be constant and there would be no contrast in the image. One way of getting contrast is by placing an opaque aperture, representative of the pupil function in equation 2.17, in the back focal plane of the objective lens. The aperture does not allow Bragg reflections to pass through to the final image which is thus formed by the direct beam and any low angle inelastic scattering, a 'bright field image'. The contrast is produced by differences in intensities of electrons scattered into Bragg reflections from various parts of the thin specimen and is consequently known as 'diffraction contrast'.

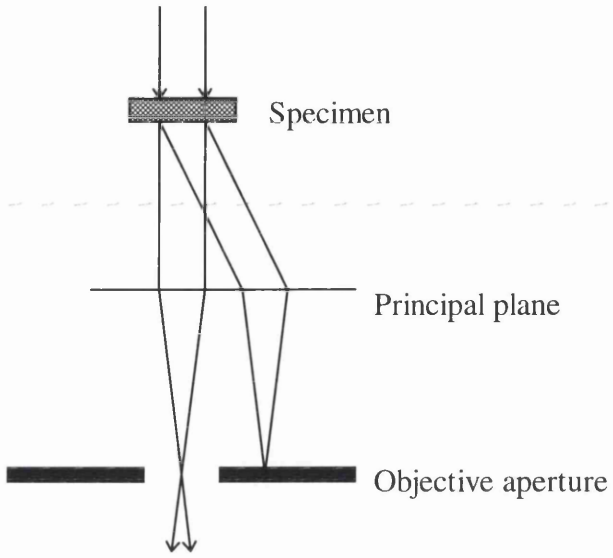

Figure 2.8 *Ray diagram of diffraction contrast.*

Images can also be formed by any one diffracted beam by either displacing the aperture to receive the beam , or by tilting the illumination so that the required beam passes down the axis of the objective. The resultant image is known as a 'dark field image'[11].

2.4.2 Fresnel imaging.

Lorentz microscopy is the branch of electron microscopy which deals with observing magnetic structure[12]. In the Fresnel mode the imaging lens is defocused introducing a non-zero value of Δz to produce magnetic contrast. The contributions from the pupil function and spherical aberration are usually unimportant in this mode so to a good approximation equation 2.17 becomes,

$$t(k_x, k_y) = \exp\left[\pi i \Delta z \lambda \left(k_x{}^2 + k_y{}^2\right)\right] \qquad [2.20]$$

This imaging mode shows contrast wherever there is any spatial variation in the magnetic induction. Classically, the domain walls are revealed as light (convergent) and dark (divergent) bands (figure 2.9). When looking at this technique from a wave mechanical viewpoint, it is found that the domain wall contrast of the convergent walls have an internal structure. This is because of the interference between the overlapping wavefronts.

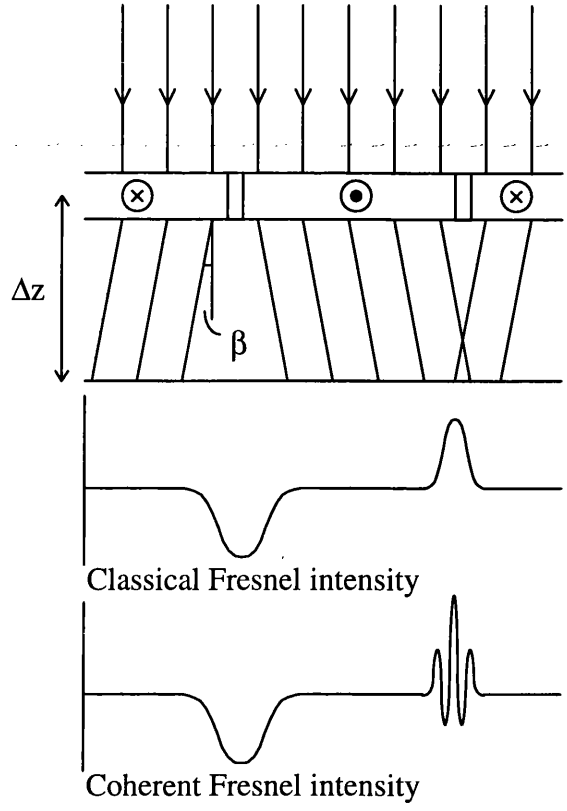

Figure 2.9 *Ray diagram of the Fresnel imaging mode.*

An example of Fresnel imaging is shown in figure 2.10. Here, we reveal the wall structures present in a small permalloy element (4μmx4μmx50nm) fabricated by electron beam lithography (section 5.3). The element possesses a regular solenoidal domain structure containing four 90° walls. In figure 2.10a we observe classical wall structures whereas in 2.10b structured bands are shown. It should also be noted that in figure 12b a larger defocus is used.

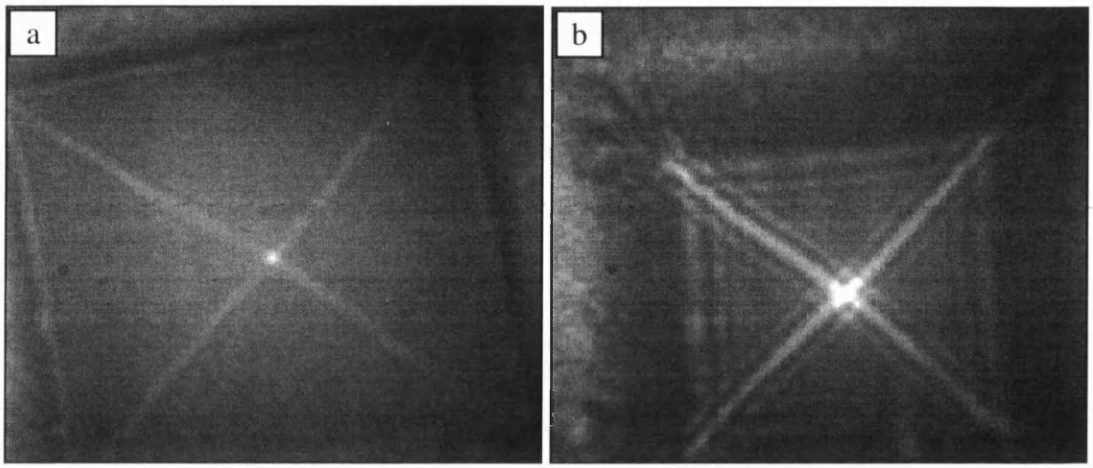

Figure 2.10 *A Fresnel image of a permalloy thin film with (a) a classical wall structure and (b) a wall showing an internal interference structure.*

Fresnel imaging is the simplest operating mode of Lorentz microscopy, providing high contrast images of domain walls with no preferred directionality. There is however no direct information on the magnetic induction direction within a particular domain. Another disadvantage is that quantitative analysis of the structured bright band proves a lengthy process. The relationship between the recorded intensity and $B_y(x)$ is decidedly non-linear[9] and it is very difficult to measure the defocus Δz accurately. At high resolution the spherical aberration term becomes appreciable and a term has to be introduced into equation 2.17 to take into account the chromatic aberration present due to inelastic scattering.

2.4.3 Foucault imaging.

In Foucault imaging[12] (figure 2.10) an opaque aperture is positioned in the back focal plane to remove electrons, deflected by the Lorentz angle, from a limited range of magnetisation orientations. This in focus technique produces magnetic contrast relating to the direction of the magnetic induction in different domains.

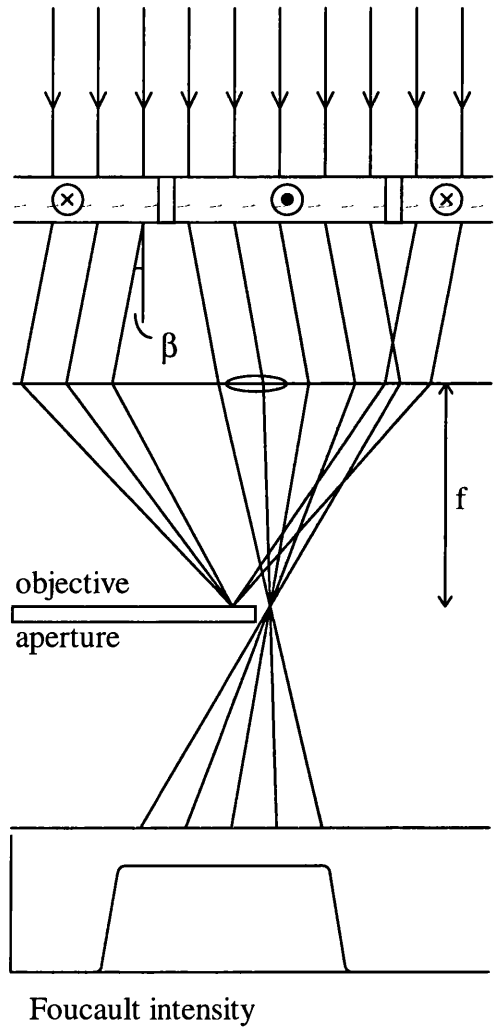

Figure 2.11 *Ray diagram of Foucault mode.*

Figure 2.12 shows Foucault images of a permalloy element (2μmx3μmx50nm), the fabrication of which is described in section 5.3. In order to reveal all the magnetic information a pair of Foucault images are required, taken with the aperture in orthogonal positions. From this pair of images we can then deduce the magnetisation distribution, shown schematically in figure 2.12c. The element shows a complex domain structure, containing 90° and cross-tie walls, which forms a solenoidal magnetisation distribution. Notice that there are differences in the contrast levels between domains where the magnetisation is mapped in opposite directions, for example in figure 12b regions p and q. This does not indicate that there is a variation in the magnitude of the magnetisation vector, but is due to the precise positioning of the aperture.

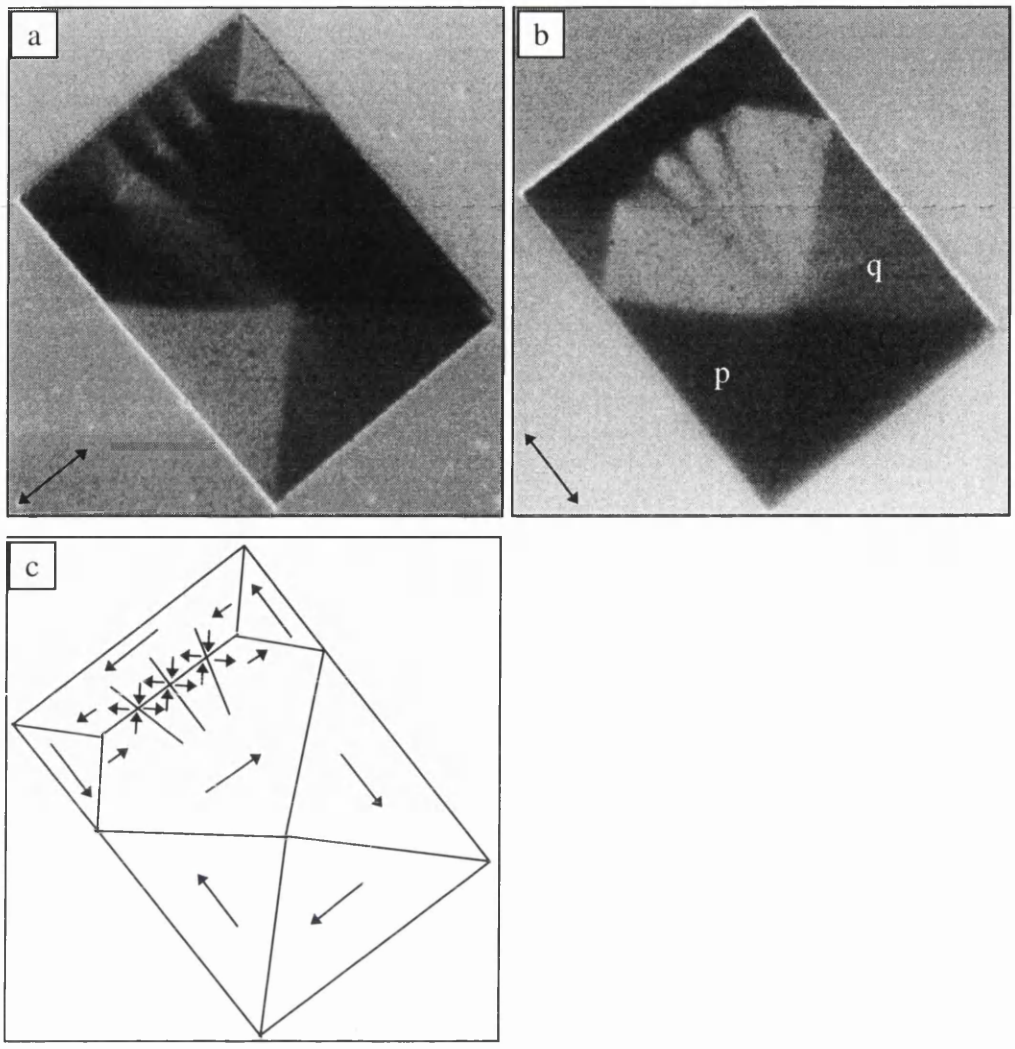

Figure 2.12 *(a) and (b) show orthogonal Foucault images of a permalloy element (inset mapping directions). The magnetisation distribution is shown schematically in (c).*

Foucault imaging provides information on domain geometry and the approximate direction of the magnetic induction within each domain. There is great difficulty in obtaining quantitative measurements because the image contrast is highly non-linear and very dependent on aperture positioning (figure 2.12). The aperture is assumed to be a perfect opaque edge but in reality the edge is non-uniform, partly electron transparent and is susceptible to charging effects. The Foucault technique complements the Fresnel mode allowing for a rapid investigation of the magnetic properties of thin films, albeit non quantitatively.

2.4.4. Holography.

A full review is given by J.M. Cowley[13] covering twenty forms of electron holography. The most common method of forming the interference pattern needed to record the hologram is based on an electron biprism[7] invented by Möllenstedt and Düker. The biprism is placed in the electron microscope, behind the objective lens, and consists of a central filament maintained at a positive voltage, with grounded electrodes on each side. Electron beams passing to either side of the filament are attracted by this positive potential and overlap in the lower plane. If a parallel electron beam is incident on the biprism, interference fringes are formed in the overlap beneath it. When the object is placed in one of the beams, a hologram is obtained (figure 2.13a), showing up to 3000 interference fringes.

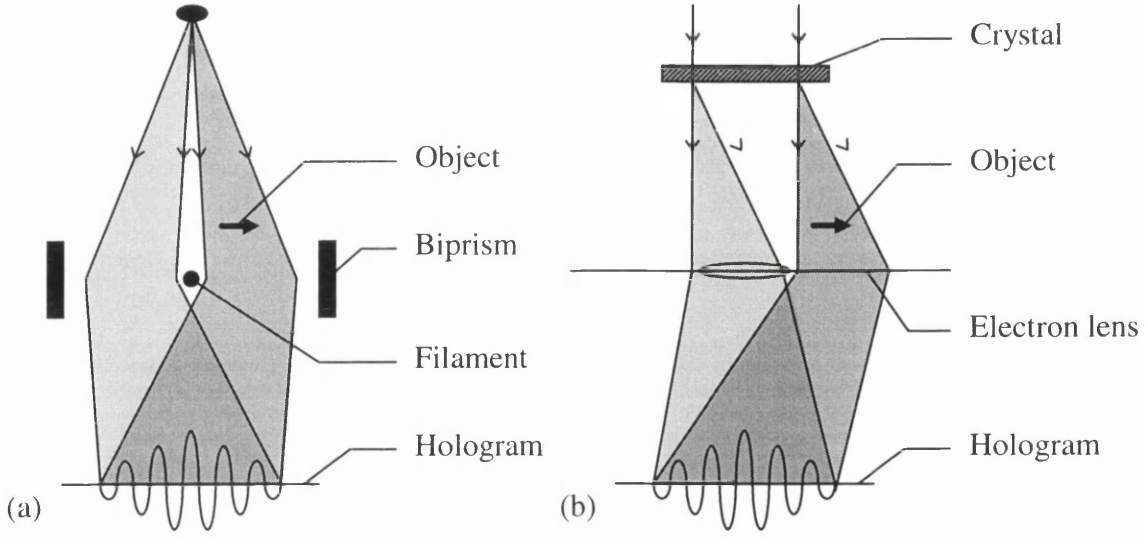

Figure 2.13 *Schematic showing electron hologram formation with (a) an electron biprism (electron lens not shown) and (b) with a single-crystalline film.*

Electron holograms can also be produced using a single crystal film. This acts as a beam splitter because some of the incident electrons are coherently Bragg-reflected at a lattice plane. If the object is placed in the Bragg-reflected beam, a hologram of the crystal lattice modulated by the object will be obtained (figure 2.13b).

When the hologram is reconstructed using a laser beam[14], an additional (complex) conjugate image is formed. Once the electron image is transformed into an optical image,

optical techniques can be used to extract information from the image that cannot be obtained with electron microscopy, for example a contour map or a phase-amplified interference micrograph[7]. Another option is to reconstruct the image numerically from the hologram, but computers are still not fast enough to do this in real time. A recent development by Tonomura allows dynamic events to be observed in real time. The electron hologram is detected with a TV camera and transferred as a video signal to a liquid-crystal panel. The reconstructed image, as well as the interference micrograph, can be obtained without any time delay by shining a laser beam onto the liquid-crystal panel.

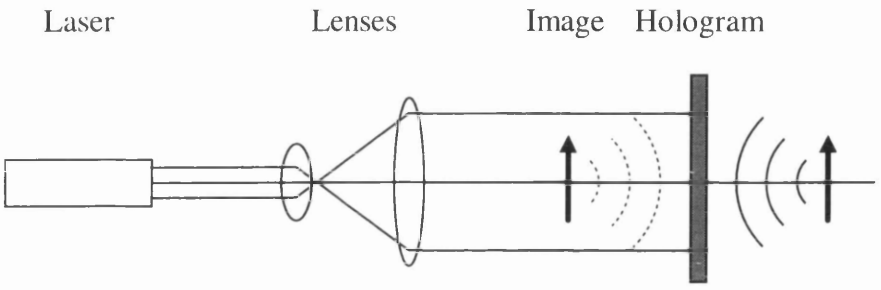

Figure 2.14 *Image reconstruction using a laser.*

The hologram contains information on both the amplitude and phase of the electron beam scattered by the object, in conventional TEM only amplitude information is recorded, and a beam of light is then used to reconstruct a three dimensional image of the object. Holography has been implemented to reveal the thickness of materials, the microscopic distribution of electromagnetic materials, the magnetic structure of ferromagnetic films[15], and the behaviour of vortices in superconductors. Whilst electron-holographic interference microscopy is quantitative, providing high resolution images, the Fresnel and Foucault modes are more convenient for dynamic observation. Another drawback is that the specimen is restricted to having an edge present, to allow a reference beam to pass through an adjacent region of free space, which complicates the investigation of continuous thin films.

2.5 Conclusion

In this chapter we have discussed the components of a TEM which are required for high resolution magnetic imaging. We have given a full description of the Philips CM20 TEM and the specially designed specimen region. We have also looked at how the electron beam interacts with ferromagnetic and electrostatic specimens. Finally, we discussed the various modes of Lorentz microscopy used in the TEM. This involved an explanation of the formation and interpretation of the contrast in the different imaging modes.

In chapter 3 the image formation principle is applied to the novel CF imaging technique to explain the interference effect, similar to holography, which is thereafter expanded upon by the computer simulations in chapter 4. In chapter 5 we give a full description of experimental CF imaging and its implementation on the Philips CM20. We make use of the micromagnetic laboratory surrounding the specimen region to apply fields in-situ to change the magnetic microstructure of small permalloy elements. The temperature rod is also successfully used to heat these specimen beyond their Curie temperature.

In chapter 6 a set of Fe_3O_4 thin films are investigated using the Fresnel and Foucault imaging technique. In these thin films the magnetic microstructure is on a very small scale. This requires high resolution magnetic imaging to reveal all the features.

In chapter 7 a set of NiFe-Ag granular thin films are investigated using the bright field and diffraction imaging modes. Here, the scanning transmission electron microscope (STEM) is introduced and the high angle annular dark field (HADF) imaging mode is discussed. There is also a full description of the energy dispersive x-ray (EDX) technique and how spectral analysis reveals the local atomic compositions within the sample.

References

[1] I.R. McFadyen and J.N. Chapman, EMSA Bulletin **22**, 64, (1992).

[2] J.N. Chapman, A.B. Johnston, L.J. Heydermann, S. McVitie, W.A.P. Nicholson and B. Bormans, IEEE Transactions on Magnetics, VOL **30**, No. 6, (1994).

[3] P.M. Mul, B.J.M. Bormans and L. Schaap, ICEM **12**, 100, (1990).

[4] Phillips TEM CM20 FEG - technical note.

[5] C.E. Hall, Introduction to Electron Microscopy, pubs. McGraw-Hill (1953).

[6] Hirsch, Howie, Nicholson, Pashley and Whelan, Electron Microscopy of Thin Crystals, pubs. Butterworths, (1965).

[7] A. Tonomura, Physics World, 39 (March 1994).

[8] B. Dieny, Journal of Magnetism and Magnetic Materials, **136**, 335 (1994).

[9] J.N. Chapman, Phys. D: Appl.Phys **17**, 623, (1984).

[10] Y. Aharonov and D. Bohm, Phys. Rev., **115**, 485, (1959).

[11] F.C. Phillips, An Introduction to Crystallography, pubs. Longmans, (1955).

[12] J.P. Jakubovics, Electron Microscopy in Materials Science vol. **4**, ed. U Valdre and E Ruedi (Brussels: Commission of the European Communities), 1303, (1975).

[13] J.M. Cowley, Ultramicroscopy **41**, 335, (1992).

[14] A. Tonomura, Rev. Mod. Phys. VOL. **59**, No 3, Part 1, (1987).

[15] A. Tonomura, IEEE Transactions on Magnetics, VOL. **29**, No. 6, (1993).

Chapter 3

Analytical approach to coherent Foucault imaging.

3.0 Introduction.

An analytical description of coherent Foucault imaging provides insight into how a fringe pattern relating to the induction distribution within a magnetic specimen is produced. The interferogram can be thought of as an 'in-line hologram' which is capable of providing a quantitative description of the induction distribution across the specimen. A basic theory (section 3.1) shows how a suitable model is created and how the corresponding diffraction pattern and image are calculated. The ideas are expanded by analysing two systems, a semi-infinite uniformly magnetised thin film (section 3.1) and a two domain element (section 3.2). Here, we discuss the CF images which are obtained when an opaque aperture is positioned carefully in the back focal plane (BFP). Finally, the advantages of using a phase-shifting aperture, rather than the opaque aperture, are discussed (section 3.37).

Throughout this chapter all the values of parameters to evaluate equations are given in appendix A.

3.1 Basic analytical theory of coherent Foucault imaging.

CF imaging can best be described from a wave mechanical approach (Section 2.2). In creating the model a few basic assumptions have been made. They are (i) lenses of the TEM have no aberrations (Section 2.1.3), (ii) a one-dimensional model is sufficient, (iii) the specimen does not modulate the amplitude of the electron wave, and (iv) the wall structures (Section 1.4) need not be considered.

Initially the image formation in CF imaging is considered in a general way. The object is described by,

$$\Psi(x) = \exp[i\phi(x)] \qquad [3.1]$$

where $\phi(x)$ is the phase function of the specimen. For a uniformly magnetised specimen with the in-plane magnetisation equal to the saturation magnetisation ($B_y(x)=B_0$) and of a uniform thickness (t) the phase function is given by,

$$\phi(x) = \frac{eB_0 t}{\hbar} x = \gamma x \qquad [3.2]$$

Taking the Fourier transform (Appendix B) of the object gives the complex disturbance in the back focal plane (BFP).

$$\overline{\Psi}_{diff}(k) = \Im\left(\exp[i\phi(x)]\right) \qquad [3.3]$$

The square modulus of equation [3.3] gives the diffraction pattern. An aperture is then positioned carefully in the BFP, altering the form of the electron disturbance. The mask is initially considered to be of a general form $A(k)$.

$$\overline{\Psi}_{masked} = A(k)\Im\left(\exp[(i\phi(x))]\right) \qquad [3.4]$$

The modified disturbance in the image plane is given by taking the Fourier Transform of the disturbance in the BFP.

$$\Psi_{modified}(x) = \Im\left[A(k)\Im\left(\exp\left[i\phi(x)\right]\right)\right] \qquad [3.5]$$

To get the image intensities the square modulus is taken. A schematic of the imaging process is shown in figure 3.1.

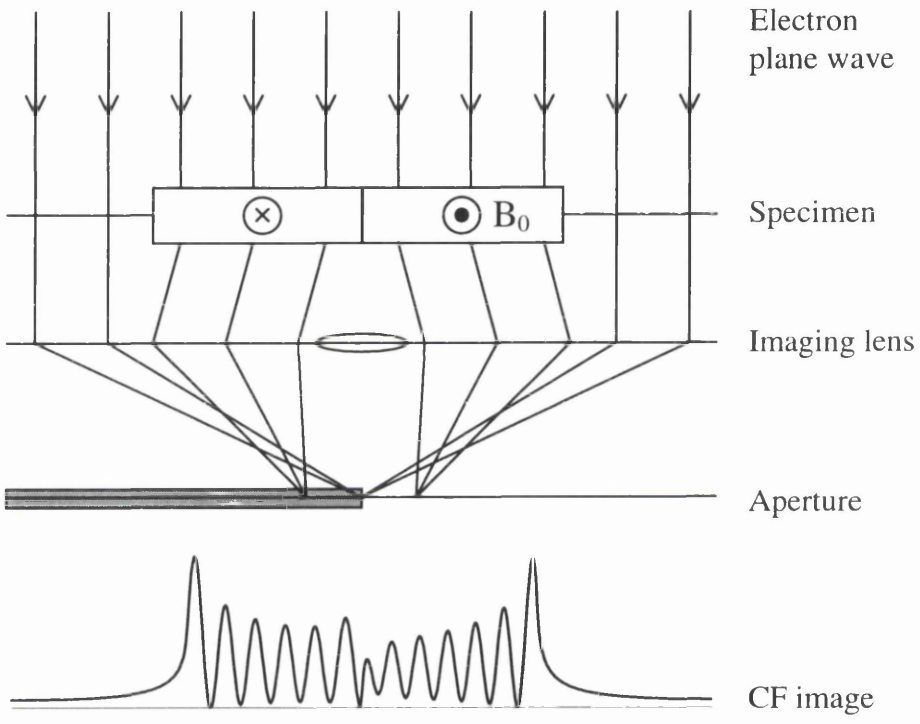

Figure 3.1 *Ray diagram of CF imaging.*

To understand the technique fully we must consider a suitable model. In the following sections a semi-infinite uniformly magnetised specimen and a two domain small element are analysed to reveal the origin of the interference effect.

3.2 Analytical calculation of a semi-infinite uniformly magnetised specimen.

As a simple model consider a semi-infinite uniformly magnetised specimen (figure 3.2), with one edge positioned at $x=0$. This is a useful illustration to understand at first, but is experimentally impractical, best simulated by a uniformly magnetised thin film with an abrupt edge.

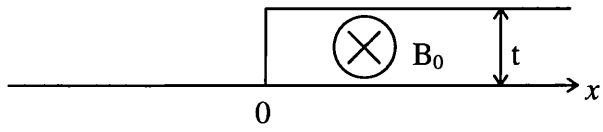

Figure 3.2 *Schematic diagram of the semi-infinite uniformly magnetised specimen.*

This model can be described by,

$$\Psi(x) = e^{i\gamma x}h(x) + (1 - h(x)) \qquad [3.6]$$

where $h(x)$ is the Heaviside function (0 for $x<0$ and 1 for $x>0$). The disturbance in the back focal plane is given by taking the Fourier Transform of the model.

$$\overline{\Psi}(k) = \frac{\sqrt{2\pi}}{2}\delta(k) + \left(\frac{\sqrt{2\pi}}{2}\delta(k) - \frac{i}{\sqrt{2\pi}k}\right) \otimes \left(\sqrt{2\pi}\delta(k-\gamma)\right) \qquad [3.7]$$

where $\otimes$ denotes the convolution of two functions (Appendix B) and $\delta(k)$ is the Dirac delta function. Equation [3.7] may be simplified to,

$$\overline{\Psi}(k) = \frac{\sqrt{2\pi}}{2}\delta(k) + \frac{\sqrt{2\pi}}{2}\delta(k-\gamma) + \frac{i}{\sqrt{2\pi}k} - \frac{i}{\sqrt{2\pi}(k-\gamma)} \qquad [3.8]$$

The complex disturbance in the BFP (Figure 3.3) shows two peaks at $k=0$ and $k=\gamma$. The peak at $k=0$ is representative of the shape of the film and the contribution from free space. The peak at $k=\gamma$ represents the magnetisation distribution within the film.

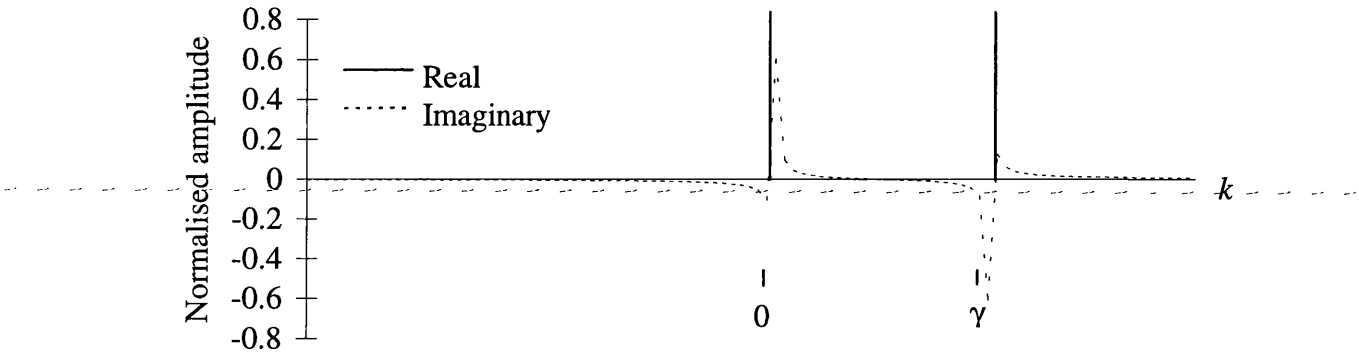

Figure 3.3 *Theoretical complex disturbance in the BFP.*

The diffraction pattern is shown schematically in figure 3.4 with aperture positions which are chosen to highlight the changes in the complex disturbance in the BFP. The peaks can be masked in various positions by a semi-infinite opaque aperture coming in from the left. The aperture takes the form of the Heaviside function that removes electrons from the final image. The following sections show how the aperture, positioned in the BFP, affects the corresponding image.

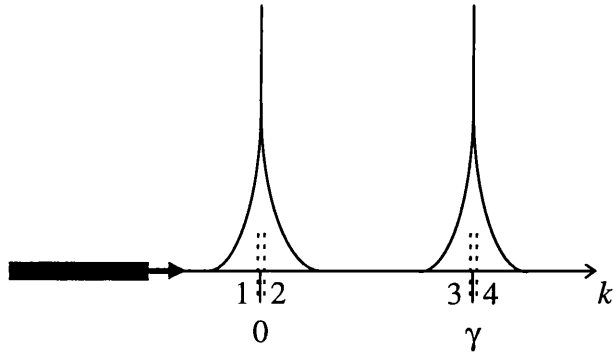

Figure 3.4 *Schematic of the diffraction pattern with aperture positions marked.*

3.2.1 Opaque aperture in position 1.

An opaque aperture is placed at position 1 in the BFP (figure 3.5) removing all negative spatial frequencies ($k<0$).

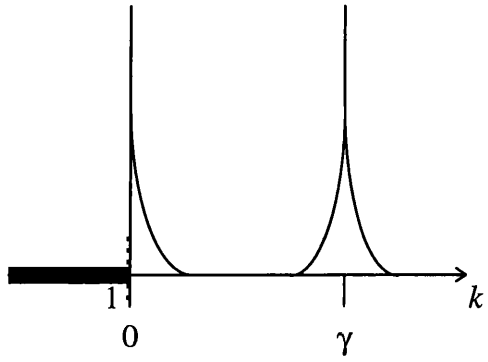

Figure 3.5 *Aperture in position 1.*

Only half of the central shape function is removed, with the other terms being negligibly affected. The complex disturbance in the BFP is given by,

$$\overline{\Psi}_1(k)=\frac{\sqrt{2\pi}}{2}\delta(k)+\frac{\sqrt{2\pi}}{2}\delta(k-\gamma)+\frac{i}{\sqrt{2\pi}k}h(k)-\frac{i}{\sqrt{2\pi}(k-\gamma)} \qquad [3.9]$$

The Fourier transform gives the complex image,

$$\Psi_1(x)=e^{i\gamma x}h(x)+\frac{1}{2}-\frac{1}{4}\mathrm{sgn}(x)+\Delta(x) \qquad [3.10]$$

where sgn(x) is the signal function defined as -1 for $x<0$ and 1 for $x>0$,

$$\Delta(x)=\frac{i}{2\sqrt{2\pi}}\left[\mathrm{sgn}(x)\otimes\frac{1}{x}\right] \qquad [3.11]$$

Equation 3.11 defines the function $\Delta(x)$ to be the difference between equations 3.9 and 3.10. This convolution is divergent so cannot be evaluated. It is however strongly peaked around the origin, falling away rapidly on either side of it. The term $\Delta(x)$ is therefore

considered to be negligible away from the origin. Figure 3.6 shows that for $x<0$ the image disturbance assumes a constant value of 3/4, giving an intensity of 9/16 in this region. For $x>0$ the complex image is of the form,

$$\Psi_{I,x>0} = [\varepsilon + \cos(\gamma x)] + i \sin(\gamma x) \qquad [3.12]$$

where ε in this case is 1/4. This value will change when there is any displacement of the aperture. Thus, the intensity distribution $I(x)$ in this region is given by,

$$I(x) = \mu + \nu \cos(\gamma x) \qquad [3.13]$$

where μ and ν are constants whose values again depend on the precise positioning of the aperture, in this case μ=17/16 and ν=1/2. The region occupied by the magnetic specimen consists of a set of interference fringes, running parallel to the induction direction, with a periodicity of h/eB_0t.

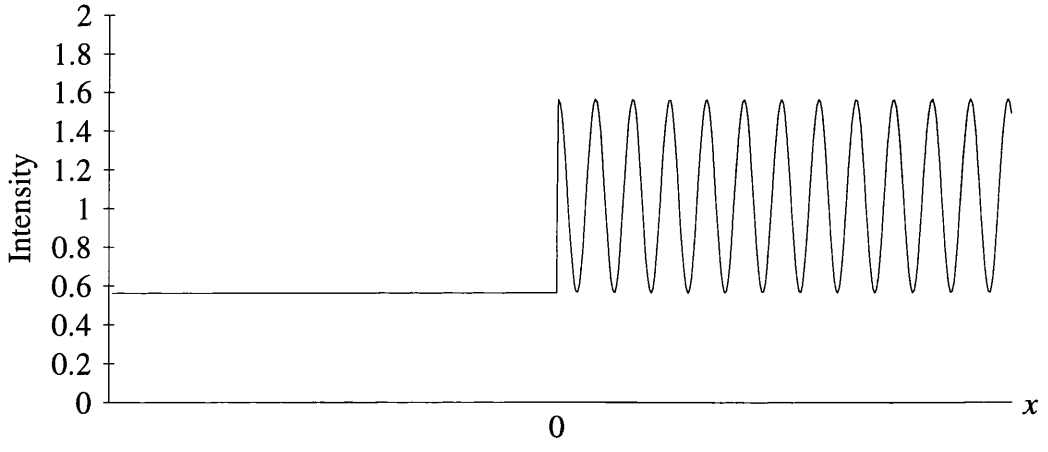

Figure 3.6 *CF image with the aperture in position 1.*

3.2.2 Opaque aperture in position 2.

An aperture is located at position 2 in the BFP (figure 3.7) removing all negative spatial frequencies including zero ($k \leq 0$).

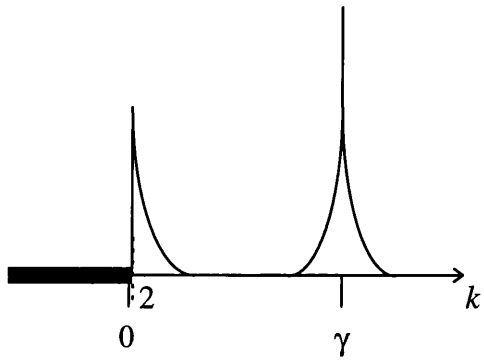

Figure 3.7 *Aperture in position 2.*

Half of the shape function is removed as in position 1, but in this case the central delta function is also removed. All other terms are considered negligible at this point. The modified disturbance in the BFP is given by,

$$\overline{\Psi}_2(k) = \frac{\sqrt{2\pi}}{2}\delta(k-\gamma) + \frac{i}{\sqrt{2\pi}k}h(k) - \frac{i}{\sqrt{2\pi}(k-\gamma)} \qquad [3.14]$$

The Fourier transform gives the image as,

$$\Psi_2(x) = e^{i\gamma x}h(x) - \frac{1}{4}\mathrm{sgn}(x) + \Delta(x) \qquad [3.15]$$

where $\Delta(x)$ is the error function (equation 2.11) and is considered to be negligible away from the origin. The image (figure 3.8) in the region $x<0$ shows a constant intensity of 1/16. Within the magnetic specimen ($x>0$) there are fringes present showing the same generic form as when the aperture is in position 1 (equation 3.12); in this case μ=17/16 and ν=-1/2. It should be noted that there is also a phase difference of π between the images using an aperture in position 1 and position 2 which can be associated with the masking of the delta function.

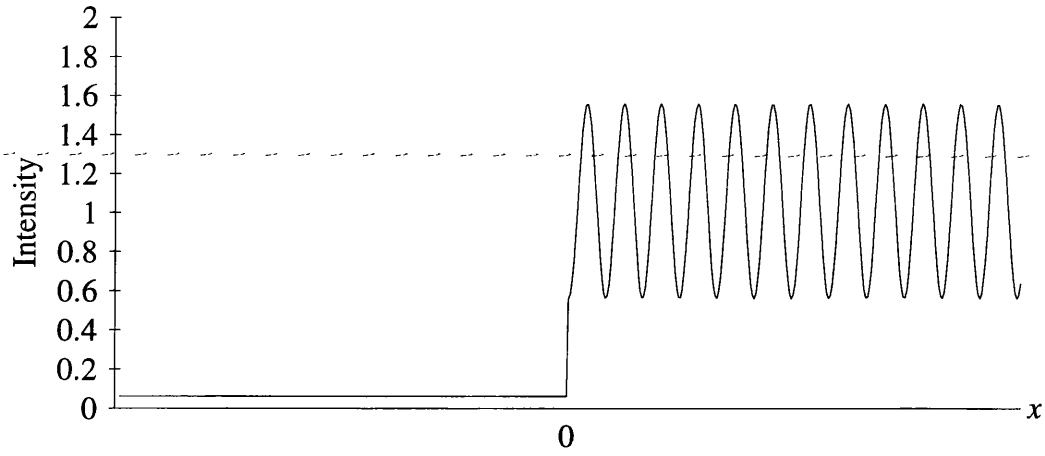

Figure 3.8 *CF image with the aperture in position 2.*

3.2.3 Opaque aperture in position 3.

The aperture is now placed at position 3 in the BFP (figure 3.9) removing all spatial frequencies $k<\gamma$.

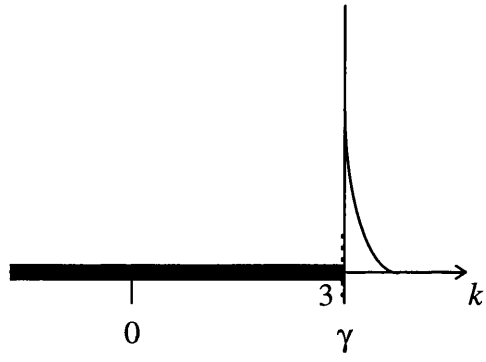

Figure 3.9 *Aperture in position 3.*

The peak representing the shape of the specimen and the half of the magnetic spot are removed. The other half of the magnetic spot and the delta function occurring at $k=\gamma$ pass unaffected. The complex disturbance in the BFP is given by,

$$\overline{\Psi}_3(k) = \frac{1}{\sqrt{2\pi}}\delta(k-\gamma) - \frac{i}{\sqrt{2\pi}(k-\gamma)}h(k-\gamma) \qquad [3.16]$$

The Fourier transform gives the image,

$$\Psi_3(x) = \frac{1}{2}e^{i\gamma x} + \frac{1}{4}e^{i\gamma x}\,\mathrm{sgn}(x) - e^{i\gamma x}\Delta(x) \qquad [3.17]$$

where $\Delta(x)$ is the error function (equation 2.11) and is again considered to be negligible away from the origin. The image (figure 3.10) in the region $x<0$ shows a constant intensity of 1/16. There are no longer any fringes in the magnetic specimen but a constant intensity of 9/16. This is because there is no reference beam to interfere with the spot passing through the specimen.

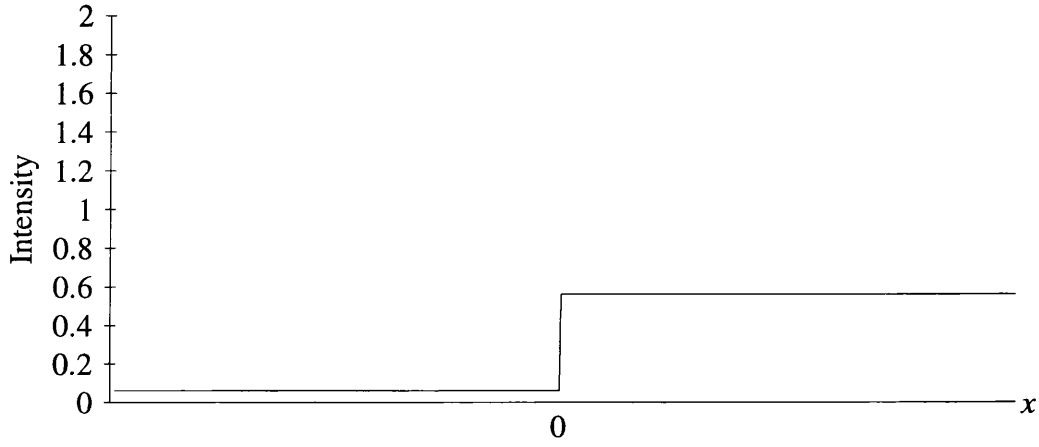

Figure 3.10 *CF image with the aperture in position 3.*

3.2.4 Opaque aperture in position 4.

An opaque aperture is placed in position 4 in the BFP removing all spatial frequencies $k \leq \gamma$.

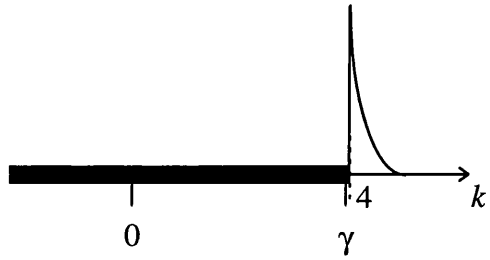

Figure 3.11 *Aperture in position 4.*

The aperture is positioned to allow only half of the magnetic spot to pass through.

$$\overline{\Psi}_4(k) = -\frac{i}{\sqrt{2\pi}(k-\gamma)} h(k-\gamma) \qquad [3.18]$$

The complex image is,

$$\Psi_4(x) = \frac{1}{4} e^{i\gamma x} \operatorname{sgn}(x) - e^{i\gamma x} \Delta(x) \qquad [3.19]$$

where $\Delta(x)$ is the error function (equation 2.11). Here there is only a small constant intensity of 1/16 throughout.

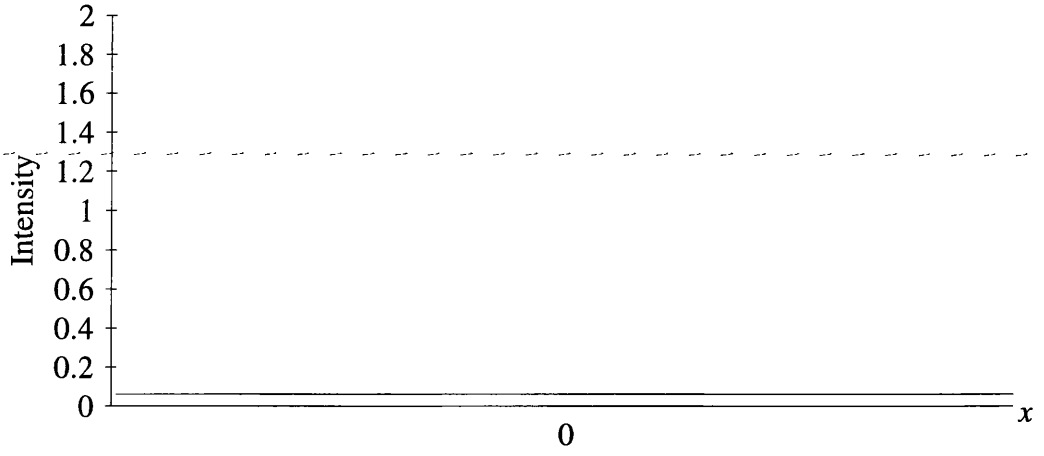

Figure 3.12 *CF image with the aperture in position 4.*

3.2.5 Investigation of the conjugate aperture positions.

To examine all possible configurations a conjugate aperture (figure 3.13), a semi-infinite aperture brought in from the right, must also be considered. This is due to the model not being symmetric about $x=0$.

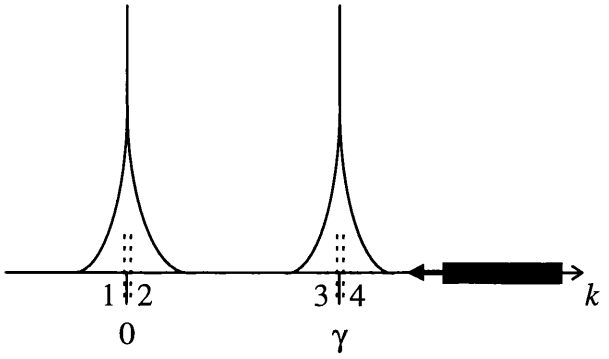

Figure 3.13 *Schematic diffraction pattern showing conjugate masking positions.*

A detailed analysis of the conjugate aperture positions is given in appendix C. Figure 2.14 shows the CF images obtained when the aperture is situated in the appropriate masking positions. The images show mirror CF images to those when using the aperture coming in from the left. Fringes are observed in free space when masking in position 4 and position 3; in position 2 and position 1 there are constant intensities.

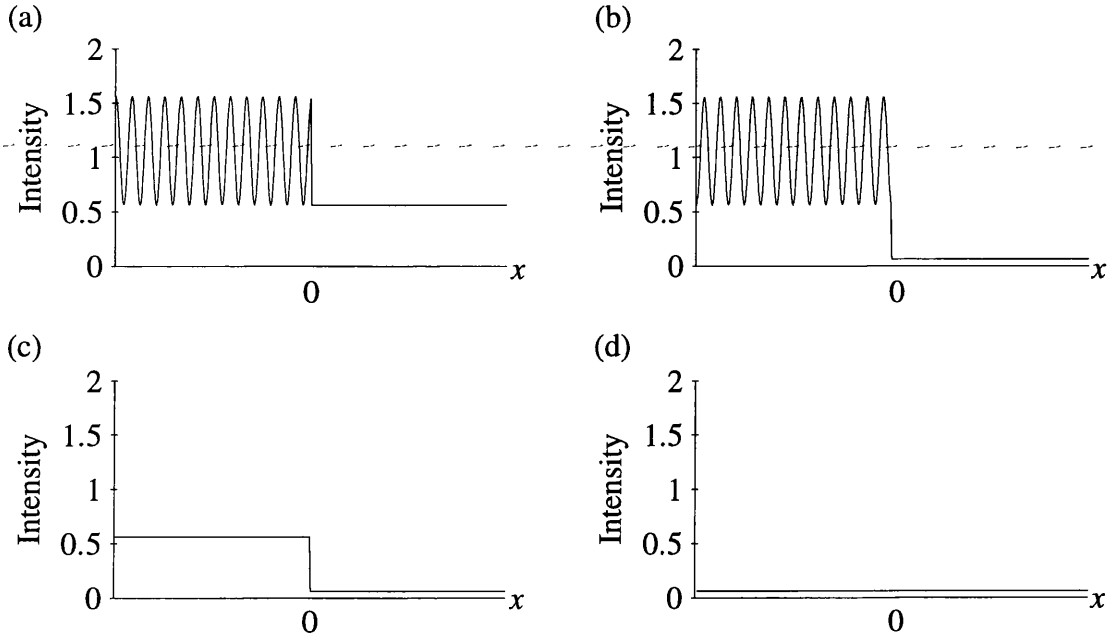

Figure 3.14 *CF images of a semi-infinite uniformly magnetised thin film with the aperture in the conjugate positions.*

3.3 Analytical calculation of a two domain element.

To further the investigation a more complex object is required. To make full use of the calculations a sensible model must be chosen, able to represent domain structures resembling those found in soft magnetic elements.

Consider an element (figure 3.15) of width L sitting in free space, containing two domains which are uniformly magnetised in opposite orientations. There is a 180° domain wall occurring at $x=0$. The wall is not under investigation and is considered to have zero width.

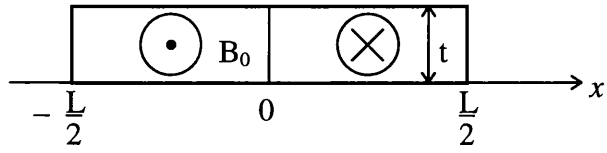

Figure 3.15 *A schematic diagram of the two domain element.*

To setup the model we must first introduce two functions (figure 3.16) ; $S_{-}(x)$ which is unity for $-L/2<x<0$ and is zero elsewhere, and $S_{+}(x)$ which is unity for $0<x<L/2$ and is zero elsewhere.

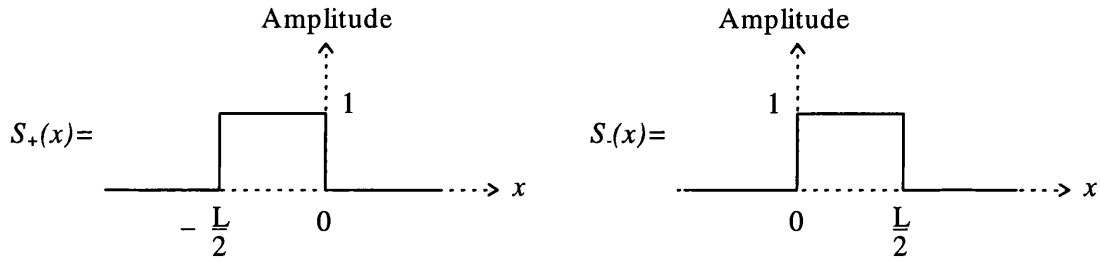

Figure 3.16 *The functions $S_{-}(x)$ and $S_{+}(x)$.*

The model used to represent this situation is:

$$\Psi_{el}(x) = S_{-}(x)e^{i\phi_{-}(x)} + S_{+}(x)e^{i\phi_{+}(x)} + 1 - \left[S_{+}(x) + S_{-}(x)\right] \qquad [3.20]$$

$$\Psi_{el}(x) = e^{\frac{i\gamma L}{2}}\left(S_{-}(x)e^{i\gamma x} + S_{+}(x)e^{-i\gamma x}\right) + 1 - \left[S_{+}(x) + S_{-}(x)\right] \qquad [3.21]$$

Taking the Fourier transform (Appendix B) of the model gives the disturbance in the BFP,

$$\begin{aligned}\overline{\Psi}_{el}(k) = e^{\frac{i\gamma L}{2}}&\left(\frac{1}{\sqrt{2\pi}ik}\left(1 - e^{\frac{-ikL}{2}}\right) \otimes \sqrt{2\pi}\delta(k+\gamma)\right) \\ &+ e^{\frac{i\gamma L}{2}}\left(\frac{1}{\sqrt{2\pi}ik}\left(e^{\frac{ikL}{2}} - 1\right) \otimes \sqrt{2\pi}\delta(k-\gamma)\right) \\ &+ \sqrt{2\pi}\delta(k) - \frac{1}{\sqrt{2\pi}} L\,\mathrm{sinc}\left(\frac{kL}{2}\right)\end{aligned} \qquad [3.22]$$

which simplifies to,

$$\overline{\Psi}_{el}(k) = \frac{\left(e^{\frac{i\gamma L}{2}} - e^{\frac{-ikL}{2}}\right)}{\sqrt{2\pi}i(k+\gamma)} + \frac{\left(e^{\frac{ikL}{2}} - e^{\frac{i\gamma L}{2}}\right)}{\sqrt{2\pi}i(k-\gamma)} + \sqrt{2\pi}\delta(k) - \frac{1}{\sqrt{2\pi}} L\,\mathrm{sinc}\left(\frac{kL}{2}\right) \qquad [3.23]$$

The complex disturbance in the BFP is shown in figure 3.17. The central region consists of a delta function from the contribution from free space and a sinc $(\sin(x)/x)$ function representing the shape of the element. There are also two peaks occurring at $k=-\gamma$ and $k=\gamma$ representing the magnetic information in the left and right domains respectively.

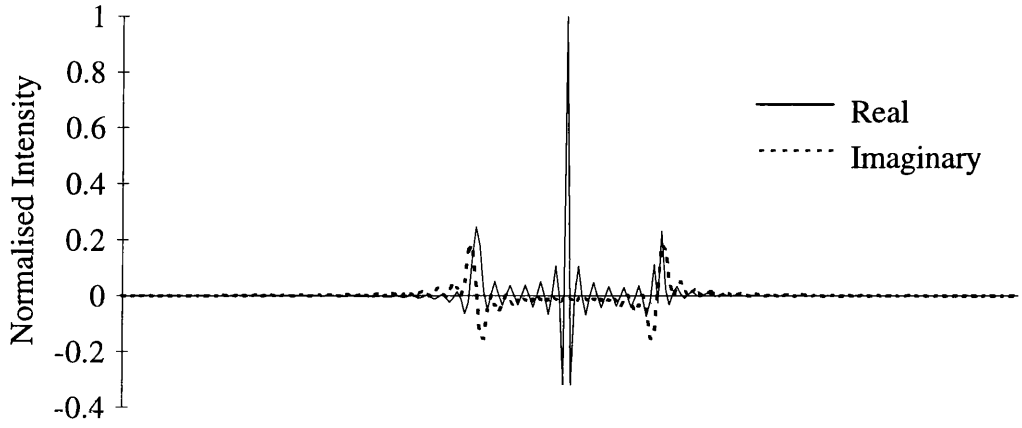

Figure 3.17 *Theoretical complex disturbance in the BFP.*

In the following sections we shall investigate how the aperture positioning affects the image. Figure 3.18 shows a schematic of the diffraction pattern with the aperture positions marked.

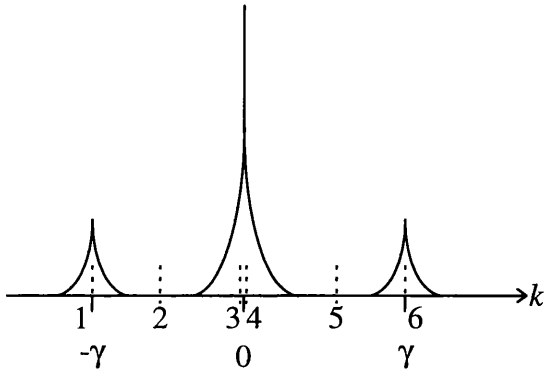

Figure 3.18 *Schematic of the diffraction pattern, masking positions are marked.*

3.3.1 Opaque aperture in position 1.

Figure 3.19 shows the diffraction pattern when the aperture is in position 1 removing the spatial frequencies $k<-\gamma$.

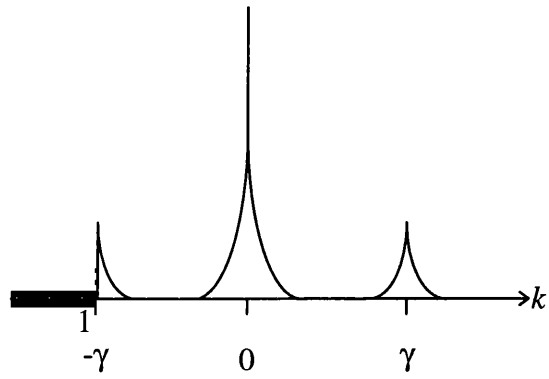

Figure 3.19 *Aperture in position 1.*

Half of the left magnetic spot is removed, with the rest of the disturbance in the BFP considered to be negligibly affected at this point. The disturbance in the BFP can be written,

$$\overline{\Psi}_{el1}(k)=h(k+\gamma)\frac{\left(e^{\frac{i\gamma L}{2}}-e^{\frac{-ikL}{2}}\right)}{\sqrt{2\pi}i(k+\gamma)}+\frac{\left(e^{\frac{ikL}{2}}-e^{\frac{i\gamma L}{2}}\right)}{\sqrt{2\pi}i(k-\gamma)}+\sqrt{2\pi}\delta(k)-\frac{1}{\sqrt{2\pi}}L\,\mathrm{sinc}\left(\frac{kL}{2}\right) \qquad [3.24]$$

Upon taking the Fourier transform the complex analytical image is obtained,

$$\Psi_{el1}(x)=\frac{1}{2}S_{-}(x)e^{i\left(\frac{\gamma L}{2}+\gamma x\right)}-\Delta_1(x)+S_{+}(x)e^{i\left(\frac{\gamma L}{2}-\gamma x\right)}+1-\left[S_{+}(x)+S_{-}(x)\right] \qquad [3.25]$$

where,

$$\Delta_1(x)=\frac{i}{\sqrt{2\pi}x}e^{i\gamma x}\otimes S_{-}(x)e^{i\left(\frac{\gamma L}{2}+\gamma x\right)} \qquad [3.26]$$

Equation 3.26 defines the error function $\Delta_1(x)$. This convolution is divergent so cannot be evaluated analytically. It is however strongly peaked around $x=-L/2$ and $x=0$, falling away rapidly on either side of each peak. The term $\Delta_1(x)$ is therefore considered to be negligible elsewhere in the image. The image (figure 3.20) shows that the intensity in free space and the left domain remains constant at unity. The left domain shows a decreased uniform intensity of 1/4.

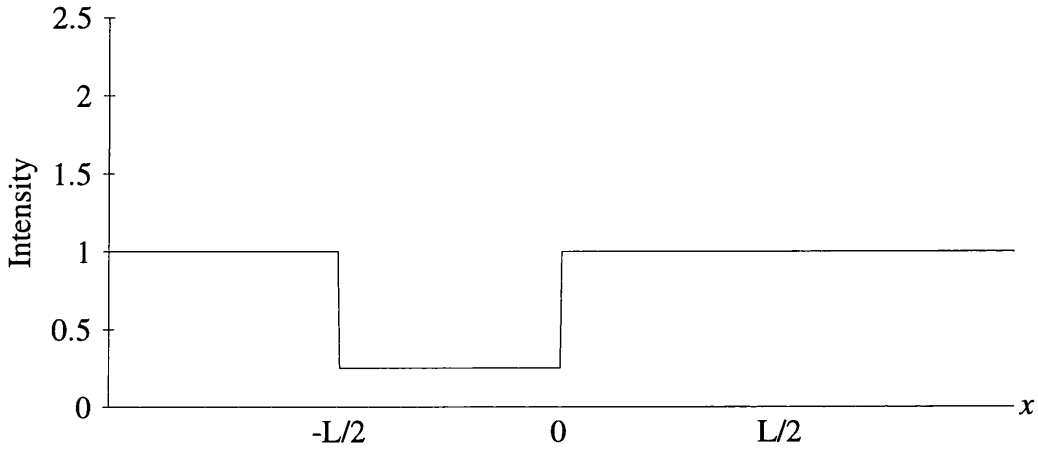

Figure 3.20 *CF image with the aperture in position 1.*

3.3.2 Opaque aperture in position 2.

Figure 3.21 shows the diffraction pattern when the aperture is in position 2.

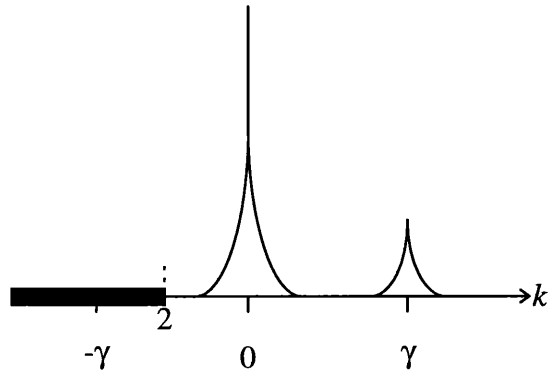

Figure 3.21 *Aperture in position 2.*

The aperture blocks all of the left hand spot with no further changes.

$$\overline{\Psi}_{el2}(k)=\frac{\left(e^{\frac{ikL}{2}}-e^{\frac{i\gamma L}{2}}\right)}{\sqrt{2\pi}i(k-\gamma)}+\sqrt{2\pi}\delta(k)-\frac{1}{\sqrt{2\pi}}L\,\mathrm{sinc}\left(\frac{kL}{2}\right) \qquad [3.27]$$

The Fourier transform yields the complex analytical image,

$$\Psi_{el2}(x)=S_{+}(x)e^{i\left(\frac{\gamma L}{2}-\gamma x\right)}+1-\left[S_{+}(x)+S_{-}(x)\right] \qquad [3.28]$$

The image (figure 3.22) shows no change in free space and the right domain, with the left domain showing a uniform intensity of zero.

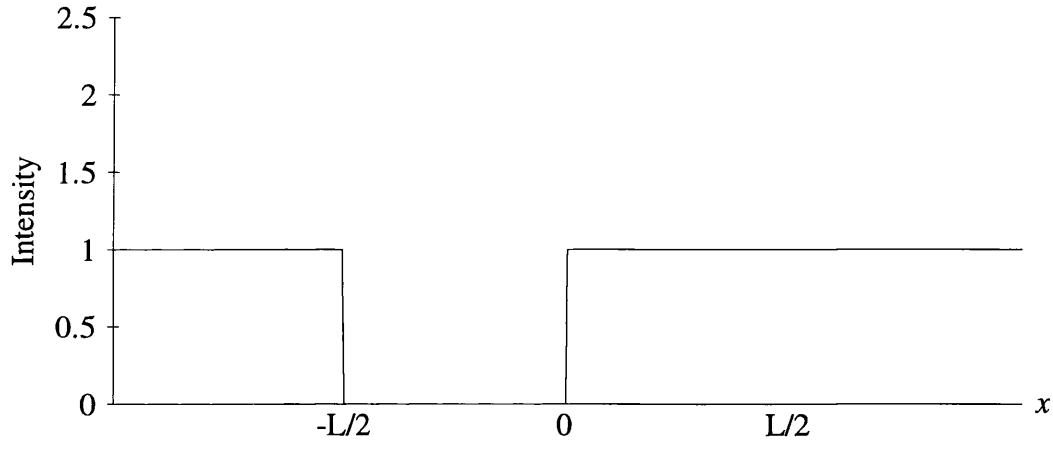

Figure 3.22 *CF image with the aperture in position 2.*

3.3.3 Opaque aperture in position 3.

Figure 3.23 shows the diffraction pattern when the aperture is in position 3 removing all spatial frequencies $k<\theta$.

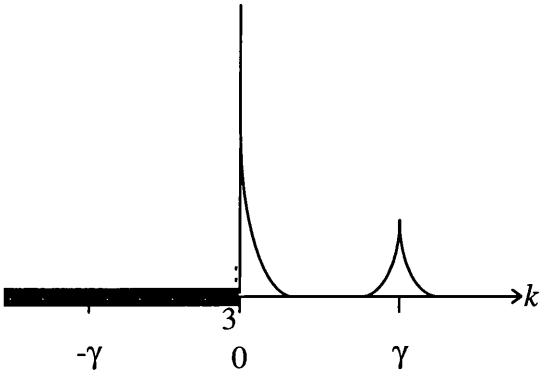

Figure 3.23 *Aperture in position 3.*

The left magnetic spot and half of the central shape function are removed, with the rest of the disturbance in the BFP being unaffected.

$$\overline{\Psi}_{el3}(k)=\frac{\left(e^{\frac{ikL}{2}}-e^{\frac{i\gamma L}{2}}\right)}{\sqrt{2\pi}i(k-\gamma)}+\sqrt{2\pi}\delta(k)-\frac{1}{\sqrt{2\pi}}L\,\mathrm{sinc}\left(\frac{kL}{2}\right)h(k) \qquad [3.29]$$

Upon taking the Fourier transform the complex analytical image is obtained,

$$\Psi_{el3}(x)=S_+(x)e^{i\left(\frac{\gamma L}{2}-\gamma x\right)}+1-\frac{1}{2}\left[S_+(x)+S_-(x)\right]+\Delta_2(x) \qquad [3.30]$$

where,

$$\Delta_2(x)=\left[S_+(x)+S_-(x)\right]\otimes\frac{i}{\sqrt{2\pi}x} \qquad [3.31]$$

Equation 3.31 defines the error function $\Delta_2(x)$. This convolution is divergent so cannot be evaluated. It is however strongly peaked around x=-L/2, 0, L/2, falling away rapidly on either side of each peak and is therefore considered to be negligible elsewhere. The intensity image (figure 3.24) shows no change in free space. The left domain has a slight increase in intensity of 1/4, due to the alteration to the shape function. The right domain shows fringes of a similar form to equation [3.12] with a modified phase term,

$$I = \mu + \nu \cos\left(\frac{\gamma L}{2} - \gamma x\right) \qquad [3.32]$$

where μ=*5/4* and ν=*1*. These fringes run parallel to the magnetic induction direction with a periodicity of h/eB_0t.

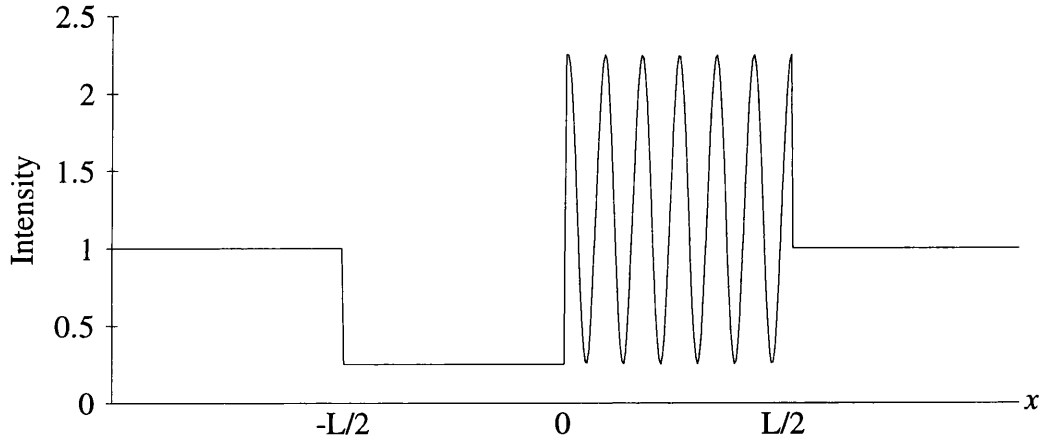

Figure 3.24 *CF image with the aperture in position 3.*

3.3.4 Opaque aperture in position 4.

Figure 3.25 shows the diffraction pattern when the aperture is in position 4 removing all spatial frequencies $k \leq 0$.

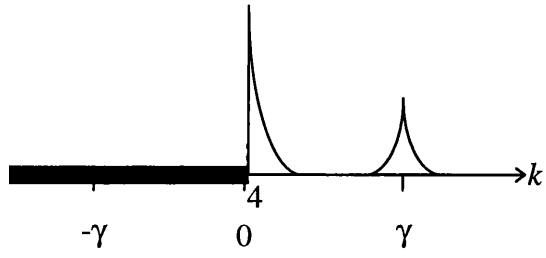

Figure 3.25 *Aperture in position 4.*

The aperture masks all of the left hand spot, half of the central spot but this time includes masking the central delta function.

$$\overline{\Psi}_{el4}(k) = \frac{\left(e^{\frac{ikL}{2}} - e^{\frac{i\gamma L}{2}}\right)}{i(k-\gamma)} - L\,\mathrm{sinc}\left(\frac{kL}{2}\right)h(k) \qquad [3.33]$$

The Fourier transform produces the complex analytical image,

$$\Psi_{el4}(x) = S_+(x)e^{i\left(\frac{\gamma L}{2}-\gamma x\right)} - \frac{1}{2}\left[S_+(x) + S_-(x)\right] + \Delta_2(x) \qquad [3.34]$$

where $\Delta_2(x)$ is given by equation 3.31 and is considered negligible in the image. Figure 3.26 shows that upon masking the delta function the free space region of the image has been completely removed. The left domain shows an intensity of 1/4 due to the modified shape function. The right domain has fringes of the same generic form as when masking in position 3, here μ=5/4 and ν=-1. Notice also that there is a phase difference of π between the fringes in the image in position 3 and position 4 due to the masking of the delta function.

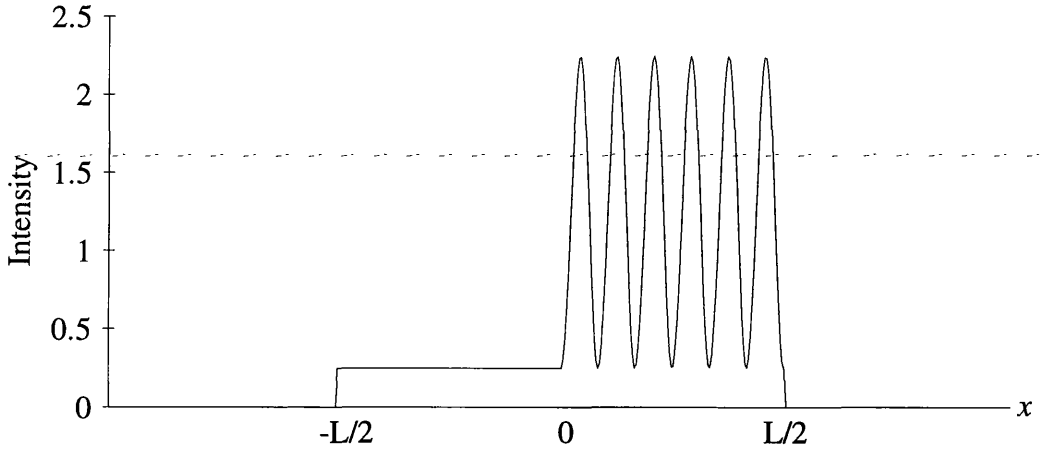

Figure 3.26 *CF image with the aperture in position 4.*

3.3.5 Opaque aperture in position 5.

Figure 3.27 shows the diffraction pattern when the aperture is in position 5.

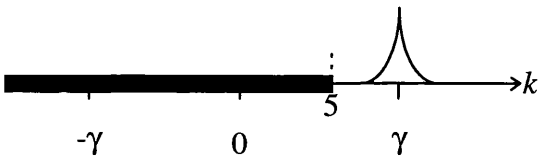

Figure 3.27 *Aperture in position 5.*

The left magnetic spot, the central shape function and the delta function are removed leaving only the right hand spot to pass unaffected.

$$\overline{\Psi}_{el5}(k) = \frac{\left(e^{\frac{ikL}{2}} - e^{\frac{i\gamma L}{2}} \right)}{\sqrt{2\pi i}(k-\gamma)} \qquad [3.35]$$

Upon taking the Fourier transform the complex analytical image is obtained,

$$\Psi_{el5}(x) = S_+(x)e^{i\left(\frac{\gamma L}{2}-\gamma x\right)} \qquad [3.36]$$

The image (figure 3.28) reveals the right domain to show an intensity of unity. Free space and the left domain show zero intensity.

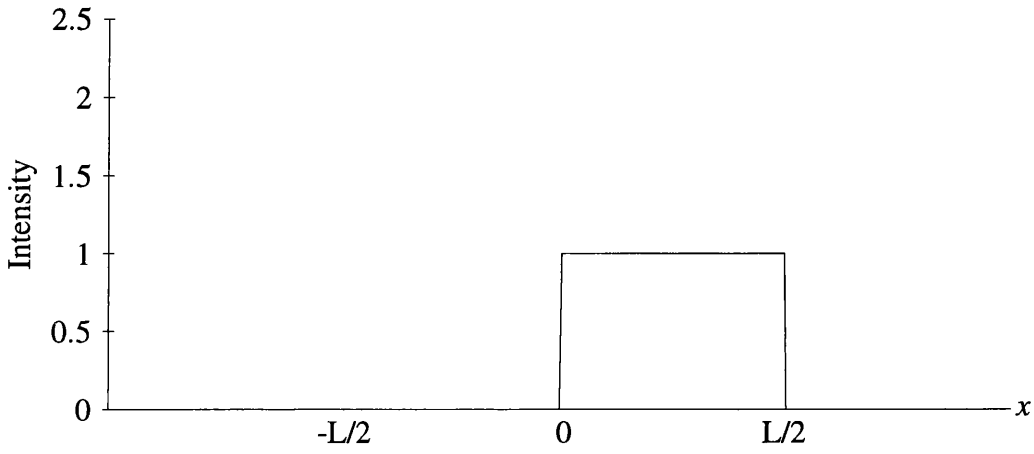

Figure 3.28 *CF image with the aperture in position 5.*

3.3.6 Opaque aperture in position 6.

Figure 3.29 shows the diffraction pattern when the aperture is in position 6 removing all the spatial frequencies $k<\gamma$.

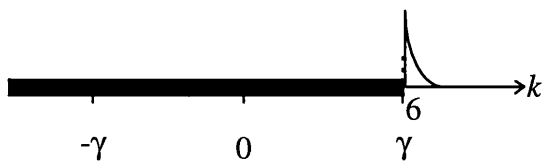

Figure 3.29 *Aperture in position 6.*

The aperture blocks everything but half of the right magnetic spot.

$$\overline{\Psi}_{el6}(k) = h(k-\gamma)\frac{\left(e^{\frac{ikL}{2}} - e^{\frac{i\gamma L}{2}}\right)}{\sqrt{2\pi}i(k-\gamma)} \qquad [3.37]$$

The Fourier transform yields the complex analytical image,

$$\Psi_{el6}(x) = \frac{1}{2}S_+(x)e^{i\left(\frac{\gamma L}{2}-\gamma x\right)} - \Delta_3(x) \qquad [3.38]$$

where,

$$\Delta_3(x) = \frac{i}{\sqrt{2\pi}x}e^{-i\gamma x} \otimes S_+(x)e^{i\left(\frac{\gamma L}{2}-\gamma x\right)} \qquad [3.39]$$

Equation 3.39 defines the error function $\Delta_3(x)$. This convolution is divergent so cannot be evaluated. It is however strongly peaked around x=0 and x=L/2, falling away rapidly on either side of each peak and is therefore considered to be negligible. The image (figure 3.30) shows the right domain to be of a uniform intensity of 1/4. There is zero intensity in the other regions.

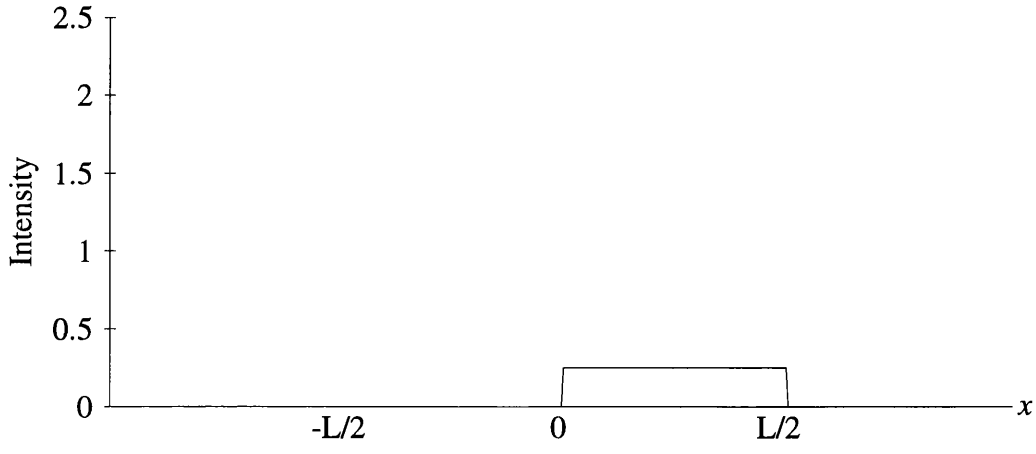

Figure 3.30 *CF image with the aperture in position 6.*

3.3.7 Investigation of position 3 using a phase shifting aperture.

Using the technique described so far, it is apparent that in any single image information is lost if the specimen is more complex than the very simple semi-infinite thin film. Electrons passing through the domain with magnetisation along the negative y-axis inevitably hit the aperture itself and play no further role in the image formation process. This problem can be overcome using a modification in which the solid aperture is replaced by an electron transparent phase-shifting aperture, such as a thin foil of uniform thickness containing a hole. A detailed description of the phase-shift introduced is given in section 2.3. Equation 2.11 shows that by varying the thickness of the film the magnitude of the phase shift can be selected by the experimenter.

Figure 3.31 shows the diffraction pattern when the aperture is in position 3 phase-shifting all electrons where $k<0$.

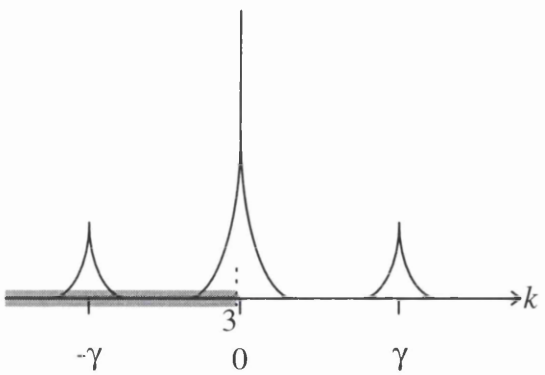

Figure 3.31 *Phase shifting aperture in position 3.*

The aperture introduces a phase-shift to the left magnetic spot and half of the shape function. The other half of the shape function, the central delta function and the right magnetic spot pass unchanged. The disturbance in the BFP is given by,

$$\overline{\Psi}_{el7}(k) = e^{i\alpha}h(k)\frac{\left(e^{\frac{i\gamma L}{2}} - e^{\frac{-ikL}{2}}\right)}{\sqrt{2\pi}i(k+\gamma)} + (1-h(k))\frac{\left(e^{\frac{ikL}{2}} - e^{\frac{i\gamma L}{2}}\right)}{\sqrt{2\pi}i(k-\gamma)} + \sqrt{2\pi}\delta(k) \qquad [3.40]$$
$$- e^{i\alpha}h(k)\frac{1}{\sqrt{2\pi}}L\,\mathrm{sinc}\left(\frac{kL}{2}\right) - (1-h(k))\frac{1}{\sqrt{2\pi}}L\,\mathrm{sinc}\left(\frac{kL}{2}\right)$$

Taking the Fourier transform to give the modified image.

$$\Psi_{el7}(x) = S_-(x)e^{i\left(\frac{\gamma L}{2}+\gamma x\right)}e^{i\alpha} + S_+(x)e^{i\left(\frac{\gamma L}{2}-\gamma x\right)} + 1 + \frac{1}{2}\left(S_+(x)+S_-(x)\right)\left(1+e^{i\alpha}\right) + \Delta_4(x) \qquad [3.41]$$

where,

$$\Delta_4(x) = \left[S_+(x)+S_-(x)\right] \otimes \frac{i}{\sqrt{2\pi}x}\left(1-e^{i\alpha}\right) \qquad [3.42]$$

It is assumed that $\Delta_4(x)$ is an error function, only significant very close to $x=-L/2,\ 0,\ L/2$. Furthermore, choosing the magnitude of the phase-shift to be $\alpha=\pi$, then gives $e^{i\alpha}=-1$. This reduces equation 3.41 to give,

$$\Psi_{el7} = -S_-(x)e^{i\left(\frac{\gamma L}{2}+\gamma x\right)} + S_+(x)e^{i\left(\frac{\gamma L}{2}-\gamma x\right)} + 1 \qquad [3.43]$$

and the error term $\Delta_4(x)=0$. The image (figure 3.32) shows no change in the free space region, but there are now fringes, of the same generic form as in equation 3.32, present in both the left and right domains simultaneously. There is however a discontinuity occurring at $x=0$ where the fringe pattern is out of phase by π. This is because the electrons in the magnetic peak at $x=-\gamma$ are phase-shifted by π relative to the electrons in the magnetic peak at $x=\gamma$. To overcome this problem a small-hole aperture can be used to phase-shift both magnetic spots with only part of the central shape function passing unaffected, this is investigated fully in section 4.3.

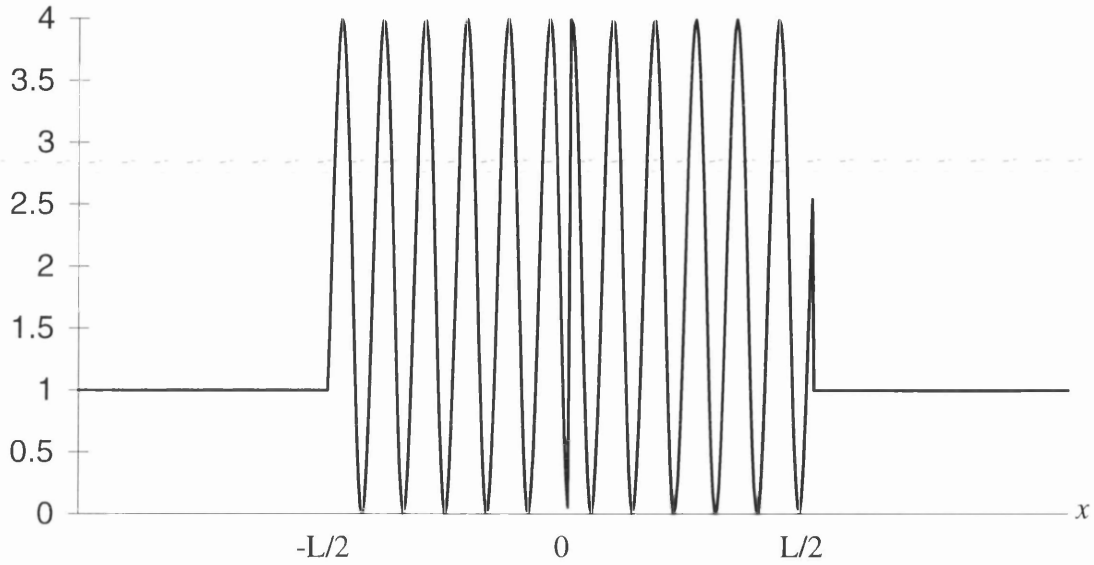

Figure 3.32 *CF image using a phase-shifting aperture in position 3.*

3.3.8 Investigation of position 4 using a phase shifting aperture.

Figure 3.33 shows the diffraction pattern when the aperture is in position 4 introducing a phase-shift to all electrons where $k \leq 0$.

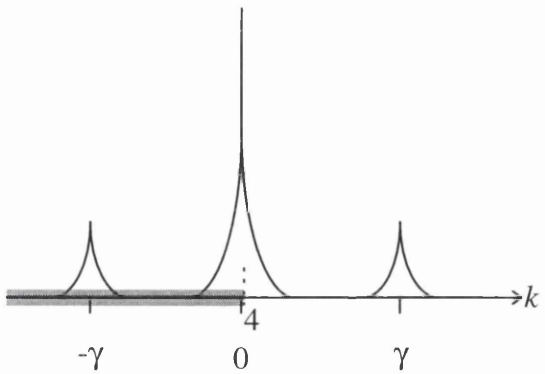

Figure 3.33 *Phase-shifting aperture in position 4.*

The left magnetic peak, half the shape function and the central delta function are phase-shifted. The other terms pass unaffected. The disturbance in the BFP is given by,

$$\overline{\Psi}_{el8}(k)=e^{i\alpha}h(k)\frac{\left(e^{\frac{i\gamma L}{2}}-e^{\frac{-ikL}{2}}\right)}{\sqrt{2\pi}i(k+\gamma)}+(1-h(k))\frac{\left(e^{\frac{ikL}{2}}-e^{\frac{i\gamma L}{2}}\right)}{\sqrt{2\pi}i(k-\gamma)}+\sqrt{2\pi}\delta(k)e^{i\alpha}h(k) \qquad [3.44]$$
$$-e^{i\alpha}h(k)\frac{1}{\sqrt{2\pi}}L\,\mathrm{sinc}\left(\frac{kL}{2}\right)-(1-h(k))\frac{1}{\sqrt{2\pi}}L\,\mathrm{sinc}\left(\frac{kL}{2}\right)$$

Taking the Fourier transform to give the modified image.

$$\Psi_{el8}(x)=S_-(x)e^{i\left(\frac{\gamma L}{2}+\gamma x\right)}e^{i\alpha}+S_+(x)e^{i\left(\frac{\gamma L}{2}-\gamma x\right)}+1e^{i\alpha} \qquad [3.45]$$
$$+\frac{1}{2}(S_+(x)+S_-(x))(1+e^{i\alpha})+\Delta_4(x)$$

As before $\Delta_4(x)$ is (equation 3.42) only significant very close to x=-L/2, 0, L/2. Choosing the phase-shift $\alpha=\pi$, then gives $e^{i\alpha}=-1$. Equation 3.45 can be reduced to give

$$\Psi_{el8}(x)=-S_-(x)e^{i\left(\frac{\gamma L}{2}+\gamma x\right)}+S_+(x)e^{i\left(\frac{\gamma L}{2}-\gamma x\right)}-1 \qquad [3.47]$$

The image (figure 3.34) shows a uniform intensity of unity in free space. Fringes are present in both domains simultaneously. Both sets of fringes show a phase change of π compared to when the aperture is in position 3 due to the phase-shifting of the central delta function in this case.

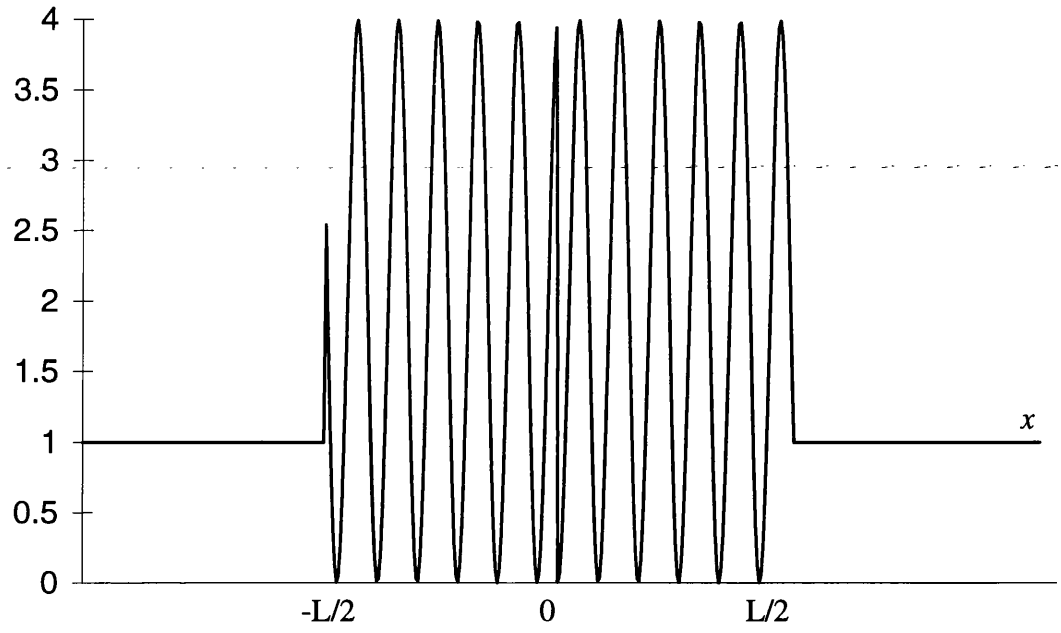

Figure 3.34 *CF image using a phase-shifting aperture in position 4.*

3.4 Conclusion

In this chapter we have discussed the image formation process of CF imaging and analysed two simple magnetic systems. The analytical investigation has shown that when an opaque aperture is positioned, in the central region of the diffraction pattern, fringes form running parallel to the direction of the magnetisation. These fringes run parallel to the direction of the local magnetic induction and so reveal the magnetic microstructure. The fringes have a periodicity of h/eB_0t. Therefore, by measuring the fringe spacing we can quantify the value B_0t.

CF images obtained when using an opaque aperture lose some of the magnetic information due to the electrons being deflected into the aperture. This problem can be resolved by taking another CF image when the aperture is in the complementary position. An attractive option is to replace the opaque aperture with a phase-shifting aperture. In this case, only a single image is required to reveal the magnetic microstructure because the fringes form in all domains simultaneously.

In chapter 4 computer simulations are used to further the analysis of CF imaging. The computer simulations can evaluate the error terms which we have encountered. This allows us to study small positional changes of the aperture to check the stability of this technique. We also, introduce the small-hole phase-shifting aperture and discuss its benefits in reducing the artefacts present in the CF images.

The implementation of experimental CF imaging is discussed in chapter 5. CF images of small permalloy elements are presented which confirm the basic analytical theory. We then investigate more complex micromagnetic structures and show how CF imaging can be used to reveal stray fields. We can also use CF imaging to quantify the magnetic induction (B_0) in specimens of a known thickness. We also investigate the changes in B_0 when the temperature of the specimen is increased to beyond the Curie temperature. Finally, CF imaging is used to reveal the degradation in magnetic properties when specimens are fabricated using different processes.

The future of CF imaging is discussed in chapter 8. Here, we apply similar analytical considerations to small non-magnetic elements, in which the electrostatic term dominates the specimens phase function. Fringes form in the image, of a similar nature to those present when CF imaging magnetic samples, from which we get a measure of the inner potential (V_0). We also investigate a magnetic force microscopy (MFM) tip. This is a complex situation where both a magnetic and an electrostatic contribution must be considered in the phase function.

Chapter 4

Computer simulation of coherent Foucault imaging.

4.0 Introduction.

The one dimensional computer simulation (section 4.1) of CF imaging goes beyond the simple analytical study and allows us to investigate how fringe visibility and spacing vary with precise positioning of the aperture in the diffraction plane (section 4.1.1 and 4.1.2). CF imaging with a small-hole phase-shifting aperture is also studied (section 4.1.3), with specific attention being paid to how the imaging conditions vary with the size of the small-hole. The magnitude of phase-shift introduced by the phase-shifting apertures is then discussed (section 4.1.4), to find how important its precise value is for experimental use. Thereafter, calculations are performed in which the angle subtended by the source is extended (section 4.1.5) to show why a FEG source is favoured for CF imaging.

These considerations are further discussed in the context of two-dimensional simulations (section 4.2) which facilitate direct comparison with experimental images. A simple two domain element (section 4.2.1) and a small element containing four domains in a closure structure (section 4.2.2) are investigated.

4.1 One-dimensional computer simulation of CF imaging.

The one-dimensional computer simulation is carried out using Microsoft Excel, utilising the fast Fourier transform (FFT) routine. The one-dimensional object to be investigated is shown in figure 4.1.

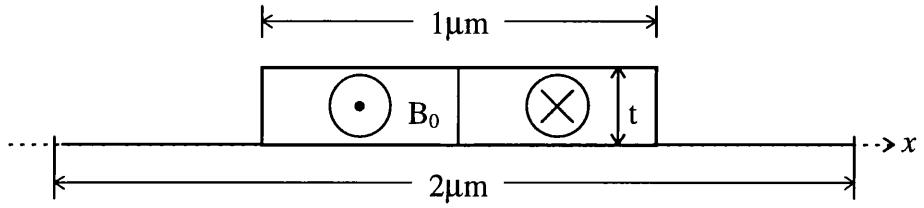

Figure 4.1 *A schematic diagram of the two domain element.*

To carry out numerical simulations, values must be assigned to all parameters. The values chosen are appropriate to the experimental investigations, described in appendix A. The width of each domain is taken as 0.5μm and the total window size is 2.0μm. The window is required to represent free space and its size is chosen to set the sampling rate. By using a 512 point array to represent the object, the sampling interval is ≈4nm. This is considered appropriate as it is comparable to the resolution of the microscope when used for CF imaging.

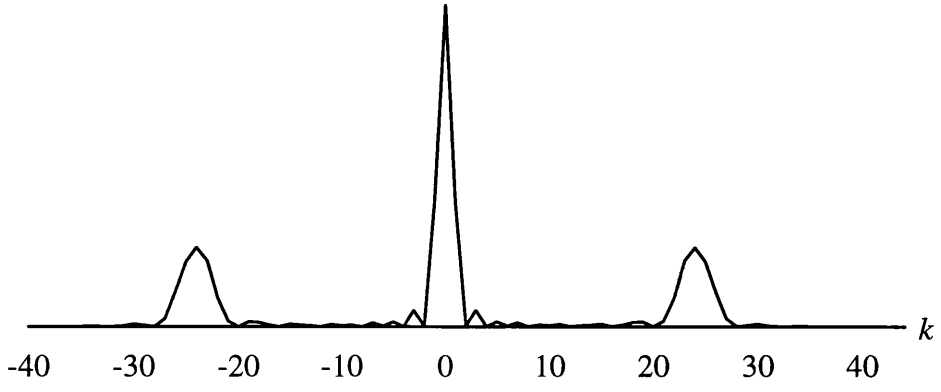

Figure 4.2 *Computer simulated diffraction pattern.*

A FFT is used to calculate the disturbance in the back focal plane. Given a real space sampling interval of ≈4nm it follows that the maximum spatial frequency in the window in Fourier (reciprocal) space is ≈0.125nm^{-1} which corresponds to a scattering angle of

≈320μradian if the electron energy is 200keV. The classical Lorentz deflection angle is given by $eB_0t\lambda/h$ (where λ is the electron wavelength, section 2.2) and for the parameters given above is ≈30μradian. Thus the magnetic peak occurs around a pixel value of 24 and the whole diffraction pattern is ≈50 pixels in extent.

The computer programme allows the calculated disturbance to be modified multiplicatively by a second array representing the aperture function. Thereafter a second FFT is performed and the square modulus of the resulting distribution taken to give the intensity distribution in the image.

4.1.1 Semi-infinite opaque aperture.

Figures 4.3a-c show three CF images formed using a semi-infinite opaque aperture. Fringes are present only in the right domain with the intensity in free space reducing as the central spike is masked in accordance with the analytical study (section 3.3). The difference between the images is due to the positioning of the aperture. In figure 4.3b the aperture edge is located at the exact centre of the diffraction pattern whilst in figure 4.3a and 4.3c it is displaced by -1 and +1 pixels respectively. Such a displacement corresponds to an angular shift of ≈2.5μradian which is well within our positional capability experimentally. Clearly the visibility of the fringes decreases as the aperture moves away from its central position although the periodicity does not change significantly. The latter has an average wavelength of 82nm which compares well with the 80nm expected from the simple analytical theory of section 3.3.

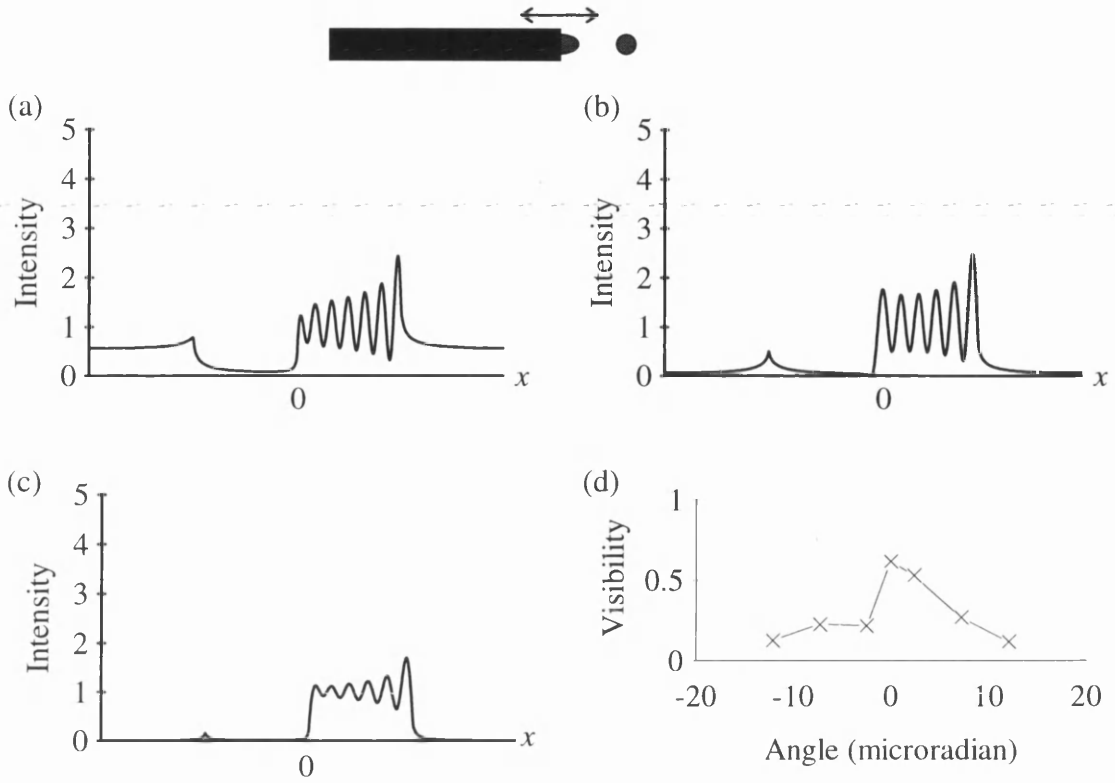

Figure 4.3 *CF images using a semi-infinite opaque aperture. The aperture edge is displaced from the centre of the diffraction pattern by (a) -1, (b) 0 and (c) 1 pixel. (d) shows how the visibility varies with aperture position.*

Figure 4.3d shows quantitatively how the fringe visibility depends on aperture position. The visibility is defined as $(I_{max}-I_{min})/(I_{max}+I_{min})$, where I_{max} and I_{min} are respectively the mean fringe intensity maxima and minima across each image. Clearly fringe visibility drops off rapidly as the aperture is moved from the centre of the disturbance in the diffraction plane. However, the fringes remain visible even when the aperture is significantly displaced from the optimum position.

4.1.2 Semi-infinite phase-shifting aperture

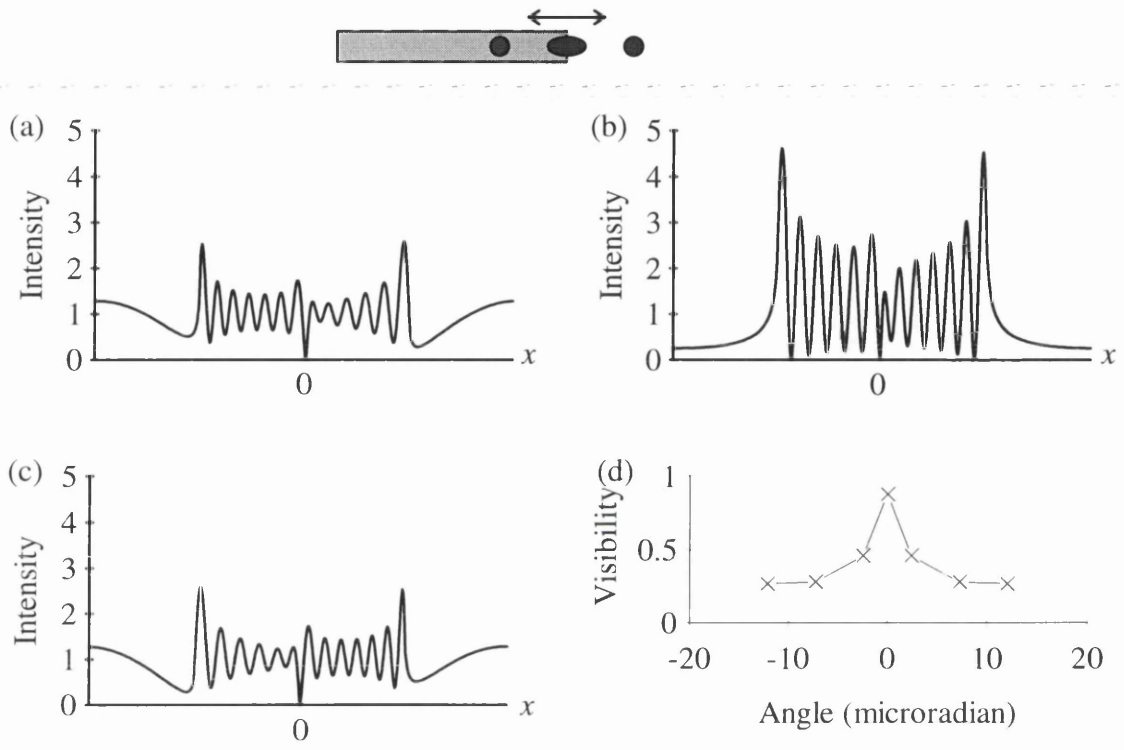

Figure 4.4 *CF images using a semi-infinite phase-shifting aperture. The aperture edge is displaced from the centre of the diffraction pattern by (a) -1, (b) 0 and (c) 1 pixel. (d) shows how the visibility varies with aperture position.*

Figures 4.4a-c show three CF images formed using a semi-infinite phase-shifting aperture where the phase change introduced is π radian. It is immediately apparent that fringes are present in both domains simultaneously. The difference between the images is due to the positioning of the aperture (section 4.1.1). It is clear that the visibility of the fringes decreases as the aperture moves away from its central position. The average wavelength is found to be 82nm, the same as when using the semi-infinite opaque aperture. Also of note are the marked discontinuities in the images at $x = 0$ where the two domains meet. This is due to the fact that one magnetic spot in the diffraction pattern is phase-shifted whilst the other is not. It is clear that fringe visibility (figure 4.4d) drops off rapidly as the aperture is moved from the centre of the disturbance in the diffraction plane but that fringes remain visible even when the aperture is significantly displaced from the optimum position.

4.1.3 Small-hole phase-shifting aperture.

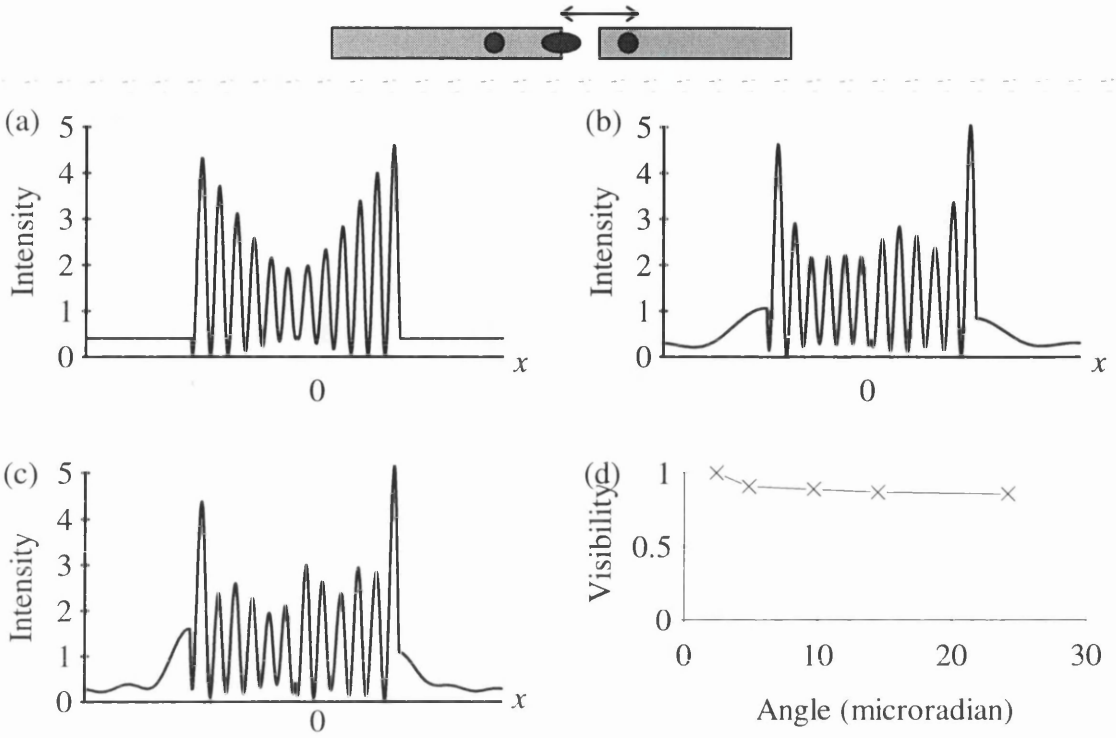

Figure 4.5 *CF images using a small-hole aperture of size (a) 1, (b) 3 and (c) 7 pixels. (d) shows how the visibility varies with aperture position.*

An attractive variant on the semi-infinite phase-shifting aperture is to use a phase-shifting aperture containing a hole which is small compared with the overall extent of the diffraction pattern. If one edge of the aperture coincides with the centre of the diffraction pattern, both magnetic spots suffer a constant phase change whilst only the central spot is affected differentially. Figures 4.5a-c show CF images using small-hole apertures of different sizes. One edge of the hole is held at $k = 0$ whilst the other is located 1, 3 or 7 pixels away from it. Thus the size of the largest hole is approximately 25% of the distance between the central and magnetic spots in the diffraction pattern (figure 4.2). As will be seen in section 5.2, apertures of this size can readily be fabricated. The CF images in figure 4.5 show similar fringes to those in figure 4.4 but there is no longer a discontinuity where the domains meet at $x = 0$. Furthermore, figure 4.5d shows that the fringe visibility remains at a high value as the size of the hole is increased.

4.1.4 Variation in phase-shifting magnitude.

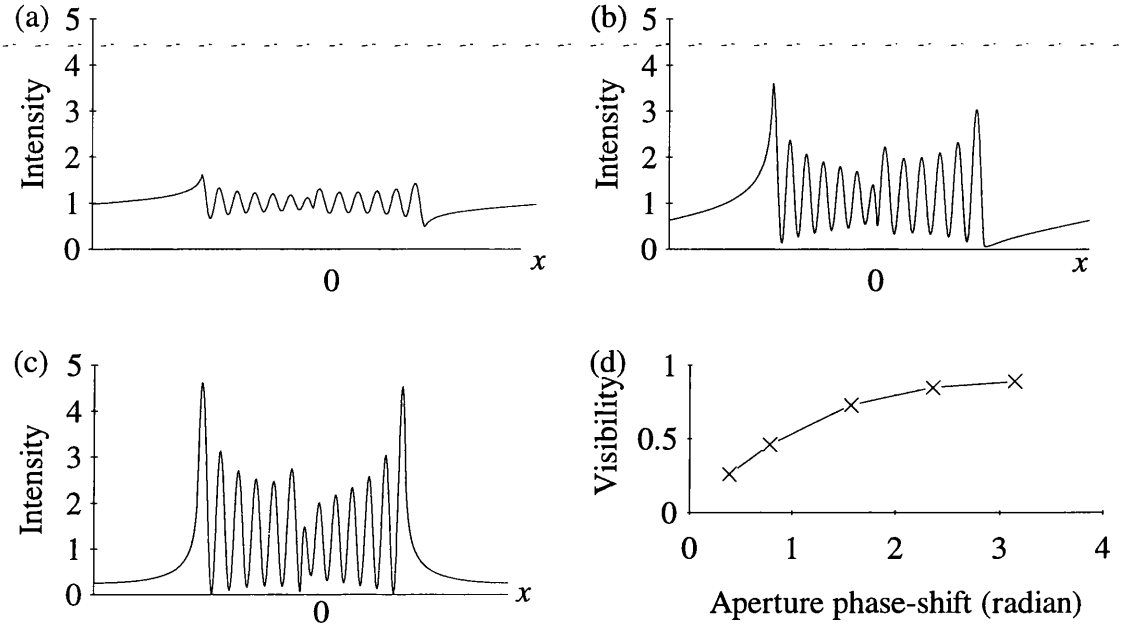

Figure 4.6 *CF images using a semi-infinite phase-shifting aperture with the aperture edge at the centre of the diffraction pattern. The apertures introduce a phase-shift of (a) π/8, (b) π/2 and (c) π radian. (d) shows how the visibility varies with phase-shift.*

So far we have assumed that the magnitude of the phase-shift introduced by the aperture is π radian. It is of interest to investigate how the fringe pattern changes with the magnitude of the phase-shift so that the importance of selecting the correct thickness (section 2.3) for the phase-shifting film can be evaluated. Figures 4.6a-c show CF images obtained using semi-infinite phase-shifting apertures of various strengths optimally positioned in the diffraction plane. Also shown (Fig. 6d) is how the visibility of the fringes varies with the magnitude of the phase-shift. From these data it is clear that as the phase shift decreases from π radian only a modest decrease in visibility is experienced until a phase-shift < π/2 radian is reached. After this the fringe visibility decreases more rapidly but fringes can still be seen for values as low as π/8 radian. Hence, whilst a phase shift of π radian is optimal it is clear that appreciable variations can be experienced without undue performance loss being experienced.

4.1.5 Extending the source.

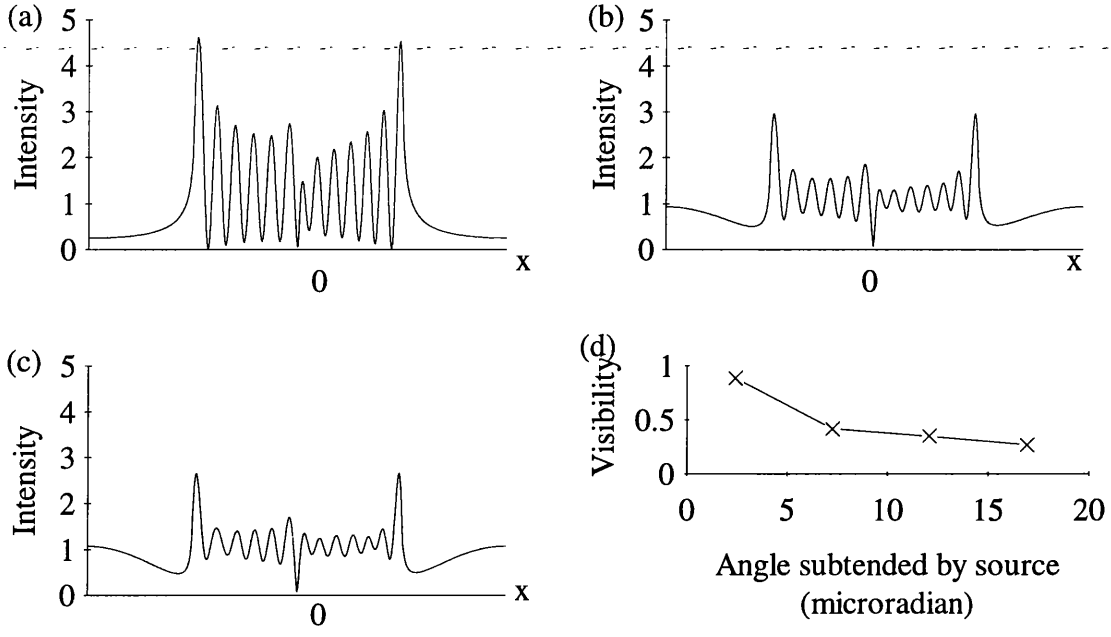

Figure 4.7 *CF images using a semi-infinite phase-shifting aperture with the aperture edge at the centre of the diffraction pattern. The source size is (a) 1,(b) 3 and (c) 5 pixels. (d) shows how the visibility varies with the angle subtended by the source.*

A further parameter of interest is the angle subtended by the source. In the preceding images we have assumed this is infinitesimally small corresponding to the condition of perfect spatial coherence. However, a study of how the fringes are affected as the angle subtended by the source is extended is readily amenable to investigation by computer simulation. The source lies in a plane conjugate to the diffraction pattern. Therefore, if the angle subtended by the source is extended we effectively have a super-position of shifted diffraction patterns each of which is cut by a stationary aperture in a different place. In figure 4.7 we assumed that the illumination could be represented by a one-dimensional top-hat function, that a semi-infinite aperture with a phase-shift of π radian is used and that the aperture is positioned optimally. Figures 4.7a-c show the resulting CF images corresponding to sources subtending total angles of 0, 7.5 and 12.5μradian. The visibility of the fringes decreases rapidly as the source size increases emphasising the advantage of using an instrument with a FEG for CF imaging of magnetic microstructures.

4.2 Two-dimensional computer simulations of CF images.

A two-dimensional computer simulation (figure 4.8) allows more complex objects to be considered. Here we have written a programme in Interactive Data Language (IDL) which runs on a DEC-α workstation[1,2].

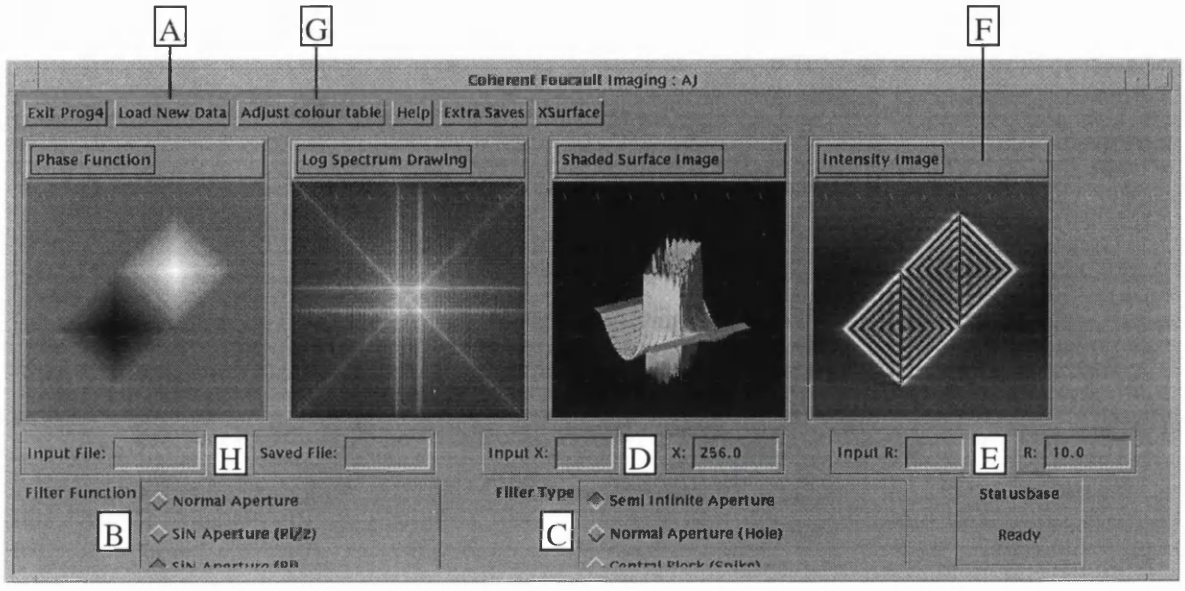

Figure 4.8 *Two dimensional computer simulation.*

The program reads in a pre-written data set (figure 4.8A) which represents the phase-function describing the specimen to be imaged. As before, a FFT generates the complex disturbance in the diffraction plane which is subsequently modified by multiplication by a suitable aperture function. Apertures of all the kinds discussed previously can be created for interactive use. The buttons indicated by figure 4.8B and C are used to create the aperture function (e.g. phase-shifting semi-infinite) which is positioned by inputting co-ordinates into the specified boxes (figure 4.8D and E). Thereafter, the square modulus of a second FFT gives the intensity distribution in the image plane. For an object represented by a $(512)^2$ array, the program takes 2 minutes to run and 20 seconds to calculate a subsequent image if the aperture is repositioned or changed in type. The program consists of four display windows (figure 4.8F), each of which can show one of nine different image types to investigate the CF imaging process. These are: scaled phase function, diffraction pattern, logarithmic diffraction pattern, diffraction linescan at 0°, diffraction linescan at 45°, scaled image, image linescan at 0°, image linescan at 45° and a shaded surface plot of

the image. Additional features allow for the colour to be adjusted (figure 4.8G) to enhance the image contrast and introduce different colour tables. The image in the furthest right window can also be saved (figure 4.8H) to a file in the CompuServe GIF format[3].

Over ten phase functions have been created representing the domain structures found in small magnetic elements. In the following sections we discuss a two domain element and an element containing four domains in a closure structure.

4.2.1 Two domain element

To illustrate the use of the program and for comparison with the one-dimensional computer simulation a simple model is first considered. The object (figure 4.9a) has the parameters given in appendix A. It represents a small element of width 1μm and of infinite length, situated in a window of $2\mu m^2$. The diffraction pattern (figure 4.9b) comprises a central spot, broadened by the object shape function, surrounded by two magnetic spots located at a distance of 24 pixels from the centre.

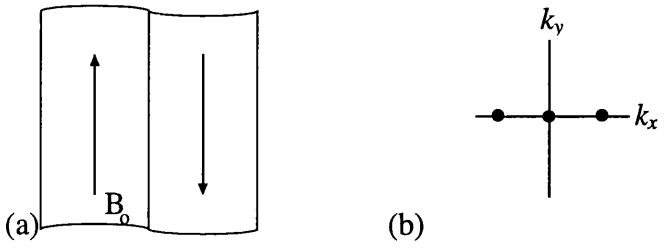

Figure 4.9 *(a) Schematic of the two domain element and (b) the corresponding diffraction pattern.*

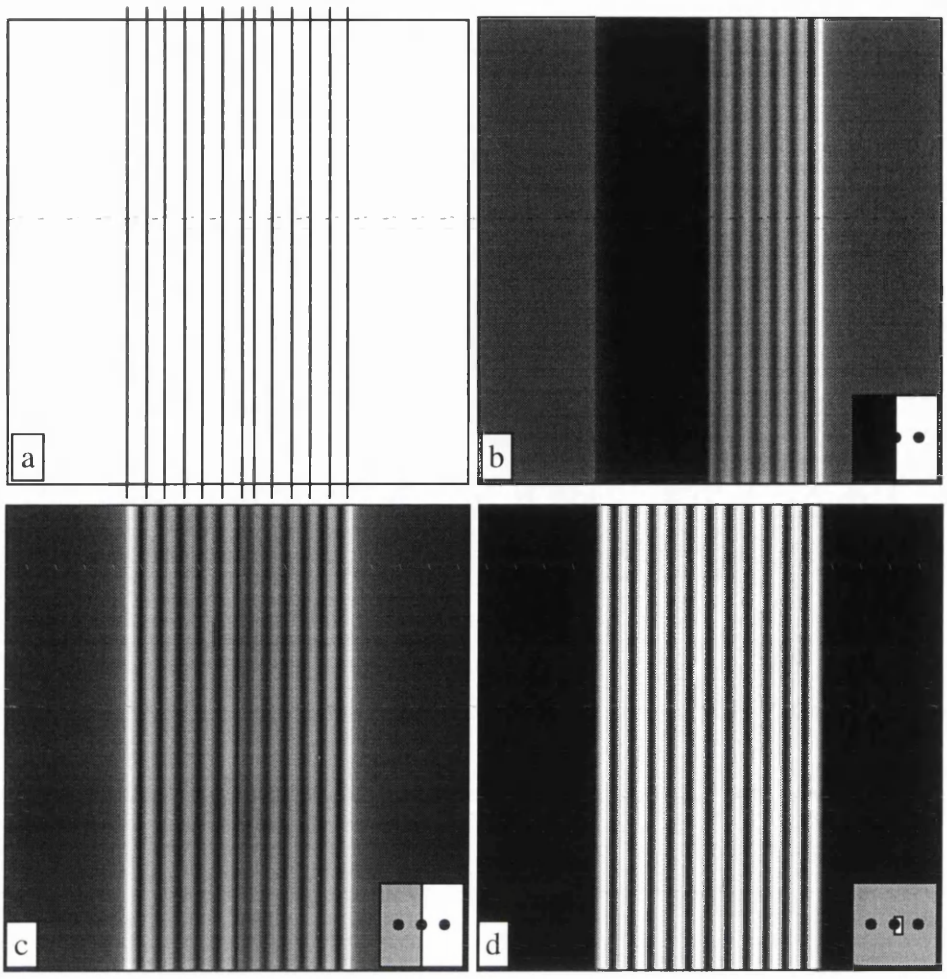

Figure 4.10 *(a) shows a phase contour plot of the element. CF images using (b) a semi-infinite opaque aperture, (c) a semi-infinite phase-shifting aperture and (d) a small-hole phase-shifting aperture both introducing a phase-shift of* π.

Figure 4.10a shows a phase contour plot corresponding to the object of figure 4.9a. In that the phase function relates directly to the magnetic induction distribution in the specimen we may regard this as the idealisation of a CF image. For comparison, figure 4.10b-d show calculated CF images using various apertures each optimally positioned so that an edge cuts the middle of the central diffraction spot. In figure 4.10b an opaque aperture is assumed so that fringes are seen only in right domain, there being no information available about the induction distribution in the left domain. For figure 4.10c and d phase-shifting apertures introducing shifts of π radian are used and fringes can be seen in both domains simultaneously. However, it is apparent that when a semi-infinite aperture is used (figure 4.10c) a discontinuity occurs in the fringe system along the boundary of the domains. This is again avoided by the use of a small-hole phase-shifting aperture and figure 4.10d approximates very closely to the ideal image, there being no artefacts present to render its

interpretation difficult. However, figure 4.10d is simulated assuming an aperture only 1 pixel in extent which is unrealistically small. Figure 4.11a and b repeat the calculations for larger apertures, square in shape, and located as shown in the inset. It can be seen that modest increase in size to 12 pixels (equivalent to an aperture subtending an angle of 30μradian) results in little deterioration. Significant artefacts are present when the size is increased to 24 pixels (60μradian) where the aperture extends to cut the right magnetic spot. Fortunately apertures sufficiently small for these problems not to be experienced can be realised in practice as the results in the chapter 5 demonstrate.

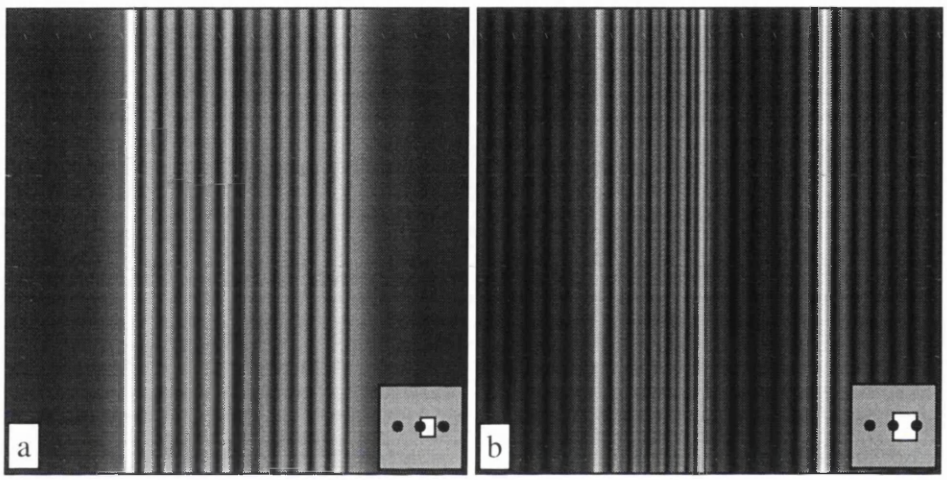

Figure 4.11 *CF images using a small-hole phase-shifting aperture, with the size of the hole being extended to (a) 12 and (b) 24 pixels respectively.*

4.2.2 Four domain element forming a closure structure.

For comparison with the experimental images presented in the next chapter, the object considered is a small square magnetic element containing four domains forming a closure structure (figure 4.12a). The element has parameters given in appendix A, is 1μm across a diagonal and is centred in a window of 2μm square. The diffraction pattern (figure 12b) comprises a central spot, broadened by the object shape function, surrounded by four magnetic spots located a distance equivalent to 24 pixels from the pattern centre.

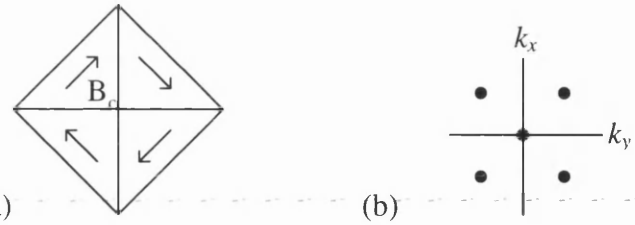

Figure 4.12 *(a) Schematic of the four domain element and (b) the corresponding diffraction pattern.*

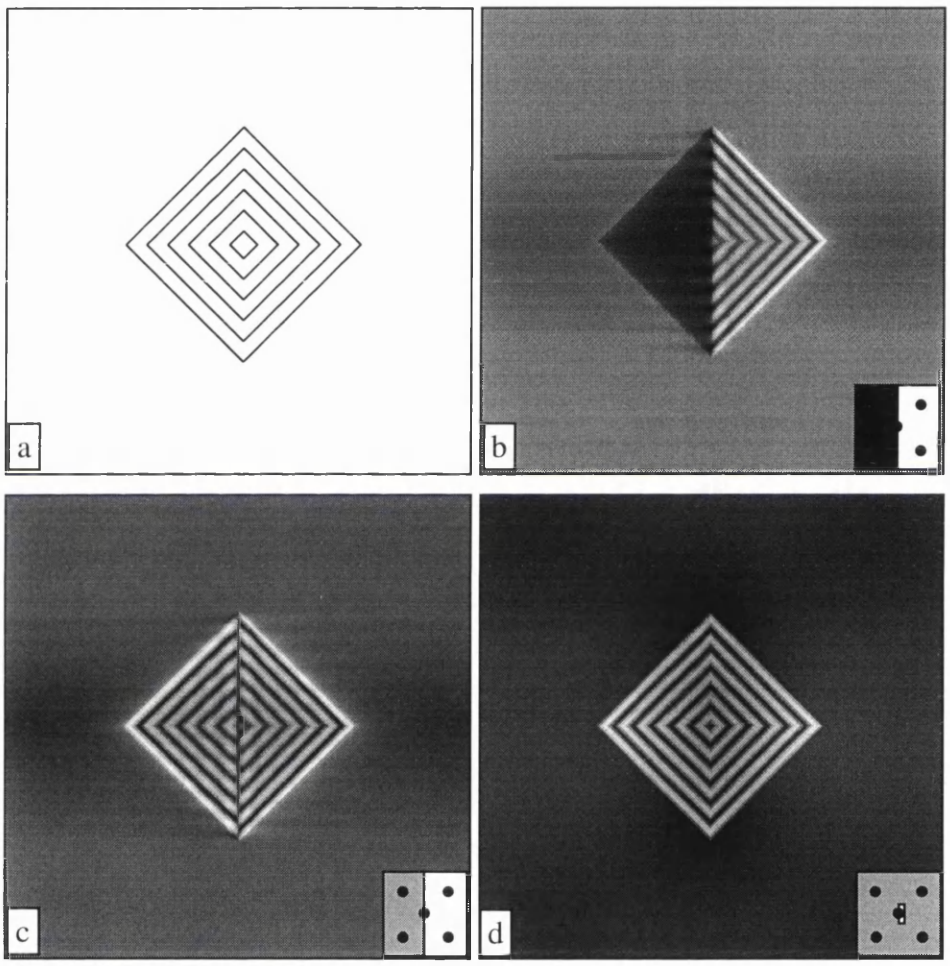

Figure 4.13 *(a) shows a phase contour plot of the element. CF images using (b) a semi-infinite opaque aperture, (c) a semi-infinite phase-shifting aperture and (d) a small-hole phase-shifting aperture both introducing a phase-shift of* π.

Figure 4.13a shows a phase contour plot corresponding to the object of figure 4.12a. Figures 4.13b-d show calculated CF images using various apertures each optimally positioned so that an edge cuts the middle of the central diffraction pattern spot. In figure 4.13b an opaque aperture is used so that fringes are seen only in two domains there being

no information available about the induction distribution in the other two. There is contrast in the left domains which shows a smeared fringe pattern extending from the vertical boundary. This is due to the abruptness of the cutting aperture. For figures 4.13c and d phase-shifting apertures introducing shifts of π radian are used and fringes can be seen in all domains simultaneously. However, it is apparent that when a semi-infinite aperture is used (figure 4.13c) a discontinuity occurs in the fringe system, along a line through the centre of the magnetic element running parallel to the aperture edge. This is again avoided by the use of a small-hole phase-shifting aperture (figure 4.13d). However, figure 4.13d is simulated assuming an aperture only 1 pixel in extent. Figure 4.14 repeats the calculations for larger apertures. It can be seen that modest increase in size to 12 pixels (30μradian) results in little deterioration and serious artefacts only start to appear when the size is increased to 24 pixels (60μradian).

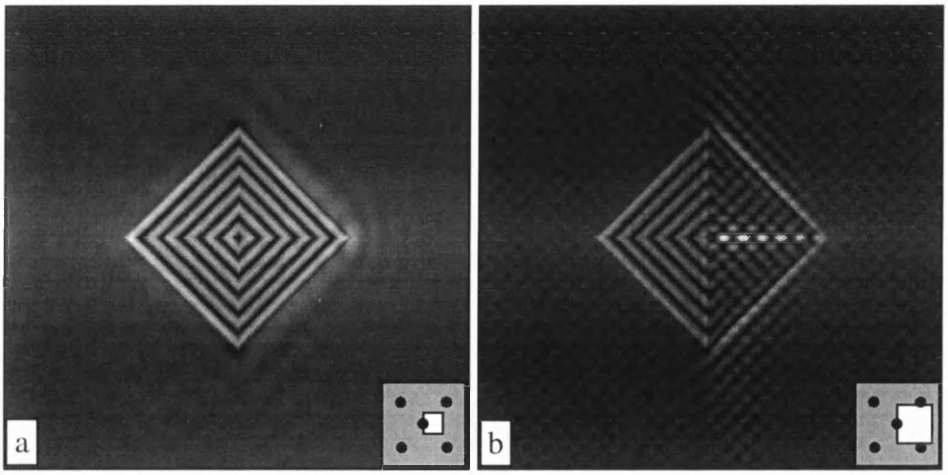

Figure 4.14 *CF images using a small-hole phase-shifting aperture, with the size of the hole being extended to (a) 12 and (b) 24 pixels respectively.*

4.3 Conclusion.

In this chapter we have simulated the CF image formation process by computer. The one-dimensional computer simulation has been used to confirm the basic analytical theory of CF imaging (chapter 3). Here the fringes show an average fringe periodicity of 82nm which compares well with the 80nm predicted analytically. We have investigated the positioning of semi-infinite opaque and phase-shifting apertures and the results suggest

that the aperture stability required is well within experimental sensitivity (chapter 5). The small-hole phase-shifting aperture is introduced to show CF images containing minimal artefacts can be generated. We establish the optimum phase-shift to be π radian but note that deviations from this value are not critical to the CF imaging conditions. We have also revealed a significant deterioration in the CF image visibility as the angle subtended by the source is increased. This re-enforces the requirement for the TEM to be fitted with a FEG source.

Two-dimensional CF imaging has allowed for more complex objects to be studied. Here, a two domain element and an element containing four domains in a solenoidal structure have been analysed.

In the next chapter we discuss the implementation of CF imaging experimentally and the fabrication techniques required to make each type of aperture. CF images are obtained using these types of apertures to confirm the basic analytical theory. The small-hole phase-shifting aperture, as expected, produces CF images with the minimum of artefacts and high visibility fringes. This type of aperture is then used to obtain the CF images when carrying out a selection of experiments on small shapes which have in-plane dimensions ranging from 0.5-4μm.

Chapter 8 looks at the application of the CF imaging technique to investigate specimen in which the electrostatic term is dominant in the phase function. A further development is to consider the magnetic force microscopy (MFM) tip. This involves the combination of both electrostatic and magnetostatic terms in the specimen phase function.

References

[1] R. Comerford, IEEE spectrum, **Vol. 29**, No. 7, 26 (1992).

[2] D. Andrews, BYTE, **Vol. 18**, No. 5, 26 (1993).

[3] Wm. Liaw, Dr Dobbs Journal, **Vol. 20**, No. 2, 56 (1995).

Chapter 5

Experimental coherent Foucault imaging of magnetic microstructures.

5.0 Introduction.

CF imaging has been realised on a modified Philips CM20 FEG TEM to obtain magnetic interferograms of small permalloy elements fabricated by electron beam-lithographic and evaporation techniques[1] (section 5.3). Individual elements with magnetic induction of 1T and thicknesses of 50nm and 30nm have been investigated, their in-plane dimensions are between 0.2μm and 4.0μm. Elements studied were rectangular, triangular or rhomboidal in shape, forming a near-ideal model micromagnetic system. Their dimensions are comparable with what might be expected for the next generation of pole-tip regions of recording heads and magnetoresistive sensors in ultra-high density recording systems.

Initially, the different aperture types are discussed confirming the CF imaging theory discussed in chapters 3 and 4. This study provides insight into the effect of size (section 5.5) and shape (section 5.6) on magnetic properties of the elements. Thereafter, the elements are investigated while being magnetised along their easy (section 5.7) and hard axes (section 5.8). The effect of increasing the temperature in-situ (section 5.9) is also considered, the domain structures and the changes in the magnetisation of the elements being analysed as they approach the Curie temperature. Finally, two samples prepared using different etching techniques are compared, for the purpose of determining how the magnetic properties of material change during fabrication processes.

5.1 Microscope imaging conditions.

The principal modifications to the TEM relevant to the work described here are the inclusion of two additional super-mini lenses situated above and below the main objective lens[2] (section 2.2.5). These so-called Lorentz lenses are non-immersion lenses and allow high quality images to be obtained whilst the specimen remains in magnetic field-free space. Using these lenses, suitably excited, it is possible to accurately locate the diffraction pattern in the relevant aperture plane. Images can then be seen either on the microscope viewing screen or, through the use of a low-light-level TV pick-up system, on a TV monitor (section 2.2.7). The latter is recommended as it facilitates the accurate final positioning of the aperture which is done by maximising the visibility of the fringes in the image.

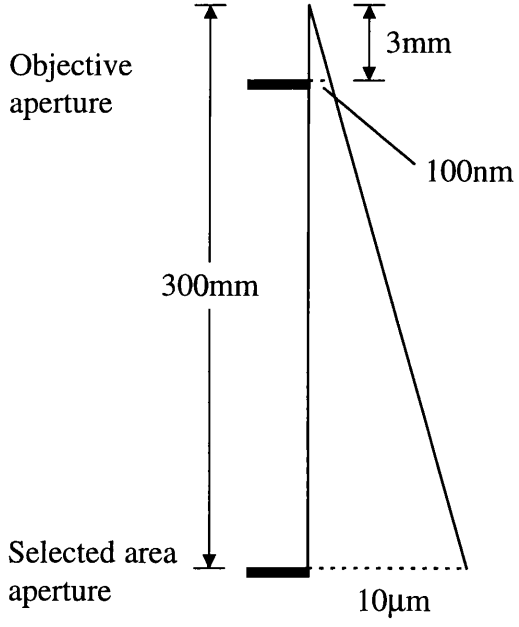

Figure 5.1 *Extent of the magnetic deflection in the diffraction and SA planes.*

A choice exists between forming the diffraction pattern in the plane of the objective aperture or the selected area aperture. Figure 5.1 shows that the magnetic deflection extends to 100nm in the diffraction plane and 10μm in the SA plane. In practice we tend to use the latter option as the camera length in the selected area plane is ≈10x greater.

This means that larger aperture sizes can be tolerated, the correct positioning of the aperture is more easily accomplished and the requirements on the mechanical stability of the aperture blade are less. However, an inevitable consequence of working in the higher camera length mode is that the image magnification is reduced by the same factor by which the camera length is increased. Nonetheless, images with magnifications in excess of 20kx can still be obtained on the pick-up system that are perfectly adequate for most micromagnetic studies.

5.2 Opaque and phase-shifting TEM apertures.

The opaque aperture that has been used to obtain the experimental images is simply a standard TEM aperture with a large hole. In practice the edges of such apertures are neither completely abrupt nor uniform but, with care, regions suitable for blocking part of the magnetic diffraction pattern could be found.

The phase-shifting apertures that have been used in this work are fabricated from silicon nitride (Si_3N_4) membranes[3]. These are prepared by chemical vapour deposition of a 15-70nm layer of Si_3N_4 on a silicon wafer of thickness 335μm. Fabrication of the membranes involves a series of photolithographic and etching steps which result in the structure shown in figure 5.2. The membranes are produced in the centre of a 2mm square so the can fit into most TEM specimen holders. Small holes are then plasma etched in the silicon nitride membrane to represent the phase-shifting aperture discussed (section 3.7 and section 4.4).

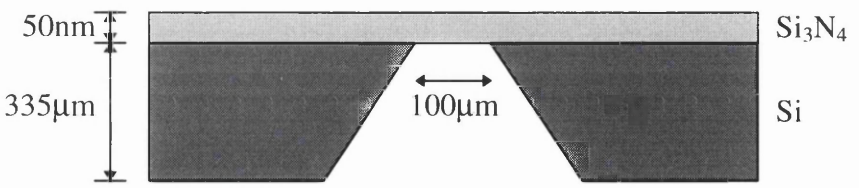

Figure 5.2 *Cross-section view of Si_3N_4 membrane.*

The extent of the magnetic diffraction pattern in the plane of the selected area aperture (figure 5.1) is ≈10μm with and holes ≈30μm are used as approximations for half-plane

phase-shifting apertures. However, when the phase shift is to be applied to the central portion of the diffraction pattern alone, holes in the range 0.5μm-2.0μm in diameter are needed. In practice a number of holes of varying size are etched in the same membrane to accommodate different experimental investigations.

As the silicon nitride was in the form of a uniform amorphous thin film and plasma etching allowed regular-shaped sharp-edged holes to be introduced, the phase-shifting apertures were in many ways more satisfactory than their opaque counterparts. However, one problem that remained was the appropriate thickness to ensure a phase shift of π radian. Equation (2.23) shows how this depends on both the film thickness and the mean inner potential. Unfortunately, the authors are unaware of any measurement of the latter quantity in the literature. Guided by measured values for similar materials[4] a value of 10eV was assumed. With this value, a film thickness of 50nm and an electron energy of 200keV, a phase shift very close to π radian is predicted. We should also recall that figure 4.10 shows that differences introduced due to departures from π radian are very small suggesting that a precise knowledge of inner potential is not required.

5.3 Specimen preparation.

The techniques in fabricating small elements are varied, the most common procedure being that of standard photolithography[5]. This technique is limited by a fundamental resolution limit due to the wavelength of light achieving a resolution of 1μm in practice[6]. The technique used in this study is electron beam lithography[7], where a resolution approaching 10nm can be attained and is described in this section. Two specimens have been fabricated in this way, specimen 1 by L. Zhou and specimen 2 by B. Khamsehpour.

Membranes, as described in section 5.2, with a 15nm thick Si_3N_4 layer are used to support the patterned material. The first step in the element fabrication process[8] (figure 5.3) is to deposit resist onto the support material. The resist is a material whose molecular structure changes on irradiation with an electron beam. The pattern is then defined by scanning a focused electron probe across the resist. Care has to be taken to ensure that spacing of the elements on the membrane is large enough so that they are non-interacting[3]. Subsequently the electron exposed areas dissolve out when the sample is immersed in a solution of developer, in the case of positive resist which is used here. The next step involves deposition of the material to be studied. The excess metal and resist are then removed in the 'lift off' process[9]. The remaining metal on the substrate now forms the elements which were scanned out by the electron beam.

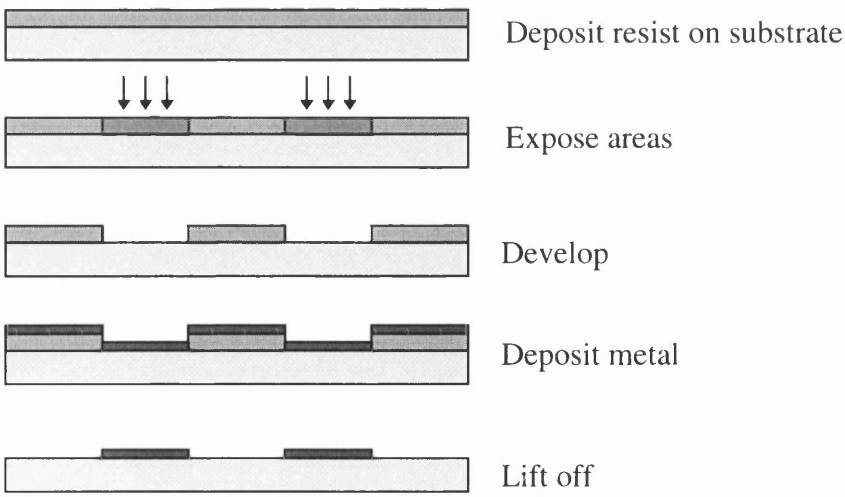

Figure 5.3 *Schematic of the lithographic process.*

The material used in this section is permalloy (Py) which is a nickel iron binary-alloy[10,11], the composition being close to $Ni_{80}Fe_{20}$. This material has a relatively high magnetisation (0.9-1.05T) with a high permeability, and is of low intrinsic magnetocrystalline anisotropy and magnetostriction. This leads to the domain structures observed in regularly shaped elements being primarily determined by their shape and size.

The deposition of the thin permalloy layer[12] is achieved by resistive heating in a vacuum chamber at a pressure of $<10^{-5}$Torr. A quartz crystal is used to monitor the thickness of the deposited film, 50nm for sample 1 and 30nm for sample 2 in these experiments. A slow evaporation, not greater than $0.3nms^{-1}$, is used to reduce stress to prevent the metal peeling off the substrate. A bright field image (figure 5.4) of a 100nmx100nm element shows a micropolycrystalline structure and exhibits the high edge acuity (≈10nm) available using e-beam lithography. The grain size is estimated to be in the 5-10nm range.

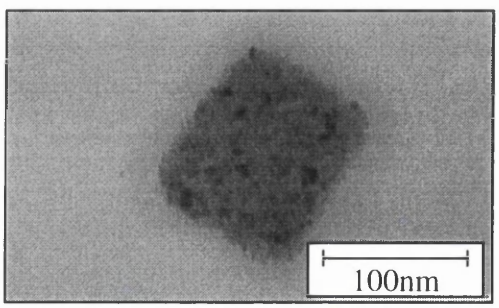

Figure 5.4 *Bright field image of an element 100x100nm^2.*

5.4 CF images using different apertures.

An initial experiment is to compare CF images when using semi-infinite opaque, semi-infinite phase-shifting and small-hole phase-shifting apertures. Figure 5.5 shows experimental CF images of a permalloy element from specimen 1 (50nm thick) with in-plane dimensions 2μm by 1μm.

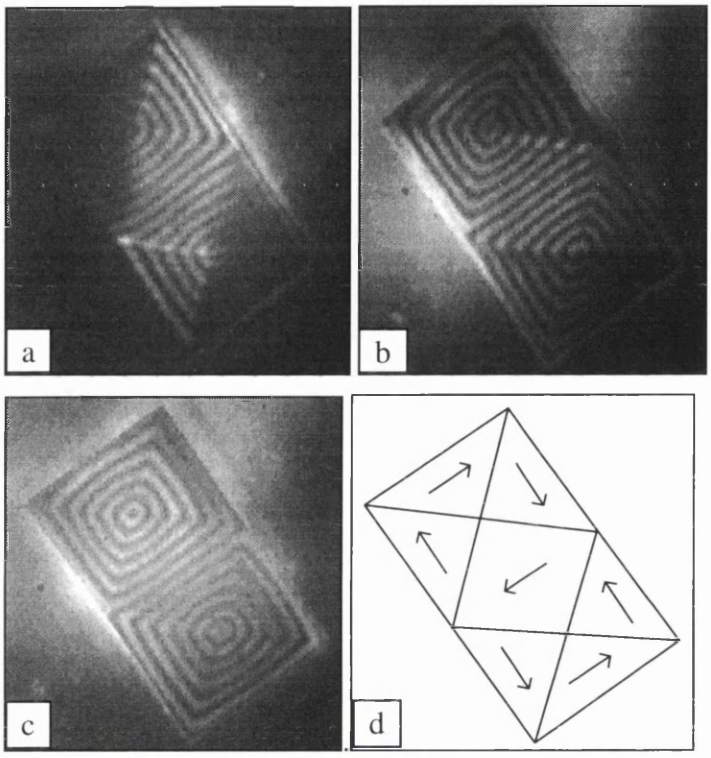

Figure 5.5 *Experimental CF images of a 2μm by 1μm element using (a) a semi-infinite opaque, (b) a semi-infinite phase-shifting and (c) a small-hole phase-shifting aperture. The schematic of the induction distribution is shown in (d).*

As predicted, fringes are present in only some of the domains when the opaque aperture is used. Furthermore, a small amount of blurring is visible close to the boundaries between those domains where fringes can be seen and those which appear simply as regions of low intensity. This is a result of a lack of abruptness and consequent incomplete opacity at the aperture edge. The other images in figure 5.5 show the advantages of using a phase-shifting aperture. High visibility fringes of the predicted periodicity are apparent across the magnetic element as a whole and give a direct and immediate picture of the spatial variation of induction. The magnetic structure, shown schematically in figure 5.5, consists

of a solenoidal distribution comprising two flux closure circuits of the kind used in the simulations of chapter 4. The number two is simply a consequence of the aspect ratio of the magnetic element under investigation (section 5.6). Whilst figures 5.5b and c both show fringe systems running across the entire element, artefacts are more apparent when the semi-infinite aperture is used in accordance with the simulations shown in chapter 4.

5.5 Observation of domain structures found in small rectangular elements.

Observations of the magnetic microstructure associated with small regular elements fabricated by standard photolithography have been discussed by various authors[13,14]. The size and shape of elements fabricated by electron beam lithography are discussed by McVitie[1,3] (1988), where the Fresnel (section 2.4.2) and differential phase contrast (DPC) imaging[15] modes are implemented. DPC provides information on the magnetic induction orientation within the element and can give an indication of any stray fields present. CF imaging is complementary to both the aforementioned techniques giving a quantitative description of the magnetic induction within the element and is indicative of the stray fields, although these are difficult to quantify in certain cases.

The square and rectangular elements that are discussed in this chapter can be classified in terms of shape, size and domain structure. Domain structures are divided into two main categories; category I structures are those in which flux closure is essentially complete within the element whereas category II elements display incomplete flux closure within the elements. Further classification denotes the dimensions of the elements by L_1, L_2 and L_3 where L_1 is the larger in-plane dimension and L_3 is the element thickness. Figures 5.6-5.7 show the possible flux closure structures for a set of elements where the dimension L_1 is kept constant at 3μm an the other dimension L_2 is varied from 1.5μm-0.5μm. The images in this section are obtained when using the elements with a thickness L_3=30nm (specimen 2).

Category Ia structures are defined as those with the domain configuration as in figure 5.6a where the element has the dimensions 3μmx1.5μm; the corresponding schematic diagram is shown in figure 5.6b. It is noted that this structure reflects the fact that the ratio of L_1 to L_2 is integral so that domains can be separated entirely by 90° walls. Figure 5.6c shows an element of 3μmx1μm containing a category Ib structure. Essentially the magnetisation configuration is the same as the category Ia structure with the magnetisation parallel to the edges of the element and the domains separated by straight walls. The difference in this case is that although the straight 90° walls are still present, sections of 180° wall are introduced. Also of importance is the appearance of cross-tie walls in the 180° wall section that are expected in permalloy films of thickness 30nm. The mean fringe periodicity in both these images is 133nm, which corresponds with the theoretical considerations which predict a fringe periodicity of 135nm.

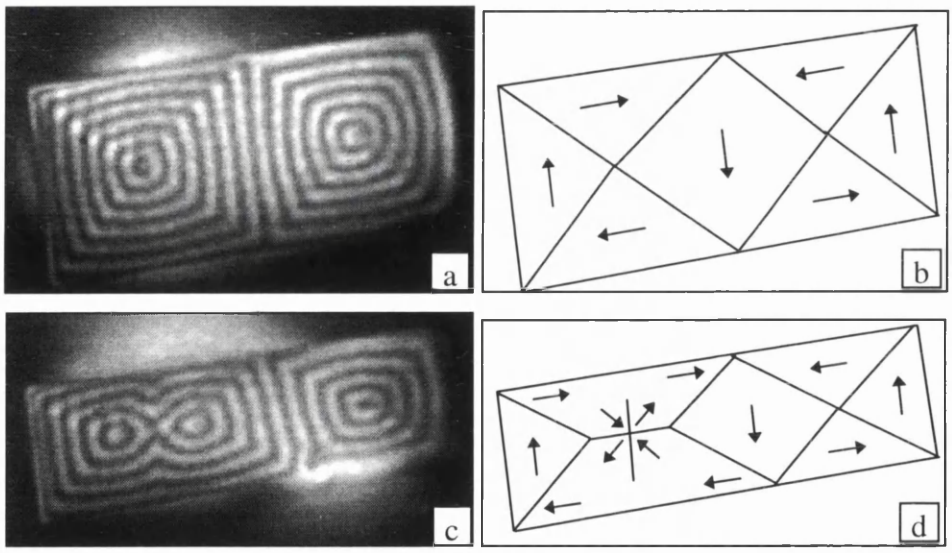

Figure 5.6 *CF images showing category I structures within two elements with dimensions (a) 3μmx1.5μm and (c) 3μmx1μm. The corresponding schematics are shown in (b) and (d) respectively.*

The division between the two categories occurred at an aspect ratio of $n=L_1/L_2$ having a value of about 4 such that those elements with $n\leq4$ possess category I structures. Category II domain structures are defined as those in which a closed flux path does not exist within the element itself. Elements possessing these structures are those with $n\geq4$ and two examples are shown in figures 5.7a and c. Evidently the domain structures present in

these elements are not as simple as the category I geometry and the magnetic contrast could be interpreted as giving rise to incomplete flux closure within the element. The curved walls are in marked contrast to the walls in the category I structures. Category IIa structures are defined as those in which the rotation of the magnetisation at both ends of the element is in the same sense as in figure 5.7a. By comparison in the IIb structure the magnetisation at both ends is in the opposite sense (figure 5.7c). The two structures appear in the sample with about the same frequency with no apparent association between the structure and the aspect ratio of the element.

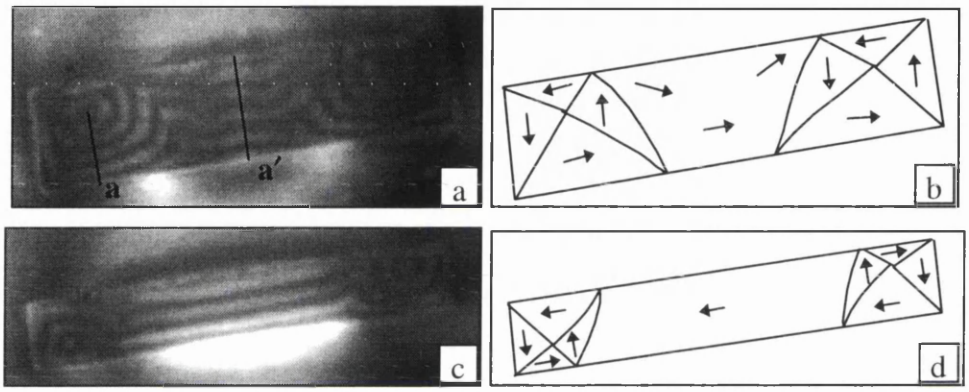

Figure 5.7 *CF images showing category II structures of a rectangular element with dimensions (a) 3μmx0.75μm and (c) 3μmx0.5μm. The corresponding schematics are shown in (b) and (d) respectively.*

The intensity variation outside the element is indicative of the formation of free poles along certain walls required to generate such contrast. It is apparent that the element is uniformly magnetised along its length in the centre although the magnetisation at the ends deviates strongly from this direction. This rotation of magnetisation at the ends of the element appears to provide a degree of flux closure although it is evident from these images that there exists a region of magnetic volume charge where $\nabla.\underline{\mathbf{M}}\neq 0$. There is also a small contribution to the stray field from the edges of the elements where the magnetic surface charge $\underline{\mathbf{M}}.\underline{\mathbf{n}}\approx 0$. This is due to the formation of free poles along the edges of the element indicated in the image by fringes which run into the edge of the element. It should also be noted that the fringes are not of a constant periodicity throughout the images. A closer look at figure 5.7a reveals the fringes along the line **a** have a periodicity of 133nm whereas the line **a′** shows a periodicity of 166nm. This change in periodicity

can be associated with the stray fields around the central region through which the incident electrons are deflected. The measured in-plane magnetic induction ($\underline{B}^{in}_{tot}$) is related to the in-plane demagnetising field ($\underline{B}^{in}_{stray}$) by the relationship,

$$\int_{-\infty}^{\infty} \underline{B}^{in}_{tot} dz = \mu_0 \underline{M}_o t - \int_{-\infty}^{\infty} \underline{B}^{in}_{stray} dz \qquad [5.1]$$

where $\underline{M}_o$ is the saturation magnetisation of permalloy and μ_0 is the magnetic permeability constant. Therefore the measured difference in fringe spacings gives an indication of the local stray fields which are present integrated along the electrons trajectory. Along the line **a'**, the fringe periodicity of 166nm can be translated into an integrated stray field strength of 0.2T.

5.6 CF imaging of different shapes.

The advantages of CF imaging over other Lorentz microscopy techniques are apparent when elements showing a more complex micromagnetic system are investigated. The two shapes of interest in this section are the rhombus and the triangle. These elements are defined on specimen 2 which is of thickness 50nm. These shapes can be classified by their edge width (L_1), and the angle (θ) between the edge and the x-axis as shown in figure 5.8.

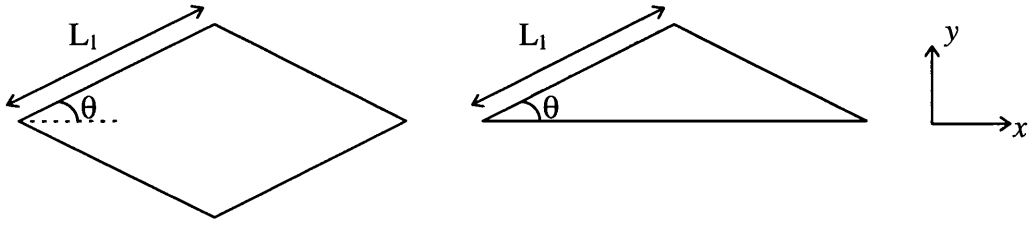

Figure 5.8 *Definition of the parameters used to define the rhombuses and triangles.*

Figure 5.9 shows CF images of four elements, rhomboidal in shape, with the corresponding schematic diagrams of the magnetic induction distributions. The element in figure 5.9a has the parameters L_1=2μm and θ=50°. The solenoidal distribution that is

present is similar to those elements showing a category Ia structure. Within the element the fringes are of the expected periodicity and the magnetisation runs parallel to the edge of the element. The latter leads to the domains being separated by walls where the magnetisation rotates through either 80° or 100° depending on the angle of the corner on which the domain wall terminates. When the angle θ is reduced to 40° (figure 5.9c), a somewhat complex domain structure is present, as highlighted in the schematic diagram (figure 5.9d). CF imaging provides a clear indication of the magnetisation distribution within the element which would be very difficult to achieve using the other Lorentz microscopy techniques. The magnetic induction appears to be near solenoidal which is confirmed by the absence of stray fields. The domain configuration in figure 5.9e, where L_1=2μm and θ=30°, is very regular in comparison. There is a central region where the magnetisation forms a hexagonal structure. There are four main domain walls in which the magnetisation rotates by 63.5° and two others in which the rotation is 53°, and there are two small closure structures within the acute corners. It should also be noted that the magnetisation bends at the centre of the large domains to follow the edge of the sample and appears to bow in the two domains connected to the closure structures. Although the magnetisation appears to form a solenoidal distribution there are stray fields arising from the obtusely angled corners. Consequently, this changes the fringe periodicity along the line **b** to 92nm which corresponds to an integrated stray field of 0.15T. As the angle is further reduced to θ=20° (and L_1=2μm), the element shows a single domain structure where the magnetisation is attempting to follow the sample edges but bends towards the centre of the element. There are stray fields surrounding the element concentrated at the acute corners. The change in fringe periodicity along the line **c** is 19nm which corresponds to a local integrated demagnetising field of 0.24T.

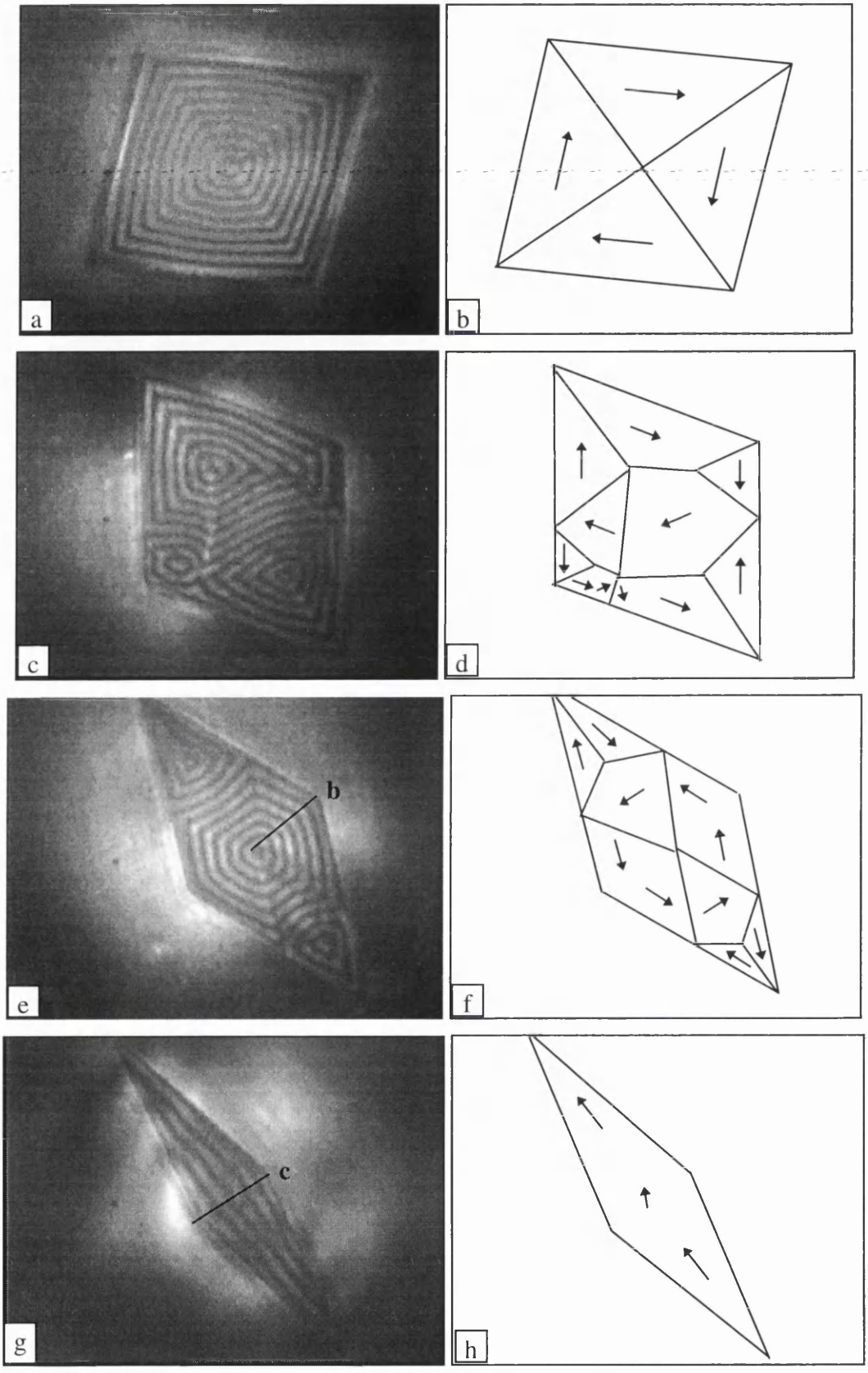

Figure 5.9 *CF images of four rhomboidal elements with the corresponding schematic of the micromagnetic structure. The element has dimensions L_l=2μm and the angles are (a) θ=50°, (c) θ=40°,(e) θ=30° and (g) θ=20°.*

The triangular elements show many features in common with the rhomboidal shapes. Figure 5.10 shows CF images of four elements triangular in shape with the corresponding schematic diagrams of the magnetic induction distributions. The element in figure 5.10a has the parameters L_l=2μm and θ=50°. The magnetic induction is highly non-solenoidal in this case. There are three 90° domain walls present within the element with the magnetisation rotating in the vicinity of the two non-central walls. Stray fields are apparent throughout the image, concentrated at the corners of the element. A quantitative description of these demagnetising fields is limited due to the poor contrast at the acute corners of the element, and by the fact that the fringes show a slight variation in periodicity across the element. A rough estimate of the stray field strength is given by looking along the line **d** in figure 5.10a. The fringes show a mean periodicity of ≈100nm which can be translated into an integrated demagnetisation field of ≈0.25T. As the angle θ is reduced to 30° it is found that the element is effectively uniformly magnetised along the long axis. However, there is a 60° rotation of the magnetisation in the central region, as indicated in the schematic (figure 9.10d). The fringe periodicity within the element and the stray field contrast surrounding the element are of a similar nature to the previous element.

The pattern of elements has been designed so that they would be non-interacting and calculations were undertaken to determine a reasonable spacing between the elements[3]. An exception to this case is given in figure 5.10e where the elements were put very close together. The CF image suggests that these elements are indeed interacting; the schematic distribution is given in figure 5.10f. It is expected, from the stray field distributions, that the magnetisation is pointing in opposite directions in the elements. If the upper element is uniformly magnetised the stray field follows a path between the two surfaces where $\underline{\mathbf{M}}.\underline{\mathbf{n}}\neq 0$. Thus provided the lower element is magnetised in the opposite direction to the lower element there is an easy return path for the stray field. A configuration with the two elements magnetised in the same direction would lead to an unfavourable stray field distribution and would be a higher energy state. It should also be noted that the slight variation in magnetisation direction in the upper element may not necessarily be due to the stray field from the lower element. The varying stray fields yet again make a quantitative

measurement very difficult. A rough estimate of fringe periodicity is ≈84nm, along the line **e**, which corresponds to an integrated demagnetisation field of ≈0.05T. This reduction in stray field strength is consistent with the theory that the elements are interacting and provide a certain amount of flux closure within the system.

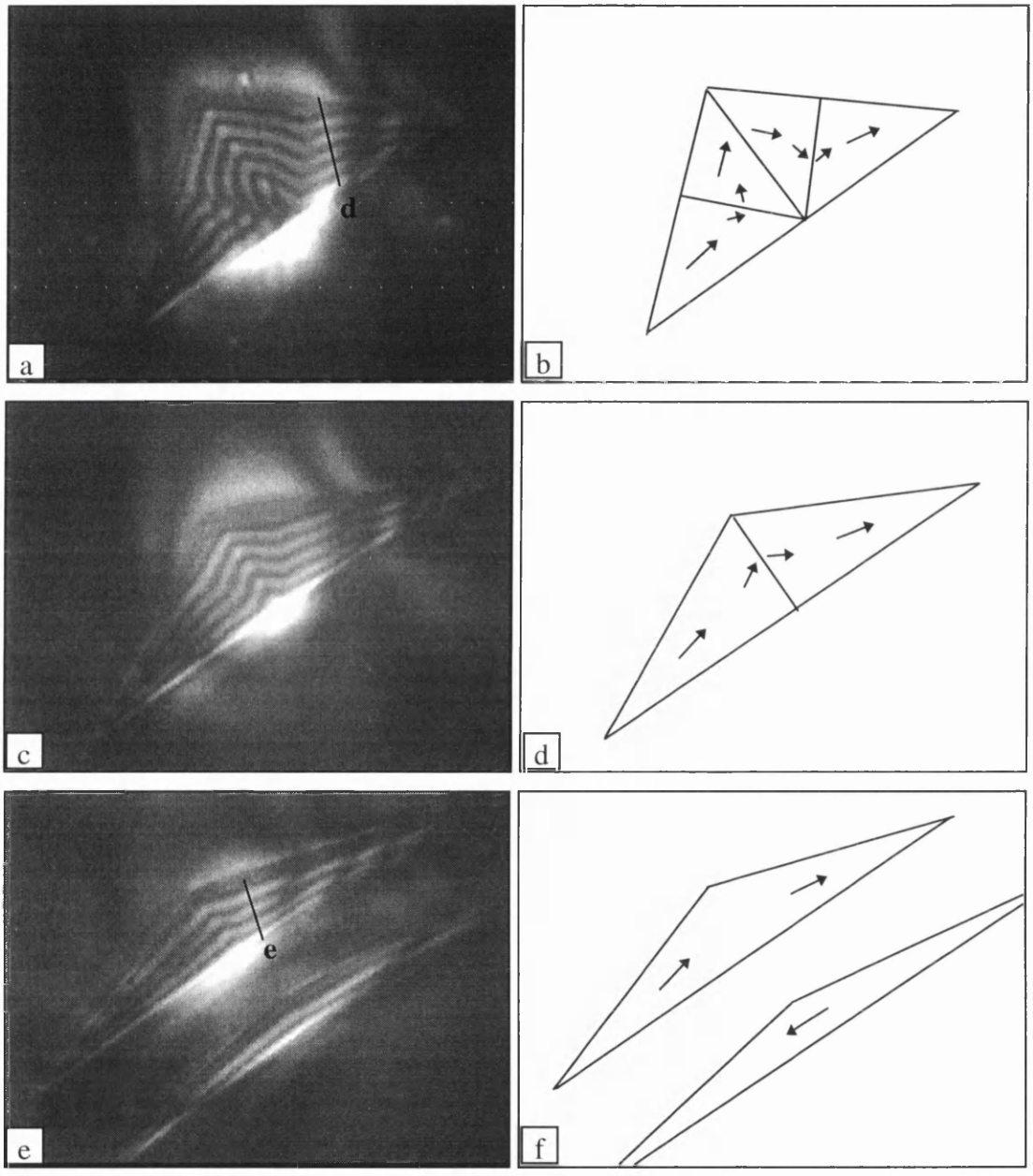

Figure 5.10 *CF images of four triangular elements with the corresponding schematic of the micromagnetic structure. The element has dimensions L_l=3μm and the angles are (a) θ=50°, (b) θ=40°,(c) θ=30° and θ=20°.*

This section has provided an insight into how CF imaging can be implemented to investigate the complex domain structures in a selection of rhombuses and triangles. The fringe periodicity gives a quantitative description of the magnetic induction distribution within the element and is indicative of the stray fields surrounding the element.

5.7 Magnetisation of a rectangular element along the easy axis.

Previous studies of the application of fields to small regularly shaped elements have been carried out by McVitie[16] (1988) using the Fresnel imaging technique. The domain wall configurations of an element showing a solenoidal (category I) structure in the demagnetised state were investigated. This work was expanded upon by Hefferman[17] (1991) where Foucault imaging was implemented. The magnetisation distributions within and the stray fields surrounding elements with $L_1>4L_2$ (non-solenoidal category II structures) were investigated whilst under the influence of an external field. This section looks at an element of dimensions 3μmx1μm magnetised along its easy axis. Subsequently, a similar treatment for the hard axis is given in the following section.

The Philips CM20, on which CF imaging is realised, can facilitate the application of large vertical magnetic fields in-situ. When the sample is subsequently tilted in this field, the in-plane component can be used to magnetise the elements. Fields in excess of 0.65T can be applied vertically using the objective lens at full excitation. However, this size of field is too large to implement the CF imaging conditions. In this section a vertical field of H_{vert}=400Oe is found to be appropriate, the in-plane component is given by $H_{vert}\sin(\xi)$, where ξ is the tilting angle. At this value of field strength CF imaging can be successfully implemented as well as being able to near uniformly magnetise the element to be investigated in its easy axis. To achieve this condition in the hard axis requires far greater fields.

Hefferman[17] (1991) discussed the hysteresis loop[18] (figure 5.10) of an element with similar dimensions to the element that is investigated here. In the ac demagnetised state the element supports a regular solenoidal domain structure which changes to a non-

solenoidal distribution on application of a field H_{s1}. This state persists as the field is increased to H_{max} but, on reduction of the field, the transition back to a distorted solenoidal distribution occurs at a field H_{s2} which satisfies $0<H_{s2}<H_{s1}$. Thus in their remanent state these elements have a zero net moment and exist in only a single solenoidal state.

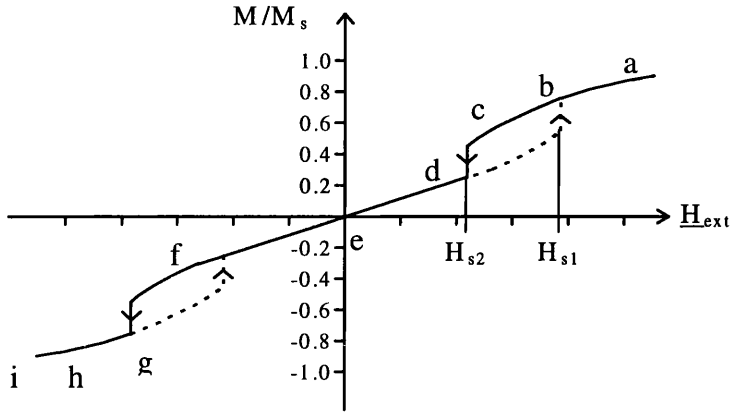

Figure 5.11 *The easy axis hysteresis loop of the 3μmx1μm element showing the magnetisation path highlighted. The positions on the hysteresis loop at which the CF images in figure 5.11 occur are also indicated.*

In this study a 3μmx1μm rectangular element from specimen 2 (30nm thick) is investigated whilst being magnetised along the easy (long) axis. The initial magnetisation distribution is such that the element is uniformly magnetised along the long axis. The external field is then reduced to zero and the field direction is reversed until the element is uniformly magnetised in the opposite direction. Figure 5.12 shows CF images of the element and the main micromagnetic structures observed are shown schematically in figure 5.13. The CF images obtained are related directly to position on the hysteresis loop (figure 5.11).

Initially the element is uniformly magnetised at a field of ≈300Oe at the maximum tilt of 50°. Images are first available at a tilt of 35° due to the sample and holder blocking the field of view. Figure 5.12a shows the element with a field of 210Oe being applied along the long axis of the element. The magnetisation distribution supports a non-solenoidal (category II) structure. The magnetisation lies along the long axis of the element with the magnetisation at the ends of the element aligning to the sample edge. The result of this is

that there is little or no magnetic surface charge but a region of volume charge (where $\nabla.\underline{\mathbf{M}}\neq 0$) exists towards either end of the element. As the field is further reduced to 147Oe (figure 5.12b) and then to 80Oe (figure 5.12c) the magnetisation in the central region continues to be orientated along the long axis of the element. There is a slight change in the end structures which grow as the field is reduced. The contrast surrounding the elements in all three images is indicative of stray fields. As the field is relaxed the stray fields also reduce in strength. The fringes have a periodicity of 167nm along the line **f** in figure 5.12c compared to 133nm when there are no stray fields present. This translates as a local integrated field strength of 0.20T.

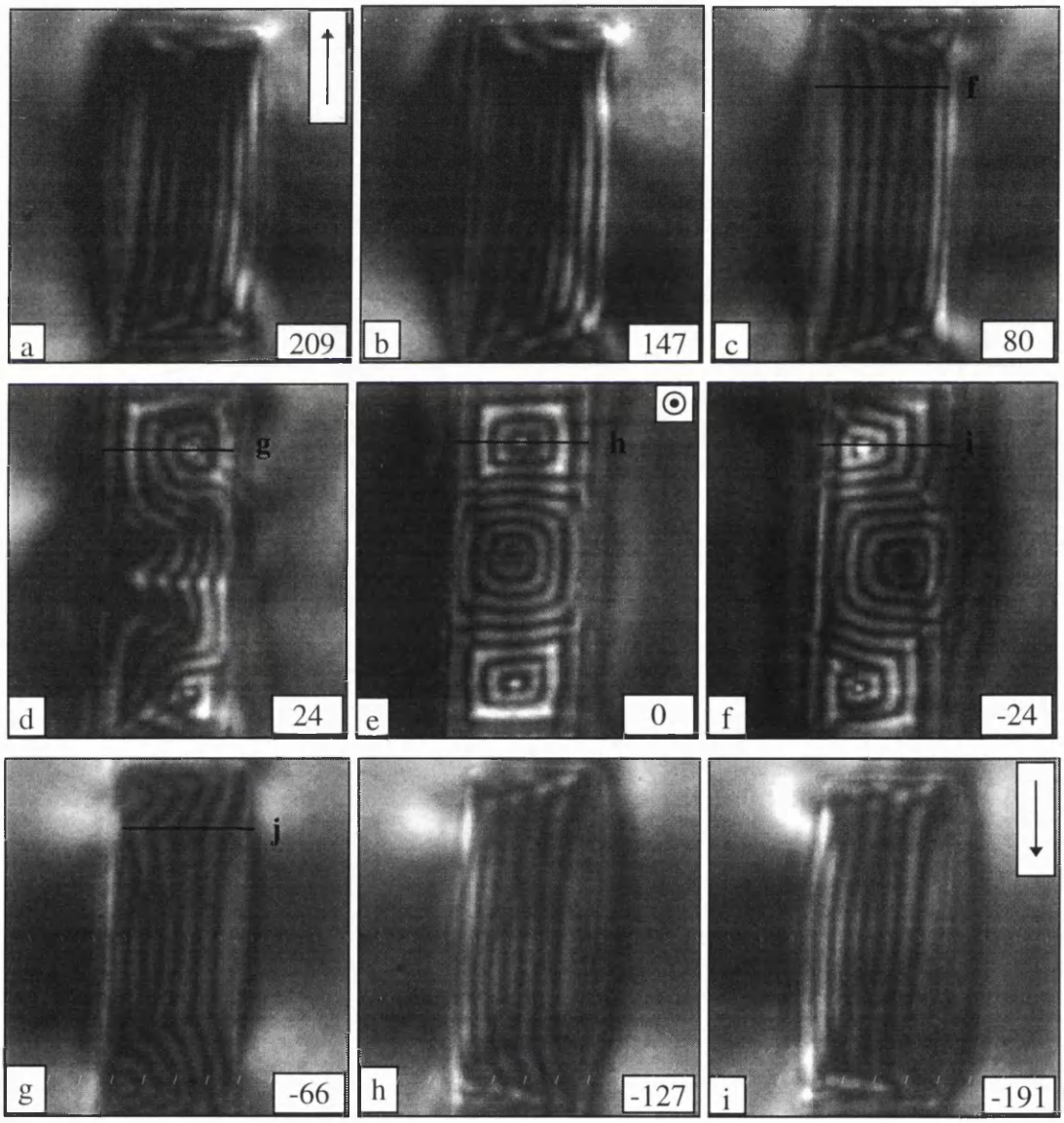

Figure 5.12 *CF images showing an element (3μmx1μm) magnetised along the easy axis. The field values in Oesterds are inset.*

When the field reaches the critical value H_{s2} the domain configuration switches from a non-solenoidal to a solenoidal distribution. Such a mechanism occurs at a field of ≈24Oe and figure 5.12d shows the element just after this transition. A cross-tie wall has nucleated in the central region indicating the formation of a Néel wall on the left. The ends of the element have also changed structure into a distorted solenoidal closure. As the field is reduced to zero (figure 5.12e), a solenoidal magnetic distribution forms containing three closure structures (category Ia). On the application of a reverse field, favourably orientated domains grow at the expense of those less suitably orientated (figure 5.12f). It should be noted that in this region of the hysteresis cycle the net moment of the element increases monotonically with field. This continues until the critical field H_{s1} is attained, whereupon an irreversible change takes place. When the fringe spacings are considered it is found that the fringes which cross the lines **g**, **h**, and **i** are all of the expected periodicity. There are no stray fields in the case of the CF image with zero applied field. When a small positive or negative field is applied, stray fields become noticeable in the central region but within the end structures there is a near closure structure where there exists a region of magnetic volume charge where $\nabla.\underline{\mathbf{M}}\neq 0$, hence the negligible change in fringe periodicity.

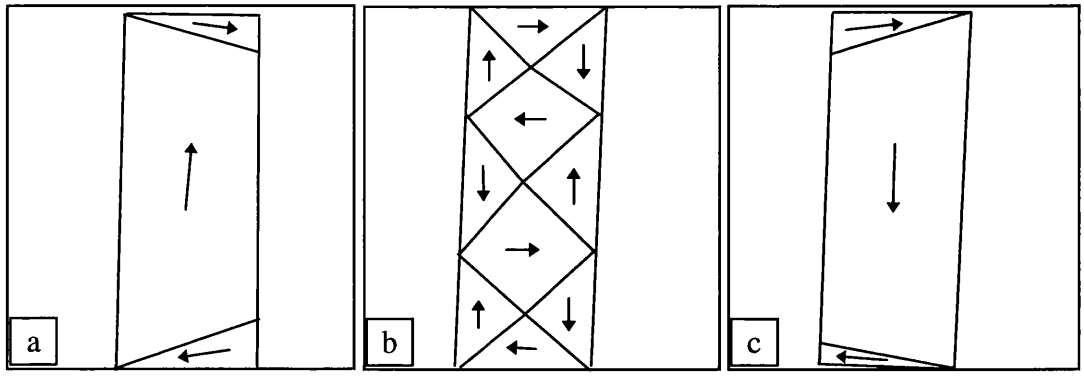

Figure 5.13 *Schematic diagram of the main micromagnetic structures found in a 3μmx1μm element magnetised along the easy axis.*

As the reverse field is increased to $-H_{s1}$ (-50Oe) the central closure structure is 'forced' into the side of the element. Figure 5.12g shows the element at a field of -66Oe where the structure has changed to a form immediately recognisable as the non-solenoidal (category II) structure. The central region again shows the magnetisation running parallel to the

long edge, but in the opposite direction, with the end regions showing a somewhat complex structure. As the field is further increased to -127Oe (figure 5.12h) and -191Oe (figure 5.12i) the end structures gradually reduce in size. The presence of stray fields yet again changes the periodicity of the fringes when an external field is applied. Along the line **j** in figure 5.12g the fringes have a periodicity of 182nm which translates as an integrated demagnetising field strength of 0.36T. When the element is subjected to greater field values it is possible to eventually remove the end regions completely leaving the element uniformly magnetised.

5.8 Magnetisation of a rectangular element along the hard axis.

The previous section has covered the application of a field along the easy axis of the element. An investigation of the magnetic microstructure when applying a field along the hard axis is given in this section.

The hysteresis loop when the field is applied along the hard (short) axis of the element is of a similar generic form to the easy axis loop in figure 5.11. The main difference being that larger fields are required to observe the switching mechanisms.

In this study a 3μmx1μm rectangular element from specimen 2 (30nm thick) is investigated whilst being magnetised along the short (hard) axis. The initial magnetisation distribution is such that the element is magnetised by the maximum field along the short axis. The external field is then reduced to zero and the field direction is reversed until the element is magnetised by the maximum field in the opposite direction. Figure 5.14 shows CF images of an element with dimensions 3μmx1μm when an external field is applied. The main micromagnetic structures observed are shown schematically in figure 5.15.

Initially the element is uniformly magnetised at a field of ≈300Oe at the maximum tilt of 50°. Figure 5.14a shows the element with a field of 210Oe supporting a highly irregular structure dominated by stray fields. A suitable explanation is that the magnetisation is lying along the short axis of the element with stray fields passing above and below the

sample. If the stray field is of the order of 1T then there is a net deflection of zero as the electrons pass through the sample.

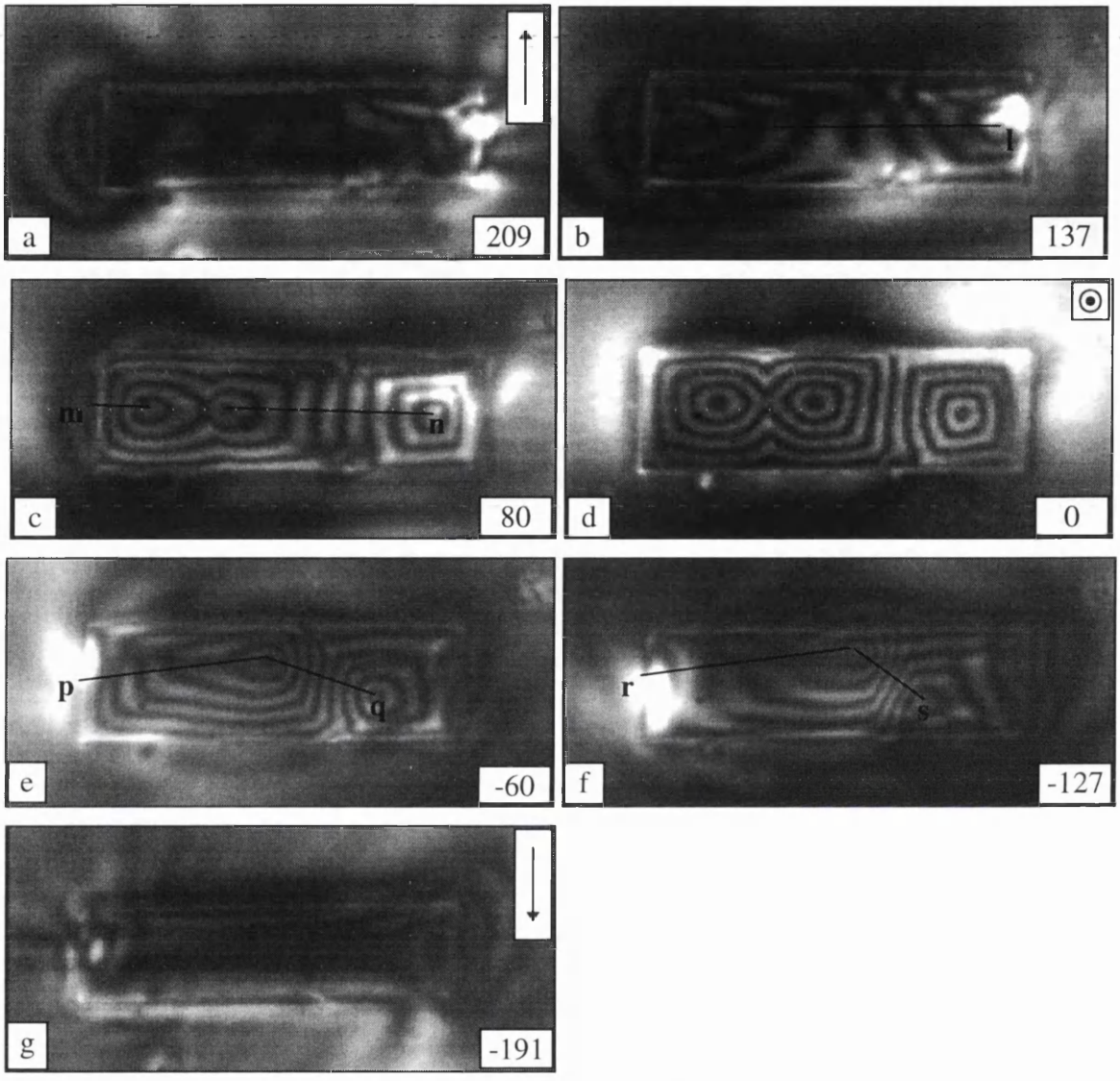

Figure 5.14 *CF images of an element (3μmx1μm) magnetised along the hard axis.*

When the field reaches the critical value H_{s2} the domain configuration switches from a non-solenoidal to a solenoidal distribution. This transition is difficult to pinpoint due to the poor image visibility but occurs around about 180Os. When the field is further reduced to 147Oe the CF image in figure 5.14b is obtained, the domain structure being represented schematically by figure 5.15a. There is a large central domain orientated along the favoured direction and a highly distorted closure structure at both of the short ends. There is some contamination on the element on the lower long edge, just off centre, which appears to be pinning the domain walls at this field value. The near solenoidal

structure occurs at far greater fields than when magnetising along the easy axis. This is due to the high magnetostatic energy stray fields being countered by the magnetisation redistributing to give a lower energy state. Stray fields increase the fringe spacing within the large central domain to 400nm which corresponds to an integrated demagnetising field of 0.67T along the line **l**. Figure 5.14c shows the element with a field of 80Oe being applied. The magnetisation distribution takes the form of a distorted closure on the right and a cross-tie structure on the left. There are still stray fields surrounding the element. The large central domain shows an increase in fringe spacing along the line **n** to 222nm which corresponds to an integrated field of 0.40T. At the ends of the element, the unfavoured domain orientation has fringes which show a decrease in periodicity to 120nm. This corresponds to a local demagnetising field strength along the line **m** of 0.11T. The difference in stray fields in these two regions is due to the domain geometry of the sample. The centre has a large domain which leads to the formation of free poles on the long edges, hence a large stray field is present. The end structures, however, provide a certain amount of flux closure which in turn greatly reduces the local stray field strength. It should be noted that the fringes running perpendicular to the field direction show a fringe periodicity independent of the applied field. As the field is reduced to zero (figure 5.15d), a solenoidal (category I) magnetic distribution forms containing a single closure structure and a cross-tie wall. The fringe periodicity is ≈135nm in the absence of stray fields as predicted theoretically.

On the application of a reverse field, favourably orientated domains grow at the expense of those less suitably orientated (figure 5.15e). The cross-tie wall is no longer energetically stable and is replaced by a highly distorted closure structure. The fringe spacings are indicative of the local demagnetising field varying dramatically along the line **p**. There is an decrease in fringe spacing to 117nm along the line **q**. This indicates that the demagnetising field is in the same direction as the magnetisation within the domain, the integrated field strength being of the order of 0.12T. The fringes running perpendicular to the field direction yet again show no change in periodicity. As the field is increased to -127Oe (figure 14.5f) the domains lying along the favoured orientation grow, and the unfavoured domain shrinks and is distorted to an angle of ≈30°. The fringe periodicity increases to along the line **r** corresponding to a local integrated demagnetising field of 0.51T. There is an decrease in periodicity along the line **s** corresponding to an

integrated stray field of 0.62T. This assumes that the local stray field is in the same direction as the magnetisation within the unfavourable domain.

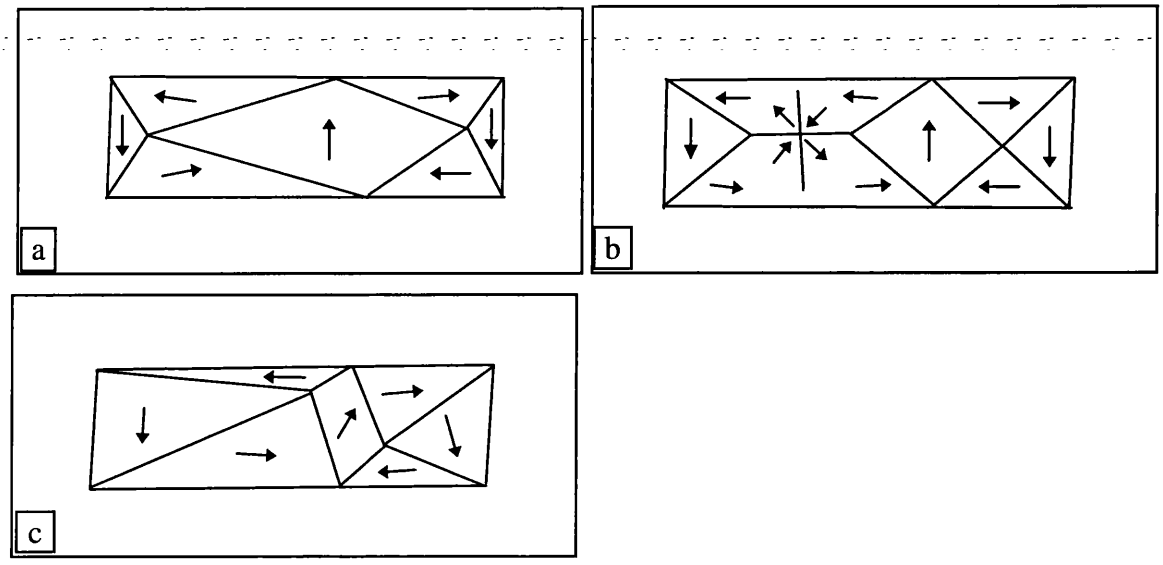

Figure 5.15 *Schematic of the main micromagnetic structures when magnetising along the hard axis of the element.*

When the applied field strength surpasses the critical field $-H_{s1}$ (figure 5.15g) the central unfavoured domain is removed. This could be due to the closure structures crossing and then being pushed into the sides of the element, or by the magnetisation within the domain bring forced to rotate to the applied field direction. The CF image is dominated by stray fields and the element supports a micromagnetic structure very similar to figure 5.15a but in this case the magnetisation is pointing in the opposite direction.

5.9 In-situ temperature variation of a rectangular element.

In this section the effect of heating a small rectangular element to beyond its Curie temperature is considered. This experiment gives an indication of the micromagnetic structure which is supported by the elements at an elevated temperature. Also of interest is the ability of CF imaging to monitor changes in the magnetic induction as the fringes change in periodicity, the thickness being constant.

To increase the temperature in-situ a Philips heating holder (PW6592) is utilised which is fitted with a ceramic heating ring below the specimen. This type of rod allows the temperature of the specimen to be elevated to a maximum temperature of 1000°C within 2 minutes. The temperature is measured using a thermocouple, located near the specimen, with a sensitivity of ±2°C. In practice perfect contact between the specimen and the holder is not achieved because the sample is a 2mm square fitted into a 3mm diameter hole. This results in the sample taking about 15s to reach the required equilibrium temperature. Guided by previous authors[18], an initial guess at the Curie temperature is 600°C in bulk permalloy, well within the heating abilities of the rod.

Figure 5.16 shows a selection of CF images of an element from specimen 2 (30nm thick) with in-plane dimensions 3μmx1.5μm at different temperatures. Figure 5.16a shows the CF image of the element at room temperature. A solenoidal (category Ib) magnetisation distribution is present within the element shown schematically in figure 5.17a. There are no apparent changes to the magnetic microstructure as the temperature is increased to 400°C. A significant change occurs at ≈450°C (figure 5.16g) where a second cross-tie wall is introduced (schematic figure 5.17b). The new domain configuration is energetically favourable at an elevated temperature due to the change in the total energy of the system. There is a reduction in the magnetostatic energy due to the magnetic induction of the permalloy element reducing as the temperature is increased. The other changes in the total energy come from the exchange and domain wall energies, both highly dependant on temperature. As the temperature is further increased to 500°C the structure changes to show a non-symmetrical but solenoidal domain configuration. At 550°C the magnetisation distribution within the element becomes highly irregular with no recognisable domain configuration. As the element approaches the Curie temperature of ≈580°C (figure 5.16j) there is no magnetic contrast in the CF image. This is expected as the permalloy changes magnetic phase from a ferromagnetic to a paramagnetic material.

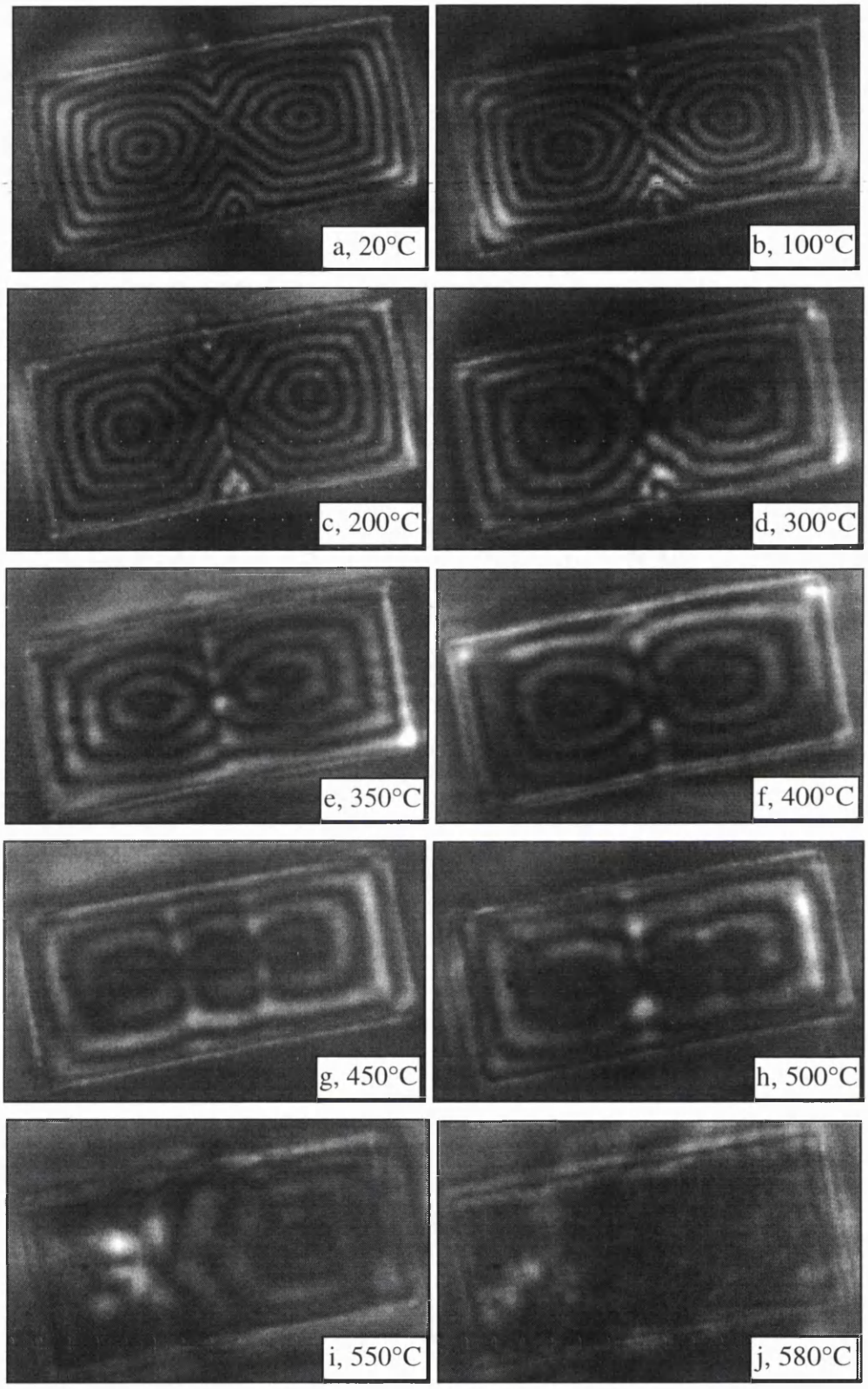

Figure 5.16 *CF images showing an element (3μmx1.5μm) at different temperatures.*

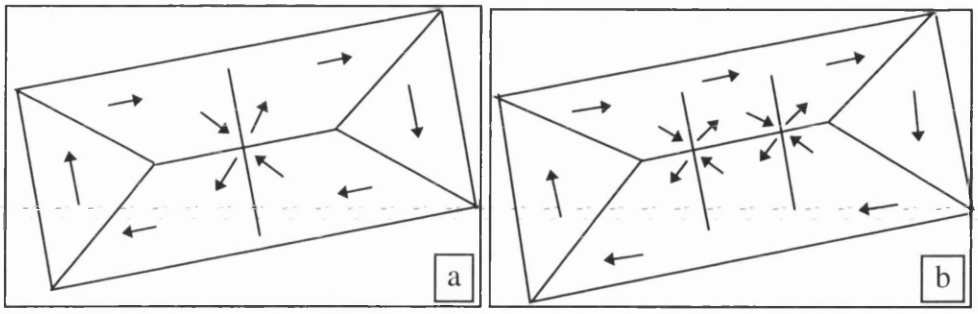

Figure 5.17 *Schematic of the magnetic induction distribution at (a) 20°C and (b) 450°C*

As the element is returned to room temperature (figure 5.18a) the magnetic microstructure forms a solenoidal distribution containing two closure structures (shown schematically in figure 5.18b). It should be noted that there does not appear to be any significant changes in the fringe periodicity. We can therefore conclude that the permalloy has kept its magnetic integrity after being subjected to the heating process.

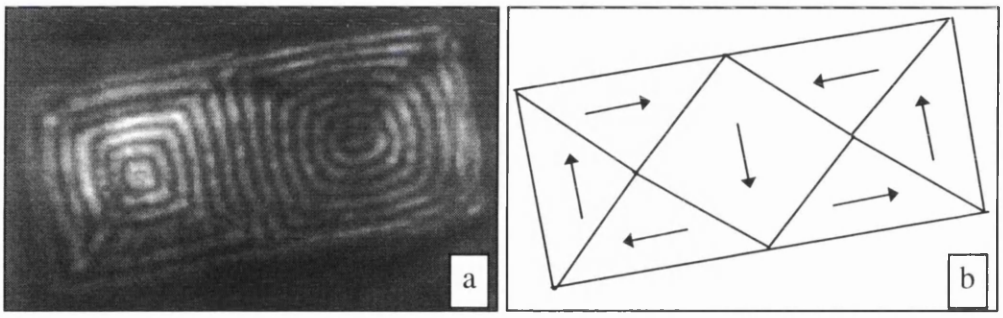

Figure 5.18 *(a) CF image of a 3μmx1μm element at room temperature after annealing to the Curie temperature, (b) shows the corresponding schematic diagram.*

An investigation of the fringe spacing gives a measure of the magnetic induction at the different temperatures. Figure 5.19 shows the calculated magnetic induction versus the sample temperature. Initially the magnetisation falls off slowly until 250°C. The section of data between 300°C and 400°C lies just below the actual magnetisation values due to the strained micromagnetic structure showing stray fields, although they are very small in size. When the micromagnetic structure changes at 450°C there is a jump in the measured induction due to there being no demagnetising fields surrounding the element. Beyond 500°C the magnetic induction becomes very difficult to quantify due to the highly irregular structure. As the temperature is further increased to 580°C there is no magnetic

contrast let alone a fringe pattern. This confirms that the Curie temperature has been reached.

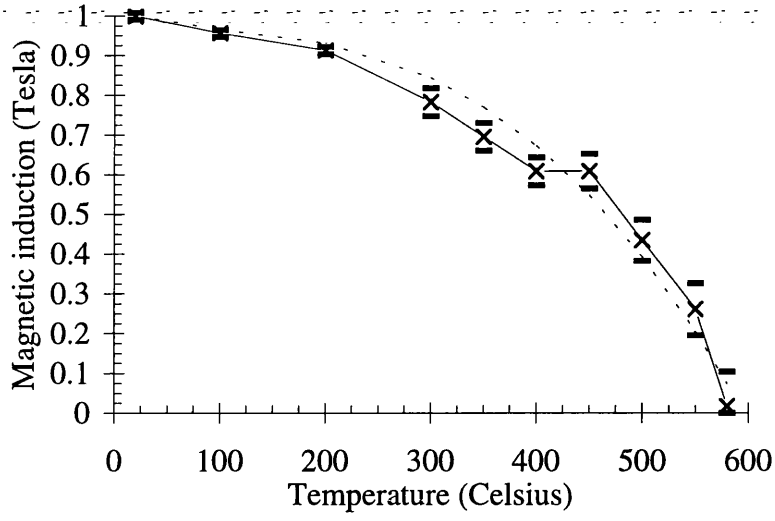

Figure 5.19 *Graph of the magnetic induction as the temperature is increased.*

Although the specimens in this study are in the form of thin films they exhibit a temperature dependence on magnetisation and Curie temperature like that of the bulk material. It should be noted that an increase in the Curie temperature occurs only in thin films consisting of a few atomic layers[19]. Figure 5.20 shows the calculated bulk magnetisation as a function of temperature using Weiss molecular field theory[20]. The section of the graph to the right of the dashed line (room temperature) can be compared directly to figure 5.19. As T increases the magnetisation decreases smoothly to zero at $T=T_c$. This behaviour classifies the usual ferromagnetic to paramagnetic transition as second order.

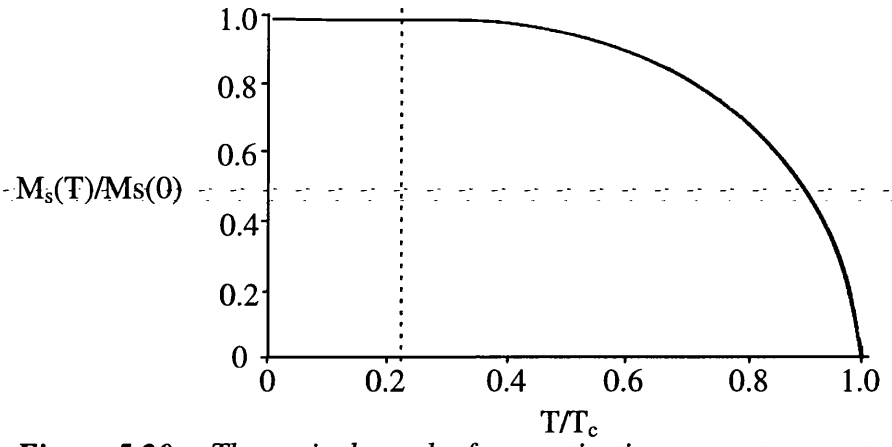

Figure 5.20 *Theoretical graph of magnetisation verses temperature.*

These results have given an insight into how the micromagnetic structure of an element changes as the temperature is elevated. The power of CF imaging has yet again been shown in allowing for a direct measure of the magnetic induction at different temperatures.

5.10 Comparison of elements fabricated using lift-off and an alternative etching route.

In this section we compare the magnetic properties of two element samples using two different fabrication techniques. The first being the "lift-off" technique (section 5.3) and, as explained in this section, a second "etching" technique. The later employs electron beam lithography and dry etching which can be used to prepare magnetic elements from materials which are not usually lift-off compatible[21]. These are materials which are deposited at too high a temperature to allow lift-off using polymeric resists, or those which are deposited by sputtering leading to problems such as unsuccessful lift-off or where wing-like flaps due to side wall deposition protrude and hang over the element. Finally, we characterise the thin film elements fabricated using the alternative etching process and compare them to elements produced by the lift-off method.

A schematic of the fabrication process is given in figure 5.21. Initially, a permalloy thin film is deposited directly onto a Si_3N_4/Si membrane substrate (section 5.2). This is

achieved by thermal evaporation with a deposition rate no greater than $0.1 nms^{-1}$. A thin layer of Ta, typically 20nm, is then deposited onto the NiFe thin film by RF sputtering at a rate of $0.05 nms^{-1}$. This acts firstly as a protection layer during further processing and, more importantly, helps yield elements with a better edge profile following the etching process.

A bi-layer system of PMMA suitable for lift-off applications is used in the first step of the process of pattern definition to produce magnetic elements. The first layer is a lower weight polymer while the second is made of higher molecular weight molecules[22]. A maximum temperature of 180°C is attained during this process, the highest to which the magnetic thin film is subjected.

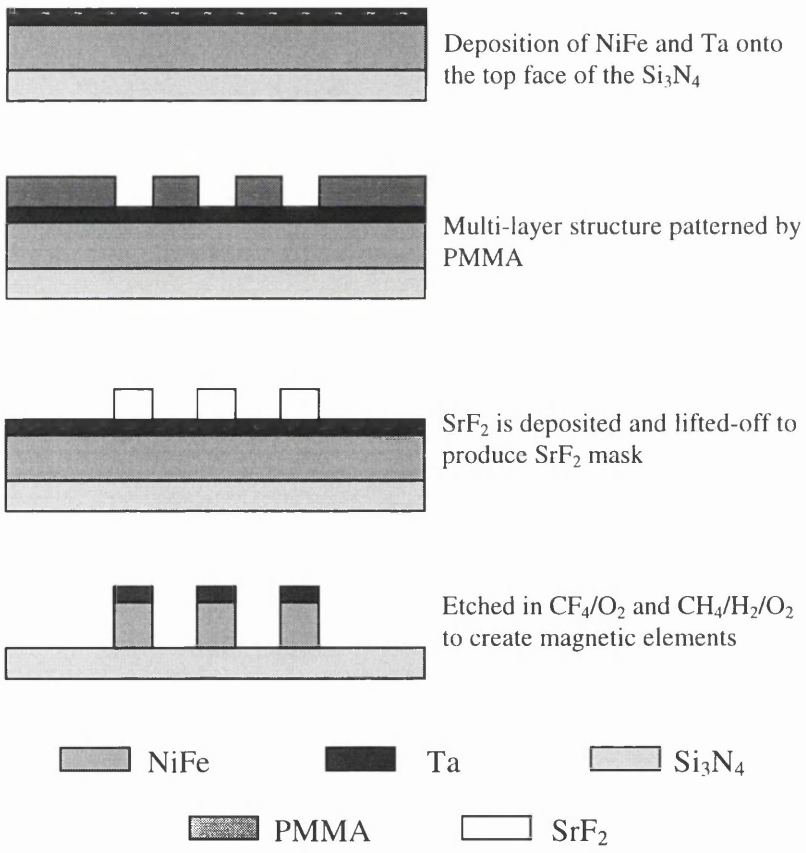

Figure 5.21 *Schematic of the etching process.*

Electron beam writing is then carried out to define the pattern for the elements. The development of the exposed pattern in PMMA is achieved using a IPA-MiBK (2.5:1)

solution. This leaves a PMMA pattern which is used as a means for defining the mask during etching and pattern transfer into the Ta/NiFe to create the magnetic elements.

For the mask, we have used SrF_2, thermally evaporated at a rate of 0.1-0.2nms^{-1}, onto the PMMA-patterned sample. The SrF_2 is subsequently obtained by lift-off of the SrF_2/PMMA in acetone. Following the production of the SrF_2 mask, the Ta thin film is patterned by reactive ion etching in a CF_4/O_2 (9:1) environment[23]. The 20nm Ta film is removed in under 2 min. After a delay of about 1 min following the termination of the CF_4/O_2 flow and pumping down, etching is continued in a $CH_4/H_2/O_2$ environment to further transfer the pattern into the NiFe[24]. This is achieved at a rate of ≈4.5nmmin^{-1}. The SrF_2 mask thickness is adjusted so that the Ta layer is also removed at about 0.5nmmin^{-1} in the $CH_4/H_2/O_2$ etching environment. Thus, overall scattering by a thinner film of Ta, which is a high atomic mass element, during Lorentz microscopy will relatively reduce, resulting to a better contrast in the magnetic domain image. Figure 5.22 shows a bright field image of a corner of an element fabricated by this process. We observe an edge acuity of ≈15nm which compares well with the acuity observed in elements which have fabricated by the lift-off process (≈10nm).

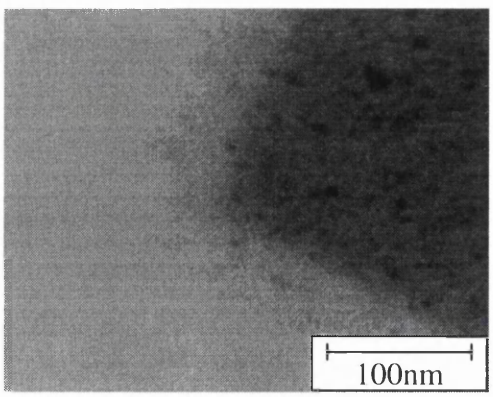

Figure 5.22 *edge acuity.*

We have used CF imaging to obtain a measure for the product B_0t, where B_0 is the saturation magnetisation and t the thickness of the magnetic thin film. Thus, results for different elements fabricated by the etching route and those fabricated by lift-off have been compared. For this, the NiFe material was simultaneously deposited on plane and PMMA-patterned substrates. Ta was subsequently deposited on the former before it was

taken through the etching route, while NiFe elements were created on the latter by acetone. Fabrication of all the elements under investigation were carried out by B. Khamsehpour (University of Glasgow).

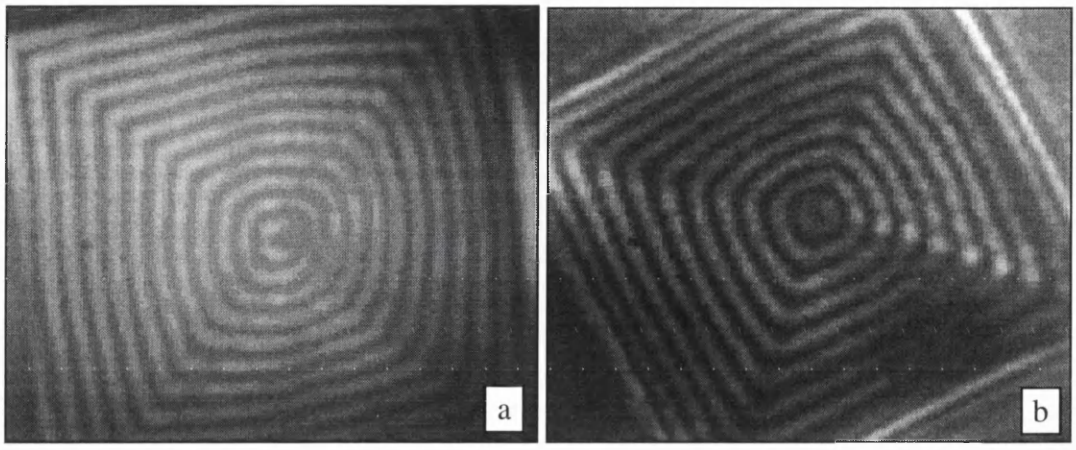

Figure 5.23 *CF images of a 3μmx3μm element fabricated by (a) lift off and (b) etching.*

Figure 5.23a and b show images of similarly sized elements produced by the two routes. The number of fringes for elements of different size have been measured for those having dimensions of 3,2, and 1.5μm. The ratio of B_0t in the etched elements have been measured to be 0.94, 0.93 and 0.88 respectively. Therefore, a similarly prepared NiFe thin film with a Ta overlayer taken through the etching route shows a reduction of between 6 to 12% in the product of B_0t. This could be explained to be due to a reduced magnitude of B_0 and/or a reduced thin film thickness, t. Obviously, any degradation in B_0 must be process related and could have been caused by penetrating hydrogen species through the overlying Ta into the NiFe lattice[24] . Reduction in the effective thickness of the magnetic thin film could have been caused by passivation. The coherent Foucault results of initial elements fabricated with no Ta overlayer had indicated stray fields and domain irregularities. Addition of a Ta overlayer has certainly removed those problems by protecting the NiFe surface during the processing steps. However, in these experiments the Ta overlayer was deposited in a different chamber. It is expected that the interface between the Ta and the NiFe would contain the sort of "contamination" expected of a surface exposed to atmospheric condition, i.e. oxygen , water vapour and hydrocarbons. These species could actively take part in passivation of a fraction of the NiFe layer by grain boundary diffusion following long baking hours which are involved in the PMMA patterning stage. For a 46nm NiFe thin film as used here, a reduction in B_0t being totally

as a result of passivation, would mean a passivated NiFe thickness of 4.6nm. Whether the small degradation in the value of the product, B_0t, is due to hydrogen penetration or passivation of the NiFe thin film, it should be possible to improve the reduction by driving the hydrogen out through thermal annealing and/or depositing the Ta overlayer on NiFe, without breaking the vacuum, in the same deposition chamber.

Overall, the above results indicate that the etching route can be used to produce elements with magnetic properties comparable to those produced by the lift-off route. B. Khamsehpour has also successfully implemented this etching process on different magnetic materials currently under investigation[21], such as Co/Pt, NiFe/Cu multilayers and Cu/Co superlattices.

5.11 Conclusion.

In this chapter the experimental considerations of CF imaging were discussed. This has included sections on the preparation techniques employed to obtain the different aperture types and the "lift-off" process that is used to fabricate the small permalloy elements. Initially, we looked at a simple micromagnetic structure using the CF imaging technique when using the different aperture types. These images were then compared, successfully, to the 2-D computer simulation images (chapter 4.4).

In the latter sections of this chapter we carried out a range of experiments which give an insight into the magnetic microstructure supported by differently shaped elements. We have seen how CF imaging gives a clear description of the magnetisation distribution and can lead to quantification of the local magnetic induction distribution within the elements; furthermore it can be used qualitatively to show the presence of stray (demagnetising) fields surrounding the elements. CF imaging has proved to be a stable and versatile imaging mode which has allowed a range of in-situ experiments to be carried out. Small elements have been imaged whilst magnetising them along their easy and hard axes, with individual CF images being related to points on the hysteresis loop. We have also heated the sample in-situ to show how the magnetic microstructure supported by the elements changes as we approach the Curie temperature. This experiment also gives an indication

of how the magnetic induction of the permalloy is reduced as the temperature is increased. This results in the permalloy changing magnetic phase (ferromagnetic to paramagnetic) as the Curie temperature is surpassed. Finally, we examined two sets of magnetic elements, one of which has been prepared using the lift-off route and the other by a reactive ion etching process. The latter fabrication method allows for small elements to be prepared from existing continuous thin films and from materials which are not usually compatible with the lift-off route. Such films have been successfully prepared with magnetic properties comparable to those produced by the lift-off route.

References.

[1] S. McVitie & J.N. Chapman, IEEE Trans. Mag., **24**, p1778 (1988).

[2] J.N. Chapman, R.P. Ferrier, L.J. Heyderman, S. McVitie, W.A.P. Nicholson and B. Borman, Electron Microscopy and Analysis, p1 (1993).

[3] S. McVitie, Ph.D. Thesis, University of Glasgow, (1988).

[4] M Gajdardzidka-Josefovska, M.R. McCartney, W.J. Ruijter, D.J. Smith, J.K. Weiss and J.M. Zuo, Ultramicroscopy, **50**, p285 (1993).

[5] Glang and Gregor in 'Handbook of Thin Film Technology', eds. L.I.

[6] F.A.N. Van der Voort and H.A.M. Van den Berg, IEEE Trans. Mag., **MAG-23**, p250 (1987).

[7] 'Electron-Beam Lithography in Microelectric Fabrication', ed. G. Brewer, pub. Academic Press, (1980).

[8] W.S. Mackie, Ph.D. Thesis, University of Glasgow, (1984).

[9] S.P. Beaumont, P.G. Bower, T. Tamamura and C.D.W. Wilkinson, Appl. Phys. Lett., **38**, p436 (1985).

[10] M Prutton, 'Thin Ferromagnetic Films', Butterworth (1964).

[11] R.M. Bozorth and J.G. Walker, Phys. Rev, **89**, p624 (1953).

[12] H.Y. Wong, J.N. Chapman, S McVitie and S.J. Hefferman, J. Magn. Magn. Mater., **104-107**, 329 (1992).

[13] E. Huijer and J.K. Watson, J. Appl. Phys., **50**, 2149 (1979).

[14] H.A.M. Van den Berg, Ph.D. Thesis, Delft University, (1984).

[15] J.N. Chapman, I.R. McFadyen and S. McVitie, IEEE Trans. Mag., **26**, 5 (1990).

[16] S. McVitie, J.N. Chapman, S.J. Hefferman and W.A.P. Nicholson, Journal de Physique, 49, 1817 (1988).

[17] S.J. Hefferman, J.N. Chapman and S. McVitie, J. Magn. Magn. Mater., **95**, 76 (1991)

[18] R.M. Bozorth, 'Ferromagnetism', D. Van Nostrand Co., Princeton, N.J (1951).

[19] P.J. Jensen, H. Dreyssé, K.H. Bennemann, Europhys. Lett., **18**, 463, (1992).

[20] C. Kittel, 'Introduction to Solid State Physics', John Wiley and Sons (1953).

[21] B. Khamsehpour, A.B. Johnston, C.D.W. Wilkinson and J.N. Chapman, (to be submitted for publication).

[22] C.D.W. Wilkinson and S.P. Beaumont, NATO ASI Series B, **180**, 373 (1988).

[23] J.C. Martz and D.W. Hess, J. Appl. Phys., **Vol. 67**, 3609 (1990).

[24] M. Hirscher and H. Kronmuller, J. Less-Common Metals, **Vol. 172**, 658 (1991).

Chapter 6

Transmission electron microscope investigation of ferrite thin films.

6.0 Introduction.

Several studies have examined the epitaxial growth of Fe_3O_4 on single crystal MgO, because of the good lattice match[1-4]. The distances between the oxygen atoms in the FCC lattices of MgO and Fe_3O_4 along <100> directions are 2.1060Å and 2.0994Å respectively, corresponding to a 0.31% lattice mismatch. Margulies[5] (1994) investigated 3000Å Fe_3O_4 films prepared by dc magnetron reactive sputtering onto <100> and <110> MgO substrates. The X-ray diffraction data revealed highly orientated Fe_3O_4 films under a tensile stress which may be modelled as isotropic. The high field in-plane magnetisation at 300K was measured with a superconducting quantum interference device (SQUID). These results showed good agreement with the bulk Fe_3O_4 saturation magnetisation, but also revealed the presence of a large anisotropy component randomising the moments, the origin of which is still unknown. This effect was confirmed by conversion electron Mössbauer spectroscopy (CEMS). It was found that the moments do not all lie in the plane of the film which shows that there is a large anisotropy component in these films, larger than the shape anisotropy, responsible for randomising the moments. In-plane torque measurements on the <100> orientated Fe_3O_4 agreed well with the magnitude and temperature dependence of the crystalline anisotropy constant K_1 of bulk Fe_3O_4[6]. However, in-plane torque measurements on <110> orientated Fe_3O_4 show the presence of a dominant uniaxial anisotropy that is shown to arise from the stress induced by epitaxy.

In this study we would like to see if high resolution domain studies can provide any information on the spatial distribution of the random anisotropy. However, the Fe_3O_4 specimens grown on MgO substrates have proved difficult to remove, so instead, polycrystalline films have been prepared on silicon nitride (Si_3N_4) window substrates (section 5.3). This is not the ideal situation because the Si_3N_4 is in the form of an amorphous thin film which promotes polycrystalline growth. This type of substrate provides a more complex material but is readily amenable to investigation using the transmission electron microscope (TEM). Initial measurements (section 6.3) show these films to have good magnetic properties and to contain a random anisotropy component as in the epitaxially grown specimens. Although these two types of film have a different crystallographic structure it is believed that the same mechanism is responsible for the random anisotropy.

These specimens provide a challenge to the microscopist in that they are rather weakly magnetic (low M_s) whilst crystal contrast is high. Furthermore it transpires that both are on a comparable length scale. The TEM study undertaken here investigates the crystallite structure and magnetisation distribution in four Fe_3O_4 thin films of different thicknesses. Bright field imaging (section 6.4) has been used to determine the crystallite size whilst Fresnel and Foucault imaging (sections 6.5 and 6.7 respectively) have been employed to examine the magnetic microstructure. The samples are initially imaged in the as-grown state and are subsequently magnetised in-situ (section 6.6) to gain insight into the magnetisation process at a microscopic level.

6.1 Microscope imaging conditions.

The TEM study of Fe_3O_4 thin films has been carried out on the Philips CM20 (section 2.1). The microscope is aligned such that the objective lens is switched off, the upper Lorentz lens is used as the final probe forming lens and the lower Lorentz lens is used as the imaging lens. This ensures that the sample resides in field free space and allows for high resolution magnetic images to be obtained. In this study bright field imaging (section 2.4.1) is used to investigate the crystallite size and determine whether there is any

crystallite directionality present within the thin films. Fresnel imaging (section 2.4.2) is used to reveal the domain walls. This technique shows up the complexities of a system containing both magnetic and crystallite information, and the difficulties involved in obtaining micromagnetic information.

In the following section of this chapter the specimens are also magnetised in-situ using the standard objective lens. When the objective lens is run at a weak excitation it produces a vertical field in which the specimens can be tilted to introduce an in-plane component. Fresnel images are collected using the low-light-level TV pickup system on the CM20 (section 2.1.7) and then enhanced using the Arlunya TF6000 image processing unit. A hard copy can then be stored on video tape or images can be captured directly onto a PC using a Creative Labs FS2000 Video Blaster, which facilitates frame grabbing. Further image enhancement is achieved using the Paint Shop Pro 3 software package on the PC.

In the final sections we implement Foucault imaging (section 2.4.3) in an attempt to reveal the magnetisation distribution within these films.

6.2 Specimen preparation.

The Fe_3O_4 thin films where deposited by dc magnetron reactive sputtering from a Fe target directly onto a Si_3N_4 membrane window by Margulies (University of California, San Diego). This was done at a temperature of 500°C with a deposition rate of approximately $1 Å s^{-1}$. The Ar pressure during sputtering was 2mTorr, the O_2 pressure was 0.06mTorr and the background pressure was $5x10^{-7}$ Torr. Four Fe_3O_4 thin films have been prepared using this method with thicknesses of 100nm, 50nm, 25nm and 10nm.

6.3 Initial studies.

As well as preparing the specimens, Margulies has also carried out some initial studies on a 50.7nm Fe_3O_4 thin film grown on a silicon substrate with an 80nm layer of Si_3N_4 on the surface. This film was grown alongside the films investigated in this study to assist and compare with the TEM results. The SQUID data shows that the magnetisation at 300K for bulk Fe_3O_4 is 471 emu/cc [6], whereas for this film a value of 420 emu/cc is reached. This value is lower than is usually observed when MgO is the substrate material, but the thickness dependence of the magnetisation for films grown on Si_3N_4 has not yet been studied. It should also be noted that this film showed a random anisotropy component, of a similar nature to the thin films which were epitaxially grown on MgO. The hysteresis loop of the film (figure 6.1) shows the sample to have a coercive field of 253Oe. This provides useful information for estimating the fields to be used in the in-situ magnetisation experiments. Another technique used to analyse this film is CEMS. These studies reveal that the film is very close to stoichiometric with δ=0.0035, where δ is defined in $Fe_{3(1-\delta)}O_4$ [7].

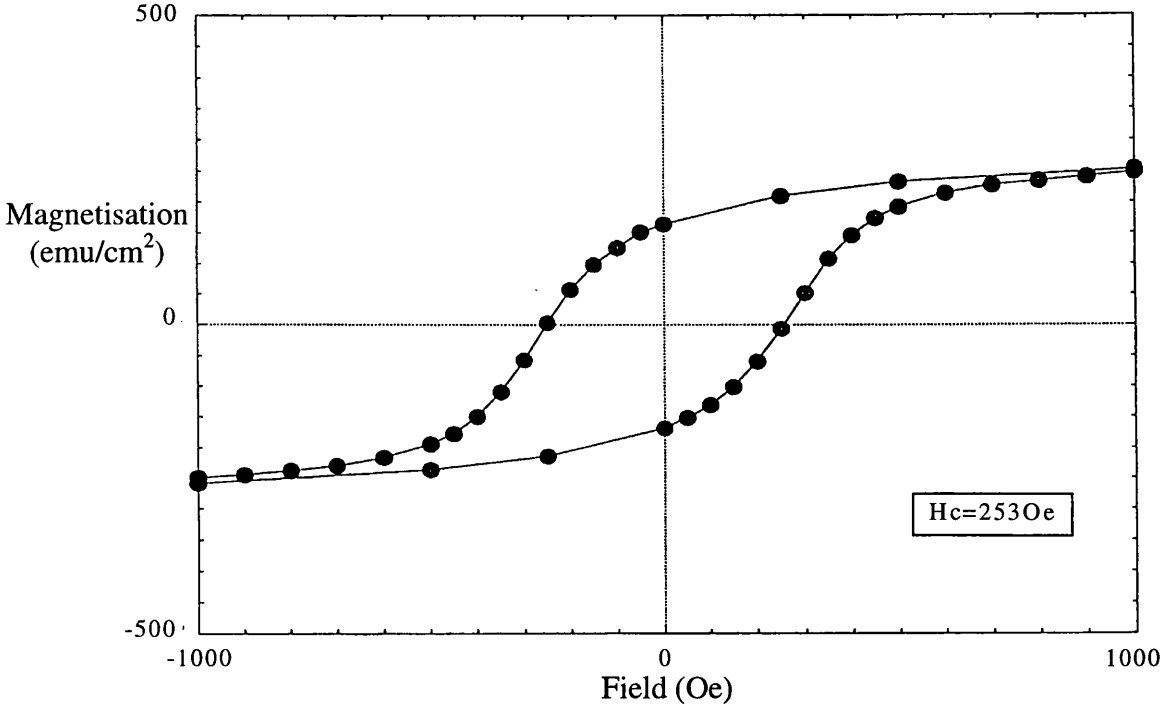

Figure 6.1 *Hysteresis loop of the 50.7nm Fe_3O_4/Si_3N_4 at 300K. (D. Margulies, University of California, San Diego).*

6.4 Bright field imaging.

Figure 6.2 shows bright field images of the 100nm, 50nm, 25nm and 10nm thin films in the as-grown state. Analysis of bright field and Fresnel images used the following approach. Fixed length lines where drawn in four directions at 45° intervals and the number of "features" crossing the lines counted. From these data the mean feature size could be estimated and the extent to which there was any anisotropy in the images determined. In the case of the bright field images these "features" were grain boundaries.

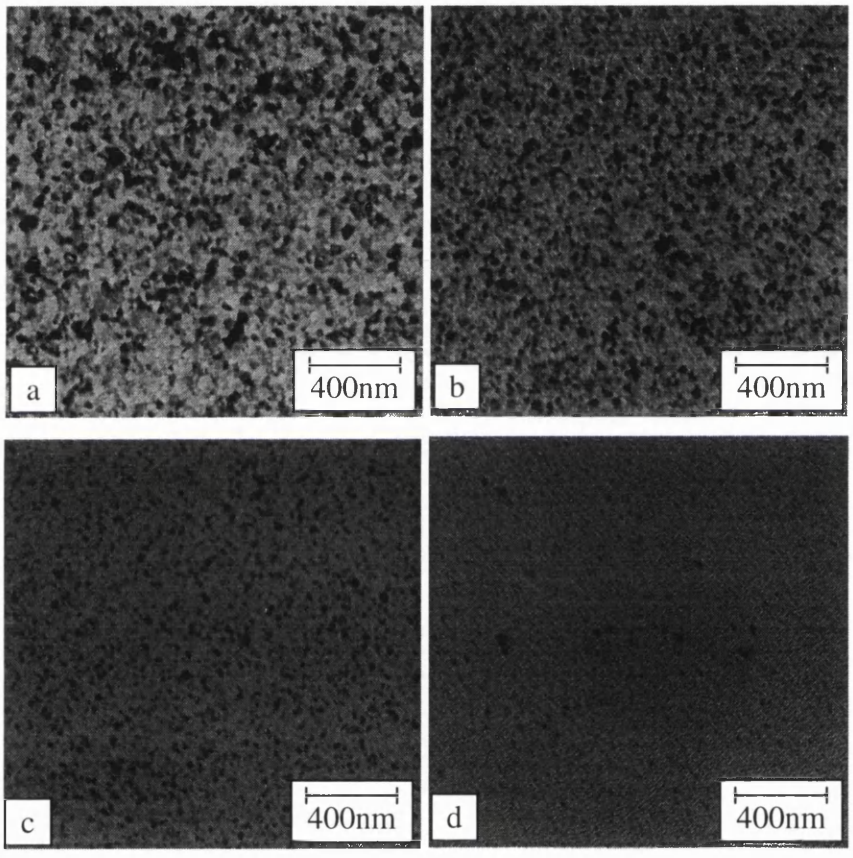

Figure 6.2 *Bright field images of Fe_3O_4 films of thickness (a) 100nm, (b) 50nm, (c) 25nm and (d) 10nm.*

No directionality is seen in any of the crystallite images. Mean crystallite sizes and the associated standard deviations are shown in table 6.1 and plotted in figure 6.3 for the four films. The greatest inhomogeneity is seen in the thickest film. Here, we believe the mean grain size is appreciably less than the film thickness (a cross-section specimen is required to confirm whether columnar growth is present). The observed contrast is due to crystallite

superposition effects. The crystallite size appears to increase slowly with increasing sample thickness. As the overall errors are small we believe that this is a real effect, but it is possible that the increase could be accounted for by the difficulty of defining crystallite boundaries in the thicker sample. However, increasing crystallite size with film thickness has been observed in many metal film systems[8]. There were also problems in defining the crystallite size in the 10nm film due to the low crystallite contrast. Therefore, the quoted size of these crystallites was obtained by measuring individual crystallites and subsequently evaluating the mean value and the associated standard deviation. Here, the crystallite size is much smaller than in the other films. This is explained in the earliest stages of deposition, when the material is made up from small nuclei which then grow to form a continuous film by diffusion processes[8]. Therefore, we cannot consider the 10nm sample to be typical of this system as it is not a continuous film (agglomerated structure).

Sample Thickness (nm)	Crystallite size (nm)
100	33.2±1.4
50	30.8±0.8
25	28.1±0.5
10	15.3±2

Table 6.1 *Crystallite sizes.*

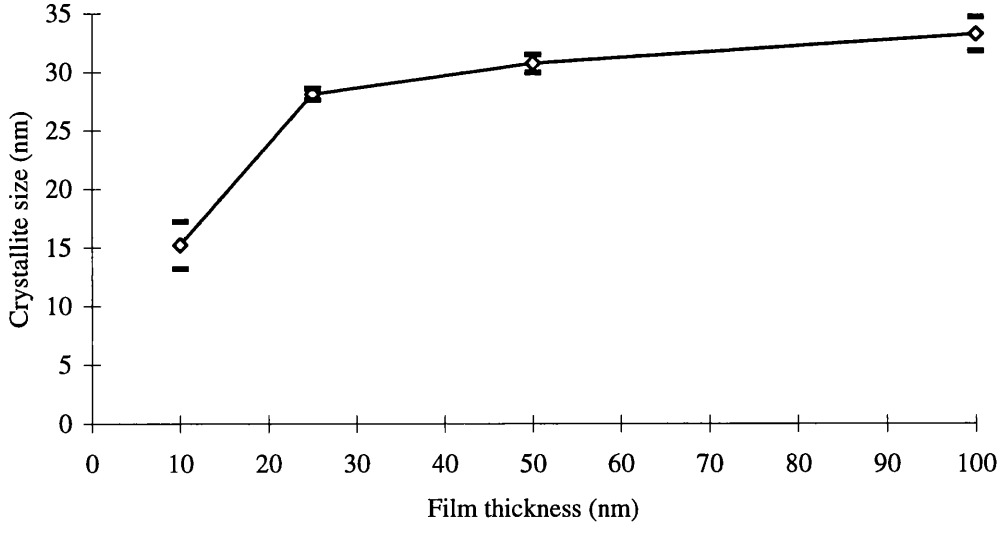

Figure 6.3 *Graph of the variation in crystallite size with thickness.*

6.5 Fresnel imaging.

In the images taken in the Fresnel mode (figure 6.4), we count the number of bright lines to measure the average feature size. Table 6.2 and figure 6.5 show the variation of these features with film thickness. Again there is no evidence for any preferred directionality and there is a small increase in feature size with film thickness. Note, however, that again we experience some difficulty in knowing what to measure in the film where contrast variation is strongest. Such a variation could again be due to overlapping effects throughout the film thickness whilst in the thinner three films this effect is negligible.

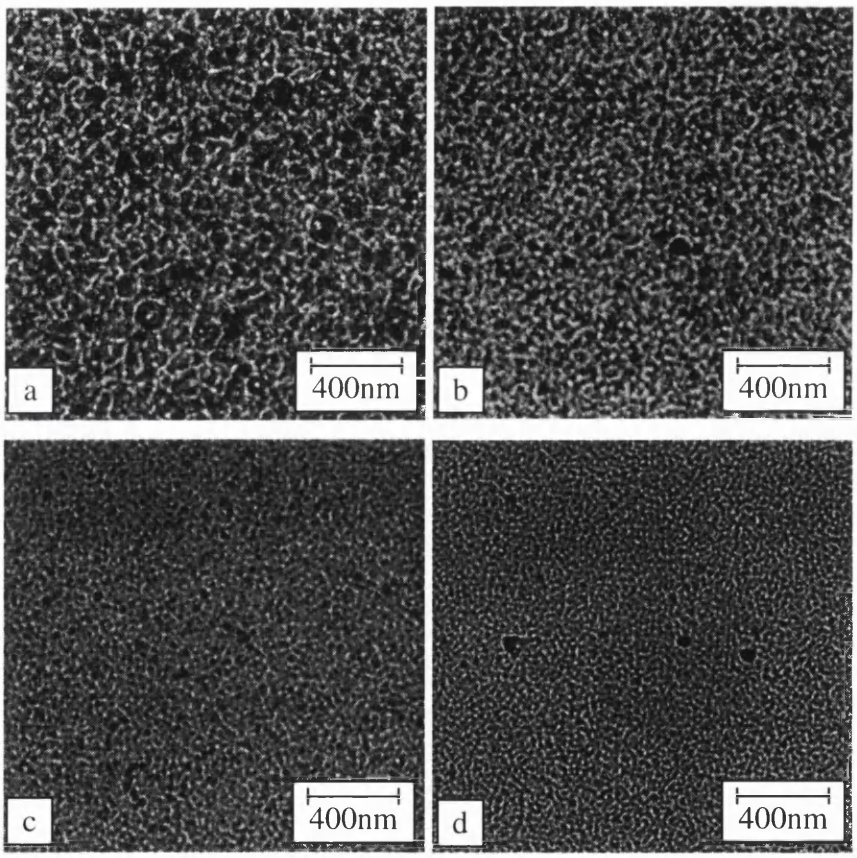

Figure 6.4 *Fresnel images of Fe_3O_4 films of thickness (a) 100nm, (b) 50nm, (c) 25nm and (d) 10nm.*

Sample Thickness (nm)	Feature size (nm)
100	33.6±1.2
50	31.8±1.4
25	27.5±0.9
10	18.0±1.5

Table 6.2 *Feature sizes.*

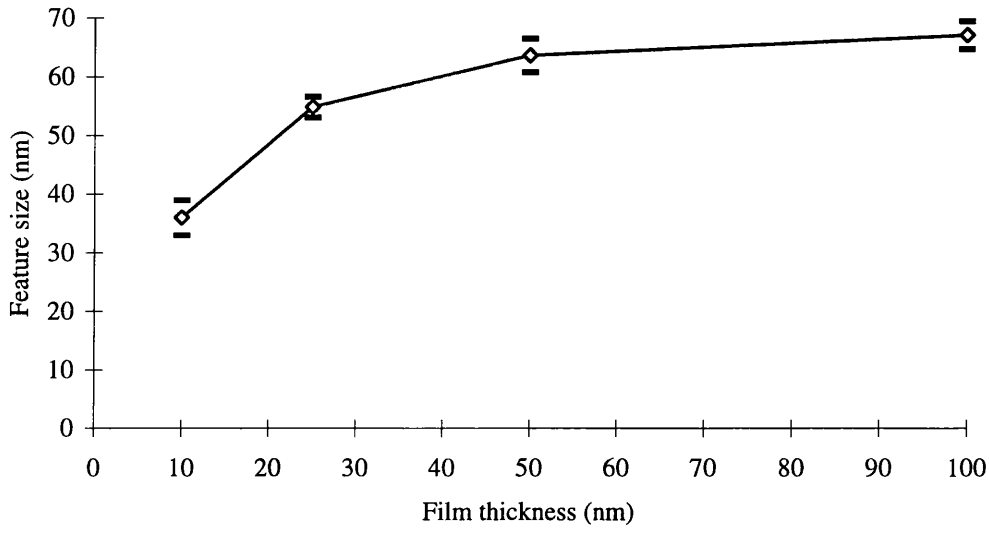

Figure 6.5 *Graph of the variation in feature size with thickness.*

What these features represent is very difficult to interpret. Here we are imaging the defocused crystallites and domain walls, both of which could show contrast on a similar scale. If the latter is dominant, the contrast observed could represent the convergent domain walls which appear as high contrast narrow bands whilst divergent wall images are more diffuse and difficult to detect in small scale structures. Further experiments are, therefore, required to distinguish between these contrast formation processes.

In an attempt to alter the magnetic microstructure we applied a large vertical field to the sample of 6800Oe, using the standard objective lens. We note that the applied field exceeds the demagnetising field for the thin films in question which is given by $4\pi M_s$=5300Oe. Great care was also taken in aligning the TEM, to ensure that there was no hysteresis effects in the magnetic lenses which could alter the imaging conditions. Then by

choosing an appropriate part of the specimen, we could return to the exact location and record a second set of images. Since the specimen has not been tilted any differences present in these images are due to changes in the magnetic microstructure. These results showed no significant changes from the first set of Fresnel images. Therefore, we conclude that the majority of the contrast present in figure 6.4 is crystallite related. In the following sections we try to reveal the magnetic microstructure by applying a field in-situ.

6.6 Fresnel imaging when applying a magnetic field in-situ.

In this section the 500Å Fe_3O_4 thin film is magnetised in-situ using a vertical field, and then by tilting the specimen a component in its plane can be introduced. By changing the in-plane component of the applied field we will try to distinguish between crystallite and Fresnel contrast. The crystallite contrast observed is mainly due to Bragg scattering (the other changes are due to inelastic mechanisms) which changes the individual crystallite contrast instantaneously as the specimen is tilted. In comparison, the main changes in Fresnel contrast are due to the motion of domain walls throughout the film which can be observed as the discrete "jumping" of the bright lines (convergent domain walls).

Figure 6.1 shows the hysteresis loop of the 507Å Fe_3O_4 thin film (deposited on an 800Å layer of Si_3N_4 which is on a silicon substrate). Assuming that the TEM samples show similar properties, we can estimate the coercive field (H_c) of the 500Å Fe_3O_4 thin film to be ≈250 Oe. We therefore chose the objective lens excitation to give a vertical field of 800Oe which enables images to be obtained with a maximum in-plane component of 514Oe. The demagnetising fields were estimated in the previous section to be ≈5300Oe, an order of magnitude greater than the applied field. Therefore, we can assume any out-of-plane magnetisation is linked to the anisotropy and not the effect of the vertical field surpassing the demagnetising fields to align the moments.

Initial observations reveal the changes in the Fresnel contrast as the sample is tilted through 10° steps, which effectively changes the in-plane component of the magnetic field. After a few seconds the specimen reaches an equilibrium structure and the signal is then integrated

for ≈10s. Figure 6.7 shows Fresnel images as the in-plane component of the applied field changes from positive to negative values. Here, the images are acquired at a lower magnification and at a higher defocus than the images presented in figure 6.4.

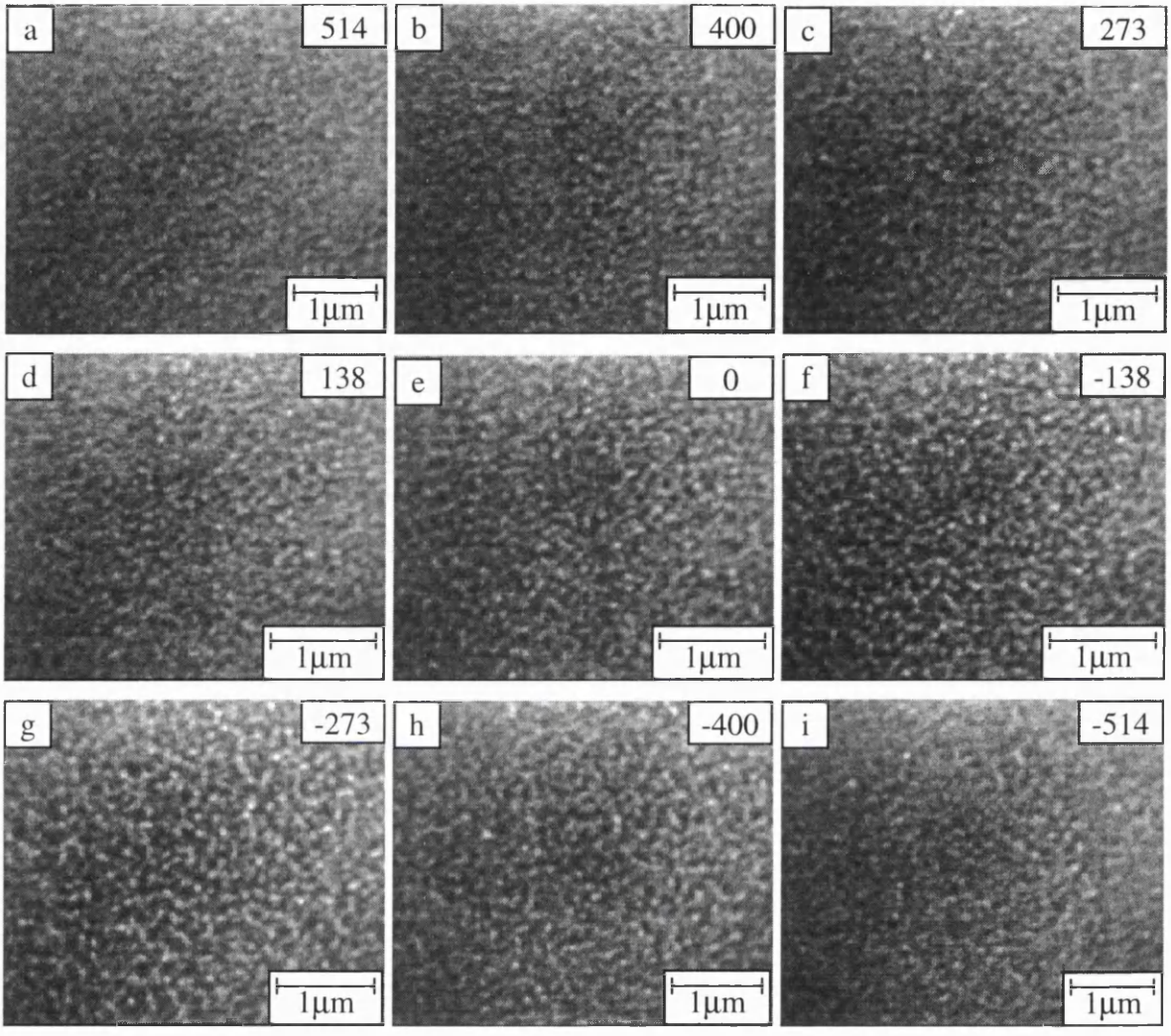

Figure 6.7 *Fresnel images of the 500Å thin film when applying a vertical field of 800Oe in-situ. The in-plane component of the field changes from positive to negative values. (inset are the values in Oe.)*

Initially the sample is subjected to the maximum in-plane field of 613Oe, where the majority of the magnetic moments are aligned to the field direction. It should be noted that all of the moments would be aligned along the field direction if the specimen were in the saturated state. Images are first obtained at a tilt of 40° which corresponds to a field of 514Oe. As the field is reduced there is an increase in image contrast. When the field is then reversed it is found that the maximum image contrast occurs within the range 138Oe-

273Oe (figures 6.7f and g). When the in-plane component of the applied field is changed from negative to positive a similar set of results are obtained (figure 6.8). These Fresnel images show a maximum contrast when the field is ≈-200Oe. The maximum contrast is observed as the magnetic moments align to give a net magnetisation of zero, which corresponds to the coercive field being attained. Therefore, from the images in figures 6.7-6.8, a rough estimate of the coercive field is 230±30Oe which compares well with the hysteresis loop value of 253Oe. This also shows that the contrast we observe does have a significant magnetic component and is not all due to the defocused crystallites, since the maximum contrast occurs at an angle of ≈15° after applying a field in the opposite direction. In comparison, the crystallite contrast in a polycrystalline film with no texturing present is approximately constant for all tilting angles. If texturing is present, we would expect to see a maximum contrast when tilting through the same angle to both sides of the zero position.

Again, to estimate the feature size we measure the number of bright features crossing four lines drawn at 45° intervals. The mean feature size from the images in figure 6.7 is calculated to be 177±4nm. It should be noted that there are negligible changes in the feature size in the four directions along which we measure, indicating no directionality in the image. If the majority of contrast is indeed magnetic, a domain size of 83.5±2nm is expected. This would correspond to the domain width being ≈2/3 crystallite diameters.

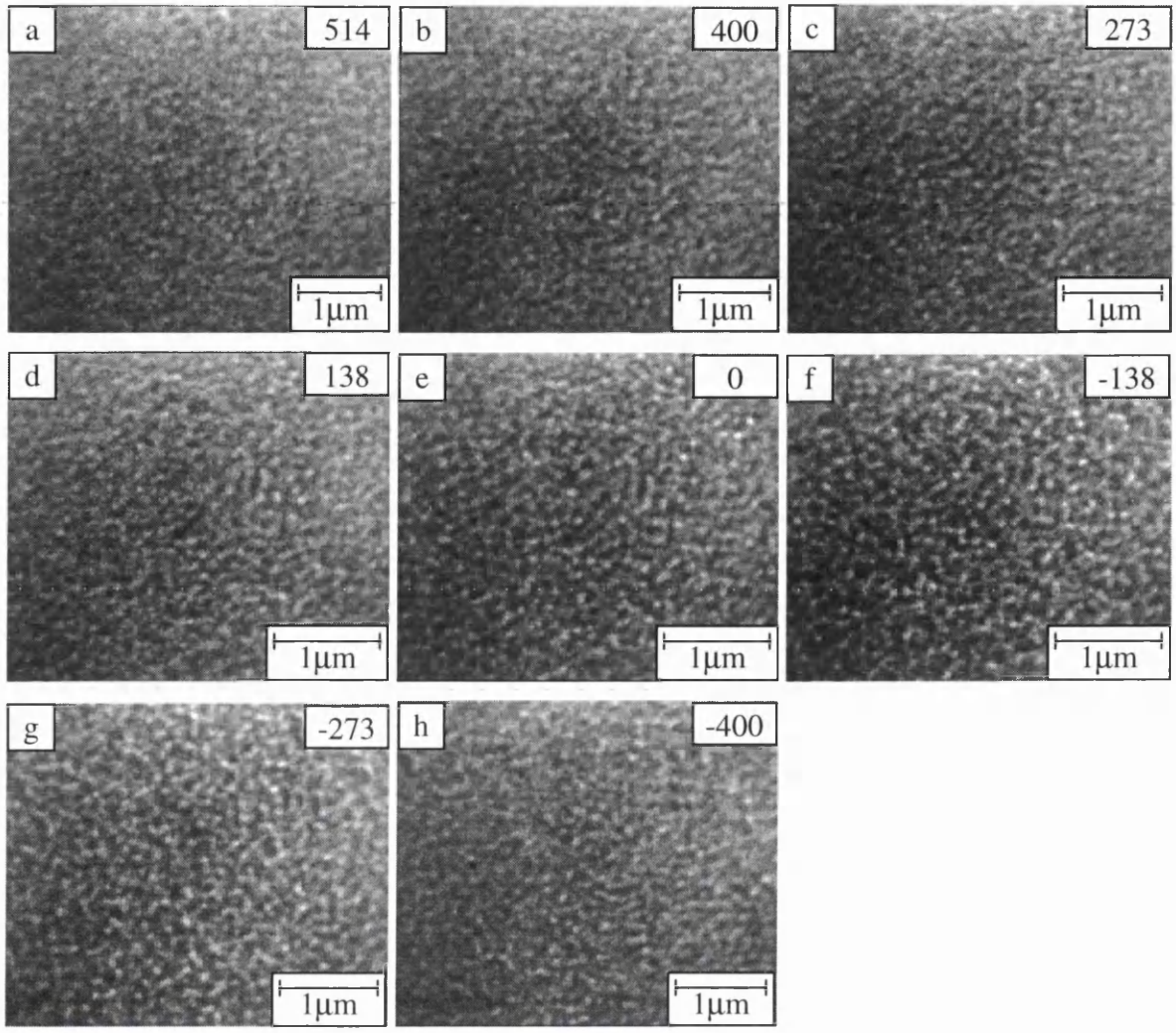

Figure 6.8 *Fresnel images of the 500Å thin film when applying a vertical field of 800Oe in-situ. The in-plane component of the field changes from negative to positive values. (inset are the values in Oe.)*

Another approach to reveal the magnetic microstructure is to record on video a set of Fresnel images as the sample is tilted by the rotary motor in the goniometer. This provides a constant tilt of 0.75° per second. As the tilting angle is reduced, the crystallite contrast changes within individual crystallites and a "twinkling" effect occurs as the electrons are scattered from the different atomic planes. We also observe changes in the image contrast which arise from the changes in the magnetic microstructure; these are manifested by the increase in image contrast which is at a maximum when the in-plane component of the applied field is equal to the coercive field, and by the "jumping" motion of domain walls within the specimen. The latter effect shows, typically (after looking at 10 wall jumps),

sections of length ≈150nm which jump ≈35nm. This switching distance is comparable with the size of an individual crystallite.

Two possible explanations for this behaviour are; (1) that the magnetisation within an individual crystallite has changed orientation to align along its easy axis in the direction which is energetically favourable in the presence of an external field (section 1.2.4), i.e. a component of the magnetisation lies in the field direction, and/or (2) through exchange coupling (section 1.2.1) where the moment switches along is easy axis such that a component of the magnetisation lies in the net direction of its nearest neighbours. A fuller explanation requires knowledge of the large anisotropy component present in the sample. When a single crystallite changes orientation the system then has to return to an equilibrium structure. This could explain why we observe sections of ≈150nm jumping, if the crystallites are coupled then it could be energetically favourable for the moments in neighbouring crystallites to also switch (a domino effect).

This effect cannot easily be revealed using single frames from the video of Fresnel images because the magnetic contrast subtly changes over a period of several seconds and when the sample is tilting there are also changes in crystallite contrast.

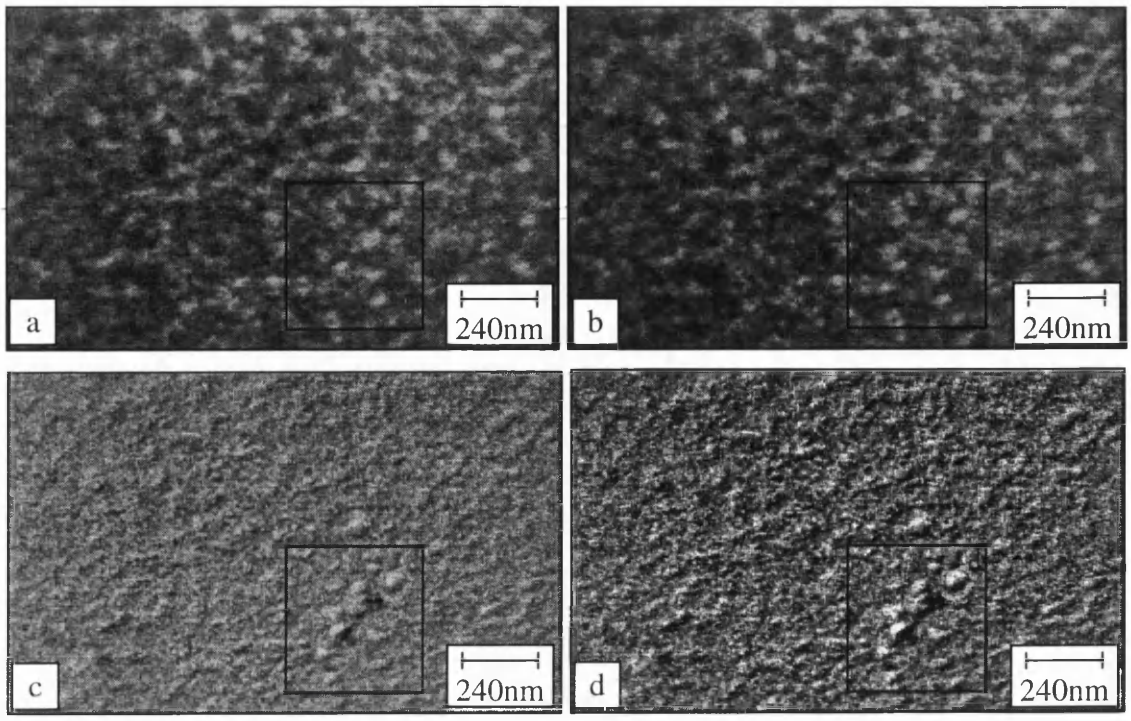

Figure 6.9 *Domain switching in the 500Å Fe_3O_4 thin film. (a) and (b) show, respectively, the Fresnel images of before and after the domain has switched. (c) shows the difference image (a)-(b), and (d) shows image (c) with the contrast expanded.*

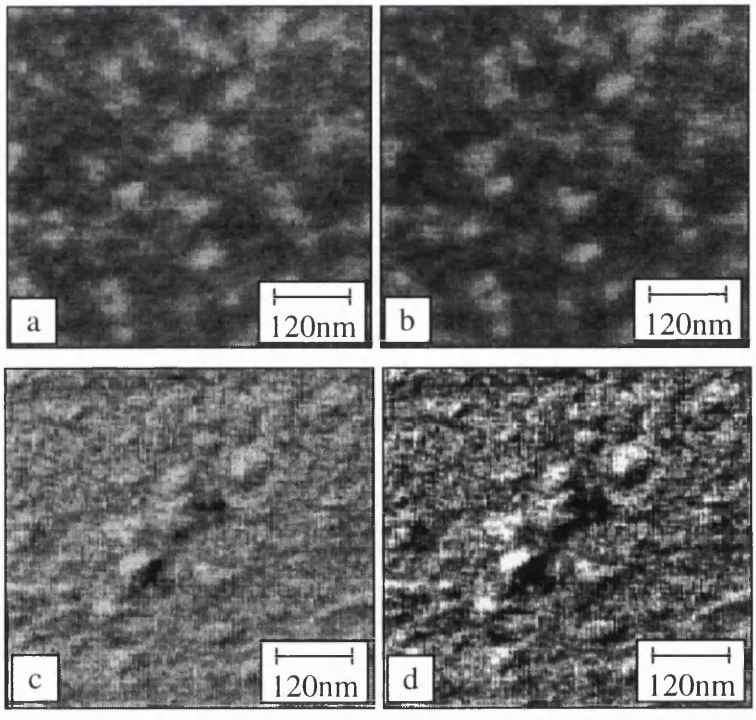

Figure 6.10 *The switching of a domain wall in the 500Å Fe_3O_4 thin film. (a) and (b) show, respectively, the Fresnel images of before and after the domain has switched. (c) shows the difference image (a)-(b), and (d) shows image (c) with the contrast expanded.*

To get round these problems we can quickly change the applied field and then stop tilting the specimen at a position where domain walls are most likely to switch. The position at which domains are most likely to switch occurs at the maximum gradient of the B-H hysteresis loop. This criterion is satisfied around the coercive field when the total magnetisation of the sample is zero. To experimentally achieve this, the specimen is initially subjected to the maximum field of 613Oe. The specimen is then quickly rotated round to -15° (corresponding to ≈250Oe). We observe the majority of walls to change instantaneously, but a small number can be observed to change after a few seconds[9]. We can therefore take one image as soon as the specimen stops moving (figure 6.9a) and another after a few seconds (figure 6.9b). There is no change in the crystallite contrast as the specimen has remained at a constant tilt, therefore any changes in contrast are magnetic in origin. To show this effect the two images are aligned to be coincident and subsequently subtracted (figure 6.9c and after contrast enhancement figure 6.9d). The motion of the domain wall is apparent from the image contrast. Bright and dark regions show the wall positions before and after the switching mechanisms respectively, the grey regions indicate that there are no differences between the two original Fresnel images.

Figures 6.9 and 6.11 show images as discussed above. Figures 6.10 and 6.12 show the boxed regions, in the respective figures, where domain walls have been observed to switch. Figure 6.10 shows what appears to be a domain wall ≈120nm in length jumping a distance of ≈35nm. In figure 6.12 the contrast is particularly complex, with more than one domain wall moving in the time between frames. Yet again, we observe the walls to have jumped ≈35nm. This technique, in general, shows similar effects to what we observe when the sample is tilted at a constant rate.

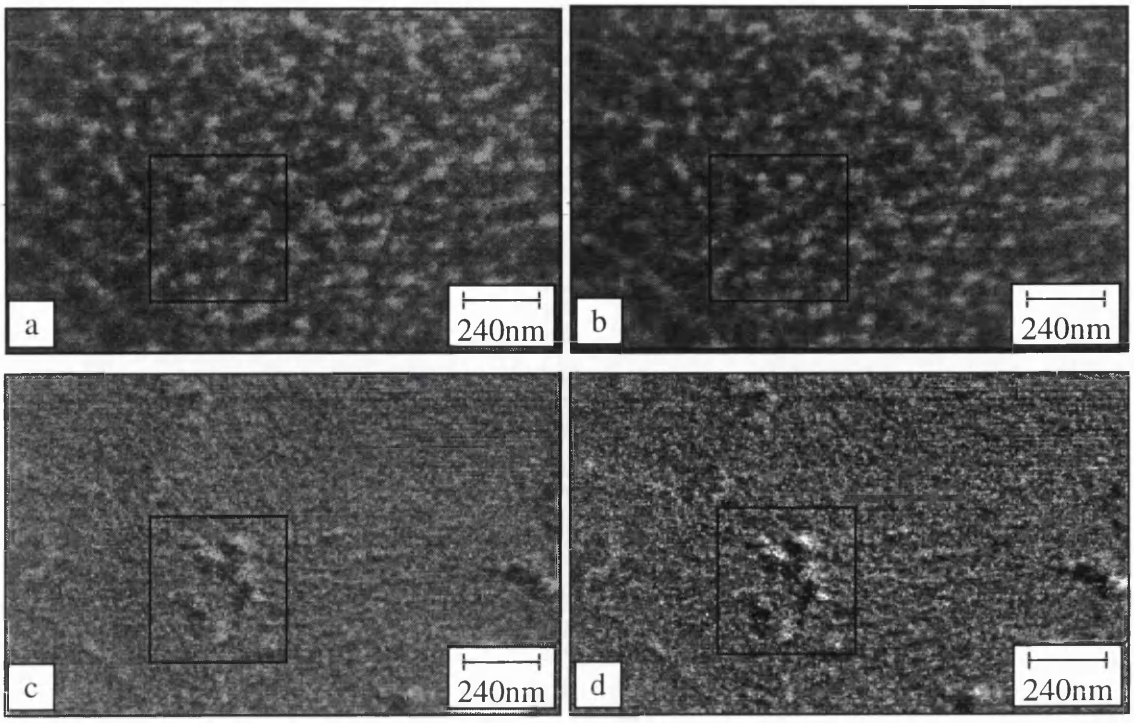

Figure 6.11 *Domain switching in the 500Å Fe_3O_4 thin film. (a) and (b) show, respectively, the Fresnel images of before and after the domain has switched. (c) shows the difference image (a)-(b), and (d) shows image (c) with the contrast expanded.*

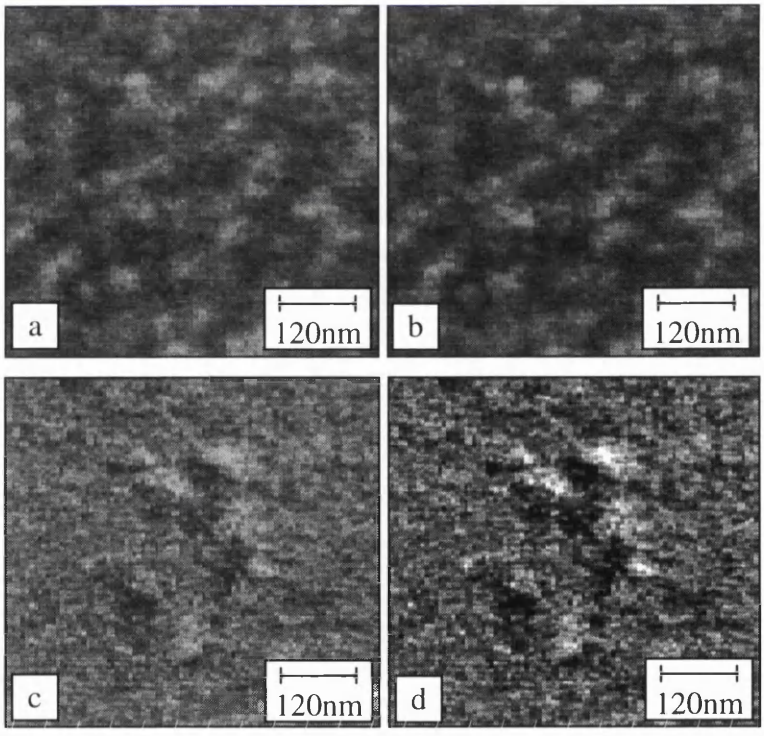

Figure 6.12 *The switching of a domain wall in the 500Å Fe_3O_4 thin film. (a) and (b) show, respectively, the Fresnel images of before and after the domain has switched. (c) shows the difference image (a)-(b), and (d) shows image (c) with the contrast expanded.*

6.7 Foucault imaging.

Fresnel images provide information on where changes in magnetisation direction take place but do not provide any direct information on the local magnetisation direction themselves. This can be obtained from Foucault images, pairs of which, sensitive to orthogonal induction directions, provide a useful indication of the magnetic induction distribution within the film. Light and dark regions within an image correspond to regions in which the component of the induction mapped is positive and negative respectively. The width of each dark or bright region can be equated with the size of a domain.

No reproducible Foucault images were obtained from the 25nm or 10nm thick films due to the small Lorentz deflection whilst the contrast variation from the 100nm film was particularly complex (figures 6.13a and b). However, the 50nm samples yielded perfectly satisfactory images (figures 6.13c and d) and we once again counted the bright features crossing a line. In this case, however, 3 equally spaced lines running in a single direction were used on each image, that direction being perpendicular to the induction direction mapped. The change in the procedure reflects the fact that Foucault, unlike the other imaging modes, is highly directional. It should also be noted that the observed contrast is highly dependant on the positioning of the aperture in the diffraction plane which further complicates the interpretation of these images.

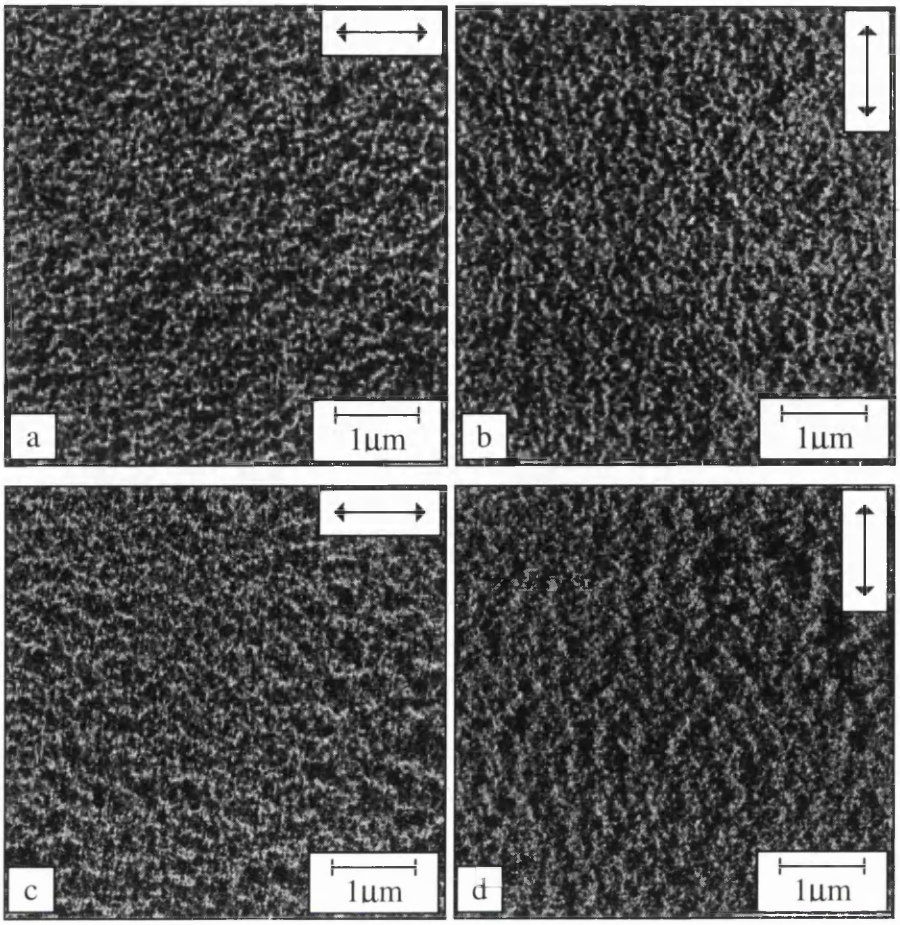

Figure 6.13 *Foucault images of Fe_3O_4 thin films in the as-deposited state; (a) and (b) show the 100nm thick, and (c) and (d) show the 50nm thick films when mapping in orthogonal directions.*

The feature sizes are 141±10nm and 147±7nm, in figures 6.13c and d respectively, which indicate an average domain size ≈73±4nm in width. The domain width varies little with direction and has a mean value of ≈2/3 crystallite diameters. This corresponds well with the results at the start of section 6.6.

To check that the magnetic distances were representative of the films and not artefacts reflecting a far from equilibrium state locked in during the growth process, we subjected the films to large fields (6800Oe) perpendicular to their planes and recorded a new set of images. From these images it was apparent that any changes of the detailed pattern or mean feature size from the initial values are modest.

Finally, it is worth noting one final experimental fact and that is the central spot of the low angle diffraction (LAD) pattern (figure 6.14a) appears to be a solid disc rather that an annulus which suggests that the demagnetisation effects are not sufficiently strong to force the moments to lie in plane. We can compare this diffraction pattern with that of a line grating (figure 6.14b) to clearly see the spread in the central beam. The actual width of the LAD spot is highly dependent on the film exposure time, both having been exposed for 0.1s in this case. This renders quantitative analysis of the images to be non-trivial. The results confirm the presence of a significant local out-of-plane component of magnetisation and might help in the estimation of a lower bound to the anisotropy.

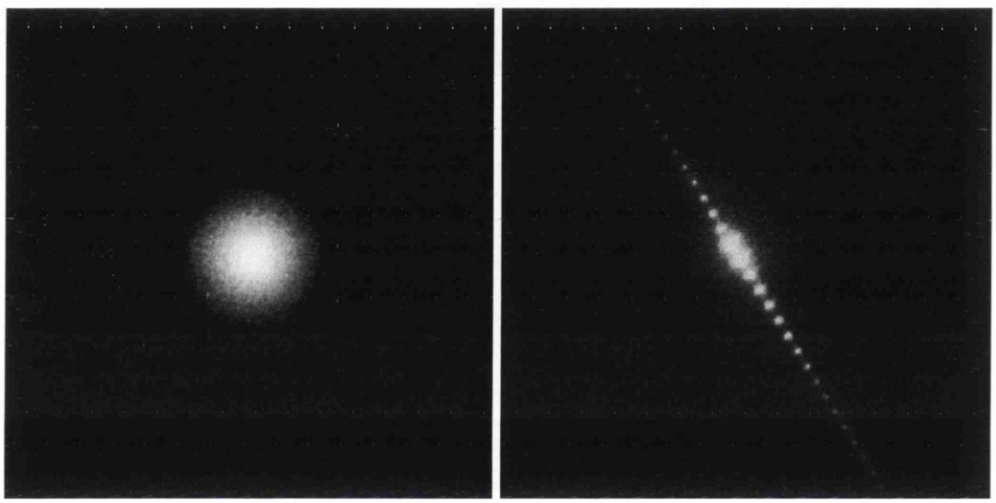

Figure 6.14 *LAD of (a) the 50nm thin film and (b) a cross-grating (1600/mm).*

6.8 Conclusion

Four Fe_3O_4 thin films of different thickness have been investigated. This study has shown that as the sample thickness is increased, the crystallite size is also increased. It is also clear from the initial Fresnel analysis that this is a complex system in which both magnetic and crystallite contrast are of the same order.

In-situ magnetising experiments have been carried out on the 500Å thin film. We have investigated the variation in image contrast as the sample is tilted. This shows that a maximum contrast condition is achieved when the in-plane component of the applied field is equal to the coercive field. We believe that the contrast in these images is mainly

magnetic and, upon analysis, reveals no directionality. The typical domain size is estimated to be ≈83±2nm which corresponds to a distance of ≈2/3 crystallite diameters. Analysis of the Foucault images indicate domain sizes on a similar scale to these images, again showing no directionality. This leads us to believe that there is exchange coupling between crystallites on a nearest neighbour scale. However, to estimate the coupling strength we require a knowledge of the local anisotropy which appears to dominate the exchange interaction.

We have also discussed the domain wall switching mechanism observed from video and subsequently revealed the magnetic changes in a system inhibited by crystallite contrast. When a large positive magnetic field is applied the magnetisation lies mainly in the direction of the applied field. As we reduce the field a small number of domain walls are observed to switch. As the field is applied along the reverse direction there is a significant increase in the number of switching walls. The maximum likelihood of a wall switching is when the applied field approaches the coercive field. Sections of domain wall, typically 150nm in length, have been observed to "jump" a distance of ≈35nm. This jumping distance corresponds to the magnetisation switching in an individual crystallite. After the first moment has switched there is a change in the local energy of the system. This makes it energetically possible for its nearest neighbours to switch direction such that the component of the magnetisation, lying along the easy axis, aligns to the field direction and/or through exchange coupling to the direction of the switched moment. Hence, we observe many crystallite moments switching in a "domino toppling" type effect, typically over a distance of 150nm which corresponds to ≈4/5 neighbouring moments switching. As we further increase the applied field there is a reduction in the number of walls switching due to the majority of moments being already aligned such that a component of the magnetisation, lying along the easy axis, is towards the field direction.

References

[1] D.M. Lind, S.D. Berry, G. Chern, H. Mathias, and L.R. Tersardi, Phys. Rev. B **45**, 1838 (1992).

[2] D.M. Lind, S.P. Tay, and S.D. Berry, J. Appl. Phys., **73**, 6886 (1993).

[3] T. Fujii, M. Takano, R. Katano, and Y. Brando, J. Cryst. Growth, **99**, 606 (1990).

[4] J. Krebs, D.M. Lind, and S.D. Berry, J. Appl. Phys., **73**, 6458 (1993).

[5] D.T. Margulies, F.T. Parker, and A.E. Berkowitz, J. Appl. Phys., 75, 6097, (1994).

[6] "Magnetic and Other Properties of Oxides and Related compounds", edited by K.H. Hellwedge, A.M. Hellwedge, and Landolt Börnstein, **Vol. 4**, Springer, Berlin (1970).

[7] Shepherd et al., Phys. Rev. B, **Vol. 43** (10), 8461 (1991).

[8] K.L. Chopra, "Thin Film Phenomena", McGraw-Hill (1969).

[9] A. Steudel and S. Stotz, Z. Physik, **151**, 233 (1958).

Chapter 7

Investigation of NiFe-Ag granular thin films which show the giant magnetoresistant effect.

7.0 Introduction.

The recent discovery of giant magnetoresistance (GMR) in Fe/Cr in magnetic multilayers[1,2] has led to much current world-wide interest in the effect. This has in part been due to its potential exploitation by the data storage, magnetometry and sensor industries. It is now generally accepted that the GMR which occurs in multilayers results from the anti-parallel alignment of the moments of alternate ferromagnetic layers. A number of theories have been developed which identify the large increase in the multilayer resistivity to be due to spin-dependent electron scattering[3,4]. This can occur both within the bulk of the ferromagnetic layers and at the multilayer interfaces. As magnetic multilayers have film thicknesses considerably less than the mean free path of conduction electrons, their resistivity is greatly affected this type of scattering.

More recently GMR has been found in heterogeneous alloys[5,6]. These are formed by the co-deposition of two immiscible materials, one of which is ferromagnetic in bulk. To promote phase segregation the film is either deposited at an elevated temperature, or annealed after deposition. This results in the formation of a superparamagnetic nanocrystalline structure in which the fine particles of the ferromagnetic material are embedded in the non-magnetic matrix. When the particles moments are randomly orientated the resistivity of the material is higher than when they are aligned by the

application of an external field. The effect has been observed in co-sputtered thin films of many materials including Co-Ag[7], Fe-Ag[8], NiFe-Ag[9], Co-Ni-Ag[10], Co-Fe-Ag[11], and Fe-Mg[12]. The magnitude of the GMR observed has been found to be a sensitive function of both the size of the ferromagnetic particles and the concentration of the ferromagnetic material in the alloy. The former effect has been postulated to be due to the existence of an optimum particle size, determined by the conduction electron mean-free path[13]. Larger particles result in a reduction of the GMR due to the onset of percolation, which acts to couple the particles ferromagnetically.

In this chapter two sets of NiFe-Ag granular thin films are studied which show the GMR effect. Although, no attempt has been made to correlate these results with the actual GMR data. This chapter exemplifies how a range of TEM techniques can be usefully deployed for characterising inhomogeneous nano-systems. Initially we discuss the bright field and diffraction imaging conditions (section 7.1), implemented on the Philips CM20 TEM. In the sections following, an extended VG HB5 scanning transmission electron microscope (STEM) is introduced (section 7.2). Included are a discussion of the microscope column, the detector systems and the equipment required to carry out energy dispersive x-ray (EDX) compositional analysis (section 7.2.1). When acquiring EDX spectral data the high-angle annular dark field (HADF) imaging mode is implemented which reveals contrast dependent on the atomic number ('Z contrast') of the investigated elements as described in section 7.2.2. To complete the microscopy section, the technique which is used to analyse the EDX spectra is discussed in section 7.2.3. The first specimens investigated are of similar composition and have been post-annealed at different temperatures. The TEM study reveals the size, texturing and phase boundary abruptness of the individual crystallites. EDX spectral analysis is also utilised to investigate small areas showing different Z contrast in the HADF images to reveal the local compositions of Ni, Fe and Ag. The second set of specimen are of identical composition and have also been post-annealed at different temperatures. However, only the TEM study is achieved due to these samples being prepared on Ni grids rendering an accurate compositional study impossible.

7.1 Transmission electron microscopy techniques to investigate granular thin films.

The TEM investigations of NiFe-Ag granular thin films are carried out on the Philips CM20 electron microscope (section 2.1). The TEM is aligned in the standard imaging mode as described in section 2.4. Diffraction patterns are obtained at a camera length of 80cm. The diffraction rings reveal information on the crystal structure and lattice constant of each sample (see below). The width of each individual ring is also indicative of the quality of the phase segregation. Further analysis of the diffraction ring intensities when the sample is tilted gives an indication of any texturing present. Also investigated are bright field images which give an indication of the distribution of crystallite sizes and their grain boundary abruptness. In the remainder of this section the technique to analyse the diffraction patterns is considered.

Following Edington[14] (1973), a polycrystalline film comprises of a large number of small perfect crystals randomly orientated with respect to the surface. If an electron wave is incident on a crystallite at a particular angle θ, which satisfies the Bragg equation,

$$\lambda = 2d_{hkl} \sin\theta \qquad [7.1]$$

where λ is the wavelength of the incident electrons (=2.51pm), and d_{hkl} is the crystal lattice spacing where hkl are the Miller indices to describe a particular set of lattice planes. If all possible orientations of crystallite are present in the thin film, it follows that electrons will emerge from the bottom surface of the specimen travelling along cones of half angle 2θ for all values of θ permitted by the Bragg equation. These rays are brought to a focus in the back focal plane by the imaging lens, so that a series of concentric rings should be seen in this plane. Furthermore, for small angles of θ, the radii of these rings relate to the Bragg angle by,

$$r_{hkl} = 2f\theta_{hkl} \qquad [7.2]$$

where f is the focal length of the imaging lens (typically 3mm). When the diffraction pattern is displayed on the viewing screen, the radii of these rings are given by,

$$R_{hkl} = 2L\theta_{hkl} \qquad [7.3]$$

where L is the camera length of the diffraction pattern. We also recall that for cubic structures,

$$d_{hkl} = \frac{a}{\sqrt{h^2 + k^2 + l^2}} \qquad [7.4]$$

where a is the lattice constant[15]. Combining equations [7.1]-[7.4] we get,

$$R^2 = \left(\frac{\lambda L}{a}\right)^2 \left(h^2 + k^2 + l^2\right) = \left(\frac{\lambda L}{a}\right)^2 N \qquad [7.5]$$

where $N=h^2+k^2+l^2$ which is an integer number. Therefore, if we plot the values of R^2 in the y-axis we can associate integer values of N to give a straight line. From the values of N we can then deduce the Miller indices *hkl* and from the gradient of the line evaluate the lattice parameter. It should also be noted that for simple cubic structures all values of *hkl* are permitted, for a fcc structure *hkl* must be all even or all odd, and for a bcc structure $(h+k+l)$ must be even. Therefore, from the numbers which N takes in the above analysis the structure of lattice can also be found.

7.2 Scanning transmission electron microscope (STEM) and techniques employed to investigate granular thin films.

In a STEM a small electron probe is formed in the specimen plane and scanned across an area of specimen in a raster fashion. Detectors are positioned in the column which enable a quantitative analysis of the elastically scattered electrons and x-rays from the specimen. Figure 7.3 shows a schematic of the extended VG HB5 STEM column at the University of Glasgow.

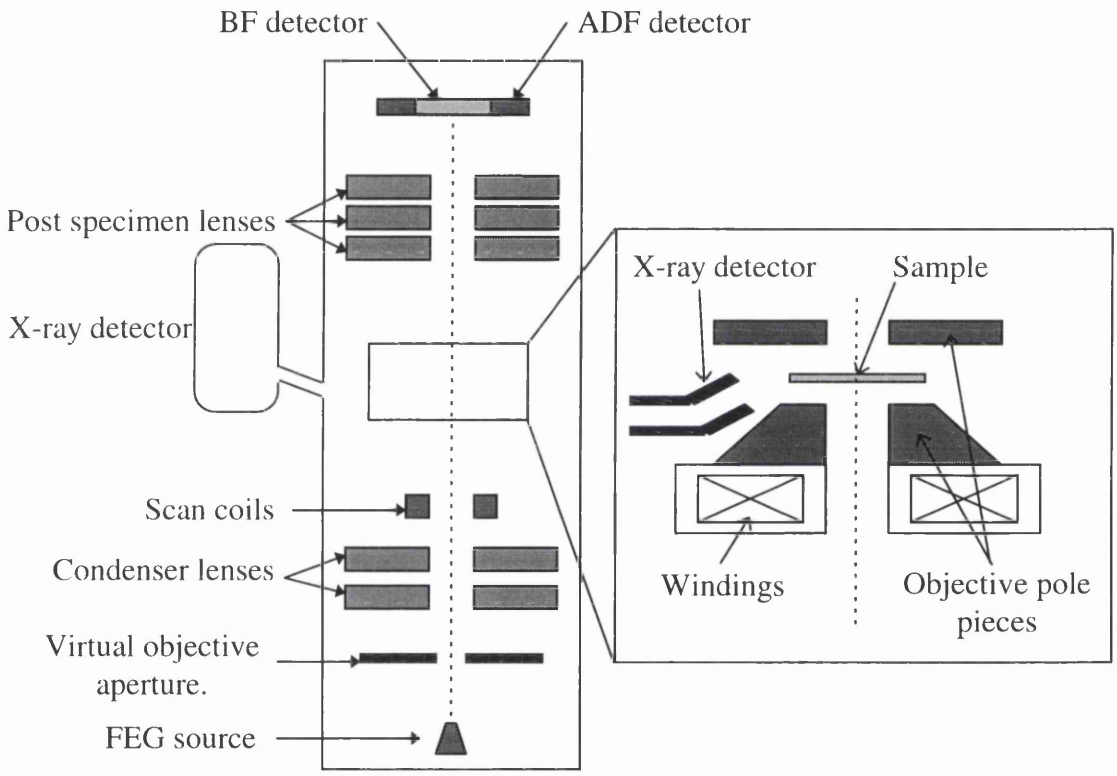

Figure 7.3 *HB5 STEM schematic.*

The electron source in the HB5 STEM is a cold field emission gun[16] (section 2.2.2). The energy spread in the emitted electrons is typically between 0.2 and 0.5eV with the virtual source approximately 6.5nm in diameter[17]. A single condenser lens with a short focal length demagnifies the effective source size. The probe is then scanned across the specimen by means of coils arranged in front of the objective lens, the prefield of which acts as the final probe forming lens. The virtual objective aperture is used to define the probe angles; this is discussed in section 7.2.2.

In a STEM the electrons transmitted by the specimen are collected with an electron detector rather than being imaged on a viewing screen or a photographic plate. Different imaging modes can be selected by varying the size and geometry of the detector and the image contrast is controlled by the size and position of a detector aperture. Additionally, each pixel of the image is acquired sequentially unlike the CTEM where the whole image is acquired simultaneously. Several images can be collected in parallel in either analogue or digital form, allowing for contrast enhancement, noise filtering and signal combination. Images are saved in digital form using a Link Analytical AN10000 with the precision set at 8 bits per pixel with each pixel being allocated a dwell time of 51μs.

7.2.1 Energy dispersive x-ray microanalysis instrumentation.

Energy dispersive x-ray (EDX) microanalysis is a technique which can be employed in a STEM to determine the local elemental composition of a thin specimen[18,19]. The method relies on the production of characteristic x-rays from a volume of specimen excited by a focused electron probe scanned across the specimen. The x-ray detector used in this project is a Link Analytical lithium drifted silicon (Si(Li)) detector. The detector subtends a solid angle of 0.04sr at the specimen and its axis is orientated at an angle of 10.5° to the horizontal in the specimen plane. Between the crystal and the microscope there is a protective beryllium window ≈8μm thick which reduces the detector efficiency to less than unity for incident x-ray energies below ≈3keV. The characteristic x-ray photons enter the semiconductor in the microscope and produce photoelectrons which ionise the detector atoms. The atoms in turn de-excite and generate electron-hole pairs. The number of pairs produced is directly proportional to the energy of the original photo-electron. The crystal itself is held between two gold electrodes with a potential difference of 500V. This biasing voltage separates the electrons and holes and a current proportional to the incident photon energy is generated. The current pulse is measured and the channel of a multi-channel analyser corresponding to this photon energy is incremented accordingly. This produces an x-ray spectrum from which it is possible to quantify the local concentrations of the elements in the spectrum. The x-ray spectra are recorded using the AN10000 and the

average count-rate, dead time and current recorded on the VOA are noted for each acquisition.

7.2.2 High-angle annular dark field (HADF) imaging.

When conducting EDX microanalysis in a STEM it is important to select a suitable imaging mode in which to position the electron probe before spectrum collection. Signals collected from the electrons scattered through high angles have intensities which are predominantly attributed to elastic scattering. These signals show a strong dependence on atomic number Z and a low susceptibility to crystallographic contrast[20]. It is possible to form an image at such scattering angles using an annular dark field (ADF) detector in a STEM.

In the ADF and HADF imaging modes a 100μm VOA defines a probe angle (α_0) of 11mrad, probe diameter 2.4nm (defined as containing 90% of the beam current)[21] and the current in the probe 0.2nA. Additionally, a 25μm selected area aperture is inserted to act as a spray aperture to prevent stray electrons from exciting unwanted instrumental contributions from, for example, the substrate material or the objective aperture. The ADF detector is an annular scintilator which is coupled to a photomultiplier tube. It has inner and outer diameters of 3.3mm and 25mm respectively. The range of acceptance angles (α_d) for the scattered intensity distribution is determined by the post specimen lens settings. To achieve angular compression in the scattered beam, required to form a high angle ADF image, a camera length of 55mm is chosen. McGibbon[21] (1989) measured the inner and outer acceptance angles of the ADF detector to be from ≈60mrad to 200mrad at this setting.

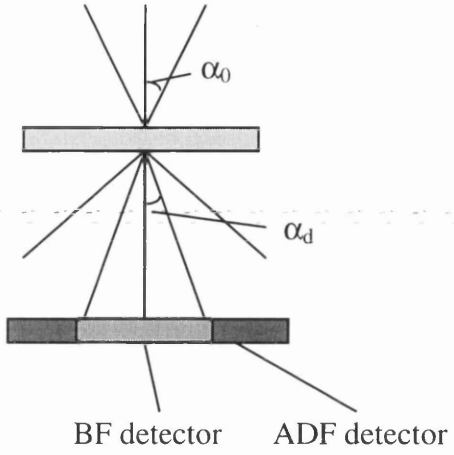

Figure 7.4 *ADF detector geometry.*

7.2.3 EDX analysis technique.

In an x-ray spectrum the channel about which a given peak is centred corresponds to the photon energy, and the total number of counts in the peak is proportional to the number of photons at that energy incident on the detector. In practice, however, spectra also include energy contributions from bremsstrahlung radiation and characteristic x-rays emitted by other elements present in the excited volume[22,23]. It is therefore necessary to calculate the number of counts which actually correspond to the elements to be investigated before the relative concentrations can be deduced. In the vicinity of the characteristic Ni, Fe and Ag x-ray peaks there are no overlapping peaks from contaminants present on the specimen or in the column. It should also be noted that in these spectral areas the energy variation of the bremsstrahlung is approximately linear. The number of counts in the peak can therefore be deduced by defining two background regions surrounding the peak of interest (Figure 7.5). The number of counts in the relevant peak is given by,

$$N_{peak} = N_{total} - \left(\frac{N_{bg1}}{chan_{bg1}} + \frac{N_{bg2}}{chan_{bg2}} \right) / 2 * chan_{peak} \qquad [7.6]$$

where N_{peak} is the number of counts after background correction, N_{total}, N_{bg1} and N_{bg2} are the total number of counts in the characteristic peak and the two background regions

respectively, and the number of channels over which each region extends is represented by $chan_{peak}$, $chan_{bg1}$ and $chan_{bg2}$ in the aforementioned regions.

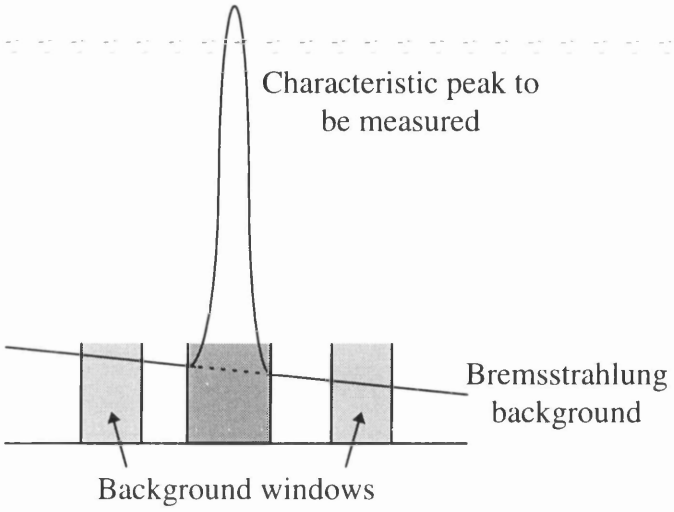

Figure 7.5 *Removal of background radiation from the measured peak.*

The ratio of the numbers of K_α to K_β x-rays emitted from a given element[23] is a constant greater than 1. Comparison of the ratios of the Fe/Ag, Ni/Ag and Fe/Ni K_α peak counts from different spectra is therefore the most straightforward way of accurately analysing concentration of Ni, Fe and Ag.

To turn the total recorded x-ray counts in the corrected K_α peaks into absolute atomic compositions of the form $Ni_XFe_YAg_{100-X-Y}$ requires a knowledge of the relative efficiencies of x-ray generation and detection for the elements of interest. When using a Si(Li) detector Ni and Fe peaks are detected with similar energy efficiencies (≈1). The Ag K_α peak is detected with a lesser efficiency (≈0.85) due to the transmittance of the higher energy characteristic x-rays through the crystal. The generation efficiencies[24] of the elements can be expressed as a set of factors k_{FeAg}, k_{NiAg} and k_{FeNi} which relate the number of atoms of each element in the excited volume (n) to the measured number of characteristic x-rays corresponding to that element (N) thus,

$$R_1 = \frac{n_{Fe}}{n_{Ag}} = k_{FeAg}\frac{N_{Fe}}{N_{Ag}} \qquad R_2 = \frac{n_{Ni}}{n_{Ag}} = k_{NiAg}\frac{N_{Ni}}{N_{Ag}} \qquad R_3 = \frac{n_{Fe}}{n_{Ni}} = k_{FeNi}\frac{N_{Fe}}{N_{Ni}} \qquad [7.6]$$

where R_1, R_2 and R_3 are defined as the respective count ratios. The k_{FeAg} is given by Gray[25] (1983) to be,

$$k_{FeAg} = \frac{\omega_{Ag} p_{Ag} \sigma_{Ag} \varepsilon_{Ag}}{\omega_{Fe} p_{Fe} \sigma_{Fe} \varepsilon_{Fe}} = k_{AgFe}^{-1} \qquad [7.8]$$

where ω is the fluorescence yield (probability of emission of a characteristic x-ray rather than an Auger electron), p is the partition function, σ is the ionisation cross-section with 100keV incident electrons and ε is the energy efficiency of the detector (Table 7.1).

Element	K_α peak (keV)	p	ω	σ (cm^2sr^{-1})	ε
Fe	6.40	0.8818	0.34	12.65	1
Ni	7.48	0.8803	0.406	10.80	1
Ag	22.16	0.8251	0.831	3.53	0.85

Table 7.1 *Parameters required to calculate k factors.*

The other k factors are evaluated in a similar fashion yielding $k_{FeNi} = 0.987$, $k_{FeAg} = 0.263$ and $k_{NiAg} = 0.266$. The atomic percentage of each element can then be calculated from ratios in equation 7.6 as,

$$At\%Fe = \frac{100R_1}{1 + R_1 + R_2} \qquad At\%Ni = \frac{100R_2}{1 + R_1 + R_2} \qquad At\%Ag = \frac{100}{1 + R_1 + R_2} \qquad [7.9]$$

7.3 NiFe-Ag granular thin films (1).

In this section two NiFe-Ag granular thin films are investigated. The first specimen D1 has atomic composition of 81.5%Ag, 4.4%Fe and 14.2%Ni. The second specimen H1 (of composition 82.6%Ag, 3.8%Fe and 13.6%Ni) has also been annealed at 450°C for 10 minutes on a glass substrate. The films have been investigated by bright field TEM imaging and diffraction pattern analysis on the Philips CM20 and EDX analysis using a VG HB5.

7.3.1 Specimen preparation.

The specimen preparation and post-annealing processes were carried out by M.L. Watson (University of Coventry). The NiFe and Ag were r.f. sputtered onto a membrane window (section 5.3) using a Nordiko 2000 sputtering system. The base pressure was less than $2x10^{-7}$ Torr, the sputtering pressure was 8 mTorr of Argon and the sputtering power was 300 W. The target used consisted of a 4″ Ag (99.999%) disc onto which were placed $Ni_{80}Fe_{20}$ and Fe 0.25cm^2 squares arranged in a mosaic pattern. The film thickness was measured using a Tolansky multiple beam interferometer and the average compositions determined using EDX microanalysis. As the sputtering rate from $Ni_{80}Fe_{20}$ and Fe are very similar the film composition could be easily controlled by adding or removing squares of either of the two magnetic materials. For this study the Ag content of the films was fixed at 80-85 atomic percent. To promote post deposition phase segregation and magnetic particle growth, the specimen H1 was rapidly thermally annealed in a custom built vacuum system with 2kW halogen bulbs which produce a power density at the substrate of 80W/cm^2. The bulb illumination is computer controlled and the temperature of the sample was measured using a thermocouple mounted directly onto the sample holder.

7.3.2 TEM investigation.

The diffraction patterns from both specimens are shown in figure 7.6. From the spacing of the rings the crystalline structure is found to be FCC with a lattice constant of 4.10±0.02A, as discussed in section 7.1. This value is associated with the lattice constant of Ag, which

makes up the majority of the sample and is the greater electron scatterer. The as-deposited film (D1) shows quite diffuse diffraction rings whereas in the annealed film (H1) the rings are better defined, consistent with improved long range order. Texturing is present in both samples and can be seen from the non-uniform intensity distribution around individual rings when the samples are tilted. This is marked in the {200} and {220} rings.

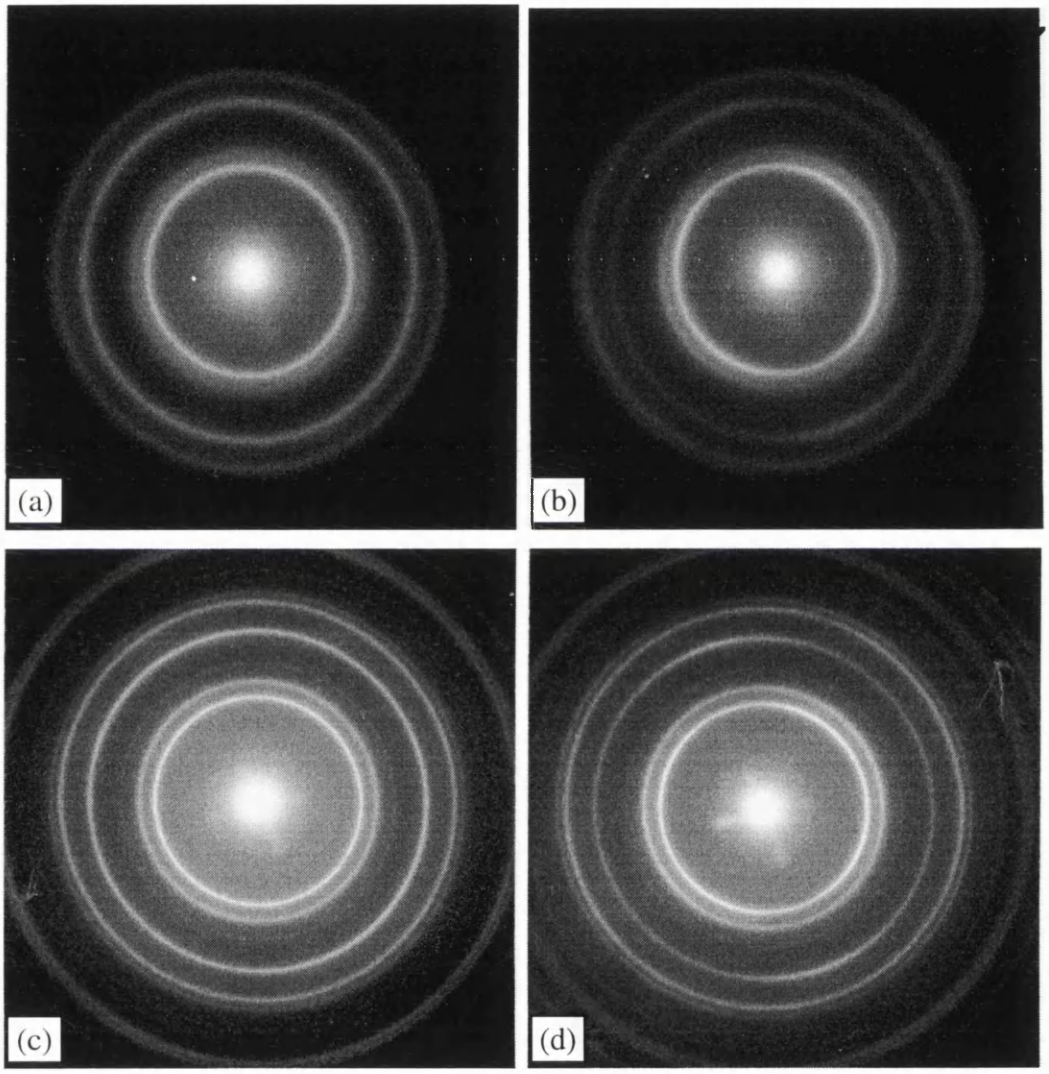

Figure 7.6 *Electron diffraction patterns of sample D1 (as-deposited) at a tilt of (a) 0° and (b) 30°, and sample H1 (annealed at 450°C for 10 minutes) at a tilt of (c) 0° and (d) 30°.*

The bright field images (figure 7.7) show crystallites with a wide distribution of sizes, predominantly in the range 5-20nm. The crystallites in H1 have more clearly defined grain boundaries, consistent with the annealing treatment to which that film has been subjected. These features are more easily revealed in figures 7.6b and d where the image contrast is drastically expanded.

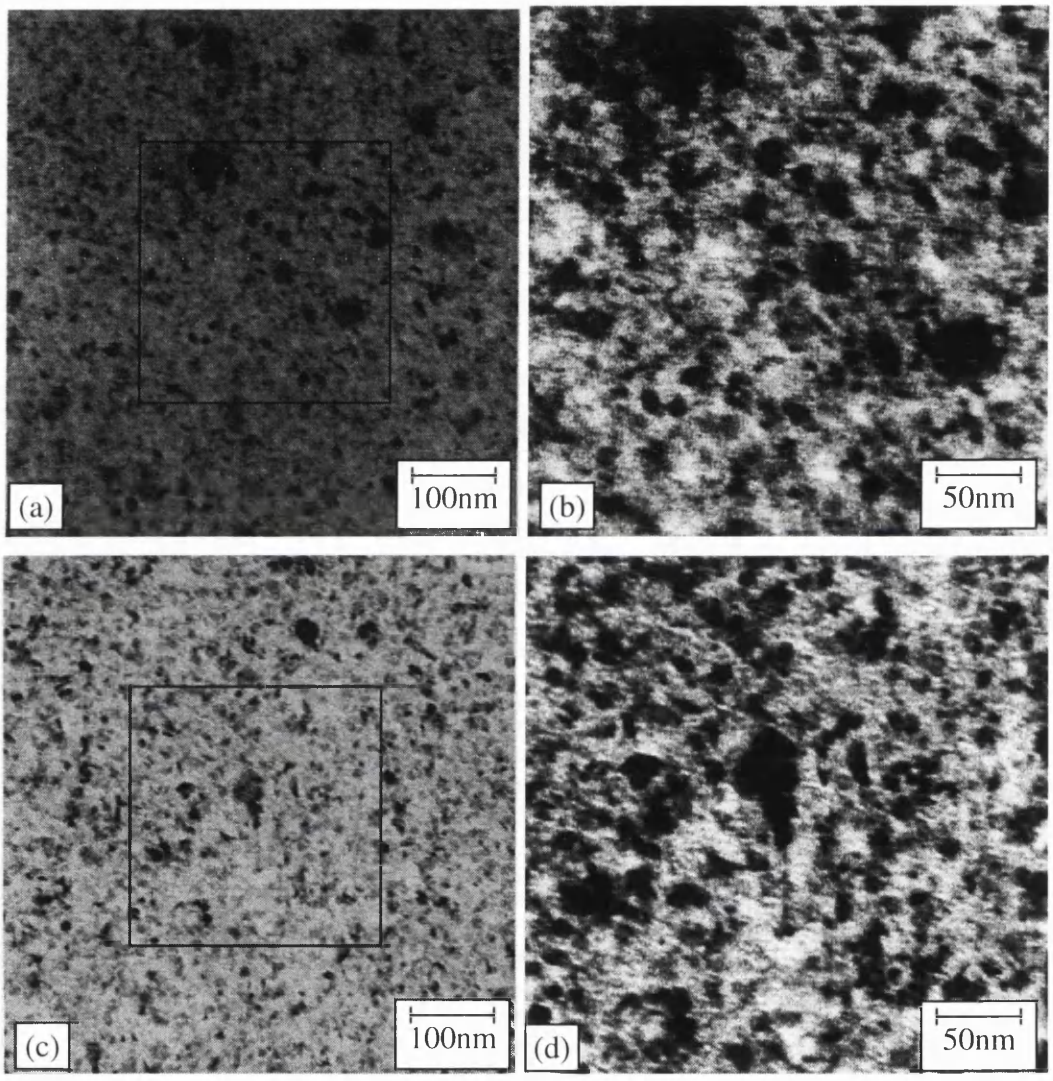

Figure 7.7 *Bright field TEM images for (a) sample D1 (as-deposited) and (b) sample H1 (annealed at 450°C for 10 minutes). (b) and (d) show images of the boxed regions at a higher magnification with an expanded contrast.*

7.3.3 STEM investigation.

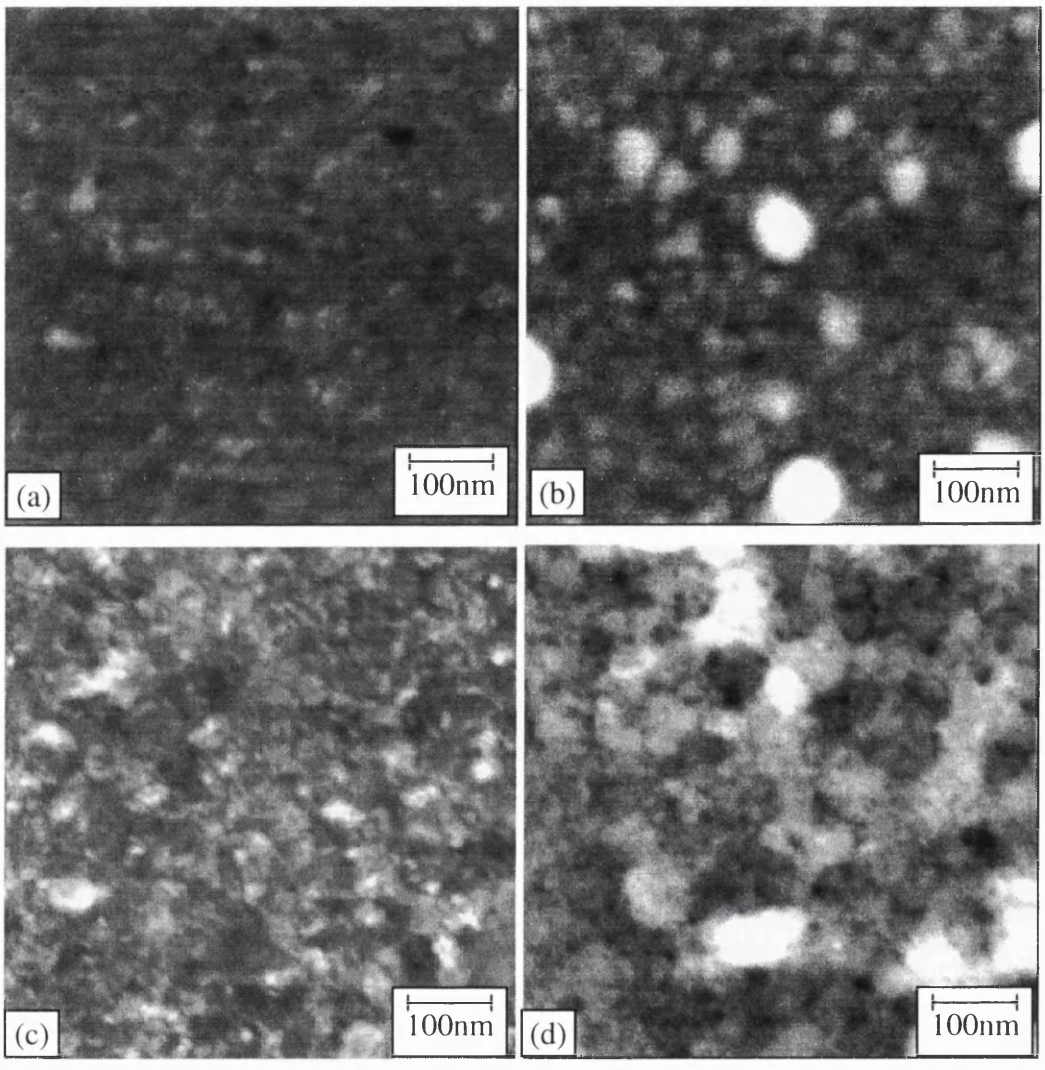

Figure 7.8 *Specimen D1 is in the as-deposited state and specimen H1 has also been annealed at 450°C for 10 minutes. The ADF image (a) and (c) and the HADF image (b) and (d) of specimen D1 and H1 respectively.*

Figure 7.8 shows ADF and HADF images of the specimen. These images are formed using electrons which have been scattered away from the direction of the incident beam, the difference between them being that HADF images are formed using only those electrons which are scattered through relatively large angles (60-200mrad). The ADF images show predominately the crystallite structure and, as such, can be thought of as being complementary to the bright field images of figure 7.7. However, in the HADF images, crystallographic contrast is substantially suppressed and the contrast observed is strongly related to the local atomic number as discussed in section 7.2.2. Hence, for the systems

under investigation here light regions are expected to be Ag rich and the darker regions richer in NiFe.

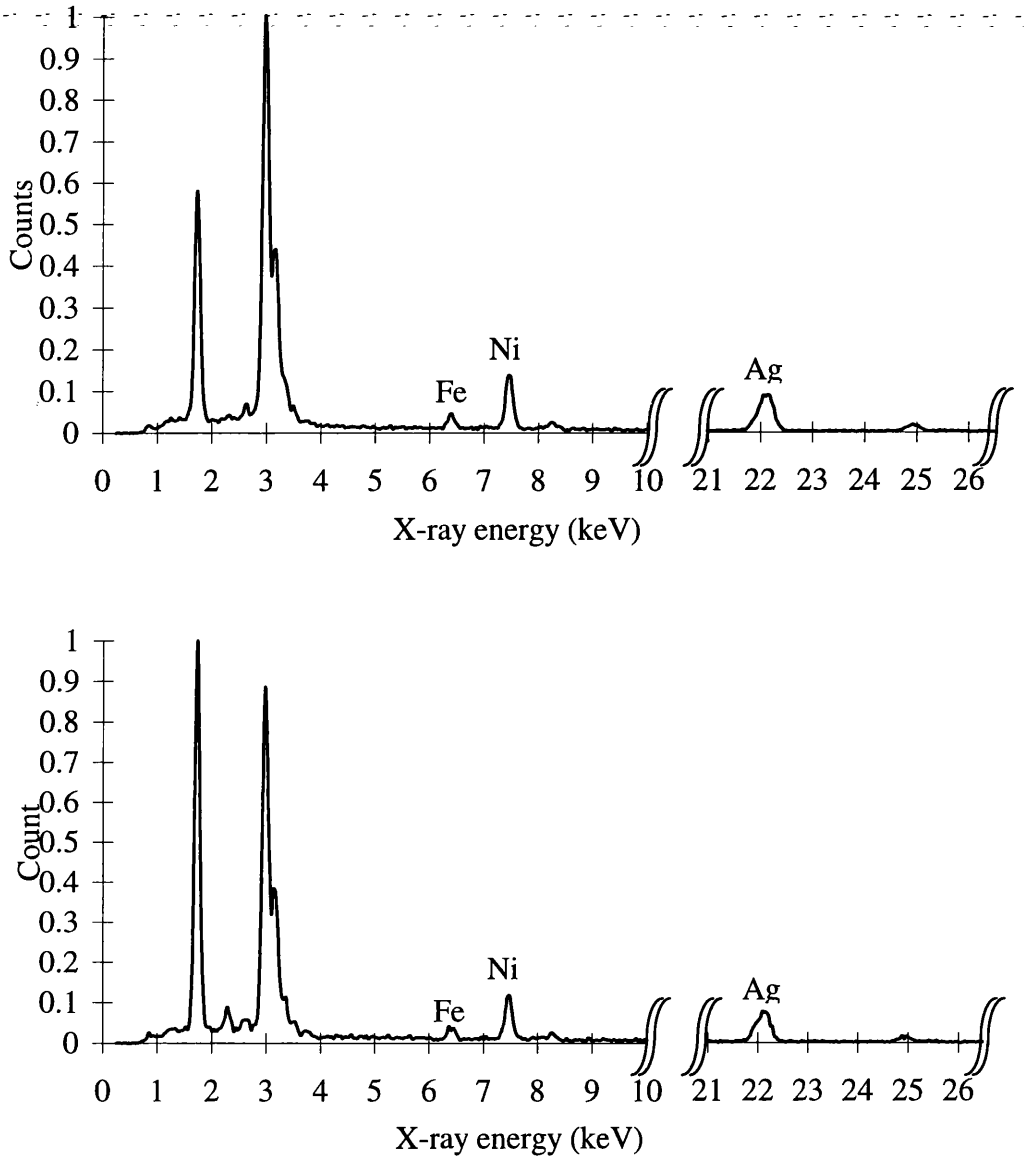

Figure 7.9 *Normalised x-ray spectra of the matrix region from the (a) as-deposited sample (D1) and (b) the sample annealed at 450°C for 10 minutes (H1).*

EDX microanalysis is used to obtain further information on the elemental distribution throughout the specimen. Analysis of the EDX spectra (figure 7.9) gives the compositional information in tables 7.2a and b. X-rays are detected whilst an electron probe of diameter 1.5nm is rastered over areas of $\approx 10 \times 10 nm^2$. In each case the probe is centred about a region that appears light or dark in the HADF image for 20 seconds. After completion of

this procedure, a spectrum was recorded with the probe rastering over an area of $0.5x0.5\mu m^2$ to determine the average film composition. Typical x-ray spectra from the matrix regions in both specimen are shown in figure 7.9.

As previously discussed, the analyses themselves are based on the counts in the K_α peaks of the elements of interest. Errors reflect the counting statistics and the count in the Fe K_α peak (the smallest of the three of interest) is typically 600 with an associated Poisson error of ±25. The results in tables 7.2a and b show that there is significant local compositional inhomogeneity in both samples as indicated by the HADF images and that the brighter regions are indeed rich in Ag. However, the effect of annealing is once again apparent there being a much wider spread in composition in H1 than in D1. A full analysis of the EDX spectra is given in Appendix D.

Specimen D1	Ag	Fe	Ni
Light	87.6±1.4	2.8±0.4	9.6±1.2
Dark	78.9±1.7	4.7±0.2	16.4±1.5
Matrix	81.7±0.4	4.1±0.2	14.2±0.5

Table 7.2a *Specimen D1 (as-deposited) compositional data.*

Specimen H1	Ag	Fe	Ni
Light	91.0±0.9	2.7±0.3	6.3±1.0
Dark	66.6±13.5	5.7±1.3	27.8±13.2
Matrix	82.2±1.8	3.8±0.7	14.0±1.2

Table 7.2b *Specimen H1 (annealed) compositional data.*

7.4 NiFe-Ag granular thin films (2).

The second set of NiFe-Ag thin films consists of four specimens of identical atomic compositions which have been annealed at different temperatures. These specimens were prepared in a similar fashion to the first set, but in this case the substrate material was in the form of nickel grids which were coated in carbon. The specimens are of the atomic compositions of Ag 78.7%, Fe 4.4% and Ni 16.9%. These values are considered to be approximate due to the inclusion of the signal from the nickel grids which cannot be removed. The specimens can be categorised in terms of their annealing temperatures and the heating times (Table 7.3). These values were chosen to give nominally identical characteristic heating and cooling curves thus allowing the effects of the magnitude and duration of the thermal pulse to be studied. The films have been investigated by bright field TEM imaging and diffraction pattern analysis on the Philips CM20. EDX analysis is not considered due to the problem arising from the nickel grids as discussed above.

Specimen	Annealing temperature (°C)	Pulse duration (s)
As-deposited	-	-
C1	200	80
D1	750	1
E1	400	20

Table 7.3 *Categorisation of NiFe-Ag thin films (2).*

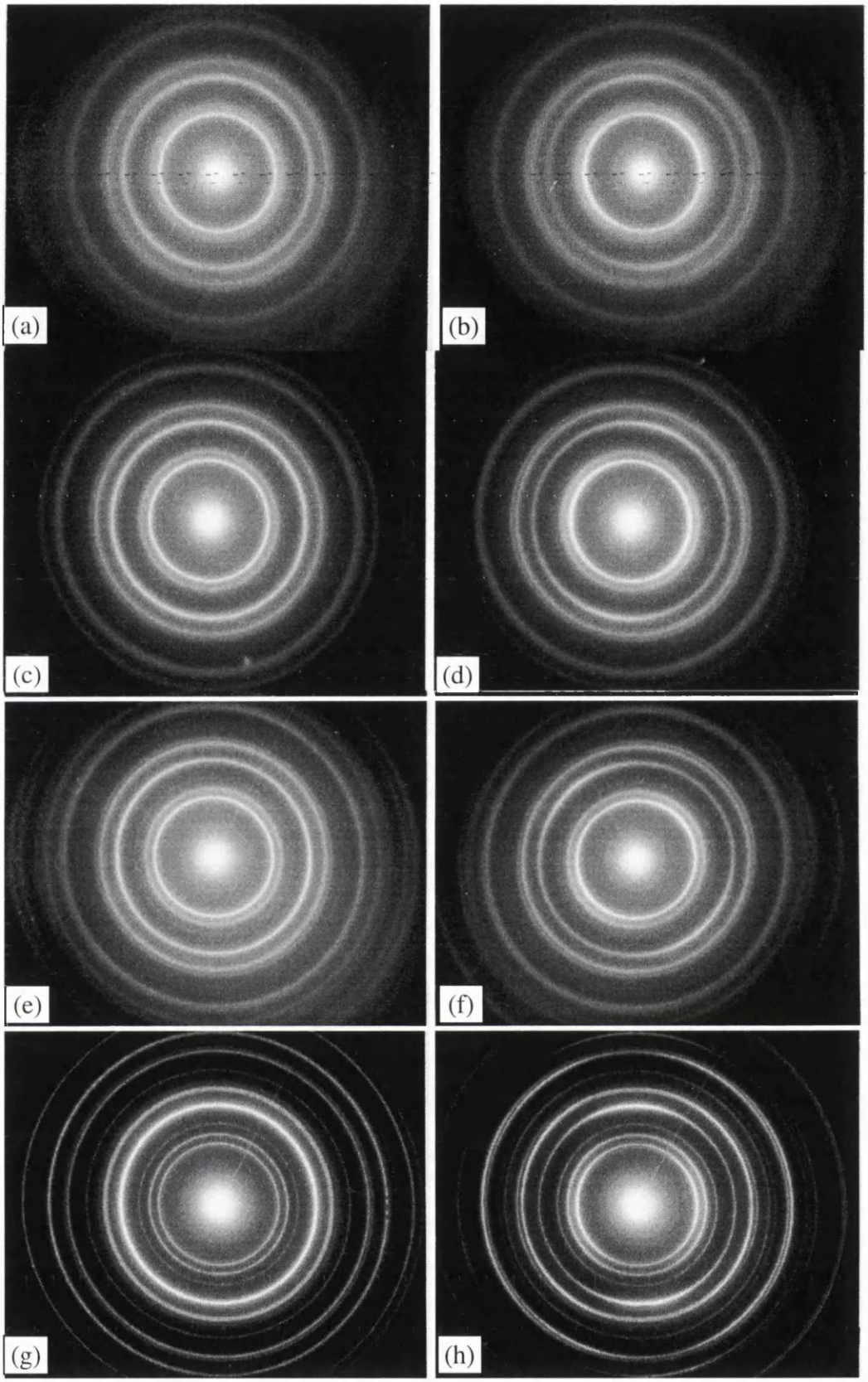

Figure 7.10 *Diffraction patterns of the as-deposited sample at a tilt of (a) 0° and (b) 30°, sample C1 at a tilt of (c) 0° and (d) 30°, sample E1 at a tilt of (e) 0° and (f) 30°, and sample D1 at a tilt of (g) 0° and (h) 30°.*

7.4.1 TEM investigation.

The diffraction patterns from the second set of specimen are shown in figure 7.10. From the spacing of the rings the crystalline structure is found to be FCC with a lattice constant of 4.09±0.01A. Yet again, this value is associated with the lattice constant of Ag which makes up the majority of the sample. The as-deposited film shows diffuse diffraction rings which sharpen up, as expected, as the post-annealing temperature increases. Texturing is present in all four samples and can be seen from the non-uniform intensity distribution around individual rings when the samples are tilted. In figures 7.10e and f there is a very diffuse diffraction ring lying between the {200} and {220} Ag rings. The diffraction patterns from the sample D1 (figures 7.10g and h) shows this ring more pronounced as well as revealing additional rings. Figure 7.11 shows the analysis of the diffraction patterns from specimen D1, as discussed in section 7.1. There are two lines present in this graph, one from the Ag matrix and the other from the NiFe ferromagnetic particles. This confirms the segregation of the NiFe and Ag within the sample at higher post-annealing temperatures. From the gradient of these lines, the lattice parameters are evaluated to be 4.09±0.01Å and 3.52±0.03Å for the Ag and NiFe respectively. These compare well with the normal lattice parameters of 4.09Å and 3.54Å respectively.

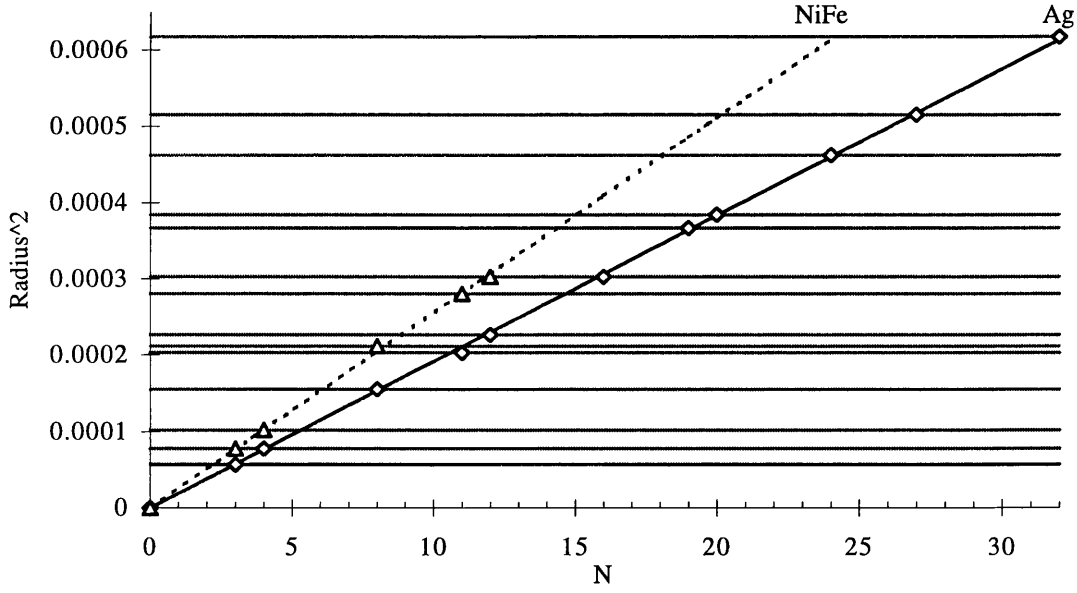

Figure 7.11 *Indexing the diffraction pattern from specimen D1.*

Figure 7.12 shows the indexed diffraction pattern from specimen D1. The individual rings are identified as coming from the Ag matrix or from the NiFe ferromagnetic particles.

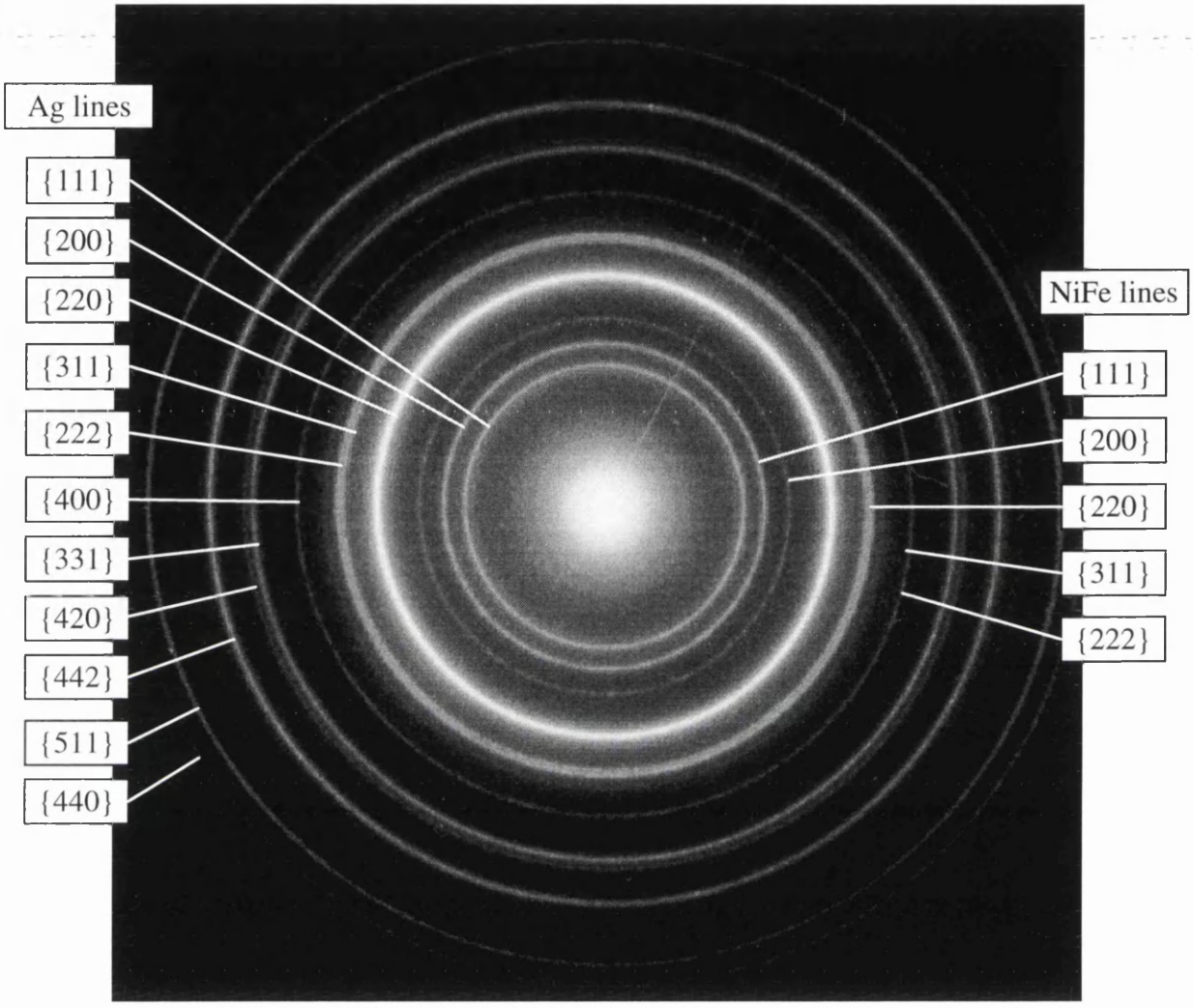

Figure 7.12 *Indexing the diffraction pattern from specimen D1.*

The bright field images (figure 7.12) show crystallites with a wide distribution of sizes. In the as-deposited sample the crystallites are predominantly in the range 5-20nm. This is also the case in samples C1 and E1 which have more clearly defined grain boundaries, consistent with the annealing treatment to which those films have been subjected. However, in specimen D1 crystallites are observed in the range 20-40nm and fringes occur within individual crystallites indicating the presence defects such as crystal stacking faults or twinning.

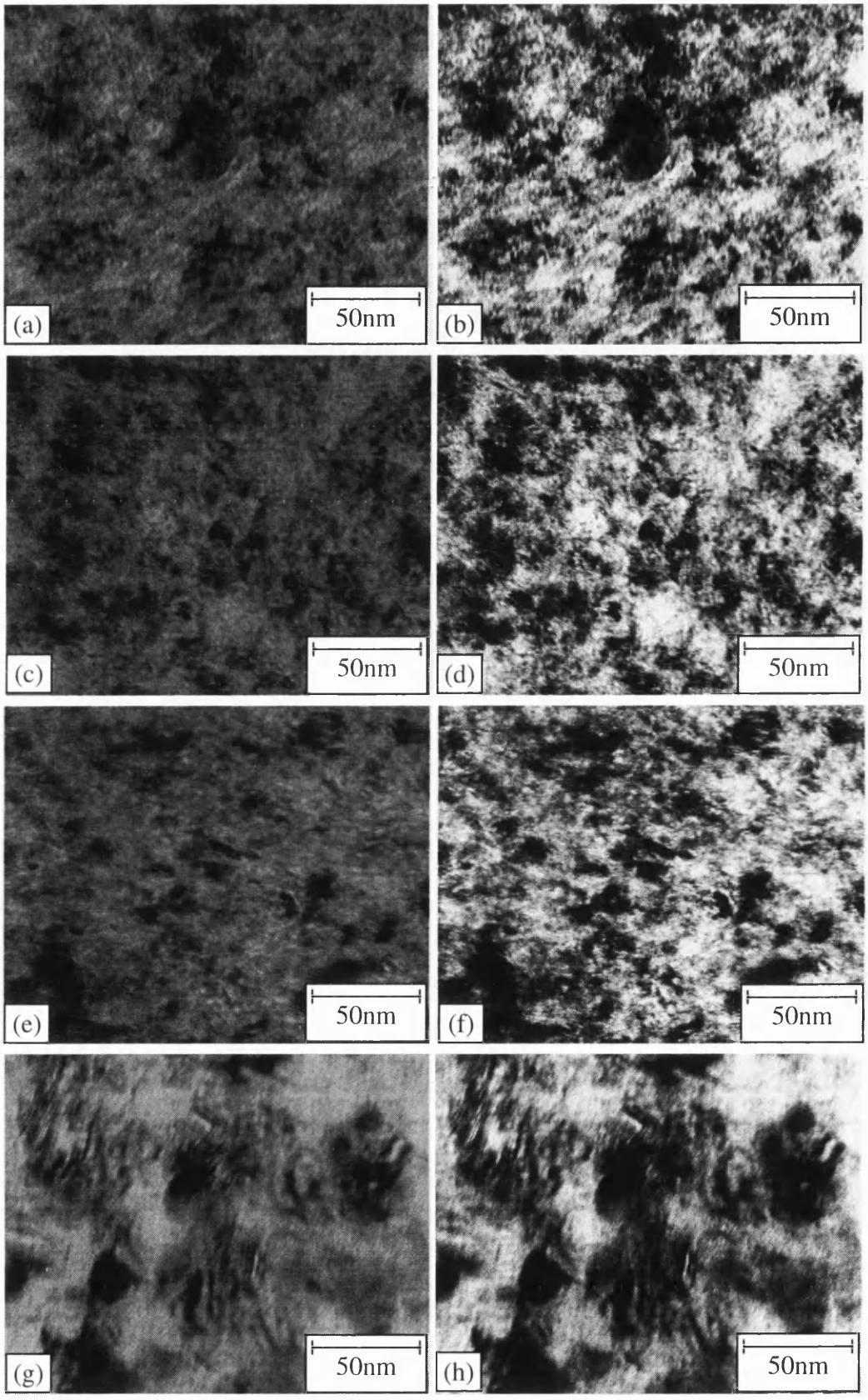

Figure 7.12 *Bright field images of (a) the as-deposited sample, (c) sample C1, (e) sample E1 and (g) sample D1. (b), (d), (f) and (h) show the respective bright field images where the contrast is expanded.*

7.5 Conclusion

In this chapter we have discussed the TEM techniques which can be used to investigate granular thin films. STEM has been introduced, emphasising the HADF imaging mode and the implementation of EDX microanalysis. The latter technique is further discussed to give a description of the analysis required to obtain information on the local atomic compositions.

Two sets of NiFe-Ag thin films prepared by r.f. sputtering have been investigated. Phase segregation was promoted by rapidly thermally annealing the films once deposited. The first set of samples were of similar compositions, one which was in the as-deposited state and the other annealed at 450°C for 10 minutes. The diffraction patterns showed <111> texturing of the samples. Bright field images confirmed a wide distribution of crystallite sizes, from 5-20nm, with the annealed film displaying greater contrast and more distinctly defined phase boundaries. High angle annular dark field images showed both lighter Ag-rich and darker NiFe-rich regions, which were analysed by EDX in order to obtain atomic composition. The second set of samples where of identical compositions but subjected to various annealing conditions. Diffraction analysis showed the phase segregation of the ferromagnetic materials from the Ag matrix on annealing and identified the formation of NiFe rings in the samples which had been subjected to greater post-annealing temperatures. Bright field images revealed the crystallite sizes, typically 5-20nm, and the enhanced order present in the specimen D1.

References

[1] M.N. Baibich et. al., Phys. Rev. Lett. **61**, 2472 (1988).

[2] G. Binasch et al., Phys. Rev. **B39**, 4828 (1989).

[3] R.E. Camley and J. Barnas, Phys. Rev. Lett. **63**, 664 (1989).

[4] B. Dieny, Europhys. Lett. **17**, 261 (1992).

[5] A.E. Berkowitz, J.R. Mitchell, M.J. Carey, A.P. Young, S. Zhang, F.E. Spada, F.T.

Parker, H. Hutton and G. Thomas, Phys. Rev. Lett. **68**, 3745 (1992).

[6] J.A. Bernard, A. Waknis, M. Tan, E. Haftek, M.R. Parker and M.L. Watson, J. Magn. Magn. Mat. **144**, L230 (1992)

[7] M.J. Carey, A.P. Young, A. Starr, D. Roa and A.E. Berkowitz, Appl. Phys. Lett. **61**, 2935 (1992).

[8] A. Tsoukatos, H. Wan, G.C. Hadjipanayis, K.M. Unruh and Z.G. Li, J. Appl. Phys. **73**, 5509 (1993).

[9] M.L. Watson, J.A. Barnard, S. Hossain and M.R. Parker, J. Appl. Phys. **73**, 5506 (1993).

[10] M. Kitada, K. Yamamoto, D. Seale and G. Yang, IEEE Trans. Mag. **MAG-29**, 2711 (1993).

[11] B. Dieny et. al., J. Magn. Magn. Mat. **130**, 197 (1994).

[12] K.Pettit, E. Kita, K. Araga, A. Tasaki and M.B. Salamon, to be published in J. Appl. Phys. (1994).

[13] S. Zhang and P.M. Levy, J. Appl. Phys. **73**, 5315 (1993).

[14] J.W. Edington, "Electron Diffraction in the Electron Microscope", pubs. MacMillan (1973)

[15] Hirsch, Howie, Nicholson, Pashley and Whelan, "Electron microscopy of thin Crystals", pubs. Butterworths (1965).

[16] A.V. Crewe, "Electron microscopy and Material Science", ed. U. Valdre (1971).

[17] G.R. Morrison, PhD. Thesis, University of Glasgow (1981).

[18] T.A. Hall and B.L. Gupta, "An introduction to Analytical Electron microscopy", eds. J.J. Hren, J.C. Goldstein and J.C. Joy, Plenum (1979).

[19] G.W. Lorimer, "Quantitative Electron Microscopy", eds. J.N. Chapman and A.J. Craven, SUSSP **No.25** (1993).

[20] S.J. Pennycook, S.D. Berger and R.J. Culbertson, J. Microscopy, **Vol. 144**, Pt 3, 229 (1986)

[21] A.J. McGibbon, PhD. Thesis, University of Glasgow (1989).

[22] J.N. Chapman, W.A.P. Nicholson and P.A. Crozier, J. Microscopy, **Vol. 136**, Pt 2, 179 (1984).

[23] J.H. Paterson, J.N. Chapman, W.A.P. Nicholson and J.M. Titchmarsh, J. of Microscopy, **Vol. 154**, Pt 1, 1 (1989).

[24] G. Cliff and G.W. Lorimer, Proc. 5th European Congress on Electron Microscopy, Bristol (1972).

[25] C. Gray, Ph.D. Thesis, University of Glasgow (1983).

Chapter 8

Conclusions, incomplete and future work.

8.0 Introduction.

In this thesis we have discussed novel transmission electron microscopy (TEM) techniques to investigate magnetic microstructure. In doing so we have taken advantage of the high spatial resolution magnetic imaging as implemented on the Philips CM20 TEM. The main body of our work was concerned with the development of coherent Foucault (CF) imaging. This was achieved analytically, by computer simulations and experimentally. Two further chapters were dedicated to the magnetic imaging of Fe_3O_4 thin films, and to a structural and compositional analysis of NiFe-Ag thin films. In this final chapter, we conclude our discussions and recommend possible ideas and experiments in the future developments of the CF imaging mode and the various materials referred to above.

8.1 Coherent Foucault imaging.

In chapter 3 we discussed the image formation process of CF imaging and analysed two simple magnetic systems. The analytical investigation showed that when an opaque aperture was positioned, in the central region of the diffraction pattern, fringes form in the image. These fringes run parallel to the direction of the local magnetic induction and so reveal the magnetic microstructure. The fringes have a periodicity of $h/eB_{\perp}t$. Therefore, by measuring the fringe spacing we can quantify the value $B_{\perp}t$. CF images obtained when

using an opaque aperture lose some of the magnetic information due to the electrons being deflected into the aperture. This problem could be resolved by taking another CF image when the aperture was in the complementary position. An attractive option was to replace the opaque aperture with a phase-shifting aperture. In this case, only a single image was required to reveal the magnetic microstructure because the fringes form in all domains simultaneously.

In chapter 4 we have simulated the CF image formation process by computer. One-dimensional computer simulation has been used to confirm the basic analytical theory of CF imaging. We investigated the positioning of semi-infinite opaque and phase-shifting apertures and these results suggested that the aperture stability required was well within experimental sensitivity. The small-hole phase-shifting aperture was introduced to show CF images containing minimal artefacts can be generated. We established the optimum phase-shift to be π radians but note that deviations from this value were not critical to the CF imaging conditions. We have also revealed a significant deterioration in the CF image visibility as the angle subtended by the source was increased. This re-enforces the requirement for the TEM to be fitted with a field emission gun (FEG) source. Two-dimensional CF imaging has allowed more complex objects to be studied. Here, a two domain element and an element containing four domains in a solenoidal structure have been analysed.

In chapter 5 the experimental considerations of CF imaging were discussed. This included sections on the preparation techniques employed to obtain the different aperture types and the "lift-off" process that was used to fabricate the small permalloy elements. Initially, we looked at a simple micromagnetic structure using the CF imaging technique when using the different aperture types. These images were then compared, successfully, to the CF images from the two-dimensional computer simulation. In the latter sections of chapter 5 we carried out a range of experiments which give an insight into the magnetic microstructure supported by differently shaped elements. We have seen how CF imaging gives a clear description of the magnetisation distribution and can lead to quantification of the local magnetic induction distribution within the elements; furthermore it can be used qualitatively to show the presence of stray (demagnetising) fields surrounding the elements. CF imaging has proved to be a stable and versatile imaging mode which has

allowed a range of in-situ experiments to be carried out. Small elements have been imaged whilst magnetising them along their easy and hard axes, and when heated in-situ to show how the magnetic microstructure changed as we approached the Curie temperature. The latter experiment also gave an indication of how the magnetic induction of the permalloy was reduced as the temperature was increased. Finally, we examined two sets of magnetic elements, one of which was prepared using the lift-off route and the other by a reactive ion etching process. This method of element fabrication allows for small elements to be prepared from existing continuous thin films and from materials which are not usually compatible with the lift off route. Such films were successfully prepared with magnetic properties comparable to those produced by the lift-off route.

The present state of CF imaging leads us to believe that it is a valuable new member to the Lorentz microscopy family. CF imaging complements the existing modes of Fresnel and Foucault imaging which are usually employed to qualitatively reveal domain walls and the orientation of the magnetic induction respectively. The main advantage of these imaging modes is that they are easily implemented to allow for a rapid survey of the material in question. Holography can provide quantitative information on the amplitude and phase of the sample. However, implementation requires specialist equipment and extensive analysis to re-create the phase object. CF imaging can provide a quantitative description of the magnetic induction in real time. The simplicity of its implementation and versatility to image in-situ experiments makes CF imaging an attractive option for future experiments.

We believe there to be little future in the application of CF imaging to continuous thin films. Like holography, a reference beam passing through free space is required to observe the interference effects. Fresnel and Foucault are readily implemented to image these types of samples. However, developments in the magnetic recording industry are leading to an increasing interest in small devices typically on a micron and sub-micron scale. This should shift the emphasis from continuous thin films towards the type of elements studied in this thesis. This will secure the position of CF imaging in future research and development as a Lorentz microscopy technique to image magnetic microstructure in small devices. Such devices also show the need for novel etching techniques to provide element samples from continuous thin films, such as the reactive ion

etching process discussed in chapter 5. An example of future work would be to use CF imaging to investigate small elements which have been successfully prepared from a continuous film possessing the spin-valve structure[1].

There are, however certain drawbacks to the CF imaging technique. Above, we have discussed the inability of CF imaging to image continuous films. Also, if the sample is relatively thin (<20nm) and/or the magnetic material has a low magnetic induction, the product $B_{\perp}t$ is too small to reveal a complete fringe system within the elements. Holography may be more appropriate in this case because it can have a phase resolution of up to $\pi/100$.

Until now we have applied CF imaging to magnetic samples, but this technique can be used to image phase objects in general. In section 2.3 we discussed the interaction between the electron and the electrostatic potential present in a sample with a constant thickness gradient. In the following sections we will discuss the feasibility and application of CF imaging to samples in which the electrostatic term is dominant in the phase function. We then use CF imaging to investigate special magnetic force microscopy (MFM) tips in which we combine an electrostatic and a magnetic component in the specimen's phase function. These sections are initial investigations in which substantial progress has been made but are nevertheless incomplete.

8.2 Application of CF imaging to electrostatic objects

In the following sections we will discuss the potential of applying CF imaging to investigate electrostatic objects. This is achieved by initially considering a basic model analytically and then expanding upon this to use the two-dimensional computer simulation. Finally we discuss the possible systems in which such a technique would provide valuable information.

8.2.1 Analytical considerations.

As a simple model consider a semi-infinite electrostatic wedge (figure 8.1), with one edge positioned at $x=0$.

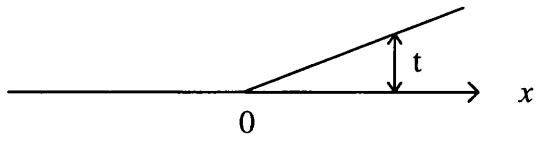

Figure 8.1 *Basic analytical electrostatic model.*

This model can be described by,

$$\Psi(x) = e^{i\phi(x)}h(x) + (1 - h(x)) \qquad [8.1]$$

where $\phi(x)$ is the phase function of the specimen. This is of the same form as in the semi-infinite uniformly magnetised thin film (section 3.1) but, in this case, we replace the magnetic phase function with the electrostatic phase function. We recall that for a specimen with a uniform inner potential (V_0) and a constant thickness gradient (α) the phase function is given by equation 2.15 to be,

$$\phi(x) = \frac{\pi V_0 \alpha x}{\lambda E} = \beta x \qquad [8.2]$$

where α is the thickness gradient of the specimen in the x-axis.

We should note that by replacing γ with β in section 3.2 (equations 3.6-3.13) we can follow through the imaging process in an identical manor to the magnetic case. This reveals that the region occupied by the electrostatic specimen consists of a set of interference fringes, running parallel to the thickness gradient, with a periodicity of $2\lambda E/V_0\alpha$. Therefore, the CF image can be thought of as a contour plot of the specimen thickness and by measuring the fringe periodicity we have a measure of $V_0\alpha$.

8.2.2 Two-dimensional computer simulations.

To illustrate the use of the program and for comparison with the one-dimensional computer simulation a simple model is first considered (figure 8.2a). It represents a small electrostatic element of width 1μm and of infinite length, situated in a window of $2\mu m^2$. The object is considered to have an inner potential of 10V and a thickness gradient of 0.8, and is imaged by 200keV electrons with a corresponding wavelength of 2.51pm. The diffraction pattern (figure 8.2b) comprises a central spot surrounded by two spots representing the thickness gradient, broadened by the object shape function, located at a distance of 16 pixels from the centre.

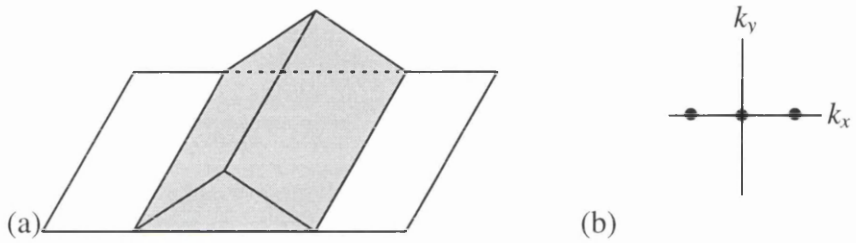

Figure 8.2 *(a) Schematic of the electrostatic element and (b) the corresponding diffraction pattern.*

Figure 8.3a shows a phase contour plot corresponding to the object of figure 8.2a. In that the phase function relates directly to the thickness gradient in the specimen, we may regard this as the idealisation of a CF image. For comparison, figure 8.3b-d show calculated CF images using various apertures each optimally positioned so that an edge cuts the middle of the central diffraction spot. In figure 8.3b an opaque aperture is assumed so that fringes are seen only on the right side, there being no information available about the thickness gradient on the left side. For figure 8.3c and d phase-shifting apertures introducing shifts of π radian are used and fringes can be seen on both sides simultaneously. However, when a semi-infinite aperture is used (figure 8.3c) a discontinuity occurs in the fringe system at the maximum thickness. This is again avoided by the use of a small-hole phase-shifting aperture and figure 8.3d approximates very closely to the ideal image, there being no artefacts present to render its interpretation difficult.

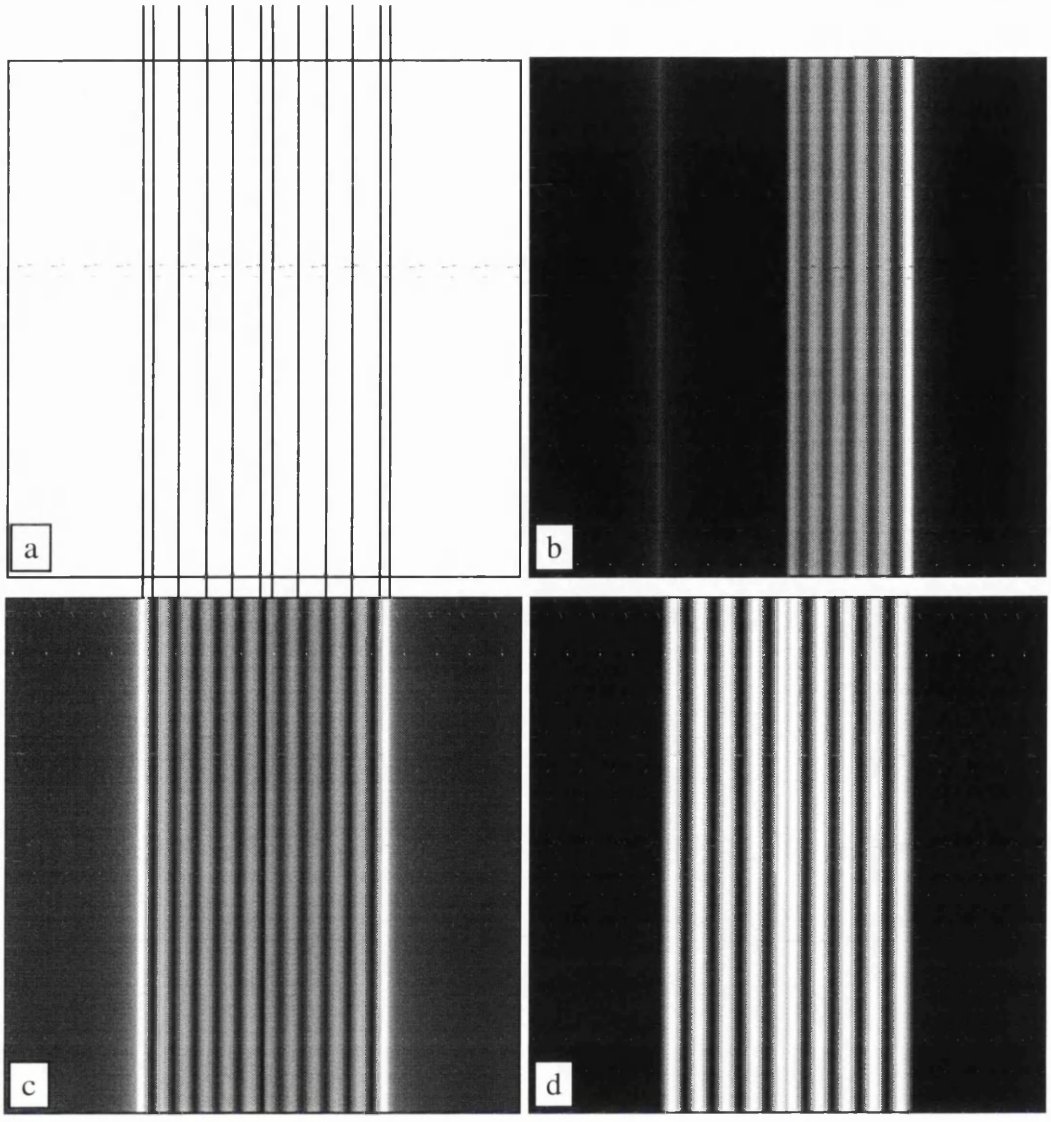

Figure 8.3 *(a) shows a phase contour plot of the electrostatic element. CF images using (b) a semi-infinite opaque aperture, (c) a semi-infinite phase-shifting aperture and (d) a small-hole phase-shifting aperture both introducing a phase-shift of* π.

8.2.3 Experimental considerations.

The above CF images represent contour maps of thickness variations and, by measuring the fringe periodicity, the product of inner potential (V_0) and thickness gradient (α). In previous TEM studies a planer projection view of many features are revealed, however it would be of great interest to image these structures in three-dimensions. One such system is in V_2O_5 which has been mechanochemically reduced with Mg or Al [2]. The Mg/V_2O_5 reaction results in the formation of spherical and isometric smoke particles of Mg, while in the Al/V_2O_5 reaction spherical and filamentous particles of γ-Al_2O_3 are formed[3].

8.3 Applications of CF imaging to magnetic force microscopy tips.

Several different magnetic materials have been investigated by means of magnetic force microscopy (MFM) [4, 5]. MFM tips frequently take the form of etched Si tips on cantilevers 225μm in length, sputter coated with Co-Cr films[6]. Tracking the shift in cantilever resonant frequency caused by external stray fields, from a sample, can be used to reveal domain walls.

In this initial study we apply CF imaging to investigate MFM tips which have been fabricated from electron beam deposited carbon needles coated with an appropriate thin film of magnetic material[7] (figure 8.4). In combining the advantages of electron beam fabricated needles with those of already widely used thin film tips, high resolution MFM tips can be prepared on all type of cantilevers. Due to the fabrication procedure[7] the magnetic tip is in the form of a homogeneous, magnetically isolated, high aspect ratio thin film element hopefully favouring single domain behaviour. To reinforce the inherent shape anisotropy an additional uniaxial anisotropy is induced along the tip axis by applying an external field during the deposition of the ferromagnetic alloy. Because of the parallel side walls and the rounded tip end, most of the stray field will emanate from the apex region. We investigate this system analytically, using the two-dimensional computer simulation and, finally, compare these results with initial experimental data.

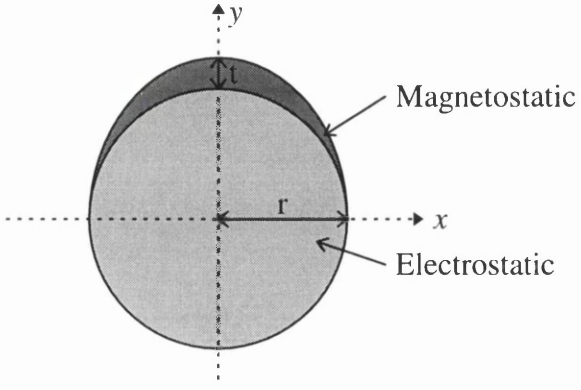

Figure 8.4 *Schematic of the MFM tip.*

8.3.1 Analytical considerations.

Consider an electrostatic spike of radius r coated with a magnetic thin film of thickness $t(x)_{mag}$. The thin film has been deposited by thermal evaporation normal to the plane of the specimens. This implies that the deposition rate is dependant on the angle between the incident ferromagnetic atoms and the round tip surface. An initial assumption is that the imaging electrons effectively pass through a ferromagnetic coating is of a uniform thickness t_{mag}. The thickness of the electrostatic spike is defined to be $t(x)_{estatic}$. To setup the model we must first introduce the top-hat function $S(x)$ (figure 8.5); defined as unity for $-r \leq x \leq r$ and zero elsewhere.

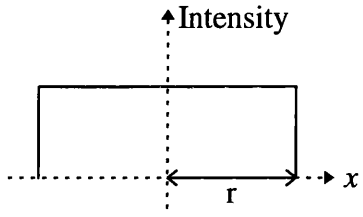

Figure 8.5 *Definition of the function S(x).*

The model used to represent the MFM tip is,

$$\Psi(x) = e^{i\phi(x)} S(x) + [1 - S(x)] \qquad [8.3]$$

where the phase function is given by,

$$\phi(x) = \frac{2\pi V_0 t(x)_{\text{estatic}}}{\lambda E} + \frac{eB_0 t_{mag} x}{\hbar} = \varepsilon\sqrt{r^2 - x^2} + \chi x \qquad [8.4]$$

where ε and χ are defined as,

$$\varepsilon = \frac{2\pi V_0}{\lambda E} \qquad [8.5a] \qquad \chi = \frac{eB_0 t_{mag}}{\hbar\lambda} \qquad [8.5b]$$

Taking the Fourier transform (Appendix B) of the model gives the disturbance in the back focal plane (BFP),

$$\overline{\Psi}(k) = \Im\left[e^{i\phi(x)}S(x)\right] + \sqrt{2\pi}\delta(k) - \sqrt{\frac{2}{\pi}}r\mathrm{sinc}(kr) \qquad [8.6]$$

This expression contains a Fourier transform which cannot be evaluated analytically. Therefore, to further this investigation we must use computer simulation.

8.3.2 Two-dimensional computer simulations.

The object in this case is two MFM tips of radii 50nm situated in a window 0.5μm in extent (figure 8.6). The electrostatic spike is made from evaporated carbon which has an inner potential of 7.8V [8]. The magnetic layer is considered to be 20nm thick Co-Cr which has a magnetic induction of 1.4T. The magnetisation in these thin films points in opposite directions to ensure that the phase function is continuous in the FFT. The electrostatic phase function (figure 8.7a) can be added to the magnetic phase function (figure 8.7b) to give the total phase function of this system (figure 8.7c).

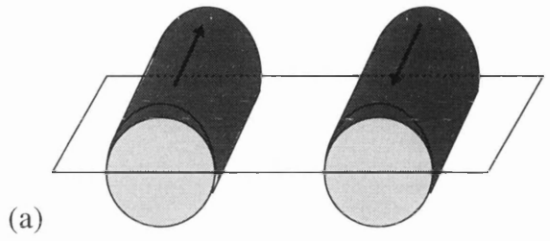

Figure 8.6 *(a) Schematic of the two domain element.*

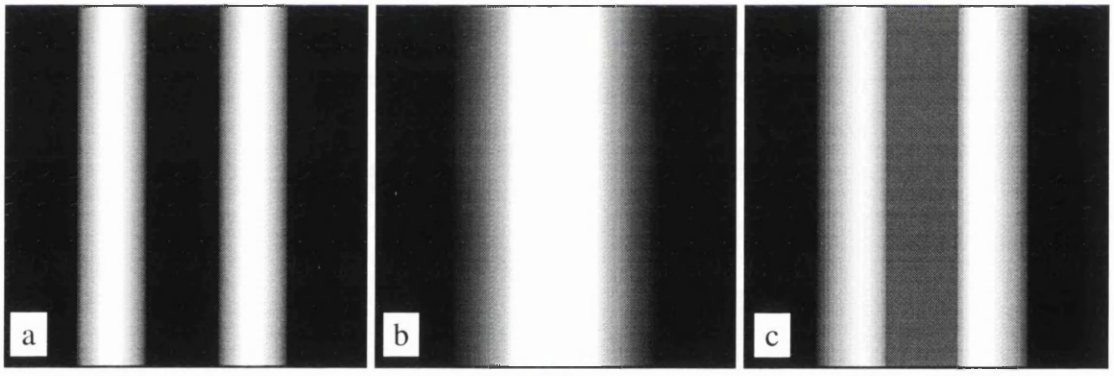

Figure 8.7 *Phase functions of the (a) electrostatic spike, (b) magnetic strips and (c) MFM tip.*

The diffraction pattern (figure 8.8) is particularly complex.

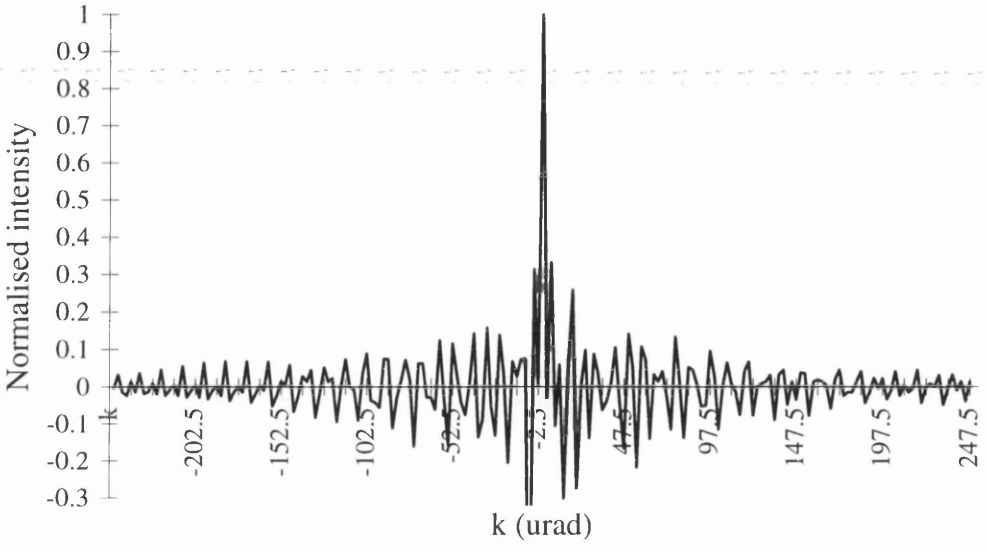

Figure 8.8 *Linescan of the computer simulated diffraction pattern.*

We then position the various apertures so that an edge cuts the middle of the central diffraction spike. Figures 8.9-8.11 show the resulting images with (a) and (b) showing the CF images of the electrostatic and magnetic contributions to the phase function, (c) shows the CF images from the MFM tip. In figure 8.9 an opaque aperture is assumed so that fringes are seen only on the left side of the electrostatic spikes (negative thickness gradient) and magnetic fringes are present on the right domain only, there being no information available about the thickness gradient on the left side (positive thickness gradient) or the magnetic information in the left domain. For figures 8.10-11, phase-shifting apertures introducing shifts of π radian are used and fringes can be seen throughout the CF images. However, when a semi-infinite aperture is used (figure 8.10) a discontinuity occurs in the fringe system at the maximum thickness. This is again avoided by the use of a small-hole phase-shifting aperture and figure 8.11 approximates very closely to the ideal image, there being no artefacts present to render its interpretation difficult.

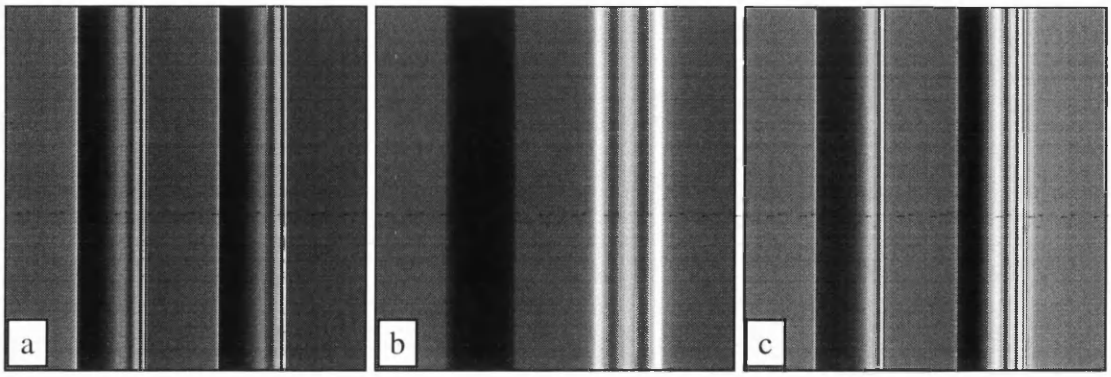

Figure 8.9 *CF images showing (a) the electrostatic component (b) the magnetic component and (c) the MFM tip when using the semi-infinite opaque aperture.*

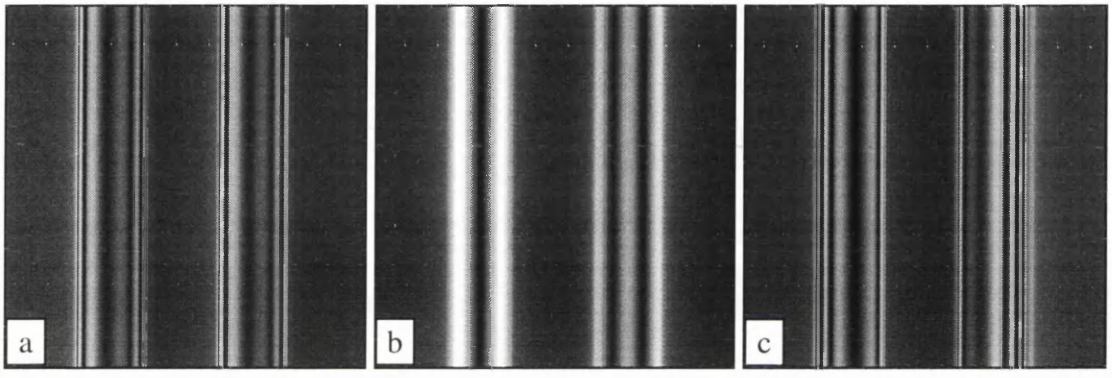

Figure 8.10 *CF images showing (a) the electrostatic component (b) the magnetic component and (c) the MFM tip when using the semi-infinite phase-shifting aperture.*

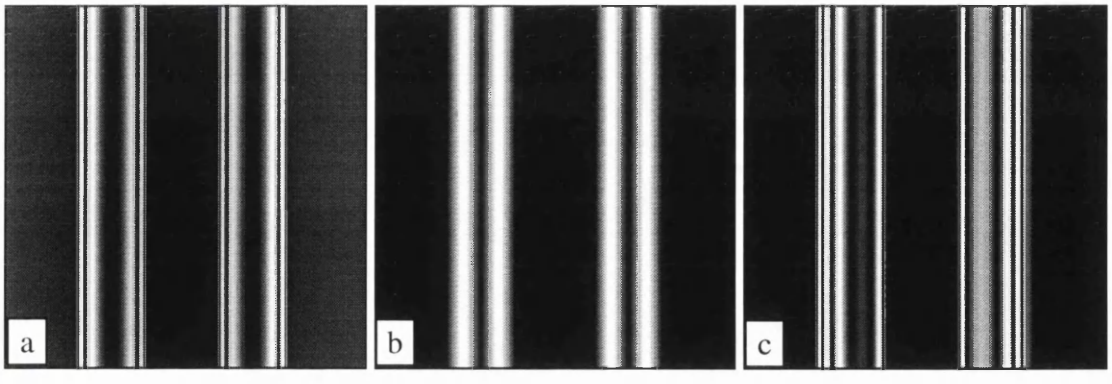

Figure 8.11 *CF images showing (a) the electrostatic component (b) the magnetic component and (c) the MFM tip when using the small hole phase-shifting aperture of 1 pixel in extent.*

The fringe patterns present in the simulated CF images of the MFM tips are very difficult to interpret. It would be favourable to re-create the phase function from the simulated images. Initially, a linescan could be taken from a two-dimensional simulated CF image to

be analysed. The re-created phase results would show discontinuities as the phase increments by 2π. Therefore we would have to add 2π to sections to create a continuous phase function. It is recommended that a simple magnetic phase function should be re-created before attempting the complex MFM case. With further development, analysis of experimental images could also be incorporated.

If it is possible to re-create the final phase functions we can reveal the magnetic and electrostatic components of the MFM tip after some image manipulation. Consider the phase functions for a MFM tip with a positive magnetisation $\phi_+(x)$ and the other with a negative magnetisation $\phi_-(x)$,

$$\phi_+(x) = \gamma x + \varepsilon\sqrt{r^2 - x^2} \qquad [8.7]$$

$$\phi_-(x) = -\gamma x + \varepsilon\sqrt{r^2 - x^2} \qquad [8.8]$$

Then by adding equations 8.7 and 8.8 we get,

$$\phi_+(x) + \phi_-(x) = 2\varepsilon\sqrt{r^2 - x^2} \qquad [8.9]$$

and if we subtract equation 8.7 from 8.8 we get,

$$\phi_+(x) - \phi_-(x) = 2\gamma x \qquad [8.10]$$

Therefore by adding these phase functions we can reveal the electrostatic contribution to the phase function and by subtracting them we can obtain the magnetic contribution.

8.3.3 Experimental CF imaging of MFM tips.

In this section we present some initial CF images of MFM tips which were acquired by L.J. Heyderman (University of Glasgow). In section 8.3 we discussed MFM tips which have been fabricated by coating a needle with a ferromagnetic material. Experimentally, the electrostatic spike is prepared by focusing an electron beam in a scanning electron microscope to make a pillar of hydrocarbon contamination. The ferromagnetic thin film is thermally evaporated Co-Cr of thickness ≈20nm.

The CM20 allows for the tips to be magnetised using a field of 6800Oe. The field is applied along the long (easy) axis and then reduced to zero. The magnetisation direction of the tips have aligned along the applied field direction. Figure 8.12a shows the CF image of two MFM tips obtained using an opaque aperture. Figure 8.12b shows the CF image after the field has been applied in the opposite direction, the opaque aperture has also to be placed in the complementary position. These CF images show fringes of the same generic form to what we predicted in the two-dimensional computer simulation.

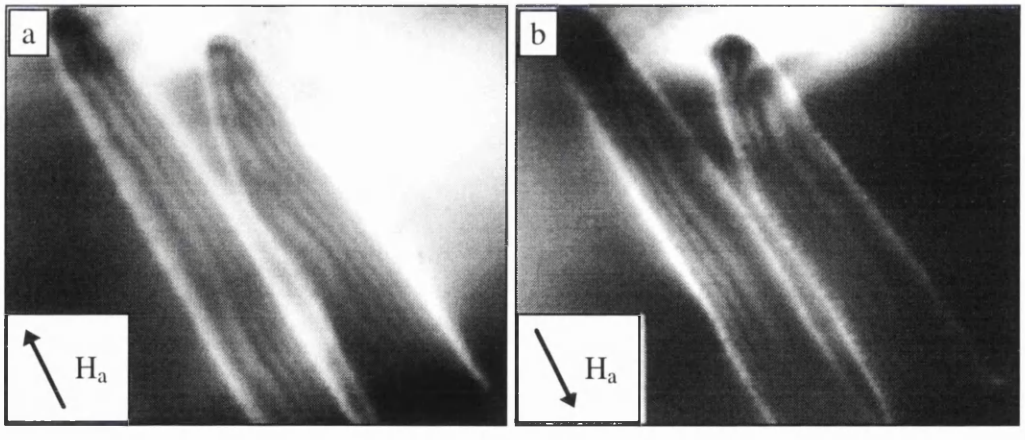

Figure 8.12 *CF images of two MFM tips when using the semi-infinite opaque aperture. The tips are magnetised along the direction of field. The aperture in (b) is in a complementary position.*

8.4 Ferrites.

In chapter 6 we investigated four Fe_3O_4 thin films of different thicknesses that contained a large anisotropy component which had a randomising effect on the moments. This study showed that as the sample thickness was increased, the crystallite size also increased. It was also clear from the initial Fresnel analysis that this was a complex system in which both magnetic and crystallite contrast were of the same order.

In-situ magnetising experiments were carried out on the 500Å thin film. We investigated the variation in image contrast as the sample was tilted. This showed that a maximum contrast condition was achieved when the in-plane component of the applied field was equal to the coercive field. We believe that the contrast in these images was mainly magnetic and, upon analysis, revealed no directionality. The typical domain size was estimated to be ≈83±2nm which corresponded to a distance of ≈2/3 crystallite diameters. Analysis of the Foucault images indicated domain sizes on a similar scale to these images, again showing no directionality.

We discussed the domain wall switching mechanism observed from video and subsequently revealed the magnetic changes in a system inhibited by crystallite contrast. Here domain walls were observed to "jump" a distance of ≈35nm which corresponds to the magnetisation switching in individual crystallites. We observed many crystallite moments to switch at once in a "domino toppling" type effect, typically over a distance of 150nm which corresponds to ≈4/5 neighbouring moments switching.

To further the analysis of these films we could implement differential phase contrast (DPC)[9] imaging, a form of scanning transmission electron microscopy (STEM). This Lorentz imaging mode maps the local orientation of the magnetic induction whilst suppressing the crystallite contrast. This could reveal the small scale domain configurations without the artefacts present in the Foucault images. This will hopefully clarify how the individual crystallites couple in this complex magnetic system and could lead to further information on the local anisotropy.

Ideally we would like to investigate the single crystal Fe_3O_4 thin films which have been discussed in section 8.0. To do this we would have to remove the MgO substrate material. If this can be achieved it would leave a sample containing magnetic contrast without the unwanted crystallite contributions, which is readily amenable to TEM investigations. Initial attempts have been made to dissolve the MgO in water but the fragile thinner regions of the thin film tended to break off. This has been proved to be unsuccessful because MgO is fairly insoluble in water. There are other approaches would could prove to be more fruitful. We could collaborate with the Chemistry department to see if there are any chemical etches available which can remove the MgO substrate whilst having no adverse effect on the Fe_3O_4. Alternatively, we could mechanically mill the MgO down to $\approx$10μm and then ion-beam mill through the sample to give suitable regions for TEM analysis. One final suggested method would be to reactive-ion etch the specimen to remove all but 20nm of the MgO and leave the Fe_3O_4 thin film untouched.

8.5 Granular thin films.

In chapter 7 we discussed the TEM techniques which can be used to investigate granular thin films. STEM has been introduced, emphasising the high-angle annular dark field (HADF) imaging mode and the implementation of energy dispersive x-ray microanalysis. The latter technique is further discussed to give a description of the analysis techniques required to obtain information on the local atomic compositions.

Two sets of NiFe-Ag thin films prepared by r.f. sputtering have been investigated. Phase segregation was promoted by rapidly thermally annealing the films once deposited. The first set of samples were of similar compositions, one which was in the as-deposited state and the other annealed at 450°C for 10 minutes. The diffraction patterns showed <111> texturing of the samples. Bright field images confirmed a wide distribution of crystallite sizes, from 5-20nm, with the annealed film displaying greater contrast and more distinctly defined phase boundaries. High angle annular dark field images showed both lighter Ag-rich and darker NiFe-rich regions, which were analysed by EDX in order to obtain atomic composition. The second set of samples where of identical compositions but subjected to

various annealing conditions. Diffraction analysis showed the phase segregation of the ferromagnetic materials from the Ag matrix on annealing and identified the formation of NiFe rings in the samples which had been subjected to greater post-annealing temperatures. Bright field images revealed the crystallite sizes, typically 5-20nm, and the enhanced order present in the specimen annealed at 750°C for 1 second.

In the near future we could investigate a new set of three NiFe-Ag granular thin films of identical compositions, one of which is in the as-deposited state and the other two annealed to 350°C and 700°C respectively. These samples should also show good GMR properties and be prepared on Si_3N_4 window substrates. We could then use the techniques discussed in this thesis to identify the crystallite structure and compositional inhomogeneities. We could then attempt to correlate the results with the GMR data. This could help in the search for the ideal granular structure showing good GMR properties. It would be unsuitable to attempt this kind of analysis on the results presented in this study due to the poor GMR properties of these films and in that we could not obtain accurate compositional information from the second set of specimen.

One final experiment would be to cool the specimen with the highest percentage of ferromagnetic material in an attempt to reveal the magnetic microstructure present in this system. This could be achieved experimentally by using the cooling rod on the CM20 (section 2.1.6) to reduce the sample temperature to ≈90K. Previous studies[10] of granular specimen have revealed the magnetic microstructure present in Co-Ag thin films. This was achieved by using scanning electron microscopy with polarisation analysis (SEMPA)[11].

References

[1] B. Dieny, Europhys. Lett. **17**, 261 (1992).

[2] G.B. Schaffer and P.G. McCormick, Appl. Phys. Lett, **55**,45 (1989).

[3] H. Yang and P.G. McCormick, J. Solid State Chem., **110**, 136 (1994).

[4] P. Grutter, H.J. Mamin, and D. Rugar, Springer Series in Surface Science, **Vol. 28**, 151, Springer-Verlag, Berlin, Heidelberg (1992).

[5] W. Rave, L. Belliard, M. Labrune, A. Thiaville and J. Miltat, IEEE Trans. Mag., **Vol. 30**, No. 6, Pt. 1, 4473 (1994).

[6] K. Babcock, V. Elings, M. Dugas and S. Loper, IEEE Trans. Mag., **Vol. 30**, No. 6, Pt 1., 4503 (1994).

[7] M. Ruhrig, S. Porthun and J.C. Lodder, Rev. Sci. Inst., **Vol. 65**, No. 10, 3224 (1994).

[8] M Gajdardzidka-Josefovska, M.R. McCartney, W.J. Ruijter, D.J. Smith, J.K. Weiss and J.M. Zuo, Ultramicroscopy, **50**, p285 (1993).

[9] J.N. Chapman, J. Phys. D.: Appl. Phys., **17**, 623 (1984).

[10] A. Garvin, M.H. Kelley, J.Q. Xiao and C.L. Chen, Appl. Phys. Lett. **66**, 13, 1683 (1995).

[11] M.R. Scheinfein, J. Unguris, M.H. Kelly, D.T. Pierce and R.J. Celotta, Rev. Sci. Instrum. **61**, 2501, (1990).

Appendix A

Physical Parameters

When looking at the graphical representations in the diffraction and imaging planes, typical values of the parameters of a small permalloy element are used.

$L=1\mu m$	L is the width of the element.
$e=1.602*10^{-19}C$	e is the electronic charge.
$B_0=1T$	B_0 is the magnetic induction.
$t=50nm$	t is the thickness of the sample.
$\hbar = \frac{h}{2\pi} = 1.055*10^{-34}Js$	h is Plank's constant.

Appendix B

Fourier Transform and Convolution definition.

The form of the Fourier transform[1] used throughout the analytical calculations is,

$$\Im[a(x)] = \frac{1}{\sqrt{2\pi}} \int_{-\infty}^{\infty} a(x) e^{ikx} dx \qquad [B.1]$$

where $a(x)$ is an arbitrary function of x.

The convolution ($\otimes$) of two functions $C(x)$ and $D(x)$ is given by:

$$C(x) \otimes D(x) = \frac{1}{\sqrt{2\pi}} \int_{-\infty}^{\infty} C(X - x) D(X) dX = \Im[c(k) d(k)] \qquad [B.2]$$

where $C(x)$ and $D(x)$ are arbitrary functions of x, transforming to $c(k)$ and $d(k)$ in frequency space.

Useful Fourier Transforms.

$$\Im\left[e^{i\gamma x}\right] = \sqrt{2\pi}\delta(k + \gamma) \qquad [B.3]$$

$$\Im\left[e^{-i\gamma x}\right] = \sqrt{2\pi}\delta(k - \gamma) \qquad [B.4]$$

$$\Im[h(x)] = \frac{\sqrt{2\pi}}{2}\delta(k) - \frac{i}{\sqrt{2\pi}k} \qquad [B.5]$$

$$\Im[\mathrm{sgn}(x)] = -\sqrt{\frac{\pi}{2}}\frac{i}{k} \qquad [B.6]$$

$$\Im[S_+(x)] = \frac{1}{\sqrt{2\pi ik}}\left(e^{\frac{ikL}{2}} - 1\right) \qquad [B.7]$$

$$\Im[S_-(x)] = \frac{1}{\sqrt{2\pi ik}}\left(1 - e^{\frac{-ikL}{2}}\right) \qquad [B.8]$$

$$\Im[S_+(x) + S_-(x)] = \frac{1}{\sqrt{2\pi}} L\,\mathrm{sinc}\left(\frac{kL}{2}\right) \qquad [B.9]$$

Fast Fourier transforms (FFT) considerations

First we have to choose the size of "window" on the specimen which we wish to simulate. In one-dimension this window is broken down into an array of W points which are of a length Δx, the real space sampling interval. These parameters should be chosen such that no feature of interest is smaller than $2\Delta x$. The fast Fourier transform (FFT) can now be safely performed on the array to give sensible results.

The FFT is a function which numerically calculates a Fourier transform. The FFT gives a reciprocal space maximum of $k_{max}=1/2\Delta x$. Therefore, the minimum sampling frequency in reciprocal space is $\Delta k=1/2W\Delta x$. If any feature is smaller than $2\Delta x$ the corresponding FFT will "rap around" to give unwanted artefact peaks in frequency space. It is also favourable that the high frequencies in reciprocal space be zero. This ensures an artefact free image if a second FFT is to be performed.

To check that the FFT is functioning correctly it is worthwhile doing a quick test. In real space create a function to represent a sin wave of a known periodicity. Then FFT this function which should show two spikes located at the ±frequencies in reciprocal space.

References

[1] Gradshteyn and Ryzhik, 'Table of integrals, series and products', Academic Press (1980).

Appendix C

Investigation of conjugate aperture positions

This section gives an in-depth analytical account of CF imaging using the semi-infinite thin film as the object. The diffraction pattern is given by equation 3.8/C1,

$$\overline{\Psi}(k)=\frac{\sqrt{2\pi}}{2}\delta(k)+\frac{\sqrt{2\pi}}{2}\delta(k-\gamma)+\frac{i}{\sqrt{2\pi}k}-\frac{i}{\sqrt{2\pi}(k-\gamma)} \qquad [C.1]$$

Equation C1/3.8 is discussed in section 3.2. Here the conjugate aperture positions are discussed (figure 3.13).

Conjugate position 4

When masking at conjugate position 4 all spatial frequencies $k>\gamma$ are removed. The assumption has been made that only half of the magnetic spot has been affected by the Heaviside function. All other terms are negligible at this point.

$$\overline{\Psi}_{c4}(k)=\frac{\sqrt{2\pi}}{2}\delta(k)+\frac{\sqrt{2\pi}}{2}\delta(k-\gamma)+\frac{i}{\sqrt{2\pi}k}-\frac{i}{\sqrt{2\pi}(k-\gamma)}\left[1-h(k-\gamma)\right] \qquad [C.2]$$

Taking the Fourier transform to give the modified complex image.

$$\Psi_{c4}(x)=1+h(x)\left[e^{i\gamma x}-1\right]+\frac{1}{4}e^{i\gamma x}\,\mathrm{sgn}(x)-\Delta(x) \qquad [C.3]$$

where $\Delta(x)$ is the error function (equation 2.11) and is considered negligible away from the origin. The image (figure 3.14a) in the region $x>0$ shows a constant intensity of 9/16.

For $x<0$ the image is of the form of equation 3.12 with $\mu=17/16$ and $\nu=1/2$. The free space region shows fringes with a periodicity of h/eB_0t.

$$\Psi_{c4}(x)=1+h(x)\left[e^{i\gamma x}-1\right]+\frac{1}{4}e^{i\gamma x}\,\mathrm{sgn}(x) \qquad [C.4]$$

Conjugate position 3

When masking at conjugate position 3 all spatial frequencies $k\geq\gamma$ are removed. The assumption has been made that half of the magnetic spot and the delta function at $k=\gamma$ have been removed by the Heaviside function. All other terms are negligible at this point.

$$\overline{\Psi}_{c3}(k)=\frac{\sqrt{2\pi}}{2}\delta(k)+\frac{i}{\sqrt{2\pi}k}-\frac{i}{\sqrt{2\pi}(k-\gamma)}\left[1-h(k-\gamma)\right] \qquad [C.5]$$

Taking the Fourier transform to give the modified image.

$$\Psi_{c3}(x)=1+h(x)\left[e^{i\gamma x}-1\right]-\frac{1}{2}e^{i\gamma x}-\frac{1}{4}e^{i\gamma x}\,\mathrm{sgn}(x)-\Delta(x) \qquad [C.6]$$

where $\Delta(x)$ is the error function (equation 2.11) and is considered to be negligible away from the origin. The image (figure 3.14b) in the region $x>0$ shows a constant intensity of 1/16. The free space region $x<0$ shows fringes of the same generic form as equation 3.12, with the constants $\mu=17/16$ and $\nu=-1/2$.

Conjugate position 2

When masking at conjugate position 2 all spatial frequencies $k>0$ are removed. The assumption has been made that all of the magnetic spot, the delta function at $k=\gamma$ and half of the central spot have been removed by the aperture.

$$\overline{\Psi}_{c2}(k) = \frac{\sqrt{2\pi}}{2}\delta(k) + \frac{i}{\sqrt{2\pi}k}[1 - h(k)] \qquad [C.7]$$

Taking the Fourier transform to give the modified image.

$$\Psi_{c2}(x) = 1 - h(x) + \frac{1}{4}\mathrm{sgn}(x) + \Delta(x) \qquad [C.8]$$

where $\Delta(x)$ is the error function (equation 2.11) and is considered to be negligible away from the origin. The image (figure 3.14c) shows in the region $x>0$ a constant intensity of 1/16 and for $x<0$ a constant intensity of 9/16.

Conjugate position 1

When masking at conjugate position 4 all spatial frequencies $k\geq 0$ are removed. Only half of the central spot passes unaffected with all other terms removed.

$$\overline{\Psi}_{c1}(k) = \frac{i}{\sqrt{2\pi}k}[1 - h(k)] \qquad [C.9]$$

Taking the Fourier transform to give the modified image.

$$\Psi_{c1}(x) = \frac{1}{2} - h(x) + \frac{1}{4}\mathrm{sgn}(x) + \Delta(x) \qquad [C.10]$$

where $\Delta(x)$ is given by equation 2.11 and is considered negligible away from the origin. the same as in masking at position 1. The image (figure 3.14c) shows a constant intensity of 1/16 in all regions.

Appendix D EDX compositional analysis.

Specimen D1

Labels	STRB	Bg2	AgL	Bg4	Bg5	FeKa	NiKa	Bg9	Bg20	AgKa	Bg24
Centre energy	0.01	2.23	3.19	4.45	5.75	6.41	7.49	9.25	20.97	22.07	23.47
Width chans	20	9	35	16	9	12	8	22	20	21	15
iabj1.SP ."	16188	1702	39069	1378	645	1302	2297	1183	483	5193	280
iabj2.SP ."	16262	1629	40393	1617	648	1273	2250	1217	482	5522	247
iabj3.SP ."	16347	1614	37573	1411	631	1316	2303	1114	451	5117	289
iabj4.SP ."	16566	1685	33539	1204	556	1189	2167	968	409	4462	230
iabj5.SP ."	16564	1389	31604	1186	542	1145	2189	866	359	4342	223
iabj6.SP ."	17366	876	18607	700	346	765	1886	579	247	2620	138
iabj7.SP ."	17496	934	18101	683	333	813	1776	569	227	2523	131
iabj8.SP ."	16711	1288	28680	1099	481	1056	2530	850	374	3941	197
iabj9.SP ."	17003	1185	23810	899	417	1088	2429	722	279	3204	176
iabj10.SP	17010	1327	24633	993	404	1046	2535	727	301	3283	167
iabj11.SP	16956	1295	25156	938	436	1131	2474	711	323	3411	160
iabj12.SP	17174	1184	24414	991	418	1154	2744	718	313	3221	202
iabj13.SP	17179	1196	24169	928	432	1145	2542	745	312	3242	172
iabj14.SP	16995	1248	24469	941	406	1178	2974	678	311	3233	186
iabj15.SP	17025	1255	25319	1019	419	1191	2640	713	281	3424	174
iabj16.SP	16359	2323	40975	1481	665	1329	2510	1147	505	5495	305
iabj17.SP	16380	1781	42037	1462	695	1451	2653	1192	480	5866	304
iabj18.SP	16279	2037	42575	1597	707	1362	2273	1137	530	5765	299
iabj19.SP	16545	1524	31899	1208	573	1079	2199	910	376	4210	221
iabj20.SP	16601	1771	32170	1226	503	1176	2219	856	388	4264	217
iabj21.SP	17281	1005	20982	806	350	919	1923	623	266	2891	150
iabj22.SP	16877	1370	28839	1058	564	1246	2709	833	367	3819	193
iabj23.SP	16812	1324	28288	1101	505	1188	2744	793	361	3783	216
iabj24.SP	16578	1449	28975	1080	494	1304	2750	903	347	3932	174
iabj25.SP	16879	1350	27891	1058	517	1214	2653	867	362	3843	205

Using the Ka peaks for Fe, Ni and Ag

	Nett Counts				Counts		
Filename	AgL	FeKa	NiKa	AgKa	Fe/Ni	Fe/Ag	Ni/Ag
iabj1.SP ."	34252.37	549.3636	1795.242	4743.425	0.306011	0.115816	0.37847
iabj2.SP ."	35456.91	509.0909	1740.727	5096.05	0.292459	0.099899	0.341584
iabj3.SP ."	32891.39	591.5152	1820.01	4677.925	0.325007	0.126448	0.389064
iabj4.SP ."	28945.74	554.3333	1743.889	4086.275	0.317872	0.135657	0.426767
iabj5.SP ."	27605.98	547.4848	1790.657	3997.425	0.305745	0.136959	0.447953
iabj6.SP ."	16138.04	376.4242	1626.949	2393.725	0.231368	0.157255	0.679673
iabj7.SP ."	15537.86	435.8182	1524.545	2312.125	0.285868	0.188492	0.65937
iabj8.SP ."	24973.52	503.5152	2161.677	3606.75	0.232928	0.139604	0.599342
iabj9.SP ."	20522.55	613.0909	2112.394	2934.325	0.290235	0.208938	0.719891
iabj10.SP	20966.63	578.3939	2223.263	3008.075	0.260155	0.19228	0.739098
iabj11.SP	21612.01	646.4242	2150.949	3129.425	0.30053	0.206563	0.687331
iabj12.SP	21027.87	679.5152	2427.677	2915.275	0.279903	0.233088	0.832744
iabj13.SP	20828.44	653.8182	2214.545	2957.8	0.295238	0.221049	0.748714
iabj14.SP	21013.11	722.4242	2670.283	2939.525	0.270542	0.245762	0.908406
iabj15.SP	21764.19	717.2121	2324.141	3154.675	0.308592	0.227349	0.736729
iabj16.SP	34838.21	572.8485	2005.899	5016.375	0.285582	0.114196	0.39987
iabj17.SP	36974.88	662.5758	2127.384	5401.2	0.311451	0.122672	0.393872
iabj18.SP	36867.45	580.5758	1752.051	5277.45	0.331369	0.110011	0.331988
iabj19.SP	27614.42	448.8182	1778.879	3857.9	0.252304	0.116337	0.4611
iabj20.SP	27385.45	607.2121	1839.808	3908.4	0.330041	0.155361	0.470732
iabj21.SP	18146.27	515.7576	1654.172	2646.35	0.311792	0.194894	0.625077
iabj22.SP	25017.92	642.8182	2306.879	3491.225	0.278653	0.184124	0.660765
iabj23.SP	24509.34	635.0606	2375.374	3442.275	0.267352	0.184489	0.690059
iabj24.SP	24976.25	728.3939	2366.263	3628.025	0.307825	0.200769	0.652218
iabj25.SP	24108.81	632.8788	2265.586	3509.45	0.279344	0.180336	0.645567

Atomic Percentage			Weight Percentage		
K(Fe/Ag)	K(Ni/Ag)	K(Fe/Ni)	K'(Fe/Ag)	K'(Ni/Ag)	K'(FeNi)
0.262727	0.266076	0.987413	0.136023	0.14477	0.93958
R1	R2				
Fe/Ag	Ni/Ag	Fe/Ni	Fe/Ag	Ni/Ag	Fe/Ni
0.030428	0.100702	0.302159	0.015754	0.054791	0.287522
0.026246	0.090887	0.288777	0.013589	0.049451	0.274788
0.033221	0.103521	0.320916	0.0172	0.056325	0.30537
0.035641	0.113553	0.313871	0.018453	0.061783	0.298666
0.035983	0.11919	0.301897	0.01863	0.06485	0.287272
0.041315	0.180845	0.228456	0.02139	0.098396	0.217389
0.049522	0.175443	0.282269	0.025639	0.095457	0.268596
0.036678	0.159471	0.229996	0.018989	0.086767	0.218855
0.054894	0.191546	0.286582	0.02842	0.104219	0.272699
0.050517	0.196657	0.256881	0.026155	0.106999	0.244437
0.05427	0.182883	0.296747	0.028097	0.099505	0.282372
0.061239	0.221574	0.27638	0.031705	0.120556	0.262992
0.058076	0.199215	0.291522	0.030068	0.108391	0.2774
0.064568	0.241706	0.267137	0.033429	0.13151	0.254196
0.059731	0.196026	0.304708	0.030925	0.106656	0.289947
0.030002	0.106396	0.281987	0.015533	0.057889	0.268327
0.032229	0.1048	0.307531	0.016686	0.057021	0.292633
0.028903	0.088334	0.327198	0.014964	0.048062	0.311348
0.030565	0.122688	0.249128	0.015825	0.066753	0.23706
0.040818	0.125251	0.325887	0.021133	0.068148	0.3101
0.051204	0.166318	0.307867	0.02651	0.090492	0.292954
0.048374	0.175814	0.275145	0.025045	0.095659	0.261817
0.04847	0.183609	0.263987	0.025095	0.0999	0.251198
0.052747	0.17354	0.30395	0.027309	0.094422	0.289226
0.047379	0.17177	0.275828	0.02453	0.093459	0.262466

Light s = Staitonary electron probe in a light area
Dark s = Stationary electron probe in a dark area
Light a = Electron probe rastered accross a light area
Light a = Electron probe rastered accross a dark area
Area = Electron probe rastered accross the matrix to determine mean composition

Type	Spectra	At%Fe	At%Ni	At%Ag	Wt%Fe	Wt%Ni	Wt%Ag
light s	iabj1.SP ."	2.69	8.90	88.41	1.47	5.12	93.41
light s	iabj2.SP ."	2.35	8.14	89.51	1.28	4.65	94.07
light s	iabj3.SP ."	2.92	9.11	87.97	1.60	5.25	93.15
light s	iabj4.SP ."	3.10	9.88	87.02	1.71	5.72	92.57
light s	iabj5.SP ."	3.11	10.32	86.57	1.72	5.99	92.30
dark s	iabj6.SP ."	3.38	14.80	81.82	1.91	8.79	89.30
dark s	iabj7.SP ."	4.04	14.32	81.63	2.29	8.51	89.20
dark s	iabj8.SP ."	3.07	13.33	83.60	1.72	7.85	90.44
dark s	iabj9.SP ."	4.40	15.37	80.23	2.51	9.20	88.29
dark s	iabj10.SP	4.05	15.77	80.18	2.31	9.44	88.25
dark a	iabj11.SP	4.39	14.78	80.83	2.49	8.82	88.68
dark a	iabj12.SP	4.77	17.27	77.95	2.75	10.46	86.79
dark a	iabj13.SP	4.62	15.84	79.54	2.64	9.52	87.84
dark a	iabj14.SP	4.94	18.50	76.55	2.87	11.29	85.84
dark a	iabj15.SP	4.76	15.61	79.63	2.72	9.38	87.91
light a	iabj16.SP	2.64	9.36	88.00	1.45	5.39	93.16
light a	iabj17.SP	2.83	9.22	87.95	1.55	5.31	93.14
light a	iabj18.SP	2.59	7.91	89.51	1.41	4.52	94.07
light a	iabj19.SP	2.65	10.64	86.71	1.46	6.17	92.37
light a	iabj20.SP	3.50	10.74	85.76	1.94	6.26	91.80
area	iabj21.SP	4.21	13.66	82.13	2.37	8.10	89.53
area	iabj22.SP	3.95	14.36	81.69	2.23	8.54	89.23
area	iabj23.SP	3.93	14.90	81.16	2.23	8.88	88.89
area	iabj24.SP	4.30	14.15	81.55	2.43	8.42	89.15
area	iabj25.SP	3.89	14.09	82.02	2.19	8.36	89.45

		Atomic Percentage			Weight Percentage		
"Colour"		Fe	Ni	Ag	Fe	Ni	Ag
dark s	average	3.79	14.72	81.49	2.15	8.76	89.10
	sd	0.55	0.95	1.40	0.32	0.62	0.90
light s	average	2.84	9.27	87.90	1.56	5.34	93.10
	sd	0.32	0.85	1.16	0.18	0.52	0.70
dark a	average	4.70	16.40	78.90	2.69	9.89	87.41
	sd	0.21	1.48	1.66	0.14	0.98	1.11
light a	average	2.84	9.57	87.58	1.56	5.53	92.91
	sd	0.38	1.17	1.42	0.22	0.71	0.86
area/mix	average	4.06	14.23	81.71	2.29	8.46	89.25
	sd	0.19	0.45	0.39	0.10	0.28	0.25

Specimen H1

Labels	STRB	Bg2	AgL	Bg4	Bg5	FeKa	NiKa	Bg9	Bg20	AgKa	Bg24
Centre energy	0.01	2.23	3.19	4.45	5.75	6.41	7.49	9.25	20.97	22.07	23.47
Width chans	20	9	35	16	9	12	8	22	20	21	15
JABJ1.SP ."	17955	1145	14784	579	263	502	648	426	210	2028	120
JABJ2.SP ."	18144	1010	13164	521	240	433	705	351	191	1773	105
JABJ3.SP ."	18164	998	13511	569	232	477	563	379	168	1822	96
JABJ4.SP ."	18206	924	14028	504	269	485	600	406	180	1929	122
JABJ5.SP ."	18290	1210	14016	521	277	473	607	428	195	1861	122
JABJ6.SP ."	18982	420	5610	268	108	352	691	200	85	720	56
JABJ7.SP ."	18769	448	5642	305	136	505	2324	214	111	726	50
JABJ8.SP ."	18875	405	7026	346	169	396	1828	269	119	874	62
JABJ9.SP ."	18814	492	7449	307	154	365	560	231	128	989	74
JABJ10.SP	18980	442	6300	273	141	365	1283	226	114	843	56
JABJ11.SP	18432	754	10198	421	186	471	920	332	144	1356	68
JABJ12.SP	18577	724	9954	413	190	401	899	312	157	1289	65
JABJ13.SP	18612	743	9335	420	211	399	874	288	132	1358	76
JABJ14.SP	18464	677	9491	407	183	379	824	286	133	1295	63
JABJ15.SP	18595	647	9092	378	158	413	903	276	125	1163	84
JABJ16.SP	17825	1384	17408	684	306	529	682	548	235	2382	134
JABJ17.SP	17794	1236	16697	703	312	539	774	555	231	2248	111
JABJ18.SP	18063	1373	15119	567	272	525	690	456	170	2042	140
JABJ19.SP	18055	1248	15071	605	282	513	800	462	212	2068	111
JABJ20.SP	18150	1091	13496	547	232	478	800	447	181	1815	94
JABJ21.SP	18802	454	4247	340	135	529	4932	237	128	606	62
JABJ22.SP	19095	627	6038	298	114	312	772	222	94	752	52
JABJ23.SP	18790	490	6710	290	133	291	1956	272	112	875	73
JABJ24.SP	18892	366	6251	242	131	392	576	214	70	789	42
JABJ25.SP	19024	362	5438	240	121	307	1121	214	87	725	40

Using the Ka peaks for Fe, Ni and Ag

		Nett Counts			Counts		
Filename	AgL	FeKa	NiKa	AgKa	Fe/Ni	Fe/Ag	Ni/Ag
JABJ1.SP ."	11924.33	210.4848	453.6566	1833.75	0.463974	0.114784	0.247393
JABJ2.SP ."	10630.27	177.2727	534.5152	1599.225	0.331651	0.110849	0.334234
JABJ3.SP ."	10948.1	218.9697	390.9798	1666.6	0.560054	0.131387	0.234597
JABJ4.SP ."	11680.08	194.9394	406.6263	1749.1	0.479407	0.111451	0.232477
JABJ5.SP ."	11093.38	171.6061	406.0707	1673.225	0.422601	0.10256	0.242687
JABJ6.SP ."	4500.208	225.4545	606.6364	636.175	0.371647	0.354391	0.953568
JABJ7.SP ."	4437.295	355.9697	2224.646	632.725	0.160012	0.562598	3.515977
JABJ8.SP ."	5860.063	209.9697	1703.98	768.125	0.123223	0.273354	2.218363
JABJ9.SP ."	6156.552	199.3333	449.5556	870	0.443401	0.229119	0.516731
JABJ10.SP	5141.962	209.3636	1179.242	743.95	0.177541	0.281422	1.58511
JABJ11.SP	8271.42	256.4545	776.9697	1232.8	0.33007	0.208026	0.630248
JABJ12.SP	8094.503	189.2424	757.8283	1161.075	0.249717	0.162989	0.652695
JABJ13.SP	7430.903	179.7879	727.8586	1235.5	0.247009	0.145518	0.589121
JABJ14.SP	7729.455	179	690.6667	1181.075	0.25917	0.151557	0.584778
JABJ15.SP	7420.507	232.3939	782.596	1038.575	0.296953	0.223762	0.753529
JABJ16.SP	13968.76	175.5455	446.3636	2164.825	0.393279	0.08109	0.206189
JABJ17.SP	13524.76	179.6364	534.4242	2049.025	0.336131	0.087669	0.260819
JABJ18.SP	11829.12	219.303	486.202	1854.75	0.451053	0.118239	0.262139
JABJ19.SP	11982.61	199	590.6667	1879	0.336907	0.105907	0.314352
JABJ20.SP	10776.33	201.4242	615.6162	1654.175	0.327191	0.121767	0.372159
JABJ21.SP	2992.347	374.3636	4828.909	495.4	0.077526	0.75568	9.747495
JABJ22.SP	4492.896	175.4545	680.9697	666.25	0.257654	0.263346	1.022093
JABJ23.SP	5440.035	128.1515	1847.434	765.1	0.069367	0.167496	2.414631
JABJ24.SP	5274.646	246.303	478.8687	722.85	0.514344	0.340739	0.662473
JABJ25.SP	4471.611	167.9697	1028.313	651.325	0.163345	0.257889	1.578802

Atomic Percentage

K(Fe/Ag)	K(Ni/Ag)	K(Fe/Ni)
0.262727	0.266076	0.987413

Weight Percentage

K'(Fe/Ag)	K'(Ni/Ag)	K'(FeNi)
0.136023	0.14477	0.93958

R1	R2	
Fe/Ag	Ni/Ag	Fe/Ni
0.030157	0.065825	0.458134
0.029123	0.088932	0.327477
0.034519	0.062421	0.553004
0.029281	0.061857	0.473372
0.026945	0.064573	0.417282
0.093108	0.253722	0.366969
0.14781	0.935519	0.157998
0.071817	0.590254	0.121672
0.060196	0.13749	0.43782
0.073937	0.42176	0.175306
0.054654	0.167694	0.325915
0.042822	0.173667	0.246573
0.038232	0.156751	0.2439
0.039818	0.155596	0.255908
0.058788	0.200496	0.293215
0.021305	0.054862	0.388329
0.023033	0.069398	0.3319
0.031065	0.069749	0.445376
0.027825	0.083642	0.332667
0.031992	0.099023	0.323073
0.198538	2.593579	0.07655
0.069188	0.271955	0.254411
0.044006	0.642477	0.068494
0.089521	0.176269	0.507869
0.067755	0.420082	0.161289

Fe/Ag	Ni/Ag	Fe/Ni
0.015613	0.035815	0.435941
0.015078	0.048387	0.311613
0.017872	0.033963	0.526215
0.01516	0.033656	0.450441
0.013951	0.035134	0.397068
0.048205	0.138048	0.349192
0.076526	0.509008	0.150344
0.037182	0.321152	0.115778
0.031165	0.074807	0.416611
0.03828	0.229476	0.166814
0.028296	0.091241	0.310127
0.02217	0.094491	0.234629
0.019794	0.085287	0.232085
0.020615	0.084658	0.243511
0.030437	0.109088	0.279011
0.01103	0.02985	0.369517
0.011925	0.037759	0.315822
0.016083	0.03795	0.423801
0.014406	0.045509	0.316552
0.016563	0.053877	0.307422
0.10279	1.411145	0.072841
0.035821	0.147968	0.242087
0.022783	0.349566	0.065176
0.046348	0.095906	0.483267
0.035079	0.228563	0.153476

Type	Spectra	At%Fe	At%Ni	At%Ag	Wt%Fe	Wt%Ni	Wt%Ag
light a	JABJ1.SP ."	2.75	6.01	91.24	1.48	3.41	95.11
light a	JABJ2.SP ."	2.60	7.95	89.44	1.42	4.55	94.03
light a	JABJ3.SP ."	3.15	5.69	91.16	1.70	3.23	95.07
light a	JABJ4.SP ."	2.68	5.67	91.65	1.45	3.21	95.35
light a	JABJ5.SP ."	2.47	5.92	91.62	1.33	3.35	95.32
dark a	JABJ6.SP ."	6.91	18.84	74.25	4.06	11.64	84.30
dark a	JABJ7.SP ."	7.09	44.91	48.00	4.83	32.10	63.07
dark a	JABJ8.SP ."	4.32	35.51	60.17	2.74	23.64	73.62
dark a	JABJ9.SP ."	5.03	11.48	83.49	2.82	6.76	90.42
dark a	JABJ10.SP	4.94	28.20	66.86	3.02	18.10	78.88
area	JABJ11.SP	4.47	13.72	81.81	2.53	8.15	89.32
area	JABJ12.SP	3.52	14.28	82.20	1.99	8.46	89.55
area	JABJ13.SP	3.20	13.12	83.68	1.79	7.72	90.49
area	JABJ14.SP	3.33	13.02	83.65	1.87	7.66	90.48
area	JABJ15.SP	4.67	15.92	79.41	2.67	9.57	87.76
light s	JABJ16.SP	1.98	5.10	92.92	1.06	2.87	96.07
light s	JABJ17.SP	2.11	6.35	91.54	1.14	3.60	95.27
light s	JABJ18.SP	2.82	6.34	90.84	1.53	3.60	94.87
light s	JABJ19.SP	2.50	7.53	89.97	1.36	4.29	94.35
light s	JABJ20.SP	2.83	8.76	88.42	1.55	5.03	93.42
dark s	JABJ21.SP	5.24	68.39	26.37	4.09	56.13	39.78
dark s	JABJ22.SP	5.16	20.28	74.56	3.03	12.50	84.47
dark s	JABJ23.SP	2.61	38.10	59.30	1.66	25.47	72.87
dark s	JABJ24.SP	7.07	13.93	79.00	4.06	8.40	87.55
dark s	JABJ25.SP	4.55	28.23	67.21	2.78	18.09	79.14

		Atomic Percentage			Weight Percentage		
"Colour"		Fe	Ni	Ag	Fe	Ni	Ag
dark s	average	4.93	33.79	61.29	3.12	24.12	72.76
	sd	1.60	21.35	20.91	1.01	19.01	19.26
light s	average	2.45	6.81	90.74	1.33	3.88	94.80
	sd	0.39	1.38	1.69	0.22	0.82	0.99
dark a	average	5.66	27.79	66.55	3.49	18.45	78.06
	sd	1.26	13.22	13.52	0.92	9.96	10.45
light a	average	2.73	6.25	91.02	1.48	3.55	94.98
	sd	0.26	0.97	0.91	0.14	0.57	0.54
area/mix	average	3.84	14.01	82.15	2.17	8.31	89.52
	sd	0.68	1.18	1.75	0.40	0.78	1.12